A VIRTUAL ENVIRONMENT SYSTEM FOR THE STUDY OF HUMAN ARM TREMOR

by

Bernard Dov Adelstein

B.Eng. in Mechanical Engineering, McGill University (1978)

S.M. in Mechanical Engineering, M.I.T. (1981)

SUBMITTED TO THE DEPARTMENT OF
MECHANICAL ENGINEERING
IN PARTIAL FULFILLMENT OF THE REQUIREMENTS
FOR THE DEGREE OF

DOCTOR OF PHILOSOPHY

at the

MASSACHUSETTS INSTITUTE OF TECHNOLOGY

June 1989

Signature of Author_____
Department of Mechanical Engineering
May 19, 1989

Certified by_____
Michael J. Rosen
Thesis Supervisor

Accepted by_____
Ain A. Sonin
Chairman, Departmental Committee on Graduate Studies

A VIRTUAL ENVIRONMENT SYSTEM FOR THE STUDY OF HUMAN ARM TREMOR

by

Bernard Dov Adelstein

Submitted to the Department of Mechanical Engineering
on May 19, 1989 in partial fulfillment of the requirements
for the Degree of Doctor of Philosophy

ABSTRACT

Understanding the causes of different tremor types can provide insight into the function of the normal and pathological neuromuscular system, and is essential for definitive diagnosis and effective treatment. The most frequently employed experimental technique to distinguish among hypothesized tremogenic mechanisms has been observation of the influence of peripheral mechanical loading on oscillation characteristics. To date, research has focused on the mechanisms of single joint tremors occurring primarily during the maintenance of static postures.

This thesis describes the design and implementation of a virtual environment system for the study of whole arm (two joint) tremor during voluntary movement. The system consists of a manual interface to apply controlled two degree of freedom mechanical loads and a video display for the presentation of volitional arm tasks.

The manual interface for the virtual environment is in essence a backdriveable electromechanical manipulator. It is based on a novel spherical closed chain configuration designed to exceed the bandwidth requirements for tremor research by minimizing the geometric computation needed for load simulation. The performance of the system was tested by simulation of mechanical load fields and physical objects such as hard walls and detents in which controller update rates of 1 kHz and higher were achieved using an LSI-11/23 microcomputer.

The applicability of the system to the study of whole arm tremor was demonstrated in preliminary experiments with a tremor disabled subject. A proposal for future two joint tremor experiments is also described.

Thesis Supervisor: Dr. Michael J. Rosen
Title: Principal Research Scientist

MEMBERS OF THE THESIS COMMITTEE

Dr. Michael J. Rosen (Chairman)
Principal Research Scientist
Department of Mechanical Engineering

Dr. Neville Hogan
Professor
Department of Mechanical Engineering

Dr. Robert W. Mann
Whitaker Professor of Biomedical Engineering
Department of Mechanical Engineering

Dr. Robert R. Young
Professor of Neurology
Harvard Medical School

Acknowledgements

The process of getting an education and completing a dissertation is not something one does alone. Many fine people helped in my pursuit and attainment of these goals. It is indeed a great pleasure to acknowledge their contributions here.

To Mike Rosen, supervisor of both my M.I.T. theses, my academic advisor, and good friend, I want to express my heartfelt thanks for everything. He has been a willing supporter—moral (always) and financial (nearly always)—for over a decade. His unfettering management style enabled me to develop both as an engineer and scientist, at my own rate, and in the direction of my own choosing (or at least, Mike had let me feel that most of the choices were really mine). Most importantly, he provided me with the opportunity to learn mechanical design by actually doing it rather than just talking about it.

I also wish to extend my thanks to Robert Young, Robert Mann, and Neville Hogan, the other members of my doctoral committee. They gave of their time to attend the meetings and read drafts of this document, and, through their comments and insight, helped shape the thesis' final form.

I am very grateful to Norm Berube, jack of nearly all trades. He took my machine drawings, often suggesting improvements, and formed them into the aluminum, Delrin, and Lexan parts that became the manipulandum described in these pages.

Many of my fellow students have been capable instructors and accomplices over the years. I deeply appreciate each of their contributions and hope that I have been able to return to them as much as they have collectively given me.

Crispin Miller came back three days after a lab seminar given when this work was in its seminal stage, knocked on my window, and beseeched me to take away a sheaf of paper and a cardboard model that had been plaguing him most of that weekend. His musings on those pages solidified the concept that became the manipulandum.

Will Durfee, whether he realizes it or not, abetted in my education in electronics; much of what I know started by watching him work. My keeping a written record of all of my thesis work stems from an effort to emulate Will's appearance of always having everything in order.

Bill Murray and Cary Abul-Haj further strengthened my understanding of digital electronics and the innards of PDP-11 computers. Bill, Ed Colgate, Mike Murphy and I have whiled away innumerable hours pondering system dynamics, modelling, kinematics, life-in-general, and academia. They taught me a lot and gave much to think about.

Ivan Baiges permitted me to use the skeleton of his thesis' whole-arm orthosis for a validation study of my apparatus. Scott Maxwell's universal subject testing chair served as the anchor and reference frame for that study. Scott's previous experience also led to the force transducer "decoupler" described herein. Janet Zahradnik donated "starter"

code which made learning and programming the Amiga computer much less painful.

In addition, Keita Ito, John Mansfield, Pete Mansfield, Greg Brown, Pat Lord, Eric Lanzendorf, and Dawei Qi provided the tangibles (computer maintenance expertise and the like) that keep a place like the Newman Lab functioning, as well as the intangibles (humor and camaraderie) that make it more than just a place in which to work.

My parents have never let their confidence in me flag. They gave me a caring home in which to grow, with as close to complete freedom as a kid could hope for; encouraged learning; and never deterred my curiosity. I offer them my undying gratitude.

Laura Demsetz, my wife and best friend, with her love, enabled me to endure the years at M.I.T. She has a hand in this thesis (literally)—I thank her for technical consultation, rendering figures on the Mac, and for unflichingly always being there when I needed it most.

Dov Adelstein

This work was performed in the Evelyn E. and Eric P. Newman Laboratory for Biomechanics and Human Rehabilitation. It was funded in part by grants from NINCDS, Public Health Service, Department of Health and Human Services (5R01-NS17610-03); NIDRR, Department of Education (G008300074); the Burke Rehabilitation Center, White Plains, NY; and a fellowship from the Sherman Fairchild Foundation.

Contents

List of Figures

List of Tables

Chapter 1

Introduction

The ability to observe the interaction of human beings with external mechanical environments under well controlled experimental conditions provides a valuable research method for the study of many aspects of human motor control, from intrinsic biomechanical and sensorimotor hardware up to commanded behavior that originates at cognitive levels. A testing facility that incorporates the means for imposing well characterized experimental conditions—both the commanded state of activity in the human and the effective mechanical environment with which the limb must interact—can serve as a tool to investigate not only properties internal to the human, but also the combined dynamics of the human-environment system and the nature of the sensory and mechanical coupling between the human and the external environment.

In devising a testbed for experimental studies of manual control and sensorimotor physiology, it is essential to note that during the performance of normal daily tasks, mechanical coupling between the human and the environment, in addition to altering the overall system dynamics, generates a rich array of sensory information. Both the intensity and texture of contact with the surroundings (tactile sensation) and the body's internal sense of its own kinematics and force generation (proprioception) present stimuli to cognitive perception and are vital for active neuromuscular regulation of dynamic interaction with the environment. The other senses, especially vision, may also play a key role in the skillful performance of many manual activities. Of necessity, a testbed

for research into human arm dynamics and manual control must first include the means to measure the combined human-environment kinematics and dynamics. Second, as mentioned above, the testbed must enable the experimenter to dictate both the volitional activity desired of the human subject, as well as the dynamics of the environment to which the subject is coupled. One approach to accomplishing the second task is to *simulate* the physical characteristics of the elements that the human acts upon.

Employing *physical simulation* offers several advantages over gathering observations during the performance of *real* tasks with a *real* system.[1] As with simulation in any field of endeavor (*e.g.*, econometric modelling, wind tunnel testing, situation room role playing in military training, *etc.*), physical simulation is driven by a *model* of the real system. A valid model strips away unnecessary detail, facilitating the observation of essential features that would otherwise be obscured by the complexity of the real system. Not only is the extraction of data often simplified, but a useful model can easily be revised. In contrast, revising the real system may be prohibitively expensive or physically unrealizable. Simulation may in fact be essential for the study of certain events because potential outcomes of the real situation or process are too hazardous. The benefits of simulation can be distilled to a single notion—the experimenter is given precise convenient control over essential experimental conditions. The insight developed by simulation may assist in predicting the outcome of real processes, aid in the design of new ones, or train users how to productively employ existing ones.

Any simulation that is computer based executes sets of mathematical equations that model key aspects of a real system and is intended to provide insight by generating useable information on how that system responds to sets of exogenous inputs. When dealing with *interactive* computer based simulations, the issue of how the human is coupled to the system arises. Most interactive computer simulations only include the human in the loop in a limited fashion. Typically, information transfer in interactive

[1]The term "physical simulation" connotes that the simulation has physical reality, *i.e.* the elements with which the human interacts have the properties of real physical entities. It is a simulation in that the characteristics of many different physical elements can be emulated.

simulations is restricted to the human operator observing graphical or numerical outflow from the simulation on a terminal monitor, and responding to the conditions unfolding in the computer model through a keyboard, a joystick, or a mouse. In that type of situation, the actual physical dynamics of human-machine interaction do not enter into consideration.

Computer based simulations which attempt to model the human as an integral component of the system under investigation pose another set of challenges. These challenges, many of them as yet unresolved, deal with generating accurate quantitative representations that capture essential aspects of complex skeletal, muscle, and nerve properties, in addition to cognitive behavior. A more successful alternative may be studies of human-environment interaction in which the actual human operator, rather than a model of the human, is interfaced to the simulation of the physical system.

A computer controlled interface for interactive simulation that couples the human to simulated physical elements must stimulate the internal self-sense of dynamics in the limb (*i.e.*, proprioception). The objective is, at minimum, to impose the desired dynamics on the human through the computer-controlled physical interface *and*, through visual presentation, to define the task that the human operator should execute. The ultimate goal is to evoke in the human operator the sense of "really being there" in a virtual space with simulated objects, performing virtual tasks. Because of the versatility of a simulation that is computer generated, artificial physical components are fabricated by simply including segments of computer code. The fidelity of these computer emulated objects depends both on an understanding of the detail and accuracy necessary for subjectively succesful simulation, and on choosing simulation hardware capable of delivering the desired performance.

1.1 Thesis Objective and Scope

The goal of this thesis is the design and implementation of a virtual environment system that simulates the mechanical characteristics of physical objects for human manual ex-

periments. The development of this system has been geared toward the investigation of a specific component of human motor activity: tremor.

This simulation system is intended to physically interact with the human operator (*i.e.*, the experimental subject) through the application of mechanical loads that simulate physical objects, and thus modify the dynamics of the operator's arm. The load simulation capabilities of the system allow the "feel" of a range of different objects and environments to be emulated. The system also gives the operator a visual representation of the virtual task he/she is performing. In addition, as a laboratory-based research tool, this system acquires and stores records of relevant performance variables for the subsequent analysis of operator performance.

While the design specifications for this testbed were directed at meeting requirements for the study of a specific component of human manual output, the applicability of the resultant system, as will be demonstrated, is more global.

1.2 Organization of the Thesis

A description of what tremor is, the motivation for its study, and the rationale for employing a physical environment simulation system as a tool for tremor research are topics of the remainder of this chapter. The concept of physical emulation of mechanical devices and systems is developed further in Chapter 2, with examples of hardware systems from a number of areas drawn upon for illustration.

Chapter 3 defines the issues relevant to the design of the arm loading and visual task presentation system. The desired performance characteristics and constraints imposed on the final system, and the strengths and weaknesses of other related devices are reviewed here.

The next two chapters span the implementation and performance of the hardware designed and built for the virtual environment system. Chapter 4 is concerned with the design of the arm loader hardware. This chapter includes the description of a new coupling mechanism that joins fixed-base electromechanical actuators to the mechanical

interface of the device with the human user, the selection of sensors and electromechanical actuators, and the measured performance of the passive (uncontrolled) machine. Chapter 5 treats the computer supervision and control of the entire system, including the implementation and performance of the impedance controller used to simulate the mechanical characteristics of a range of physical environments, the logic and hardware that maintain safe operation of the loader, and the video display. An experimental protocol for the study of whole arm tremor, using the virtual environment system, is proposed in Chapter 6. The results of some preliminary experiments with a tremor-disabled subject and the implications of these tests for the design of the experimental protocol are also discussed. The contributions of this thesis are summarized and recommendations for further work are made in Chapter 7.

1.3 Tremor

1.3.1 Normal and Pathological Tremors

Tremors are involuntary oscillations that are superimposed upon the volitional force or kinematic output of any limb segment or body part. This rhythmic mechanical activity is seen in *all* healthy people as well as in individuals with neurological disorders. Tremor can be present when the limb is supported externally such that its related musculature is at rest; when the related musculature is required to produce constant levels of force during maintenance of a limb's posture against gravity; and when dynamic force trajectories are executed by the muscles, as occurs during purposeful movement.

Because tremor is rhythmic in nature, it can be described in terms of its frequency content and the amplitude at these frequencies. It is based on these measurable characteristics that the distinction between normal ("physiological") and pathological tremors is drawn. Physiological tremor, which is present in able-bodied individuals, under most circumstances ranges in frequency from 8 to 12 Hz, and is small in amplitude, requiring special instrumentation to demonstrate its presence. Pathological tremor magnitudes are, at minimum, visually obvious without special instrumentation, and can be severe

enough to obscure concurrent voluntary motor activity in the afflicted limb to the point of functional impairment. Pathological tremor frequencies can be as low as 1.5 Hz and range up to the frequencies of normal tremor [68].

Pathological tremor may arise from degenerative neurological conditions including multiple sclerosis, Parkinson's disease, and various hereditary ataxias; toxic factors including chronic alcohol ingestion, and exposure to lithium salts; or sudden incidents such as stroke and head injury. In some individuals with these conditions, tremor may be one of many disabilities present. In others, tremor may be the only manifestation of neurological abnormality.

1.3.2 Tremogenic Mechanisms

As a result of extensive clinical observation, human and animal experimentation, and analytic modelling studies over the course of the past four decades, tremogenic (tremor causing) mechanism hypotheses have been formulated to explain the sources of particular oscillations and the factors that shape their characteristics. These hypotheses, which have their basis in the growing understanding of the roles of individual sensorimotor components and their interconnections in human movement control, have been applied to both pathological and normal tremors. Hypothesized tremogenic mechanism models have been grouped into the following three broad classes: biomechanical resonances, reflex loop instabilties, and central oscillators [133].

The biomechanical resonance model presupposes that the combined limb and external load, as depicted in Figure 1.1, have the characteristics of an underdamped second order system. In this model, the oscillatory frequency of displacement tremor is tuned by the equivalent joint stiffness and the combined limb-load inertia. The force (torque) input to the equivalent system need not be tuned at all; it can result from the broad band noise of random motor unit firing in the related musculature [136, 116].

The reflex loop mechanism, as depicted in Figure 1.2, takes the finite conduction delays inherent in neuroelectrochemical transmission into consideration—both in the de-

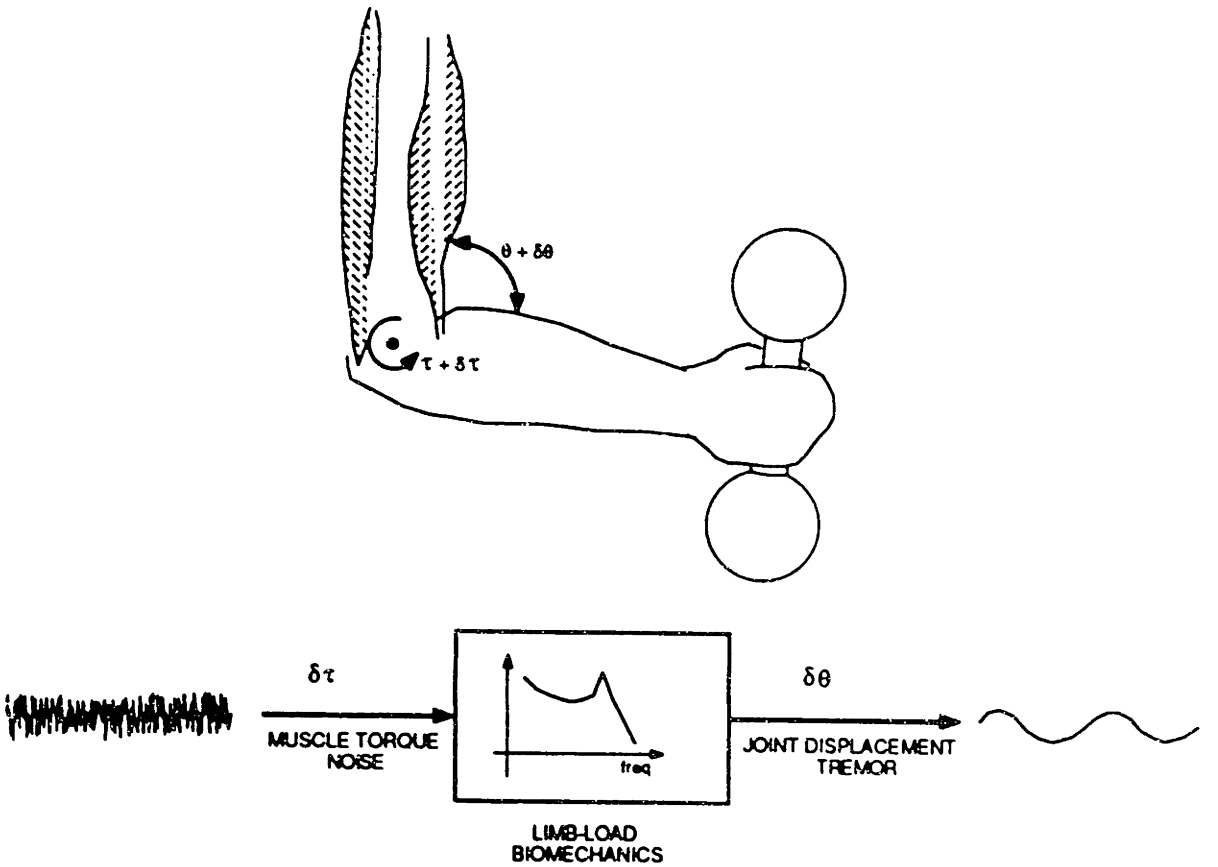

Figure 1.1: Biomechanical resonance tremor mechanism model. The mechanical load consisting of the combined forearm and external mass inertias and the equivalent muscle stiffness about the elbow are driven by broad band torque fluctuations $\delta\tau$ due to the random firing of individual motor units. The resulting narrowly tuned displacement output is rhythmic forearm flexion-extension $\delta\theta$, *i.e.*, tremor.

scending (efferent) neural command channels to the muscle and within the muscle itself, where neural signals are transformed into mechanical action, and in the ascending (afferent) pathways that carry signals back up from the rich array of internal muscle force and strain transducers. If the effective gain margin of the reflex loops from these transducers back to the muscle actuators is insufficient, sustained neural oscillations can develop at the phase crossover frequency, leading to rhythmic tremor in the mechanical output of the muscles [91].

The central oscillator hypothesis proposes that oscillatory sources in the central nervous system—unaffected by short-term peripheral feedback from muscle or other internal transducers—simply entrain groups of spinal neurons to send synchronous drive signals to the muscles, resulting in tremor. Sites postulated for central oscillators include brain areas responsible for the coordination of movement [87] and regions in the spinal cord [52], as schematized in Figure 1.3.

There is no reason to expect that any one of these mechanisms exist independently in a particular limb or muscle group under investigation. Several different oscillations may occur simultaneously in the same limb, each governed by a different mechanism [8, 9, 50, 78]. (See Figure 1.4.) It is also possible that two or three of the mechanisms may coalesce to produce a solitary oscillation [134]. The relative weighting of each tremogenic mechanism contribution depends on many factors, including pathology, emotional state, metabolic factors, and the type of concomitant voluntary activity in the muscle group. Also, the three mechanism hypotheses represented here need not be linear phenomena. Some analytic tremogenic models have incorporated nonlinear features, for instance, in considering muscle activation properties and reflex loop characteristics [132, 153].

These three general mechanism classes were elucidated here in a very brief format with the expressed intent of summarizing the hypotheses, rather than reviewing the evidence for each. It is important to note that these mechanism hypotheses were developed to explain tremors which arise due to the activity of either a single muscle group (agonist) or muscle group pairs (agonist and antagonist) that act in a single kinematic degree of

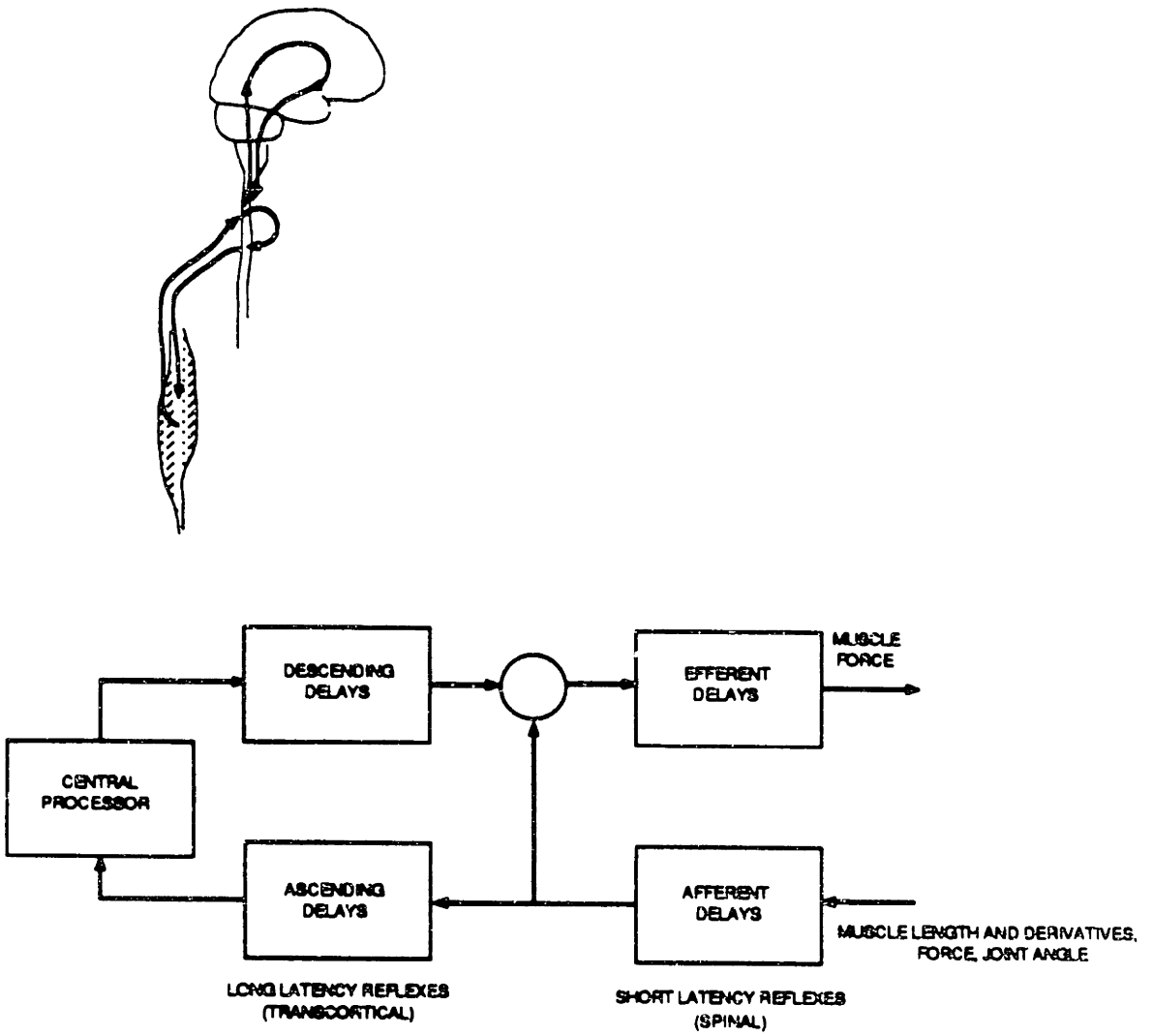

Figure 1.2: Reflex loop oscillator tremor mechanism model. Delays in muscle activation contraction and neural transmissions in the spinal reflex arc (spinal cord efferent-muscle-muscle sensor afferents) and in longer latency pathways (brain-descending spinal cord-spinal cord efferent-muscle-muscle sensor afferent-ascending spinal cord-brain) may compromise the stability margin of closed feedback loops, leading to sustained involuntary mechanical oscillations.

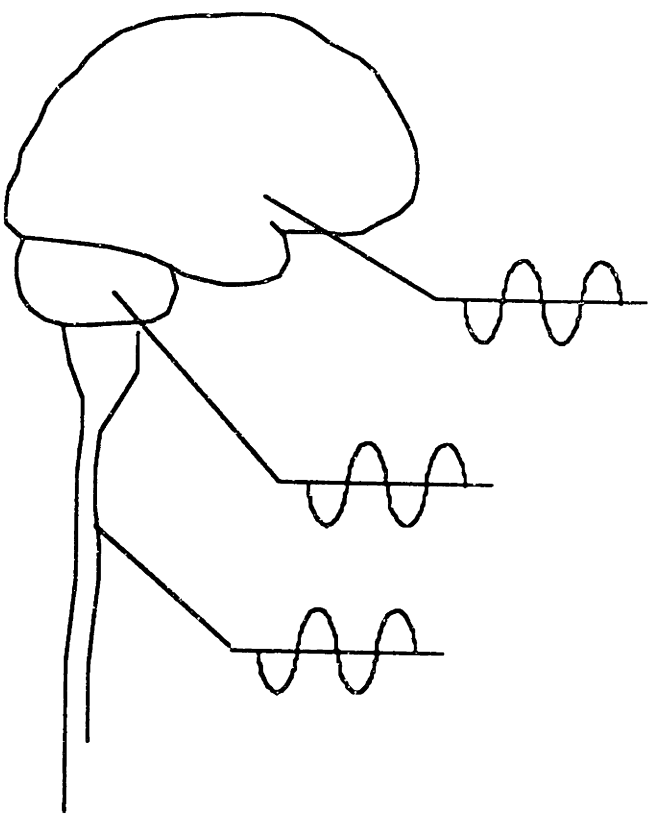

Figure 1.3: Central oscillator tremor mechanism model. Proposed origins of descending involuntary oscillatory commands to the musculature include sites in the motor cortex, cerebellum and related areas, and at the segmental level in the spinal cord.

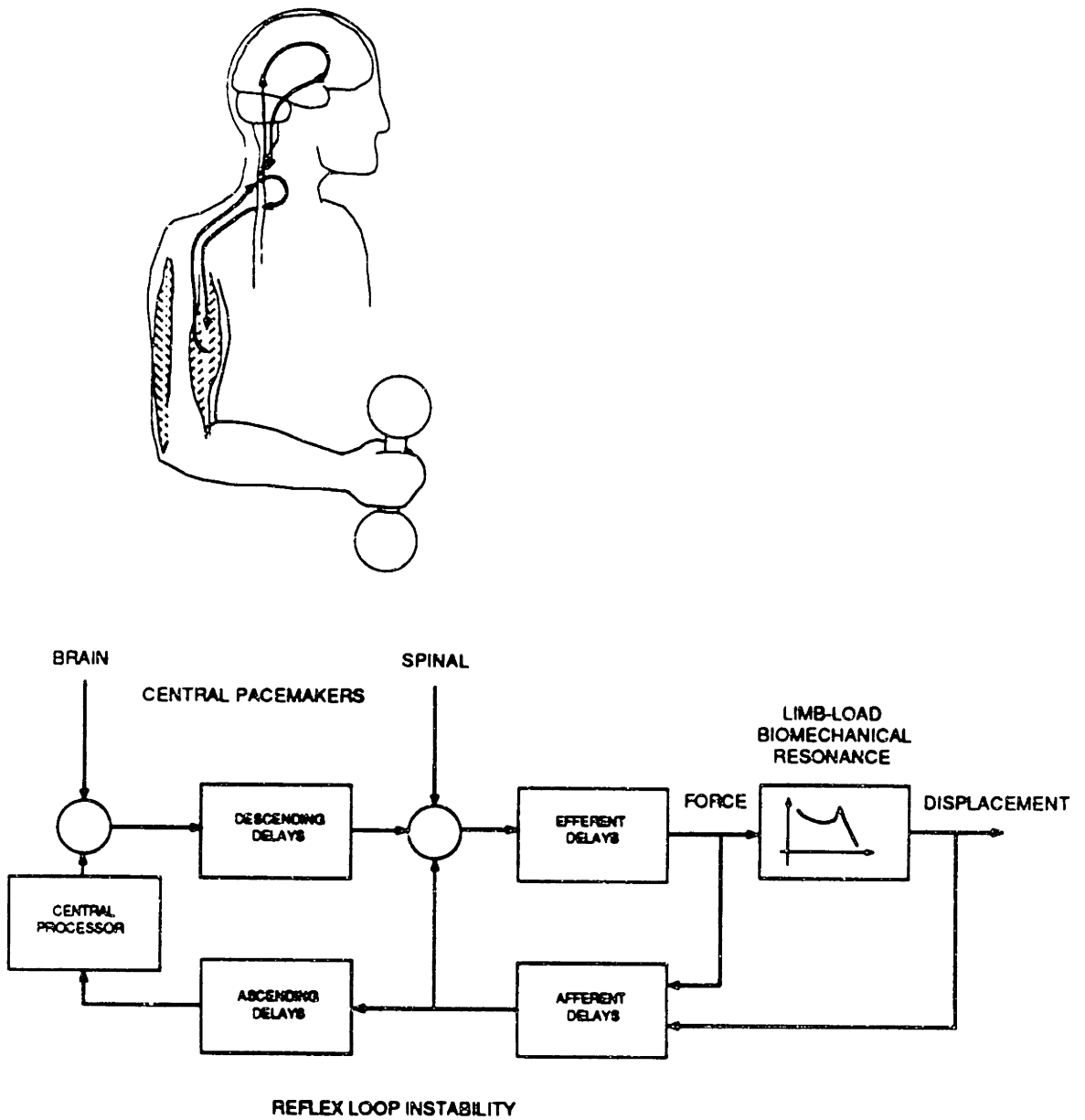

Figure 1.4: Combined biomechanical resonance-reflex loop-central source oscillator tremogenic mechanisms. See text for details.

freedom about a single joint. To date, models that consider potential tremor coupling, either mechanical or neuromuscular, between many groups of muscles in a multi degree of freedom limb have not been reported.

1.3.3 Tremor Measurement

Accurate measurement enables the mechanical and electrophysiological attributes of different tremors to be quantified, both for the experimental investigation of tremor generating mechanisms and for clinical evaluation.

The principle methods that have been employed for electronic detection of tremor *motion* include potentiometeric joint angle measurement (*e.g.*, references [6, 36, 146]), and uniaxial (*e.g.*, references [30, 78, 96, 104, 136]) and triaxial accelerometry [64, 128]. Because of the construction of rotary potentiometers, goniometric (joint angle) sensors are best suited for situations where the limb segments are constrained to single degree of freedom motion by anatomy or external apparatus. Accelerometers, on the other hand, require careful alignment if their readings are to be interpreted in terms of anatomical coordinates.

Other non-contacting arm tremor motion measurement techniques and apparatus have also been demonstrated. These range from the simplest—and least satisfactory—technique in which planar time-lapse photographs of single limb-mounted luminous markers are deciphered [73, 103], to a more elegant and accurate planar two degree of freedom capacitive transducer [86], and a three dimensional position detecting optoelectronic system [4]. To date, multi degree of freedom kinematic tremor measurements have not been decomposed into joint angle components.

Uniaxial [63, 91, 97, 139] and biaxial [117] tremor *force* measurements for quasi-isometric situations have also been reported. The term "quasi-isometric" is used here because only the contact point of the limb with the stiff fixed-base transducer is truly immobile; the skeleton of the limb can be restrained only to within internal tissue compliance. Neither joint torque components nor individual muscle forces associated with

multi degree of freedom whole limb tremor have been described in the literature.

Indications of tremor-correlated muscle activity, though, can be derived from the analysis of myoelectric signals [34, 60, 97, 135, 154]. Direct neural signals corresponding to tremor transduced by the muscle spindles (internal muscle strain sense organs) have also been recorded [152]. However, because of the nature of surface and in-dwelling electrodes for myoelectric and neural activity measurements, both of these methods are best suited for isometric or near-isometric situations. Consequently, their use may be precluded when rapid and/or large amplitude pathological tremors or voluntary motion are present.

1.3.4 Voluntary Task Specification

It was noted at the begining of Section 1.3.1 that tremor can be present when the limb is at rest, holding a static posture, or executing a dynamic trajectory. Tremor classification, a first step to clinical diagnosis, is based upon the identification of which of these general levels of volitional activity elicits the most severe form of a particular tremor in an individual patient [55]. Thus, the prescription of concomitant voluntary activity is a major element in designing the protocol for a tremor mechanism study.

Investigations of tremors that are exacerbated by *dynamic* voluntary activity, either movements or forces, necessitate stimulation of the appropriate volitional motor behavior in the subject/patient. To more easily characterize this type of motor behavior, the subject should perform pursuit tracking tasks, during which the subject is presented with a moving target and is instructed to match the excursions of the target (*i.e.*, pursue the target) with a response marker driven by mechanical output from the body segment under examination. Pursuit tracking has been employed in the study of large amplitude pathological tremors in one and two dimensional tasks, both with discrete target location jumps [27, 57, 69, 117], and continuous target trajectories [9, 11, 117].

The vast majority of human tremor experiments reported in the literature (especially those concerned with tremor mechanism identification), however, have been performed

under *static* postural maintenance conditions, and as such are more applicable to the tremor present during that class of voluntary activities. In that type of experiment, the subject's objective is simply to maintain a constant force or displacement throughout the course of a test. Often, the subject in a postural maintenance test is actually provided with visual feedback, resulting in a situation that is equivalent to a visually mediated tracking task—pursuit tracking when both the target and response markers are shown [78, 82, 91, 97]; compensatory tracking when the difference (error) between the two signals is presented [12, 91].

1.3.5 Mechanical Loading

Controlled mechanical loading, in conjunction with the mechanical and electrophysiological measurement techniques described above, has been a vital research tool for the identification of general mechanism classes involved in the genesis of different pathological and normal tremor types. Mechanical limb loading studies in which the equivalent stiffness [51, 82, 97, 118, 145], viscous damping [145], and inertia [50, 78, 136, 145] were altered have been reported. Randomly timed force perturbations [51, 90, 91, 135, 142, 145] and low frequency mechanical vibration (on the order of 100 Hz or less) [45, 111] have also been employed.[2]

Examples of how tremor response to mechanical loading has been interpreted in the above cited references, in view of the tremogenic mechanism classes described in Section 1.3.2, are as follows:

- A shift in a tremor's frequency downward with augmented inertia, or upward with heightened stiffness has served to indicate biomechanical resonance as a factor in tremogenesis.

- The ability to re-entrain (phase lock) a tremor's timing in response to a force perturbation for a period longer than the die-away response of the limb biomechanics

[2] A review of mechanical loading as a tool for tremor mechanism research can be found in reference [7].

has been used to indicate the role of reflex arc activity in sustaining the oscillations.[3]

- By default, the invariance of a tremor's mechanical properties (*i.e.*, frequency, amplitude, and timing) in response to both force perturbations and changes in inertia or stiffness has been used to implicate central oscillatory sources.

1.4 A Virtual Environment System for Whole Limb Tremor Experimentation

It was pointed out in Section 1.3.2 that tremor mechanism studies have not yet been extended beyond single degree of freedom models, and in Section 1.3.3 that multi-joint tremor torques or kinematics have yet to be measured or derived. Also, mechanical loading of tremorous limbs in greater than one degree of freedom has been reported in very few instances. Among these few instances are descriptions of viscous damping interfaces [3, 120] and an investigation of the therapeutic benefit of weighted wrist cuffs [73], all directed toward rehabilitation of the tremor disabled rather than mechanism research.

By proceeding beyond single degree of freedom tremor loading and measurement, tremor models could be extended to multi-joint whole limb cases that are more representative of "activities of daily living" (ADL) situations. Some unanswered issues to be investigated include the following:

- Whether tremors present at different locations or in different degrees of freedom of the arm have independent oscillatory sources or are cross-coupled;

- If tremor oscillations are coupled, whether the nature of the coupling is purely mechanical (*i.e.*, the result of multi-segment linkage dynamics), muscular (*i.e.*, due to biarticular muscle action), or neural (*i.e.*, due to local feedback);

[3]The contribution of nonlinear mechanical properties in generating sustained oscillations is also a possibility. Elble *et al.* [51] suggested that one could distinguish between biomechanical and neural factors by first altering the limb segment's inertia and then observing whether the re-entrained oscillation occured at the new (*i.e.*, shifted) mechanically resonant frequency.

- In whole-limb cases, as for single degree of freedom tremors, which tremogenic mechanism(s) are responsible for individual oscillations and what types of voluntary motor behavior provoke them.

The benefit of resolving these and other issues is an enhanced understanding of the mechanisms that generate whole limb tremor and, in some situations, lead to disability. This understanding will help develop more accurate tremogenic models, which in turn will contribute to the design and evaluation of improved diagnostic methods, pharmacological and surgical procedures, and rehabilitation regimens. Additionally, a more complete appreciation of the role played by the neuromusculoskeletal system in generating involuntary tremor may offer insight into the organization and planning of classes of volitional activity that use much of the same "hardware."

To extend accurately controlled tremor experimentation beyond single degree of freedom situations, the virtual environment system outlined in Section 1.1 was developed. The system includes a manual interface to permit a wide range of programmable mechanical limb loading; a visual interface to present tracking tasks that enable the specification of resting, static, or dynamic levels of voluntary activity from the subject; and instrumentation for the measurement of kinematics and forces.

Chapter 2

Review of Kinesthetic Virtual Environment Systems

This chapter presents a survey of experimental systems that incorporate physical simulation in the form of controlled mechanical loading at their interface to the real world. Examples are drawn from the areas of telemanipulation, computer interfaces, actively loaded manual controllers, and the experimental neurosciences.

2.1 Terminology

The terms kinesthetic, tactile (or tactual), proprioceptive, and haptic are used, often interchangeably, to describe the sensory input that the operators of virtual environments and other force loading manual interfaces receive from such systems. This section is intended as a very brief glossary of relevant sensory terminology.

Tactile is related to the sense of touch, specifically through cutaneous receptors that are present in the skin over the body surface [46]. According to Stedman's Medical Dictionary [2], tactual input is applied to the tactile sense.

Kinesthesia is the sense of limb movement or position, arising primarily from the output of muscle spindles, the internal parallel muscle sensors that transduce muscle length change (*i.e.*, stretch) and rate of change [72]. The role of joint capsule receptors in detecting joint angle changes has also been noted [31]. Roland [119] differentiated

between *kinesthesia* to describe the "perception of change in the position of a limb due to muscular contraction" and *statognosia* for "perception of position of a limb in space" through passive externally imposed movement.

Proprioception is the internal "self sense" of limb dynamics, and includes kinesthesia plus muscle tension as sensed by Golgi tendon organs [72, 100, 119]. Proprioception describes sensation that is caused by the actions of the organism itself, while exteroception pertains to sensation that results from external inputs from the environment [31].

Haptic acccording to Werner [147], is related to the unified and coordinated activity of the tactile and kinesthesic senses, as a higher integrated function of the nervous system. The haptic sense is equivalent to "active touch" as described by Brooks [31], employed in the active, conscious exploration of the texture and shape of objects.

The adjectives tactual and kinesthetic are typically employed to describe the sensory input that is provided to the human operator during manual interaction with a force loading interface. Thus, physical simulation systems that evoke activity in these senses have been labeled tactual, kinesthetic, or tactual/kinesthetic[1] virtual environments.

The virtual environment system designed for this thesis does not include tactual communication to the human operator in that cutaneous touch receptors are not involved, *i.e*, the user does not employ his/her fingertips or skin surface to discriminate among simulated object textures. However, because the manual interface of this system is a force loader, it does impart changing kinematics to the limb, while also necesitating active tension in muscles that work against the simulated loads. As such, the human operator depends on *proprioceptive* information to fully sense the mechanical characteristics of the physical simulation presented by the virtual environment. Even though internal muscle tension is an important contributor to the human operator's perception, the label

[1]The term "haptic" might be considered as a more compact equivalent to "tactual/kinesthetic."

"*kinesthetic* virtual environment" will be used to describe this system to conform with other work in the field.

2.2 Telemanipulation

The goal of telemanipulation is to furnish the human with the ability to manipulate objects from afar and thereby eliminate the hazards of working in hostile environments (*e.g.*, outer space or undersea) or in the handling of dangerous materials (*e.g.*, radio-isotopes or explosives). In tasks involving direct manipulation (*i.e.*, direct contact between the human and the object), the proprioceptive and tactile senses transmit information back to cognitive levels and fulfill a vital role in the identification of properties of the objects that are being handled. Especially in unfamiliar conditions, this feedback is essential to the human for evaluation of how well manual tasks are performed, and consequently for "on-line" learning so that tasks can be executed successfully. Similarly, in remote manipulation, high quality proprioceptive information is important for skillful task performance. The term "telepresence" has been used to describe the situation where full sensory information available at the remote manipulator is transferred back to the human, so that he/she has the perception of actually being at the remote site.[70, 130]. Among the desired sensory components of telepresence are "teleproprioception" and "teletouch" which would be provided by displays that reflect the forces experienced by the remote manipulator.

A convenient starting point for a brief history of remote manipulation is nuclear "hot room" work of late 1940's in which mechanical master-slave linkages originally were employed to handle radioactive materials behind shielded partitions.[2] The human operator at the "master" of such a system would experience the interaction between the "slave" and the workpiece as transmitted through the mechanical linkage. Of course, because of undesirable linkage characteristics such as friction and inertia, the fidelity of sensory perception would be degraded. Purely mechanical, passive linkages were soon

[2]A very complete history of telemanipulation can be found in reference [144].

supplanted by electromechanical and electrohydraulic devices, first with unilateral and then with bilateral master-slaves. The term unilateral indicates that the direction of information flow is from the human master to the motorized slave manipulator through the control of instrumented joysticks; the state of the manipulator could not affect the joysticks directly. In bilateral devices, not only is the slave manipulator actuated by electric motors (or hydraulic pumps), but the master station is also equipped with a motorized linkage. Information flows in both directions in these systems: from the sensors of the master to the actuators of the slave, and vice versa, from the sensors of the slave to the actuators of the master, so that forces exerted on the slave are reflected back to the master.

In earlier master-slave systems, all force and kinematic scaling was performed by analog electronic circuitry. Since digital computation was unavailable, the complexity of geometric transformations was averted by designing slaves with identical configurations to the masters. A result of building slaves that mimicked the kinematics of the master was the popularity of anthropomorphic linkages, both for the manipulator and the control station. One offshoot of anthropomorphic devices were the Handyman and Hardiman electrohydraulic "man-amplifiers" built by the General Electric Company in the 1960's [105]. The human interfaces for these devices were "worn" as exoskeletons by the operator. The Hardiman concept was particularly interesting because both master and slave were embodied as the same exoskeletal linkage. In principle, when wearing this device, the effort of the operator would be amplified by the actuators on the linkage. This "power assist" would enable the operator to produce very large forces and "lift" heavy loads. Ideally, from the perceptual point of view, the man-amplifier would have the effect of masking the inertial characteristics of massive external objects—in essence, physically simulating reduced mass properties.

The advent of laboratory interfaces (A/D and D/A conversion) for digital computers enabled telemanipulators to profit from the flexibility of programmable digital control algorithms. Aside from allowing a higher degree of autonomy on the part of the re-

mote manipulator, digital computation permitted complicated scaling and mathematical transformations between master and slave, thus freeing the master station from having to be a direct replica of the slave device.

A prime example of the computer as the programmable intermediary between the master and slave was the universal Force Reflecting Hand Controller (FRHC), built at the Jet Propulsion Laboratory in the late 1970's [24]. The FRHC was a handgrip that accommodated and measured six degree of freedom hand motion (three translations and three rotations) and could impose independent forces in all degrees of freedom from computer controlled motors. The FRHC has served to demonstrate that arbitrary geometric transformations could be processed in real-time for a master-slave system with a slave manipulator arm of completely different configuration [23, 71]. The FRHC has also been employed as a virtual environment interface, with the slave manipulator disconnected and the forces at the master handgrip the result of physical simulations of mechanical loads generated by computer [43, 22, 59]. As a benchmark for comparisons later in this document, digital control update rates of 50 Hz, corresponding to a maximum equivalent analog system bandwidth of 2.5 Hz or less, were reported for the FRHC when operating in either bilateral master-slave or virtual environment interface modes.

A current demonstration of advanced multi-processor computer technology in tele-manipulation is the very high performance tele-microrobot system developed by Hunter *et al.* at McGill University [79]. This device, used for investigation of the mechanical characteristics of individual living cells, is the mechanical analog of a microscope in that it allows the cell to be "felt" at the master. The tele-microrobot is of special interest not only because of its elegant design, but because its operation entails both spatial and temporal scaling between the master and the slave. Human hand motions of $\sim$10 cm at the master are scaled down by $\sim 10^{-6}$ so that the micro-manipulator can perturb the cell in its grippers; forces experienced at the cell interface are boosted by $\sim 10^{6}$ so that they can be felt at the master. Similarly, many events at the cell (*e.g.*, cross-bridge formation and breaking in a muscle fiber) must be slowed by several orders of magnitude

so that temporal characteristics can be kinesthetically discerned by the human operator. In addition to its use in a conventional bilateral master-slave mode, the system has also been employed as a physical simulator interface—with the slave disconnected and computer-generated virtual objects presented kinesthetically at the master.

2.3 Computer Interfaces

The notion of incorporating force reflecting or haptic interfaces to computers can be traced back to the mid 1960's, and has its roots in bilateral master-slave telemanipulation. Sutherland [138], in a visionary paper entitled "The Ultimate Display," proposed kinesthetic feedback as a means to broaden the channel from computer back to the human beyond visual and aural communication. He suggested that "the force required [of the human] to move a joystick [which by then had been utilized as a position *input* device for interactive computing] could be computer controlled." Sutherland also noted that force feedback was already available in devices such as Handyman, which, in essence, was an intricate wearable assembly of joysticks with nearly as many degrees of freedom as the human arm.

The earliest reductions to practice of kinesthetic computer displays were reported in the early 1970's. Noll [108] developed a three degree of freedom Cartesian force simulation interface that was combined with a stereoscopic video display. The three axes of the computer controlled manual interface were kinematically constrained by a serial assembly of linear guides and bearings. The translational actuation for each axis was derived from a chain-sprocket transmission driven by a rotary induction motor. Displacements were detected by rotary wire-wound potentiometers, one for each drive chain, mounted on the sprocket at the opposite end of the chain loop from the motor. Noll employed this hardware for the physical simulation of spheres and cubes. In describing his system, he noted the sponginess of the surfaces of these simulated objects and that the 2.2 N (0.5 lb) friction in the mechanism was "bothersome" to its users.

An ongoing investigation of kinesthetic virtual environment interfaces, first as ped-

agogical aids and later as intramolecular force displays for biochemistry research, was inititiated during the same period by Brooks *et al.* at the University of North Carolina. Their initial system, GROPE-I, was a planar Cartesian device programmed to simulate the profiles of force field types commonly taught in undergraduate physics classes [21]. A general six degree of freedom force loading interface named GROPE-II followed [32, 85]. The manual interface of GROPE-II was based on the refitted master of an Argonne National Laboratories E-3 electromechanical remote manipulator. It included a video display and, in addition, was capable of providing audio cues. Kilpatrick [85] employed GROPE-II to examine which qualities were desirable for an effective virtual environment interface. He reported that GROPE-II was able to achieve 15-20 Hz update rates at its manual interface (equivalent analog bandwidth of less than 1 Hz) and that kinesthetic simulations of hard surfaces with his system felt "spongy." Kilpatrick noted that the inclusion of an audible "click" as feedback enhanced the human operator's subjective impression of the hardness of contacted objects.

GROPE-III, the system used as an intramolecular force display for biochemistry research by the group at the University of North Carolina, incorporated the E-3 manipulator from Kilpatrick's six degree of freedom interface along with more powerful computation capabilities. Ming *et al.*'s review of GROPE-III [102] listed a number of manipulator shortcomings that hindered their system's performance. These shortcomings included high friction, gear backlash, and drive cable compliance which led to poor positioning accuracy; and excessive linkage inertia which, when combined with mechanism compliance, contributed to low bandwidth. Also, because of the complexity of the calculations for the kinesthetic and visual display of chemical bonding physics, and the manner in which computational resources were organized, the update rate for their manual interface was only 3 to 5 Hz (0.25 Hz maximum equivalent analog bandwidth), a value that Ming *et al.* readily admitted was too slow for realistic modelling. Among the consequences of this low bandwidth were unsatisfactory interactions with hard surface simulations: virtual walls were described as being "resilient" because of the lag in turning

off simulation forces upon leaving the wall.[3]

At about the time of GROPE-II, Atkinson *et al.* [18] at the University of Califonia at San Diego constructed "Touchy Feely," a three degree of freedom kinesthetic computer interface. One among a number of uses suggested by the authors for their system was also as a force display for modelling chemical structures. "Touchy Feely" consisted of a spherical handgrip suspended from a four cable tetrahedron, with each cable spooled around a motor/encoder shaft.[4] Its performance characteristics, however, were not been published.

2.4 Actively Loaded Manual Control Interfaces

2.4.1 Fly-by-wire Aircraft and Training Simulators

One growing field for the application of active force "feel" in manual interfaces is the control of fly-by-wire aircraft and flight training simulators. With electrical cable linking the cockpit to the flight control surfaces of commercial and military fly-by-wire aircraft, the pilot loses direct mechanical force information that was previously transferred over mechanical linkages and hydraulic lines. The advantages of kinesthetic feedback can be restored to fly-by-wire aircraft by equipping the control stick with actuators that are activated according to the sensed state of the control surfaces, much in the same manner as for bilateral master-slave telemanipulators.

Aircraft training simulators, whether they are mock-ups of fly-by-wire or mechanically controlled airplanes, retain only the equivalent of the master station. Contemporary simulators, based on precise replicas of the emulated aircraft cockpit, are provided with high quality external video presentation and six degree of freedom flight deck motion simulation. In addition, they are also equipped with force reflecting control sticks. The remote

[3]In writing about GROPE-III, Ming *et al.* [102] made the interesting observation that both kinesthetic physical simulation interfaces and conventional industrial robots share a common antecedent in bilateral force reflecting master-slave manipulators. The difference between the two is that an autonomous robot is slave to a computer master, while in virtual environment systems, the human operates the master station and the computer simulates both the slave device and its task space.

[4]In addition, Atkinson *et al.* [18] proposed several six degree of freedom force loading interface designs (including one that would be actuated by gas jets).

slave components (*i.e.*, the control surfaces), and their interaction with the environment, however, are simulated by computer for a wide variety of flight scenarios [38].

There have been several published examples of active force "feel" manual interfaces for aircraft simulation. The single kinematic degree of freedom, electrohydraulically actuated "smart stick" developed by Repperger [114, 112] could simulate a variety of inertia, damping and spring properties under computer control. Use of the "smart stick" has been reported for experimental investigations of pilot task learning [113]. NASA's Langley Research Center has described a "General-Aviation Control Loader" in the form of an electrohydraulically actuated control wheel (yoke) with computer generated load simulation in two degrees of freedom (pitch and roll) [1]. One and two axis electrohydraulically actuated control sticks and foot pedals for force feel simulation in airplane and helicopter trainers have been commercially available for at least the past two decades [99].

2.4.2 Neuromuscular Experimentation

Active mechanical loading of human and animal limbs has become a more widely employed experimental technique in neuromuscular research over the past two decades. Among the earliest systems were two single-degree-of-freedom electromechanical devices: one built at the National Institutes of Health and reported in 1973 [129]; the other at New York Medical College reported in 1974 [17]. Both of these systems were subsequently applied in tremor studies by other researchers. Teravainen *et al.* [142] used the NIH system to perturb human elbow flexion-extension and pronation-supination tremor in parkinsonian patients and in a "normal" control group. Vilis and Hore [145, 146] employed the second system at the University of Western Ontario in observations of elbow tremor in monkeys under altered joint stiffness and damping conditions and under controlled torque perturbations. More recently, Elble *et al.* [51] developed a single degree of freedom electromechanical loader to apply torque perturbations and simulate different spr tiffnesses for human *wrist* tremor research.

In addition, a number of higher power electro*hydraulic* limb loading devices for neu-

romotor studies have been described. Billian and Zahalak [25] built a programmable single degree of freedom testing system which has been used to examine passive and active muscle properties at the elbow. Ruitenbeek and Janssen [125] designed a single degree of freedom loading system combined with a video display to examine visual and proprioceptive feedback during human arm movements.

Programmable active limb loaders have also been developed as exercise and clinical assessment tools. Book and Ruis [29] constructed a two degree of freedom electrohydraulic "robotic exercise machine" capable of imposing large forces. Several commercial ventures are currently marketing single degree of freedom loading units for clinical use. Some of these devices are reconfigurable for the exercise or evaluation of specific muscle groups during the performance of stereotyped activities [26, 20].

2.4.3 Mechanical Load Simulators at M.I.T.

In addition to the kinesthetic virtual environment system described in this dissertation, a number of recent projects in other laboratories at M.I.T., as well as in the Newman Laboratory for Biomechanics and Human Rehabiltation, have involved the mechanical loading of limbs to examine different facets of human movement control. The topics of these studies range from the cognitive aspects of volitional task performance to the passive properties of the neuromuscular system. Several of these projects are summarized here with the focus on the experimental hardware that was developed or employed.

Winey [150] informally explored single degree of freedom force feedback in the operation of a *simulated* manipulator gripper as part of his Master's thesis work in the Man-Machine Systems Laboratory. The manual interface for his investigation consisted of an E-2 electromechanical manipulator master that was linked to a PDP-11/34 minicomputer. Paines' Master's thesis in the Department of Aeronautics and Astronautics [109] examined the effects of different levels of mechanical loading on the performance of manual tasks. The electromechanical system for Paines' experiments was based on a single degree of freedom translational mechanism, custom built for use in both the

laboratory and underwater (to simulate zero gravity).[5]

Mussa-Ivaldi *et al.* of the Department of Brain and Cognitive Sciences [107] utilized a planar two degree of freedom electromechanical loader to perturb the human arm in an effort to quantify passive joint stiffness. A larger scale arm loader, implemented by Faye [56] for his Master's thesis work in the Department of Mechanical Engineering, is now being used by members of this group to simulate impedance fields and virtual objects.

In the Newman Laboratory, Colgate [40] designed a three axis servo controlled pneumatic thruster for his Master's thesis. The device, which is worn on the wrist, is intended to allow passive and active dynamic properties of the human arm to be studied with a minimum of encumberance. Murray [106] developed a single axis three-state electropneumatic thruster as part of his doctoral dissertation to enable the examination of muscle activation strategies about the elbow in the presence of disturbances. Baiges [19], for his Master's thesis, implemented a three axis tremor-attenuating orthosis that incorporated viscous damping as simulated by computer controlled electromechanical brakes. Maxwell's doctoral work in progress [98] makes use of electromechanical brakes in a more general six degree of freedom loader for the management of abnormal movements in the tremor disabled.

Currently, Russo [126] and Tadros [140] are in the process of developing a kinesthetic virtual environment interface for their Masters' theses in the Department of Mechanical Engineering. Their system incorporates both electromechanical brakes *and* motors to obtain versatile, large-magnitude resistive forces and extends the two degree of freedom design presented in this document to three degrees of freedom.

[5] As an aside, Paines also observed tremor in his subjects. He noted that it decreased in magnitude with increased damping, a result reported earlier by Adelstein and Rosen [9].

Chapter 3

Design Issues

This chapter outlines basic issues which must be addressed in the design of a virtual environment testbed so that physical interaction between it and a human operator (*i.e.*, experimental subject) can occur. In addition to these basic issues, performance specifications and safety-based restrictions for *this* virtual environment system are considered here. The driving force behind the system's design, namely, the simplification of controller implementation by the selection of appropriate mechanical, electronic, and computer architecture, is also discussed.

3.1 Basic Requirements

The basic capabilities that are required of this laboratory-based virtual environment testbed can be stated succinctly as follows:

- The system must have the ability to accurately measure relevant kinematics and forces, and then store these measurements for later analysis.

- The system must enable accurately controlled loads to be imposed on the human arm. The loading should be versatile, *i.e.*, programmable to emulate a broad range of active and passive physical systems. These loads should be controllable in real-time based on the concurrently measured kinematics and forces.

- The system must include a real-time video display for visual presentation to the operator/subject of the simulated tasks that his/her arm is performing in the virtual environment.

- The system must be adaptable to a diverse subject population of both able-bodied and disabled persons. Factors such as physical stature, strength, and hand dominance should be taken into account.

3.2 Quantitative Performance Specifications

The performance characteristics of the *ideal* virtual environment system should, at the very least, match the intrinsic capabilities of the human executing the specific tasks for which the system was designed. At best, a truly versatile system should be able to exceed a wide range of human capabilities for a considerable variety of tasks and situations. This way, such a system will be useful for the investigation of a broad spectrum of deliberate motor and sensory skills, as well as passive biomechanical and involuntary motor properties, in a significant segment of the population. This section reviews the general performance requirements for both manual and visual interfaces to virtual environment systems.

Manual Interface

Factors that could be considered in the design of a manual interface are active human motor output capacity, the capabilities of the various sensory receptors in the limb, including both tactile and proprioceptive endings, and the passive mechanical properties of soft tissues and bone. The relative importance assigned to each of these factors depends strongly on the intended use of the interface. Clearly, it would be a tall order to span all three of these domains—*i.e.*, motor, sensory, and passive limb mechanics—with a single hardware setup.

The primary concern for the design of *this* system are the limb dynamics—rather than sensory perception—that result from the *mechanical* interaction of a human arm coupled

to the manual interface of the virtual environment. Most importantly, the establishment of performance goals focuses on the characteristics of the particular component of manual activity for which this system is intended: involuntary arm tremor.

Ideally, the manual interface should be capable of covering a broad range of mechanical load characteristics. At one extreme, the interface should be able to appear mechanically invisible, having no inertia or elastic storage, and causing no energy dissipation. When behaving in such a manner, the interface would not affect the dynamic characteristics of the arm, nor would it be sensed proprioceptively by the human operator/subject. At the opposite extreme, the interface should behave as if it were infinitely massive, infinitely stiff, or infinitely resistive, so that it could immobilize the human subject's arm. There is also a middle ground where the interface inertia, stiffness, and damping are of the same order of magnitude as those seen in the arm. It is in this region of matched impedances that maximum power transfer occurs, resulting in the strongest coupling between the dynamics of the arm and the interface.

Based on the objectives at the low end of mechanical loads, the quantitative goal is obvious—inertia, compliance, and dissipation should all be settable to zero, or, in practice, as close as possible to zero. The upper end of mechanical loads poses a different problem: how close to infinite is sufficient?

One approach is to match the magnitude and bandwidth capabilities of the arm with opposing forces generated by the limb loader so that motion can be eliminated. The human factors literature [48, 143] lists an upper percentile adult male as being capable of exerting as much as 1000 N at the hand on a rigid isometric interface, depending on the position, orientation, and external support of the arm and body. These high forces at zero velocity (*i.e.*, zero motion) trail away rapidly when arm speed is increased, as is evident in torque-speed curves representative of maximum and normal levels of elbow activity measured in "average" adult males [92].

Force capabilities diminish with increasing oscillatory frequency as well, as can be seen from human tremor measurements. In addition, tremor, with a maximum frequency

of 8 to 12 Hz in the arm, also confers an upper limit on the rates of repetitive alternating *movement* that can be voluntarily achieved [62]. Matthews and Muir [97] reported maximum 10 N peak-to-peak—4 N RMS in the 6 to 12 Hz band—tremor oscillations at the forearm of healthy subjects as a consequence of maintaining 160 N voluntary elbow flexion forces. Albers *et al.* [12] cited tremor up to 2 N peak-to-peak (5 to 11 Hz band) in parkinsonian patients, as measured at the hand by a rigid transducer with the remainder of the arm unconstrained. Unpublished data from Riley and Rosen [117] for whole-arm pathological intention tremor indicated hand forces of comparable magnitude.

A second approach to specifying upper performance bounds for the manual interface is to exceed the arm's inertia and impedance characteristics. Desirable inertia levels can be determined from estimates of arm segment masses. Using approximate percentages of body volume from Contini [42] and an assumption of uniform density, the masses of an 80 kg man's hand, forearm, and upper arm are respectively 0.4, 1.4 and 1.7 kg. In terms of impedances, Mussa-Ivaldi *et al.* [107] have measured postural stiffnesses of 300 to 750 N/m at the hand for human arms supported in a horizontal plane, corresponding to elbow and shoulder joint stiffnesses of up to 40 N-m/rad. Murray [106] suggested that, in the presence of maximum deliberate muscle co-contraction, postural stiffness and damping at the elbow are on the order of 100 N-m/rad and 2.5 N-m/rad/sec respectively.[1]

Visual Interface

Ideally, the video display should be versatile enough to present the human subject with any combination of quantities that are representative of any arbitrary manual task that one could perform in a virtual environment. Scaling of these quantities, as well as the detail and complexity of the scenario unfolding in the virtual environment should be completely programmable. Since this type of display would most likely be generated by computer on a video monitor, the computation update rate should be able to match the scan refresh rate fixed by the display hardware. The slowest acceptable refresh rate for

[1] For rapid stretches, Murray proposed that elbow stiffness may be in excess of 500 N-m/rad.

flicker-free television and high-quality computer graphics monitors is 30 Hz (depending on screen phosphor persistence and other factors) [58]. At minimum, most currently manufactured display hardware comply with this standard.

3.3 Constraints and Restrictions

Attainment of the performance goals described in Section 3.2 is subject to a number of constraints and restrictions, including safety, portability, and type of actuation.

Safety

A paramount concern for this human interactive system—on par with delivery of the specified performance characteristics outlined above—is that it pose no hazard to the experimental subject, both under normal operation and during unexpected system fault conditions. The hazards to be guarded against encompass all situations that may impose discomfort or danger of injury to the human subject. These situations can arise not only when the system is operated as intended by the designer, but in unintended modes of use by an unsupervised subject as well.

The potential for dangerous incidents when a powered mechanical device interacts with a human subject is obvious. Conditions which give rise to excessive force, either in transient situations or over extended periods of operation, and in concentrated locations or over large regions of the body, must be avoided.

To ensure that the passive (*i.e.*, unpowered) system will be mechanically safe, the device should be free of sharp edges and confined spaces that may cut or pinch the subject. The device itself should not demand awkward and uncomfortable postures of the subject using it. Under normal active (*i.e.*, powered) operating conditions, forces, accelerations, and velocities developed by the device should be restricted to acceptable levels. During sudden mechanical or electrical fault occurrences, there must be reliable detection of the errant behavior and effective, rapid reaction.

Since the system power source will be electrical and its controller electronically based,

safeguards against electrical shock must be implemented. Proper grounding of the entire system with respect to the electrical main, fusing of all electrical power inputs to the system, and insulation of the human operator/subject from any surface that may possibly carry current are essential.

Portability

Potential sites for operation of this system include not only the laboratory at M.I.T., but, in the case of disabled subjects, hospitals and private homes as well. To ensure that the system is not tethered to a single base in the laboratory, it should not have specialized power requirements for mechanical actuation—*i.e.*, the system should not rely on fixed-base (or bulky portable) hydraulic or pneumatic compressors, pumps and reservoirs. Likewise, all of its electrical power needs should be met by 115 volt single phase AC service, without any individual component exceeding standard 20 amp line capacity.

A further consideration is to make the system *trans*portable by restricting its size and weight. All equipment should be able to pass through standard width doors and be easily moved—either carried or rolled on wheels, or if necessary, disassembled into manageable subcomponents.

Electromechanical Actuation

Pneumatic and hydraulic systems were ruled out early during the design process in favor of electromechanical actuation. Reasons for abandoning pneumatic actuation included undesirable compliance that would arise from the compressibility of air in the system and leakage, and, as mentioned above, compromised portability due to the size and weight of pumps, compressors, and reservoirs. Size and weight concerns, plus the potential for hydraulic fluid leakage through imperfectly sealed lines to undermine system cleanliness contributed to the decision against hydraulic actuation. In addition, analyses by Abul-Haj [5] and Mansfield [93] of electrohydraulic actuation controlled from remote valves

predicted insufficient resonance-limited bandwidths for systems with force and motion requirements on the scale proposed for the manual interface.

3.4 Degrees of Freedom

Having selected electromechanical over other types of controllable actuation, the objective is to design a multi degree of freedom mechanical linkage that connects the human arm to powered electric motors. Essentially, this device will take on the form of a backdriveable robot—a manipulator that will apply controlled forces to the human subject's limb and allow the human to push back on, and move, the motors. The questions of how many degrees of freedom this device should have and how to connect it to the human subject's arm need to be addressed.

Approximately thirty different muscles have origins or insertions on the bones of the upper arm and forearm [67]. Hence, contraction of any of these muscles under neural contol contributes to motion across the one or more joints of the arm, *i.e.*, the shoulder, elbow, and wrist. If it is assumed that each of these muscles can be driven independently by the human neuromotor system (either in producing volitional motion or involuntary tremor), and that each individual muscle is to be opposed or assisted by externally developed mechanical loads, on the order of thirty independently controlled actuators would be required.

The intact shoulder (gleno-humeral), elbow, and wrist joints, as constrained by their internal geometry and ligaments, allow the position of the skeleton of the human arm to be described by seven kinematic degrees of freedom. If the kinematics of natural whole arm motion are to be loaded, a linkage and actuators must be provided to match these seven degrees of freedom. While the choice of arm kinematics over independent muscle loading would reduce the required degrees of freedom of the manual interface from thirty to seven, the complexity of such a design task is still formidable.

Rather than attempt to match actuators with the number of arm muscles or the kinematic freedom of the arm joints, loads could be applied directly to one particular

segment of the limb. In such a configuration, the remaining segments of the arm could be permitted to move freely within the limited constraints imposed by the attached limb loader; additional constraints (*i.e.*, braces or splinting) could be used to further restrict selected degrees of arm freedom. If general displacement and orientation, and force and torque, are to be allowed at the arm's point of attachment to the loading device, the loader still would require a six degree of freedom linkage with independently controlled actuators.

Further relaxing the goals for the system from six to two degree of freedom loading makes the machine design problem more tractable in terms of linkage complexity and the cost of device components such as actuators, sensors and controllers. By limiting the objectives to a two degree of freedom loader, the computer overhead associated with data acquisition and storage, for both control and analysis purposes, is reduced significantly. Furthermore, if tasks performed by the human subject during experiments are limited to only the two degrees of freedom of the manual interface, the complications of higher dimensional visual presentation of activities occurring within the virtual environment are avoided, thus allowing simpler planar video displays to be employed.

The interaction point between the human arm and the loader was chosen to be at the hand. This choice includes the entire arm in a closed kinematic chain because the torso of the human and the base of the loading device are fixed to the same mechanical ground. In principle, then, with the appropriate sensing of the kinematics and forces at the human-machine interface, and with the arm in configurations that are carefully restricted by splints or bracing, the motion of the whole arm can be studied. By placing the interface at the hand, the alternative of the human grasping the loader rather than simply having the machine fastened to some location on subject's arm becomes possible. In addition, most people are accustomed to using their hands when directly manipulating their physical surroundings, especially in applications that require precision. Because of this familiarity, experimentation with apparatus that involves whole arm activity for accurate hand placement is representative of many of the manual motor tasks in daily

life. Thus, the selection of a design in which the mechanical device interacts with the human at the hand, either as a loader to apply forces to the human or as a mechanical interface between the human and a virtual environment, seems reasonable.

While generality is lost in cutting back from a six degree of freedom loader to a simpler device, it is important to note that controlled limb loading has not been applied before with the expressed purpose of examining tremor in greater than one degree of freedom.

3.5 Electromechanical Manipulator Configurations

A fundamental characteristic with which the limb loader is to be endowed is the ability to allow the human to push back and move the machine as easily the machine can push and move the human. In terms of the mechanical transmission between the actuators and the human-machine interface, this means that the mechanism must be completely *backdriveable*, so that even very weak muscle forces encounter essentially no opposition and result in movement of the linkage. Backdriveabilty must be effected through careful selection of a mechanical configuration and individual linkage components, and may be aided through the implementation of appropriate control schemes.

As noted in Section 3.2, the loading manipulandum[2] should be considerably stiffer than the human limb when commanded to hold the arm in place. In addition to actuators that are capable of sufficient force, this range of loading requires that the mechanical linkage between the actuators and the human-machine interface be extremely rigid, without any compliance. To maximize precisely controlled actuator force available at the human-machine interface, it is also desirable to dissipate as little energy as possible to friction and damping. Furthermore, by keeping the device inertia low, less actuator effort is wasted on accelerating the loader's mechanical linkage, instead leaving more force to be applied to the attached human arm.

Another way of expressing the rationale for these desired linkage properties is some-

[2]A backdriveable manipulator linkage that is used for the study of human or animal hand motion, is called a manipulandum (see reference [129] for example).

what obvious: the transmission between the actuators and the human-machine interface should not contribute any dynamic effects to the overall system. Ideally, if the links were rigid and massless, and there were no dissipation through friction or viscous damping, the mechanism would be invisible to the human subject's kinesthetic (proprioceptive) sense as specified earlier in Section 3.2. In this manner, all changes in coupled limb-manipulandum dynamics and in human sensation of these dynamics would result from the control of the device actuators or from the actions of the subject him/herself.

In choosing to build an electromechanically actuated human interactive loader, it was noted at the begining of Section 3.4 that the machine would take the form of a robotic manipulator. It is instructive at this stage to review the basic configurations of other electromechanical robots, while bearing in mind the desirable characteristics for the arm loading already discussed in this section.

Even though the limb loader design under consideration here will only have two kinematic degrees of freedom, most industrial robots (as well as loading manual interfaces to several other virtual environment systems summarized in Chapter 2) have more—usually up to six degrees of freedom, so that the manipulator end effector can undergo general positioning and orientation. In commercial electromechanical manipulators, a single degree of freedom actuator is associated with each kinematic degrees of freedom. The relative motion associated with each degree of freedom in most manipulators takes place across a simple joint (or lower pair) that is either prismatic (translational) or revolute (rotational), and is separated from the other joints in the mechanism by links.[3]

Familiar two degree of freedom devices and substructures from more complex mechanisms can be constructed from these two types of lower pairs. Figure 3.1 depicts a planar "armlike" mechanism that arises when two revolute pairs (R-R) with parallel rotational axes are linked in series. Cascading two revolute pairs (R-R) with perpendicular

[3]The remaining single degree of freedom lower pair, the helical joint, is usually seen in manipulators as a transmission for extracting translational motion from a rotary actuator. Rotary geared transmissions which are commonly used in industrial manipulators are higher pairs and can usually be modelled as equivalent lower pairs. Relative motion across greater than single degree of freedom lower pairs (spherical, cylindrical, or planar joints) can be divided up as if they occurred in a series of several single degree of freedom joints.

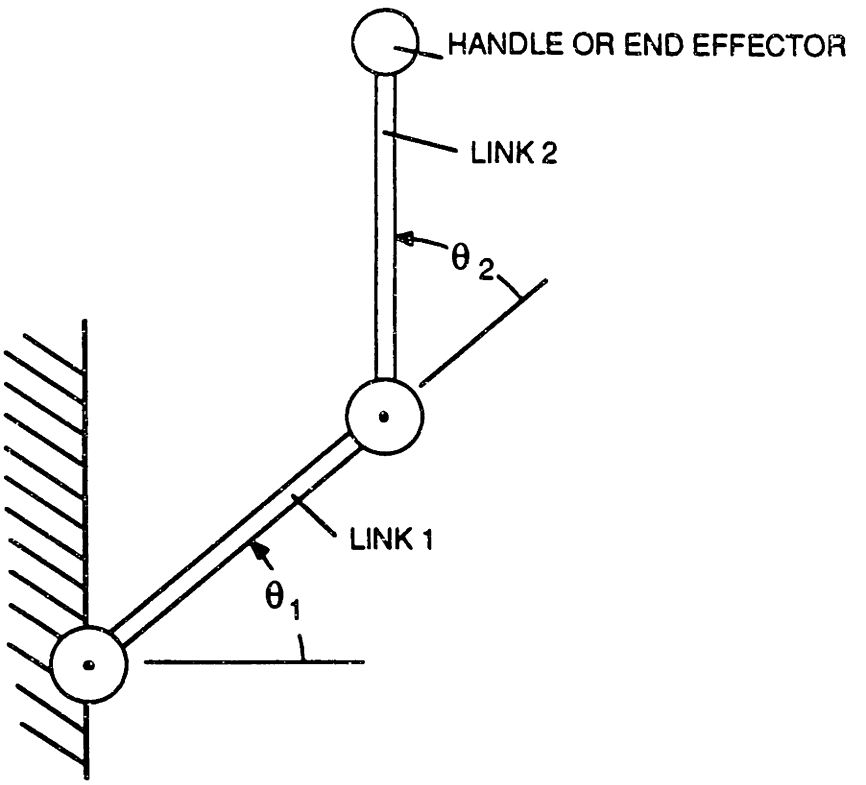

Figure 3.1: Planar revolute-revolute (R-R) serial arm linkage.

rotational axes leads to the spherical surface workspace shown in Figure 3.2. Similarly, mounting a second prismatic pair orthogonally on a first results in a Cartesian serial linkage such as the one in Figure 3.3.

Direct-Drive

If the motor associated with a particular degree of freedom is situated exactly at that joint, with the motor's base (stator) attached to, or part of, the first link and its moving element (rotor) attached to, or part of, the second link across the joint, the actuation is described as "direct-drive." Manipulators, such as the simple ones depicted in Figures 3.1, 3.2, and 3.3, if their actuators are located right at each joint, are called direct-drive robots. The distinct advantage of direct-drive is the absence of mechanical transmission

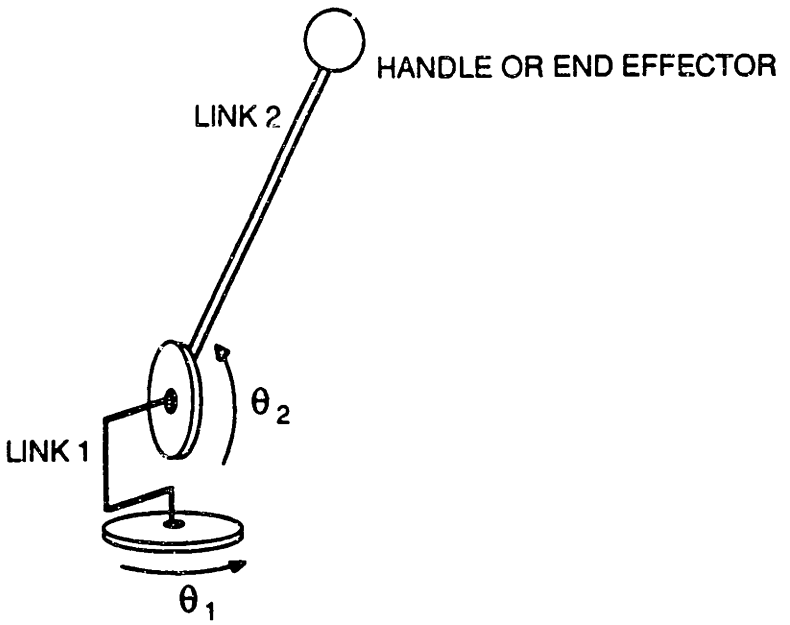

Figure 3.2: Spherical revolute-revolute (R-R) serial linkage.

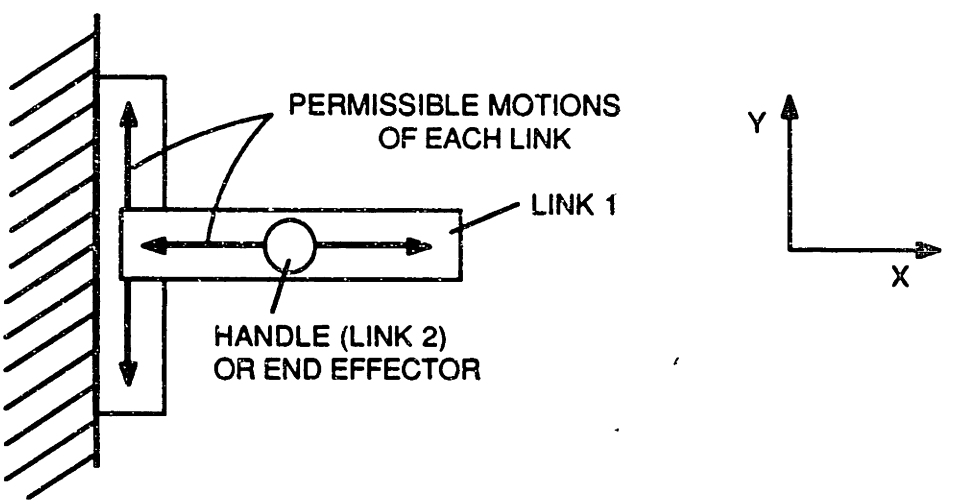

Figure 3.3: Cartesian prismatic-prismatic (P-P) serial linkage.

elements that introduce compliance, friction, or other undesirable dynamics that could compromise backdriveability. There is, however, a cost entailed in choosing a direct drive configuration—each link must carry the next link's actuator. This means that not only is the link inertia increased by the mass of the actuator itself, but also by the added material required to stiffen the linkage structurally to support the added actuator mass. The increase in combined link and actuator inertia reduces the overall bandwidth of the mechanical system and necessitates still larger actuators with greater torque capabilities (and inertia) to produce requisite accelerations. An additional factor in human movement experimentation is that the added inertia will be detectable by the human operator and will affect the passive mechanics of the coupled human-manipulandum system.

Remote Drive

The only alternative to massive manipulators with bulky electromechanical actuators at each joint, other than the design of new lightweight motors, is to locate the actuators at the base of the manipulator (*i.e.*, at mechanical ground) and drive the linkage remotely through mechanical transmissions. Transmissions from rotary actuator motion to rotary link output can take many forms, including gear trains, belts and pulleys, cable drives, chains and sprockets, and flexible drive shafts. With the exception of flexible drive shafts, these elements may also be useful in transforming rotary into translational motion. Applications of these transmission mechanisms abound in the robotics trade. The result of their use, however, is undesirable dynamic effects between the actuators and manipulator endpoint. Gears, lead screws, and chain drives may cause backlash. Belts, cables, and flexible drive shafts make for a compliant coupling between the actuator and the system output. All of these transmissions can add friction to the system. Prudent selection and thoughtful optimization of any one of these transmission designs, though, can enhance performance sufficiently for use in remotely actuated electromechanical manipulators.

Another form of remote drive depends on closed kinematic chains made up of rigid links to transmit motion from actuators to the manipulator endpoint. Because the actua-

tor rotors are connected directly to rigid links, such configurations have been represented as direct-drive by many robot designers [14]. An example of this type of transmission is the "semi-direct" parallelogram drive; the planar armlike manipulator shown in Figure 3.4 uses a four-bar mechanism to connect rotation at the elbow joint to the rotation of a motor anchored to ground at the shoulder. The advantages of semi-direct drives are that they offer lower compliance and friction than the various transmissions elements described in the previous paragraph. The disadvantages are additional inertia due to added linkage material and tighter alignment tolerances required during fabrication. If misaligned, assembly of a semi-direct drive transmission can lead to heightened joint friction and, because of the elasticity of what are in actuality not truly rigid links, binding when moved out of preferred orientations.

Implications of Configuration on Control

Manipulator linkage and transmission design not only affects device dynamics but also plays a major role in system control. The goal in most manipulator control applications is to regulate kinematics, forces or other properties at the manipulator endpoint. Usually, these objectives are specified with respect to a fixed, typically Cartesian, global reference frame. Unless the manipulator itself is Cartesian (*i.e.*, orthogonal with prismatic lower pairs), the transformation from instantaneous joint space measurements to manipulator endpoint kinematics and forces in *quasi-static* situations demands repetitive trigonometric calculations. In *dynamic* cases, the computation issue becomes significantly more involved. Not only do trigonometric transformations have to be handled, but nonlinear velocity terms necessary for the compensation of Coriolis and centripetal terms must be computed as well [15].[4]

[4]See Hollerbach [77] for a concise review of numerical issues in the computer control of manipulator dynamics.

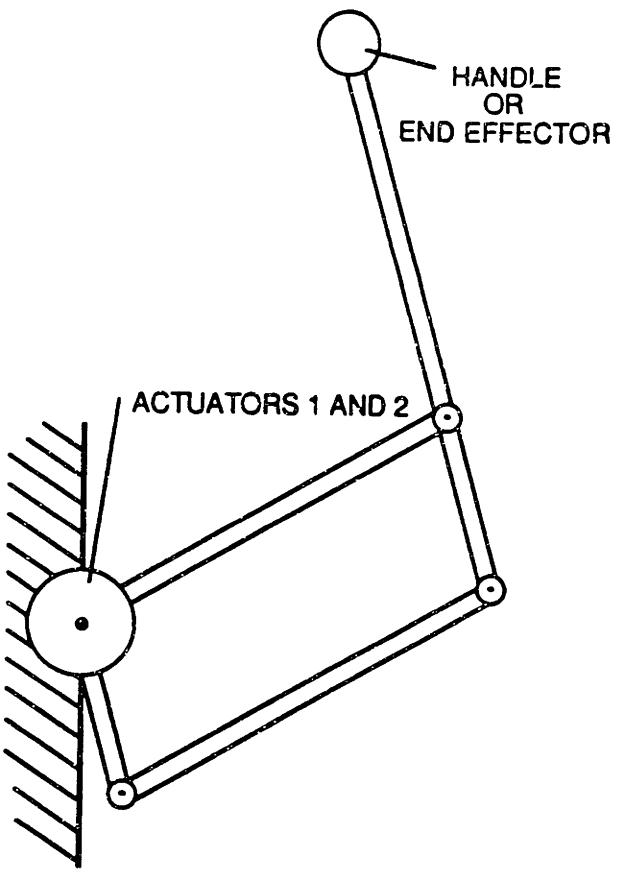

Figure 3.4: Planar five-link manipulator linkage. The five bar mechanism consists of the four-bar parallelogram links plus ground—the fifth link. The result is a closed chain linkage with five links and five revolute joints. Two of the revolute joints correspond to the bearings and shafts of the fixed base rotary actuators.

3.6 Design for Control

Another approach to the manipulator control computation problem is to design and build manipulators that are mechanically "clean"—clean in the sense that they do not have undesirable dynamical or geometric properties that need to be masked by computationally intensive control routines. This tactic of simplifying control through mechanical design was demonstrated successfully by Asada and Youcef-Toumi [15] in the elimination of Coriolis and centripetal coupling between the actuators of dynamically balanced two and three degree of freedom manipulators. A drawback with their design methodology, though, lies in the inability of these precisely balanced manipulators to cope with unpredictable external loads. Unfortunately, these are exactly the kind of loads that would be encountered by a manipulator employed as the manual interface to a virtual environment when it is coupled to time-varying mechanical input from a human arm. Furthermore, it should be noted that Asada and Youcef-Toumi's manipulators are only dynamically decoupled in *joint* space. Control of *endpoint* motion or force in orthogonal coordinates—except at specific joint configurations for a restricted set of arm link length designs—in general, still requires computation of measurement-based geometric and kinematic transformations.

For human tremor experimentation, the planned operation of the virtual environment system requires an analog bandwidth in excess of 12 Hz at the manual interface simultaneous with a 30 Hz video display update rate, data collection for subsequent off-line analysis, and safety maintenance. While the bandwidth required for this manual interface is significantly greater than that achieved in prior related systems (see Chapter 2 and Section 5.1), the capabilities of the computer available in-house for real-time control, an LSI-11/23 based processor (Digital Equipment Corp., Maynard MA) are not. One drawback is that the computer is a single processor system, and thus can only work on one task at any particular instant. The second, and more critical shortcoming is a processor architecture that restricts useable code space to only 64 kBytes, limiting the complexity of geometric and kinematic transformation computations that can be carried

out in real-time.

The title "Design for Control" at the head of this section indicates a strategy pursued throughout the design and development of this virtual environment system. This strategy was to consider the mechanical, electromechanical, and electronic facets of the design problem and organize them so that the host processor would be unburdened of many of the computationally intensive problems related to coordinate transformations and the compensation of undesirable component characteristics. By minimizing numerical computation, the host processor could then be freed for on-line experiment supervision and data collection.

While "Design for Control" in general can lead to significantly enhanced system performance, there are costs entailed. Potentially among these are a more difficult design and greater hardware expense. For the virtual environment system under consideration here, similar added expense would as likely have been incurred if the choice had been made to develop or purchase more sophisticated computing equipment.

The prescription followed to reduce and distribute computation consists of the measures described here:

- Electromechanical actuators should have high bandwidth and behave as closely as possible to ideal linear sources. Deviations from ideal behavior may necessitate computer based compensation.

- The transmission between the actuators and the human-machine interface should be stiff, have low inertia, and not contribute friction. Again, less than adequate characteristics may require compensation by the controller.

- An appropriate mechanism geometry should be selected to reduce (or eliminate) the need for computation to transform actuator inputs to desired output mappings (force or kinematics) at the human-machine interface.

- All kinematic and force variables that are needed for implementation of the controller should be sensed directly. Computer based differentiation, integration, or

spatial transformation to arrive at necessary, but unmeasured, controller inputs can significantly increase the computational burden.

- As much of the signal scaling and signal combination as possible should be performed electronically, external to the host computer.

The first two points apply exclusively to the development of the manual interface of the system; the remaining three to both the visual and manual interfaces. The extent to which these measures were employed and were successful is the topic of the following two chapters.

Chapter 4

Manipulandum Design and Implementation

4.1 System Hardware Overview

The philosophy behind the design of the manual interface for the virtual environment system was described in the previous chapter. Rather than first build a manipulator for the limb loading interface, and then attempt to "control away" undesirable characteristics in the mechanical system by writing intricate control software, it was felt that many potential problems could be circumvented by integrating the overall design process and considering the mechanical and control aspects simultaneously. By setting a goal of minimizing the amount of real-time computation associated with each facet of the design (mechanical, electromechanical, sensor, and controller architecture), the virtual environment system's performance, which to a large extent would depend on controller bandwidth, could be enhanced.

The resultant virtual environment system for the study of human arm dynamics and manual control consists of three major hardware components—a two degree of freedom manipulandum, a video display, and a supervisory host computer. The manipulandum (backdriveable manipulator) includes actuators and power conversion electronics, a linkage that transfers torques and kinematics between the actuators and the human operator, and sensors that measure two degree of freedom kinematics and force at the human-machine interface. A custom built electronic unit which conditions the sensor signals,

monitors system safety, and houses the loading controller circuitry, also ties the manipulandum to the host computer's D/A, A/D and digital I/O ports. The video display, based on a personal graphics computer, is connected to the remainder of the system through the host computer.

This chapter treats the design of the manipulandum's novel kinematic linkage and the selection of its actuators and sensors. Details of the electronic interface unit and the two computers are saved for the description of system control and performance in the following chapter.

4.2 Spherical Closed Chain Mechanism Design

4.2.1 Inspiration

Summarizing from the previous chapter, the desired characteristics for the manual interface are: 1) high bandwidth; 2) backdriveability; and 3) simple kinematics. The first of these criteria necessitated that the mechanism have stiff links and low inertia. The excessive inertia of bulky serial linkages that carry their motors, plus the heftier motors required to power these larger linkages, as described in Section 3.5, prohibits the use of a true direct drive system for this application. This indicates that while the basic device configurations illustrated in Figures 3.1, 3.2, and 3.3 cannot be employed in designs where the first link must carry the second link's actuator, they may be useful in implementations where both actuators can be anchored to a common mechanical ground. If remotely driven implementations of these configurations are considered, the bandwidth requirement also rules out the compliant drive train elements discussed in Section 3.5. The second criterion, backdriveability, further restricts the use of geared transmissions that contribute excessive friction.

At this stage, of the "conventional" manipulator configurations depicted in Figures 3.1 through 3.4, only the closed chain planar mechanism (Figure 3.4), with a rigid four-bar transmission between a fixed base motor and its second link remains. Unfortunately, as mentioned in Section 3.6, this planar five-bar mechanism fails to satisfy the third

criterion because of the need for geometric computation to resolve rotary actuators in joint space into decoupled endpoint kinematics and static forces with respect to a fixed external reference frame.

One solution, a new closed chain manipulator drive for coupling the human operator to fixed base rotary actuators that maintains low inertia, low friction, high stiffness, and kinematic simplicity is proposed here. The inspiration for this design is found in the standard position sensing joysticks that are commonly used as a manual control input for many types of equipment, from powered wheelchairs to arcade games. The main features of the standard joystick mechanism are depicted by Figure 4.1 in a form that has been slightly modified for clarity of illustration.[1] It consists of two slotted bail-shaped swing arms or yokes, A and B, each of which pivots on pin joints—C and D for yoke A, and E and F for arm B. The axes CD and EF lie in the same plane and intersect at right angles. The input handle shaft G pivots about the spherical joint H that is centered at the intersection of the CD and EF axes and is guided at its other end by the intersection of the slots in the two yokes. Note also that spherical pair H shares the same ground link with revolute pairs C, D, E and F. In some joysticks, a rectangular block, J, that slides in one of the yoke slots is fixed to the handle shaft. This curved slider prevents unconstrained rotation of the handle shaft about its center line, reducing the handle shaft to two degrees of freedom, thereby enabling the position *and* orientation of the handle shaft to be uniquely determined by the displacements of the swing arm yokes. In the conventional joystick, these displacements are measured by electronic goniometers (rotary potentiometers), one along each of the CD and EF axes. A loading manipulator based on this configuration would have rotary actuators in place of the potentiometers.

The joystick mechanism depicted in Figure 4.1 forms a multiply closed chain composed of the following joints: a spherical pair at the center of the handle shaft; two revolute pairs at the base of each yoke; a sliding contact (curved prismatic pair) between the

[1]The difference between commercial joysticks and the modified form in Figure 4.1 is that commercial ones have the yokes or bails underneath the $CDEF$ plane and are guided by an extension of the handle shaft below the spherical joint.

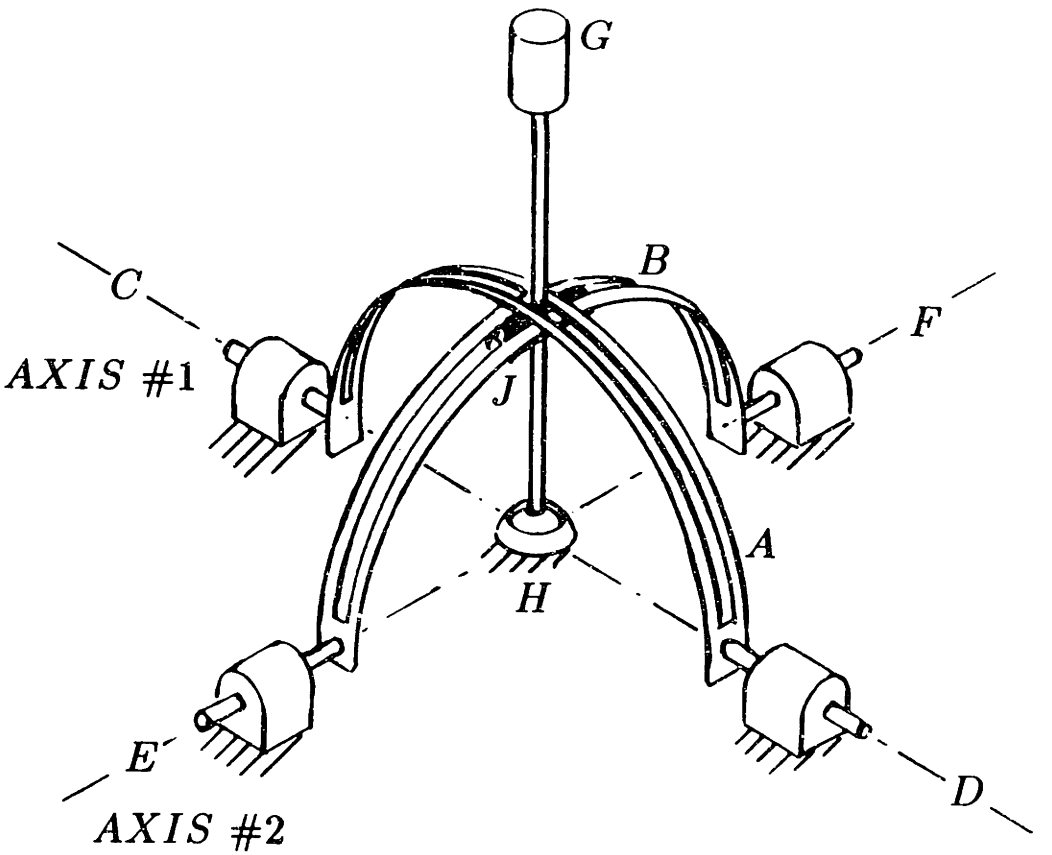

Figure 4.1: Standard two degree of freedom slotted yoke joystick mechanism. See text for details.

handle shaft and the first yoke; and a combination rolling and sliding contact between the handle shaft and the second yoke. All of the joints in the mechanism are subject to friction, including the revolute pairs, which in commercial units are not ball bearing mounted. The friction in the ball-and-socket spherical pair can be reduced by loosening the socket, and consequently increasing play in the joint. Similarly, cutting wider slots in the swing arm yokes also decreases friction, but again at the expense of greater play (*i.e.*, backlash) in the mechanism.

If the sliding contact in all these joints were to be replaced with the rolling contact of properly preloaded ball bearings, both friction and backlash in the mechanism could be decreased, enhancing its backdriveability, while still maintaining the joystick kinematics for the coupling between the human and the loading actuators.

4.2.2 Evolution

Upon examination of the standard joystick mechanism, it is evident that the multiply closed chains formed by the swing arm yokes and handle shaft and their joints involve a high degree of redundancy. The essential feature of the joystick's kinematics—spherically centered motion that is converted into unique angular displacements of two rotary potentiometer shafts—however, can be reproduced by keeping only three of the original lower pairs as shown in Figure 4.2. These three pairs include two revolute joints, both of which are mounted on the same mechanical ground, and a spherical pair that couples the moving member of one revolute joint to its ball and the moving member of the other to its socket. The question then is—given that the moving elements of two orthogonal fixed-base revolute pairs can be joined to each other without conflict through the ball-and-socket—how to form a manipulator mechanism that can still extract spherically centered handle link motion related to the rotation of the two revolute joints.

The solution is to break the three degree of freedom spherical joint down into an equivalent set of three intersecting, non-colinear, single degree of freedom revolute pairs. The result of decomposing the spherical joint into its basic elements is the five link

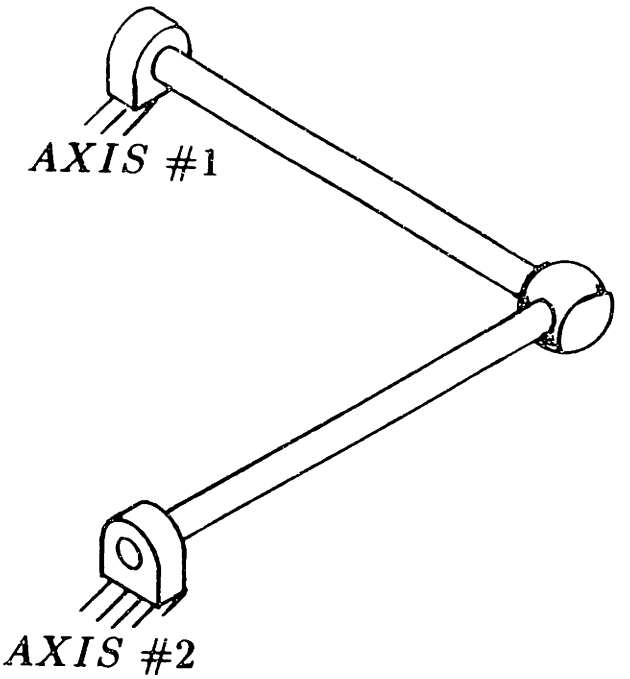

Figure 4.2: The fundamental joints of the standard joystick mechanism. Note that neither half of the spherical pair is attached to ground.

(including ground) single loop closed chain mechanism with revolute joints depicted in Figure 4.3. The handle shaft in this case is simply an extension of one of the links in the chain. This single closed chain mechanism, which forms the basis for the limb loading manipulandum, embodies the same geometric relation between actuator shaft angles and handle position and orientation as the joystick configuration of Figure 4.1. All relative motion in the new mechanism, though, takes place across revolute pairs, all of which can be implemented with ball bearings rather than sliding contact joints. By only sing ball bearings, friction and play are greatly reduced, resulting in improved backdriveability and stiffness of the transmission between the human and the manipulandum actuators.

The mobility analysis for the manipulanduin linkage is more understood by examining the equivalent spherical 5R (five revolute pairs) closed chain mechanism represented in Figure 4.4.[2] As in Grübler's criterion for planar mechanisms, the l links, by being constrained to the spherical surface, each have a maximum of three kinematic degrees of

[2]All three mechanism representations, Figures 4.1, 4.3, and 4.4, are considered spherical because the loci of motion of all points, on all links, lie on the surfaces of concentric spheres.

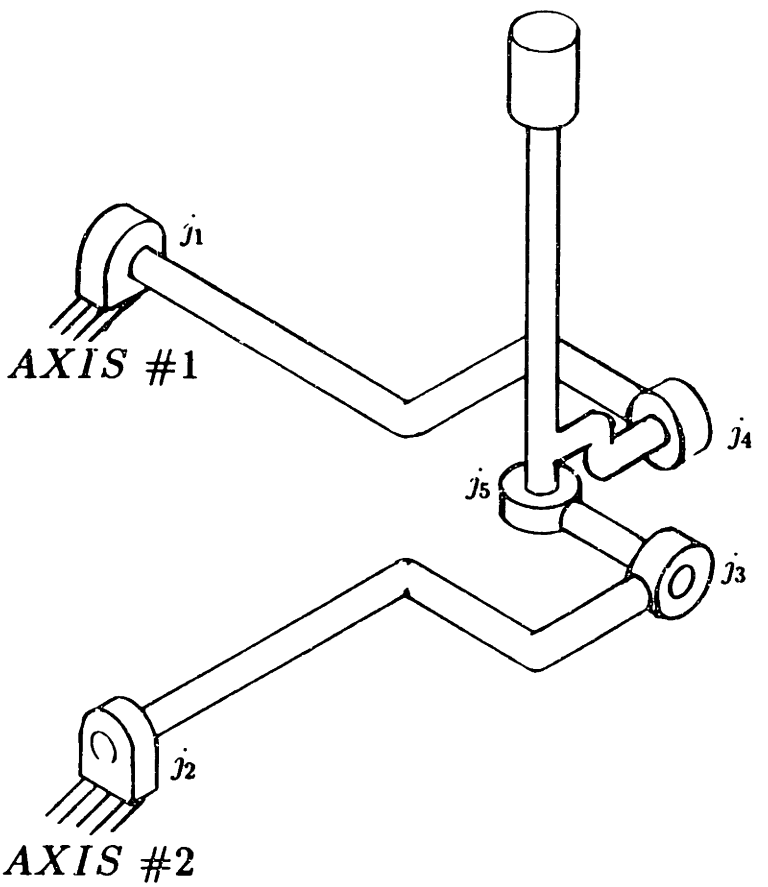

Figure 4.3: Five link closed chain joystick mechanism.

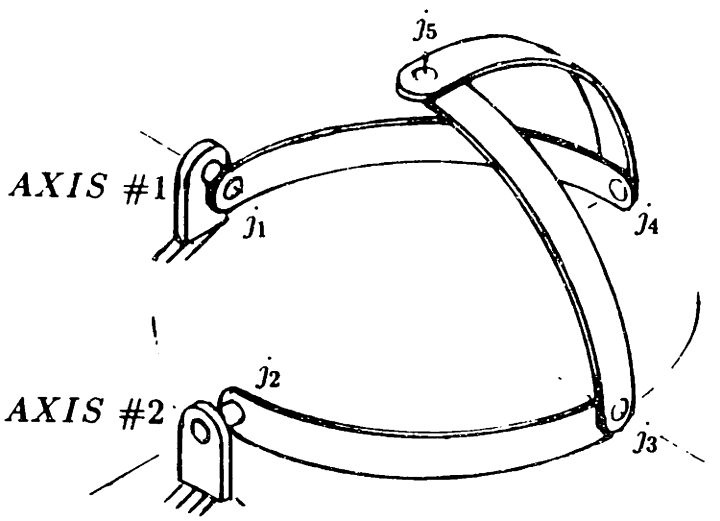

Figure 4.4: Spherical five-bar closed chain mechanism with equal link lengths.

freedom. Similarly, each of the j simple revolute joints removes two of the three available degrees of freedom on the surface of the sphere. The resultant mobility of this 5R spherical closed chain with $l = j = 5$, where one link location is arbitrary, is $3(l-1) - 2j = 2$. This verifies that the kinematics of the closed chain revolute joint mechanism can be fully described by two generalized coordinates, the same number required for the conventional swing arm joystick.

4.2.3 Kinematics and Statics

If the manipulandum based on the closed chain configuration depicted in Figure 4.3 is to be used successfully in a mechanical loading interface for human subjects, it is essential to derive the mathematical descriptions relating actuator torques and motion with forces and motion at the human interface, *i.e.* the handle shaft output. As will be seen later, these mathematical relations are necessary both for the control of the actuators and for

the interpretation of data from the sensors that measure device kinematics.

To assist in setting up the transformations between the natural actuator (or potentiometer) shaft angle coordinates and the fixed xyz Cartesian frame description of handle shaft endpoint, the construction in Figure 4.5 is developed. In the construction, two planes, P_1 and P_2, are affixed to, and rotate with, the shafts of actuators 1 and 2 that lie respectively along axes x and y. The handle shaft link, which pivots at the origin of the the xyz frame, is constrained to lie along the intersection of the P_1 and P_2 planes.[3] Hence, angle α, between plane P_1 and the xz plane, and angle β, between P_2 and the yz plane, uniquely determine the handle shaft position and orientation.

Geometric Relations

The orientations of the planes P_1 and P_2 are defined by their surface normals, $\mathbf{n}_1$ and $\mathbf{n}_2$ respectively, as

$$\mathbf{n}_1 = -\cos\alpha\,\mathbf{j} - \sin\alpha\,\mathbf{k} \tag{4.1}$$

and

$$\mathbf{n}_2 = \cos\beta\,\mathbf{i} - \sin\beta\,\mathbf{k} \tag{4.2}$$

The spatial orientation of the long axis of the handle shaft link, $\mathbf{n}_3$, is given by the intersection of these two planes. Using the cross product

$$\mathbf{n}_3 = \mathbf{n}_1 \times \mathbf{n}_2 \tag{4.3}$$

or

$$\mathbf{n}_3 = \cos\alpha\sin\beta\,\mathbf{i} - \sin\alpha\cos\beta\,\mathbf{j} + \cos\alpha\cos\beta\,\mathbf{k} \tag{4.4}$$

[3]Note that in the joystick mechanism (Figure 4.1), the swing arms' role is identical to that of planes P_1 and P_2. In the joystick, the handle shaft is constrained to lie on a line joining the intersection of the two orthogonal actuator shaft axes and the swing arm slots.

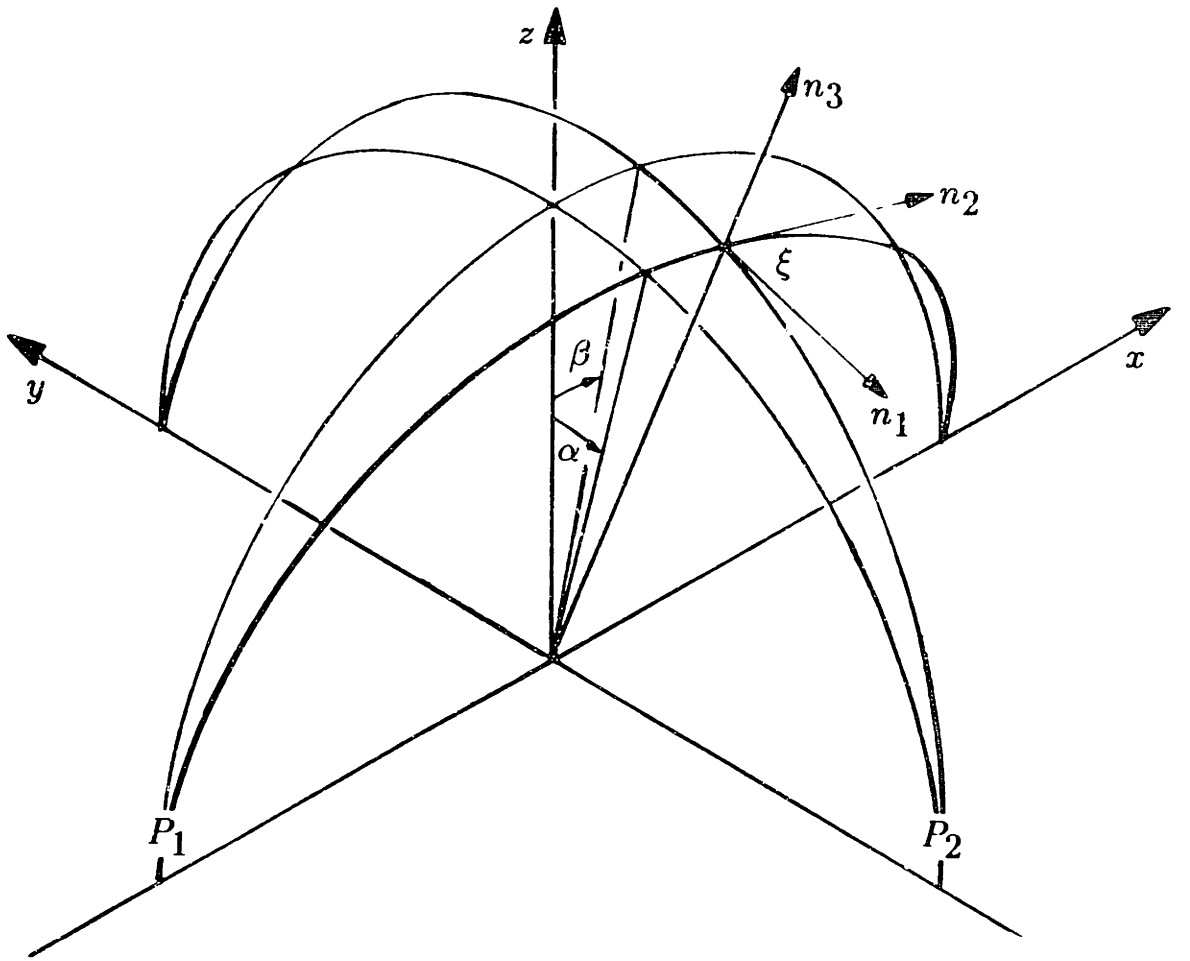

Figure 4.5: Pivoted plane joystick construction. See text for details.

Unlike $\mathbf{n}_1$ and $\mathbf{n}_2$, $\mathbf{n}_3$ is not a unit normal vector. Normalizing $\mathbf{n}_3$, the unit vector is

$$\begin{aligned} \mathbf{e}_3 &= \mathbf{n}_3 / |\mathbf{n}_3| \\ &= \frac{\cos\alpha \sin\beta}{\sqrt{1-\sin^2\alpha\sin^2\beta}}\,\mathbf{i} - \frac{\sin\alpha\cos\beta}{\sqrt{1-\sin^2\alpha\sin^2\beta}}\,\mathbf{j} + \frac{\cos\alpha\cos\beta}{\sqrt{1-\sin^2\alpha\sin^2\beta}}\,\mathbf{k} \end{aligned} \tag{4.5}$$

Values of $|\mathbf{n}_3| = \sqrt{1-\sin^2\alpha\sin^2\beta}$ are listed for a range of angles α and β in Table 4.1. As witnessed from the table, the magnitude of this divisor factor is very close to unity over this portion of the mechanism workspace, and, for approximation purposes, may be neglected.

α	β	$\lvert\mathbf{n}_3\rvert$
0°	0°	1.00000
5°	5°	0.99997
10°	10°	0.99955
15°	15°	0.99775
20°	20°	0.99313
25°	25°	0.98392
30°	30°	0.96825
20°	0°	1.00000
20°	5°	0.99956
20°	10°	0.99823
20°	15°	0.99607
20°	25°	0.98950
20°	30°	0.98527

Table 4.1: Normalizing factor $|\mathbf{n}_3|$ for $\alpha = \beta$ and for $\alpha = 20°$ over a range of β values.

The angle between the two planar surfaces as P_1 and P_2 rotate about the actuator axes is given by the dot product

$$\cos\xi = \frac{\mathbf{n}_1 \cdot \mathbf{n}_2}{|\mathbf{n}_1||\mathbf{n}_2|} \tag{4.6}$$

or,

$$\xi = \cos^{-1}(\sin\alpha \sin\beta) \tag{4.7}$$

The difference between angle ξ and 90 degrees provides a measure of the non-orthogonality of P_1 and P_2, *i.e.*, the static coupling between the actuators attached to these two planes. Values of ξ over a range of $\alpha = \beta$, the condition for which the effect on ξ is most severe for a given α, are listed in Table 4.2. Note that when either of α or $\beta = 0$, the angle between the two planes is $\xi = 90$ degrees.

α	β	ξ
0°	0°	90.0°
5°	5°	89.6°
10°	10°	88.3°
15°	15°	86.2°
20°	20°	83.3°
25°	25°	79.7°
30°	30°	75.5°

Table 4.2: Non-orthogonality angle ξ for $\alpha = \beta$.

By including a third general displacement variable, r, that lies along the handle link orientation vector, $\mathbf{e}_3$, an (α, β, r) coordinate description of three space becomes available. This in turn makes an *invertible* mapping from the α and β manipulandum based coordinates into the fixed (x, y, z) reference frame possible.[4] Thus, multiplying

[4]Because the actual manipulandum mechanism has only two degrees of freedom, α and β, its handle endpoint is restricted to trajectories that lie on a spherical surface. The transformation of endpoint motion described in the natural manipulandum coordinates α and β into (x, y, z) results in the description of a spherical surface in three-space. This two-to-three space mapping is not invertible because, while any location on the surface of the sphere traversable by the manipulandum endpoint can be expressed in (x, y, z) coordinates, there exists an infinity of points in the global Cartesian frame that do not lie on this sphere, and that therefore cannot be described solely by the angle variables α and β.

each Cartesian component of $\mathbf{e}_3$ in Equation (4.4) by r:

$$x = \frac{r\cos\alpha\sin\beta}{\sqrt{1-\sin^2\alpha\sin^2\beta}} \tag{4.8}$$

$$y = \frac{-r\sin\alpha\cos\beta}{\sqrt{1-\sin^2\alpha\sin^2\beta}} \tag{4.9}$$

$$z = \frac{r\cos\alpha\cos\beta}{\sqrt{1-\sin^2\alpha\sin^2\beta}} \tag{4.10}$$

If the handle shaft link length from its center of rotation to its endpoint is set to $r = R_o$, Equations (4.8), (4.9), and (4.10) yield the Cartesian description of the manipulandum endpoint coordinates (x_m, y_m, z_m):

$$x_m = R_o\frac{\cos\alpha\sin\beta}{\sqrt{1-\sin^2\alpha\sin^2\beta}} \tag{4.11}$$

$$y_m = -R_o\frac{\sin\alpha\cos\beta}{\sqrt{1-\sin^2\alpha\sin^2\beta}} \tag{4.12}$$

$$z_m = R_o\frac{\cos\alpha\cos\beta}{\sqrt{1-\sin^2\alpha\sin^2\beta}} \tag{4.13}$$

Equations (4.11), (4.12), and (4.13) describe the position of the manipulandum endpoint based on the handle link's long axis orientation and length. These equations, however, do not give an indication of the orientation of an orthogonal reference frame that is attached to the endpoint of the moving handle link. That derivation is presented later in Section 4.5.4.

The opposite mapping from the Cartesian description of the mechanism into (α, β, r) coordinates can also be established. First, dividing Equation (4.9) by Equation (4.10),

and then taking the inverse tangent of both sides

$$\alpha = \tan^{-1}\left(-\frac{y}{z}\right) \tag{4.14}$$

Similarly, dividing Equation (4.8) by Equation (4.10), and taking the inverse tangent

$$\beta = \tan^{-1}\left(\frac{x}{z}\right) \tag{4.15}$$

The length of a vector along the joystick handle orientation is by definition

$$r = \sqrt{x^2 + y^2 + z^2} \tag{4.16}$$

Velocities

The transformations from angular velocity at the actuators to the inertial Cartesian frame representation of translational velocity at the handle endpoint, and vice versa, can be expressed by making use of the generalized manipulandum coordinates (α, β, r).

The velocities in the two coordinate systems are related by

$$\dot{\mathbf{q}}_m = \mathbf{J}_m \dot{\mathbf{x}} \tag{4.17}$$

where,

$$\mathbf{q}_m = \begin{bmatrix} \alpha \\ \beta \\ r \end{bmatrix} \tag{4.18}$$

$$\mathbf{x} = \begin{bmatrix} x \\ y \\ z \end{bmatrix} \tag{4.19}$$

and $\mathbf{J}_m$ is the manipulandum Jacobian, defined as

$$\mathbf{J}_m = \begin{bmatrix} \frac{\partial \alpha}{\partial x} & \frac{\partial \alpha}{\partial y} & \frac{\partial \alpha}{\partial z} \\ \frac{\partial \beta}{\partial x} & \frac{\partial \beta}{\partial y} & \frac{\partial \beta}{\partial z} \\ \frac{\partial r}{\partial x} & \frac{\partial r}{\partial y} & \frac{\partial r}{\partial z} \end{bmatrix} \tag{4.20}$$

Using Equations (4.14), (4.15), and (4.16) to evaluate each element of the Jacobian in Equation (4.20)

$$\mathbf{J}_m = \begin{bmatrix} 0 & -\frac{z}{y^2+z^2} & \frac{y}{y^2+z^2} \\ \frac{z}{x^2+z^2} & 0 & -\frac{x}{x^2+z^2} \\ \frac{x}{\sqrt{x^2+y^2+z^2}} & \frac{y}{\sqrt{x^2+y^2+z^2}} & \frac{z}{\sqrt{x^2+y^2+z^2}} \end{bmatrix} \tag{4.21}$$

Substituting for x,y, and z from Equations (4.8), (4.9), and (4.10) into Equation (4.21)

$$\mathbf{J}_m = \begin{bmatrix} 0 & -\frac{\cos\alpha\sqrt{1-\sin^2\alpha\sin^2\beta}}{r\cos\beta} & -\frac{\sin\alpha\sqrt{1-\sin^2\alpha\sin^2\beta}}{r\cos\beta} \\ \frac{\cos\beta\sqrt{1-\sin^2\alpha\sin^2\beta}}{r\cos\alpha} & 0 & -\frac{\sin\beta\sqrt{1-\sin^2\alpha\sin^2\beta}}{r\cos\alpha} \\ \frac{\cos\alpha\sin\beta}{\sqrt{1-\sin^2\alpha\sin^2\beta}} & -\frac{\sin\alpha\cos\beta}{\sqrt{1-\sin^2\alpha\sin^2\beta}} & \frac{\cos\alpha\cos\beta}{\sqrt{1-\sin^2\alpha\sin^2\beta}} \end{bmatrix} \tag{4.22}$$

Using the Jacobian in Equation (4.22), the velocity relations represented by Equation (4.17) may be written. For a fixed handle length $r = R_o$, the velocities at the manipulandum actuator shafts due to handle endpoint velocity are given by

$$\dot{\alpha} = -\frac{\cos\alpha\sqrt{1-\sin^2\alpha\sin^2\beta}}{R_o\cos\beta}\dot{y}_m - \frac{\sin\alpha\sqrt{1-\sin^2\alpha\sin^2\beta}}{R_o\cos\beta}\dot{z}_m \tag{4.23}$$

$$\dot{\beta} = \frac{\cos\beta\sqrt{1-\sin^2\alpha\sin^2\beta}}{R_o\cos\alpha}\dot{x}_m - \frac{\sin\beta\sqrt{1-\sin^2\alpha\sin^2\beta}}{R_o\cos\alpha}\dot{z}_m \tag{4.24}$$

Because r is constant, the third equation essentially expresses a constraint that is due to the spherical surface that the manipulandum endpoint must traverse:

$$\begin{aligned}\dot{r} &= 0 \\ &= \frac{\cos\alpha\sin\beta}{\sqrt{1-\sin^2\alpha\sin^2\beta}}\dot{x}_m - \frac{\sin\alpha\cos\beta}{\sqrt{1-\sin^2\alpha\sin^2\beta}}\dot{y}_m + \frac{\cos\alpha\cos\beta}{\sqrt{1-\sin^2\alpha\sin^2\beta}}\dot{z}_m\end{aligned} \tag{4.25}$$

The Cartesian velocity components of a point on the joystick handle shaft can beexpressed as functions of (α, β, r) by inverting the velocity relation in Equation (4.17):

$$\dot{\mathbf{x}} = \mathbf{J}_m^{-1}\dot{\mathbf{q}}_m \tag{4.26}$$

As an aside to better understand the joystick mechanism, it is instructive to examine an intermediate stage in the calculation of the inverse Jacobian, $\mathbf{J}_m^{-1}$, according to

$$\mathbf{J}_m^{-1} = \frac{[\mathrm{cof}\,\mathbf{J}_m]^T}{\det\mathbf{J}_m} \tag{4.27}$$

The determinant of $\mathbf{J}_m$ in Equation (4.22) is

$$\det\mathbf{J}_m = \frac{(1-\sin^2\alpha\sin^2\beta)^{3/2}}{r^2\cos\alpha\cos\beta} \tag{4.28}$$

By l'Hôpital's rule, $\det\mathbf{J}_m$ is zero valued for either α or β equal to ± 90 degrees, indicating that the joystick mechanism exhibits a singularity at either of these angle conditions, *i.e.*, whenever the handle shaft lies flat in the xy plane of Figure 4.5. Physically, this implies that when one actuator shaft angle is fixed at either ± 90 degrees, it is impossible to move the handle shaft endpoint from that position directly to another in the xy plane by rotating the other actuator shaft. It is possible, however, to position the endpoint to any location on the circle in the xy plane (except, of course, where the joystick mechanism interferes with itself), provided that either of the α or β shaft angles do not start at ± 90 degrees. The singularity does not imply that the shaft angles cannot move through the xy plane—it only prevents motion constrained to it.

Completing the inversion of $\mathbf{J}_m$,

$$\mathbf{J}_m^{-1} = \begin{bmatrix} -\frac{r\sin\alpha\sin\beta\cos^2\beta}{(1-\sin^2\alpha\sin^2\beta)^{3/2}} & \frac{r\cos\alpha\cos\beta}{(1-\sin^2\alpha\sin^2\beta)^{3/2}} & \frac{\cos\alpha\sin\beta}{\sqrt{1-\sin^2\alpha\sin^2\beta}} \\ -\frac{r\cos\alpha\cos\beta}{(1-\sin^2\alpha\sin^2\beta)^{3/2}} & \frac{r\sin\alpha\sin\beta\cos^2\alpha}{(1-\sin^2\alpha\sin^2\beta)^{3/2}} & -\frac{\sin\alpha\cos\beta}{\sqrt{1-\sin^2\alpha\sin^2\beta}} \\ -\frac{r\sin\alpha\cos^3\beta}{(1-\sin^2\alpha\sin^2\beta)^{3/2}} & -\frac{r\cos^3\alpha\sin\beta}{(1-\sin^2\alpha\sin^2\beta)^{3/2}} & \frac{\cos\alpha\cos\beta}{\sqrt{1-\sin^2\alpha\sin^2\beta}} \end{bmatrix} \tag{4.29}$$

At the endpoint of the actual two degree of freedom manipulandum, the displacement r is fixed to $r = R_o$, and consequently, is fixed, $\dot{r} = 0$. As a result, the velocity at the manipulandum endpoint, as expressed by Equation (4.26), reduces to

$$\dot{x}_m = -R_o\dot{\alpha}\left[\frac{\sin\alpha\sin\beta\cos^2\beta}{(1-\sin^2\alpha\sin^2\beta)^{3/2}}\right] + R_o\dot{\beta}\left[\frac{\cos\alpha\cos\beta}{(1-\sin^2\alpha\sin^2\beta)^{3/2}}\right] \tag{4.30}$$

$$\dot{y}_m = -R_o\dot{\alpha}\left[\frac{\cos\alpha\cos\beta}{(1-\sin^2\alpha\sin^2\beta)^{3/2}}\right] + R_o\dot{\beta}\left[\frac{\sin\alpha\sin\beta\cos^2\alpha}{(1-\sin^2\alpha\sin^2\beta)^{3/2}}\right] \tag{4.31}$$

$$\dot{z}_m = -R_o\dot{\alpha}\left[\frac{\sin\alpha\cos^3\beta}{(1-\sin^2\alpha\sin^2\beta)^{3/2}}\right] - R_o\dot{\beta}\left[\frac{\cos^3\alpha\sin\beta}{(1-\sin^2\alpha\sin^2\beta)^{3/2}}\right] \tag{4.32}$$

Acceleration

The acceleration transformations between actuator based coordinates and the manipulandum endpoint in the reference Cartesian frame can be found by simply differentiating the velocity relations. The acceleration of the manipulandum endpoint in terms of angular displacements, velocities, and accelerations measured at the actuator shafts can be derived either through differentiation of Equations (4.30), (4.31), and (4.32), or through differentiation of the matrix relation in Equation (4.26). Subject again to the constraint that the shaft handle is fixed in length to $r = R_o$ and the resultant restriction that

$\dot{r} = \ddot{r} = 0$, the accelerations at the manipulandum endpoint are given by

$$\begin{aligned}
\ddot{x}_m &= -R_o\ddot{\alpha}\left[\frac{\sin\alpha\sin\beta\cos^2\beta}{(1-\sin^2\alpha\sin^2\beta)^{3/2}}\right] + R_o\ddot{\beta}\left[\frac{\cos\alpha\cos\beta}{(1-\sin^2\alpha\sin^2\beta)^{3/2}}\right] \\
&\quad - R_o\dot{\alpha}^2\left[\frac{\cos\alpha\sin\beta\cos^2\beta(1+2\sin^2\alpha\sin^2\beta)}{(1-\sin^2\alpha\sin^2\beta)^{5/2}}\right] \\
&\quad - R_o\dot{\beta}^2\left[\frac{\cos\alpha\sin\beta(1+2\sin^2\alpha\sin^2\beta-3\sin^2\alpha)}{(1-\sin^2\alpha\sin^2\beta)^{5/2}}\right] \\
&\quad - 2R_o\dot{\alpha}\dot{\beta}\left[\frac{\sin\alpha\cos\beta(1+2\sin^2\alpha\sin^2\beta-3\sin^2\beta)}{(1-\sin^2\alpha\sin^3\beta)^{5/2}}\right] \qquad (4.33)
\end{aligned}$$

$$\begin{aligned}
\ddot{y}_m &= -R_o\ddot{\alpha}\left[\frac{\cos\alpha\cos\beta}{(1-\sin^2\alpha\sin^2\beta)^{3/2}}\right] + R_o\ddot{\beta}\left[\frac{\sin\alpha\cos^2\alpha\sin\beta}{(1-\sin^2\alpha\sin^2\beta)^{3/2}}\right] \\
&\quad + R_o\dot{\alpha}^2\left[\frac{\sin\alpha\cos\beta(1+2\sin^2\alpha\sin^2\beta-3\sin^2\beta)}{(1-\sin^2\alpha\sin^2\beta)^{5/2}}\right] \\
&\quad + R_o\dot{\beta}^2\left[\frac{\sin\alpha\cos^2\alpha\cos\beta(1+2\sin^2\alpha\sin^2\beta)}{(1-\sin^2\alpha\sin^2\beta)^{5/2}}\right] \\
&\quad + 2R_o\dot{\alpha}\dot{\beta}\left[\frac{\cos\alpha\sin\beta(1+2\sin^2\alpha\sin^2\beta-3\sin^2\alpha)}{(1-\sin^2\alpha\sin^2\beta)^{5/2}}\right] \qquad (4.34)
\end{aligned}$$

$$\begin{aligned}
\ddot{z}_m &= -R_o\ddot{\alpha}\left[\frac{\sin\alpha\cos^3\beta}{(1-\sin^2\alpha\sin^2\beta)^{3/2}}\right] - R_o\ddot{\beta}\left[\frac{\cos^3\alpha\sin\beta}{(1-\sin^2\alpha\sin^2\beta)^{3/2}}\right] \\
&\quad - R_o\dot{\alpha}^2\left[\frac{\cos\alpha\cos^3\beta(1+2\sin^2\alpha\sin^2\beta)}{(1-\sin^2\alpha\sin^2\beta)^{5/2}}\right] \\
&\quad - R_o\dot{\beta}^2\left[\frac{\cos^3\alpha\cos\beta(1+2\sin^2\alpha\sin^2\beta)}{(1-\sin^2\alpha\sin^2\beta)^{5/2}}\right] \\
&\quad + 6R_o\dot{\alpha}\dot{\beta}\left[\frac{\sin\alpha\sin\beta(1-\sin^2\alpha-\sin^2\beta+\sin^2\alpha\sin^2\beta)}{(1-\sin^2\alpha\sin^2\beta)^{5/2}}\right] \qquad (4.35)
\end{aligned}$$

While somewhat unweildy, Equations (4.33), (4.34), and (4.35) are composed of recognizable factors. As grouped, the first line of each equation represents translational components due to the angular acceleration at the two motor shafts. The second and third lines are centripetal terms due to rotational velocity. The fourth line, with cross angular velocity terms are Coriolis accelerations. In the case where α and/or $\beta = 0$,

and cross-coupling between the two actuators is absent according to Equation (4.7), the acceleration expressions for $\ddot{x}_m$, $\ddot{y}_m$, and $\ddot{z}_m$ simplify: all Coriolis terms, one or both of the centripetal terms in Equations (4.33) and (4.34), and one of the angular acceleration terms in each of the three equations vanish.

Similarly, the foward acceleration relations (which are not presented here) may be derived through differentiation of velocity transformations that may be based on either form of the forward Jacobian—*i.e.*, Equation (4.21) or Equation (4.22).

Forces

As with the velocity transformations above, static torques at the actuators can be mapped into an inertial Cartesian frame representation of forces at the handle endpoint, and vice versa, by using the manipulandum Jacobian.

Static forces applied externally to the manipulandum endpoint and the resultant torques measured at the actuator shafts are related by

$$\mathbf{P}_m = \mathbf{J}_m^{-T}\mathbf{F} \tag{4.36}$$

in which

$$\mathbf{F} = \begin{bmatrix} F_x \\ F_y \\ F_z \end{bmatrix} \tag{4.37}$$

is the vector of Cartesian forces at the manipulandum endpoint, and

$$\mathbf{P}_m = \begin{bmatrix} \tau_\alpha \\ \tau_\beta \\ F_r \end{bmatrix} \tag{4.38}$$

is the vector of torques and forces measured with respect to the manipulandum's natural coordinates. τ_α and τ_β are torques along the actuator shafts that rotate through angles α and β respectively. F_r is a translational force resolved along the r handle shaft direction, even though the manipulandum neither moves in the r direction nor has an actuator that produces an F_r force component.

Using the transposed inverse Jacobian of Equation (4.29), $\mathbf{J}_m^{-T}$, the components of Equation (4.36) are

$$\begin{aligned}\tau_\alpha &= -R_o F_x \left[\frac{\sin\alpha \sin\beta \cos^2\beta}{(1-\sin^2\alpha\sin^2\beta)^{3/2}}\right] - R_o F_y \left[\frac{\cos\alpha\cos\beta}{(1-\sin^2\alpha\sin^2\beta)^{3/2}}\right] \\ &\quad - R_o F_z \left[\frac{\sin\alpha\cos^3\beta}{(1-\sin^2\alpha\sin^2\beta)^{3/2}}\right] \end{aligned} \tag{4.39}$$

$$\begin{aligned}\tau_\beta &= R_o F_x \left[\frac{\cos\alpha\cos\beta}{(1-\sin^2\alpha\sin^2\beta)^{3/2}}\right] + R_o F_y \left[\frac{\sin\alpha\cos^2\alpha\sin\beta}{(1-\sin^2\alpha\sin^2\beta)^{3/2}}\right] \\ &\quad - R_o F_z \left[\frac{\cos^3\alpha\sin\beta}{(1-\sin^2\alpha\sin^2\beta)^{3/2}}\right] \end{aligned} \tag{4.40}$$

$$F_r = F_x \frac{\cos\alpha\sin\beta}{\sqrt{1-\sin^2\alpha\sin^2\beta}} - F_y \frac{\sin\alpha\cos\beta}{\sqrt{1-\sin^2\alpha\sin^2\beta}} + F_z \frac{\cos\alpha\cos\beta}{\sqrt{1-\sin^2\alpha\sin^2\beta}} \tag{4.41}$$

Static force and torques applied in manipulandum coordinates correspond to Cartesian endpoint forces according to the inverse of Equation (4.36), *i.e.*,

$$\mathbf{F} = \mathbf{J}_m^T \mathbf{P}_m \tag{4.42}$$

Using the transpose of the Jacobian in Equation (4.22), the terms of Equation (4.42) become

$$F_x = \left[\frac{\cos\beta\sqrt{1-\sin^2\alpha\sin^2\beta}}{R_o\cos\alpha}\right]\tau_\beta + \left[\frac{\cos\alpha\sin\beta}{\sqrt{1-\sin^2\alpha\sin^2\beta}}\right] F_r \tag{4.43}$$

$$F_y = -\left[\frac{\cos\alpha\sqrt{1-\sin^2\alpha\sin^2\beta}}{R_o\cos\beta}\right]\tau_\alpha - \left[\frac{\sin\alpha\cos\beta}{\sqrt{1-\sin^2\alpha\sin^2\beta}}\right] F_r \tag{4.44}$$

$$F_z = -\left[\frac{\sin\alpha\sqrt{1-\sin^2\alpha\sin^2\beta}}{R_o\cos\beta}\right]\tau_\alpha - \left[\frac{\sin\beta\sqrt{1-\sin^2\alpha\sin^2\beta}}{R_o\cos\alpha}\right]\tau_\beta + \left[\frac{\cos\alpha\cos\beta}{\sqrt{1-\sin^2\alpha\sin^2\beta}}\right]F_r \quad (4.45)$$

Since static torques and force developed internally by the manipulandum can only be generated by the two manipulandum actuators, the F_r terms in Equations (4.43), (4.44), and (4.45) are dropped. This leads to the the following relation between static manipulandum actuator torques and the forces detected at the device endpoint in Cartesian coordinates:

$$F_x = \left[\frac{\cos\beta\sqrt{1-\sin^2\alpha\sin^2\beta}}{R_o\cos\alpha}\right]\tau_\beta \quad (4.46)$$

$$F_y = -\left[\frac{\cos\alpha\sqrt{1-\sin^2\alpha\sin^2\beta}}{R_o\cos\beta}\right]\tau_\alpha \quad (4.47)$$

$$F_z = -\left[\frac{\sin\alpha\sqrt{1-\sin^2\alpha\sin^2\beta}}{R_o\cos\beta}\right]\tau_\alpha - \left[\frac{\sin\beta\sqrt{1-\sin^2\alpha\sin^2\beta}}{R_o\cos\alpha}\right]\tau_\beta \quad (4.48)$$

In the special case where τ_β is set to zero in Equations (4.46), (4.47), and (4.48), the magnitude of the resultant force component is

$$\sqrt{F_y^2+F_z^2} = \left[\frac{\sqrt{1-\sin^2\alpha\sin^2\beta}}{R_o\cos\beta}\right]\tau_\alpha \quad (4.49)$$

The equivalent moment arm R_α in Equation (4.49) relating the force magnitude at the manipulandum endpoint to the applied torque τ_α is

$$R_\alpha = \frac{R_o\cos\beta}{\sqrt{1-\sin^2\alpha\sin^2\beta}} \quad (4.50)$$

Similarly, if τ_α is set to zero in Equations (4.46), (4.47), and (4.48),

$$\sqrt{F_x^2 + F_z^2} = \left[\frac{\sqrt{1 - \sin^2\alpha \sin^2\beta}}{R_o \cos\alpha}\right] \tau_\beta \tag{4.51}$$

The equivalent moment arm length, R_β, which relates output force magnitude to τ_β can be expressed as

$$R_\beta = \frac{R_o \cos\alpha}{\sqrt{1 - \sin^2\alpha \sin^2\beta}} \tag{4.52}$$

Note that the length of either of the equivalent moment arms represented in Equations (4.50) and (4.52) is shortened by rotation about the other actuator shaft. This indicates that greater force is available at the manipulandum handle for a given shaft torque when the other shaft is rotated from its zero angle (straight up handle) position.

Referring back to Figure 4.5, it is interesting to note from the static description of Equations (4.46) and (4.47) that x component forces can only be caused by torques from Motor 2 (*i.e.*, τ_β) and that y component forces are due only to Motor 1 (*i.e.*, τ_α). This implies that in the xy plane, the static actions of the two motors are always decoupled. The two torques, however, do combine when the z component is considered.

4.2.4 Mechanical Description of Linkage as Built

The spherical two degree of freedom linkage that couples the human to the manipulandum actuators is shown as built in Figure 4.6. The photograph depicts the manipulandum handle mechanism as well as a number of related sensor and safety subsystems. This section deals expressly with the handle mechanism, including the handle shaft link and the gimbal-like connection between the handle shaft and the motors. The sensor and safety aspects are covered later in this document.

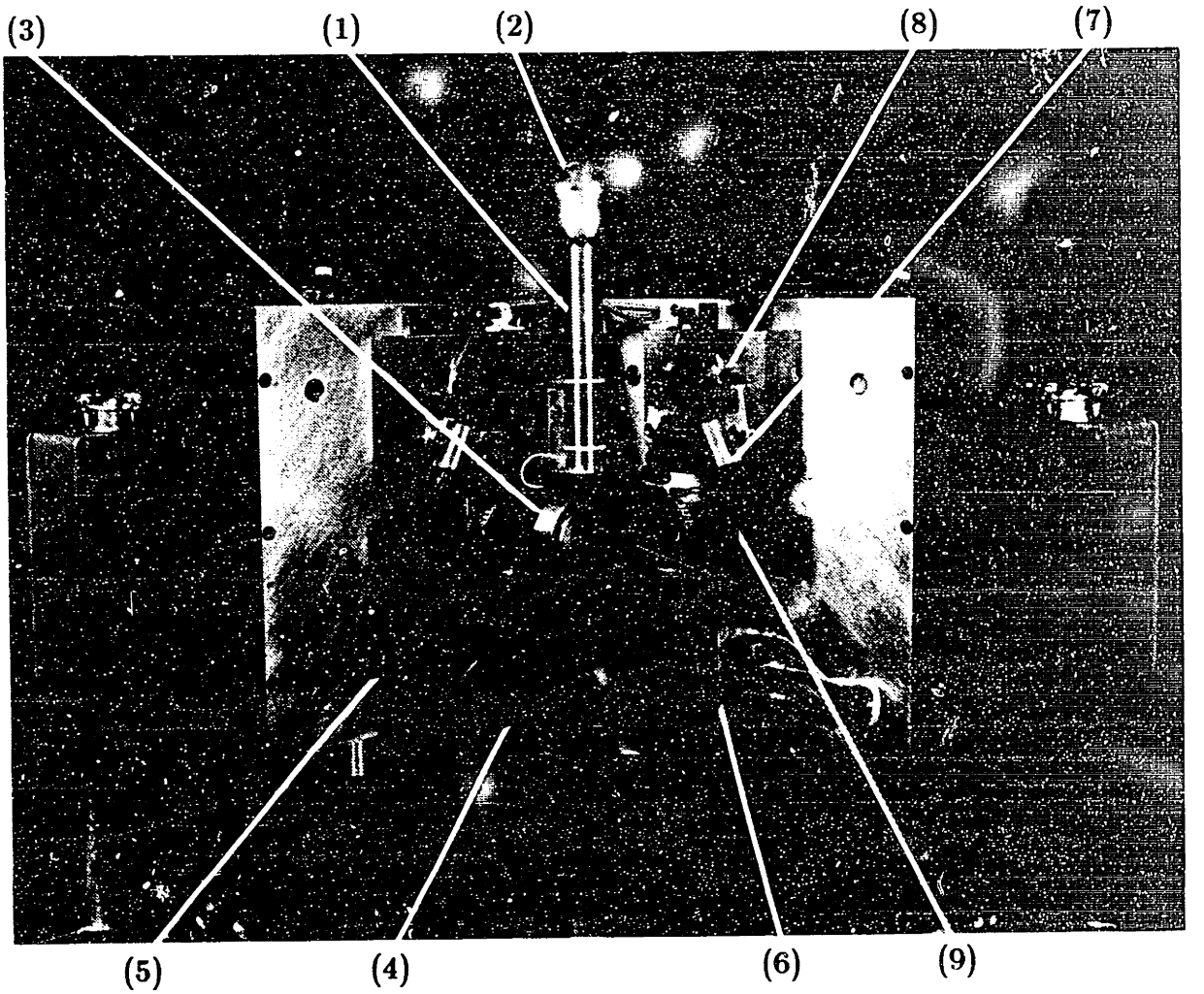

Figure 4.6: Manipulandum handle mechanism as built. Components indicated include: (1) handle link, (2) handgrip, (3) gimbal mechanism, (4) outer bearing support post, (5) motor mount face plate, (6) instrumentation pre-amplifier module, (7) limit stop switches, (8) limit stop blocks, and (9) "winged" collars (keyed to join motor shafts to gimbal mechanism).

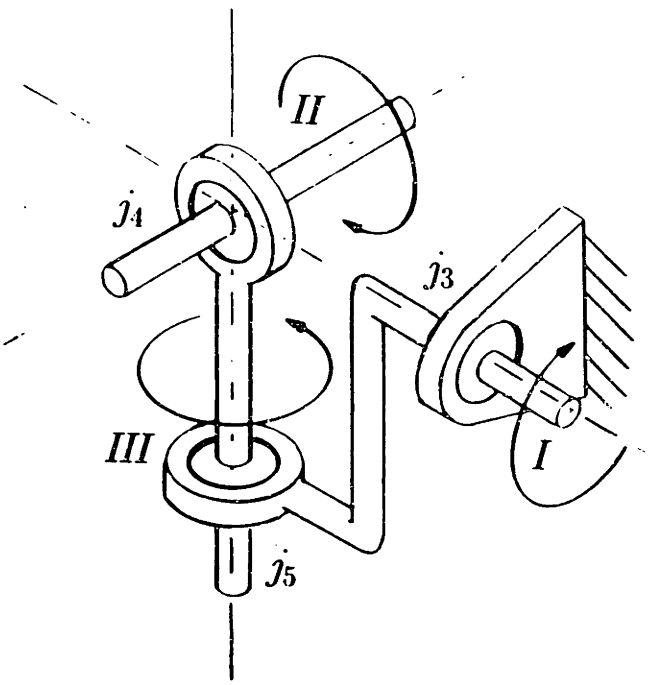

Figure 4.7: Standard 3R open chain gimbal mechanism.

Gimbal

The manipulandum mechanism coupling the handle to actuators makes unconventionaluse of a gimbal as its base. The common type of gimbal (Figure 4.7), found for instance in inertial gyroscopes, is composed of an *open* chain of three successive concentric rotary joints. Each subsequent joint axis in the chain is orthogonal to its predecessor, thus permiting general spherical motion of its final (output) link. This standard gimbal accounts for three joints and four links of the five-link five-joint *closed* chain manipulandum design.

Figure 4.8 provides a closer view of the manipulandum gimbal. The gimbal consists of three sets of nested concentric bearings, each set comprised of a pair of matched angular contact ball bearings mounted back-to-back. Comparing with Figure 4.3, bearing sets *I*, *II*, and *III* correspond respectively to Joints 3, 4, and 5. Joints 1 and 2 represent the bearings of motors shafts #1 and #2. The motor housings are bolted rigidly to the mechanism base at the face plates shown in Figure 4.6.

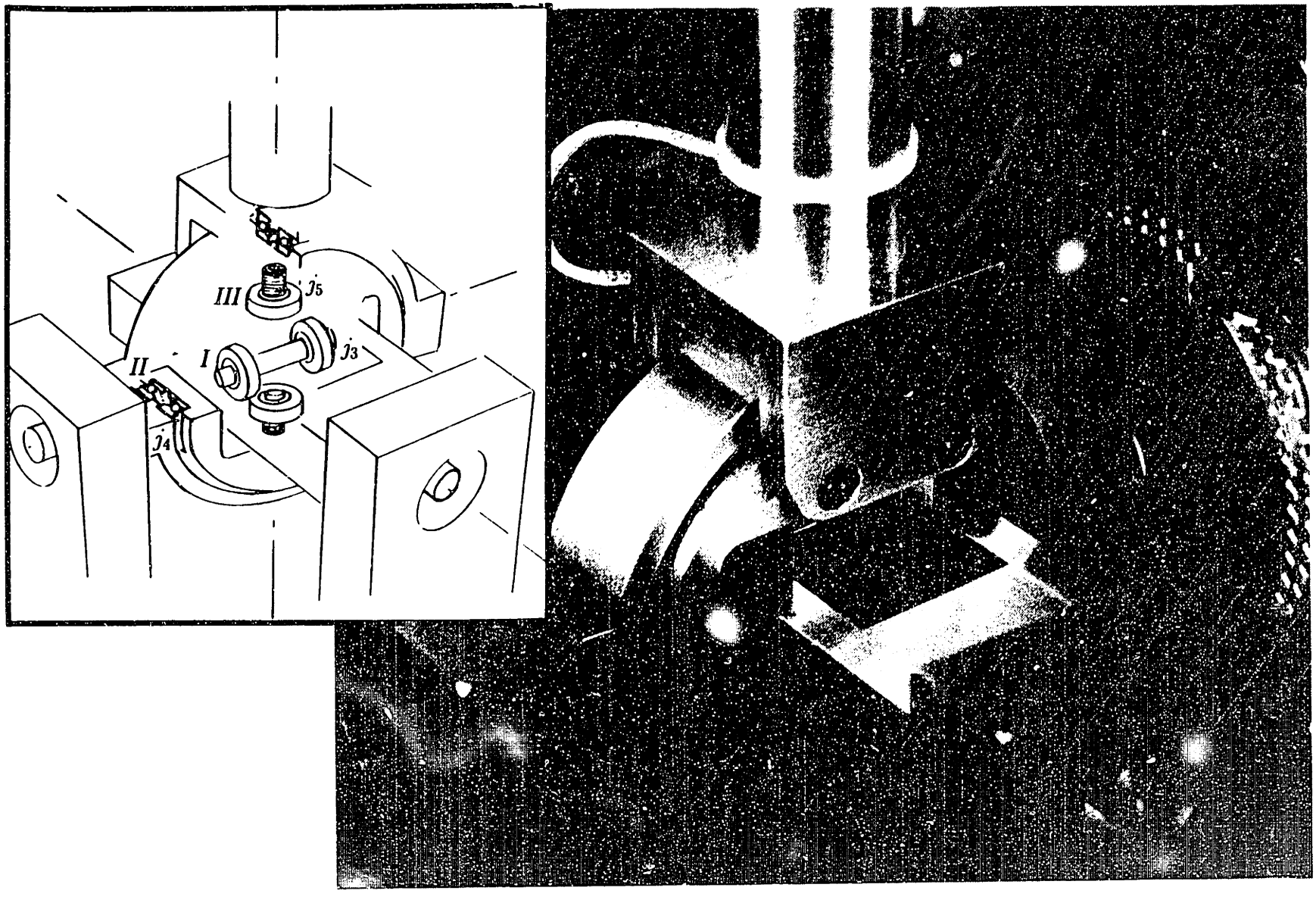

Figure 4.8: Close-up view of manipulandum gimbal. Locations of bearing sets *I*, *II*, and *III* are given in the outline drawing.

Referring to the outline drawing in Figure 4.8, the operation of the gimbal mechanism is described. As seen from the drawing, motor shaft #1 drives the outer race holder of the large bore, slender aspect ratio bearings of set *II* (Kaydon Corp., Muskegon MI; part no. KA025AR4). The inner race housing of bearing set *II*, to which the hand shaft yoke is bolted, fixes the shafts of bearing set *III*.[5] The central block houses the outer races of both bearing sets *III* and *I*. The shaft through bearing set *I* is bonded to an outer block that is in turn driven by motor shaft #2.

All bearing housings—the inner and outer race holders for bearing set *II*, the central block holding bearings *I* and *III*, and the outer block that is attached to motor shaft #2—are machined from aluminum. All shafts out from the gimbal and through the inner races of bearing set *I* are precision ground stainless steel. The shafts into the inner races of each bearing of set *III* were made by turning down two separate socket head set screws to permit assembly of the mechanism. Preloads on all bearings were adjusted by "feel" to minimize low speed friction. Preload on bearing set *III* was adjusted by turning in the screw base of the shafts; on bearing set *II* by repeated fine adjustment of the thickness of a spacer that is part of the outer race housing; and on bearing set *I* through selection of the correct thickness of precision bearing inner race spacers.

The critical factor throughout the design, machining, and assembly of the gimbal components was that the axes of rotation of all three bearing sets intersect at a single stationary point. If the gimbal was to be rigidly attached to the two fixed base motors, failure to satisfy this critical factor within sufficiently tight tolerance could lead to excessive friction in the joints and stresses in the links of the mechanism. Because the gimbal components are elastic (albeit stiff) elements, this could cause the mechanism, which is relatively free to rotate on its ball bearing mounts, to seek out preferred orientations to minimize excessive stresses.

To alleviate this precision alignment requirement, flexible couplings were incorporated between the gimbal and the motor shaft. The helical cut couplings (Helical Products

[5]It is bearing set *III* that enables the non-orthogonality angle, ξ [Equation (4.7)].

Co. Inc., Santa Maria, CA; custom order) permit parallel and angular misalignment without introducing backlash. One of the costs incurred in their use, however, is decreased torsional rigidity along the length of the drive shaft—720 N-m/rad (1 lb-in/0.009 deg) stiffness for the flexible stainless steel coupling versus 6500 N-m/rad (1 lb-in/0.001 deg) for the solid stainless steel section of smaller diameter that it replaces.

The other cost is in vertical stiffness. If the gimbal is cantilevered from the two supporting motor bases as depicted schematically in Figure 4.3,[6] the handle shaft of the mechanism could be subject to up/down motion under human loading of the device during normal use. Furthermore, an accelerometer cable drive, discussed in Section 4.5.3, when properly tensioned, will also apply a significant downward load on each shaft between the flexible couplings and the gimbal, thereby deflecting the gimbal in that direction.

To eliminate the vertical compliance problem, two vertical posts (originally part of a four post "proof of concept" base for the prototype gimbal prior to its attachment to the motors) were included to support the outboard side of the gimbals. These posts, visible in Figure 4.6, support shafts extended from the gimbal at ball bearing pivots in line with the two motor axes and prevent vertical deflection. Because the flexible couplings were already present on each shaft, high precision alignment of the additional bearing was not required.

Handle Shaft

The two motors are coupled to the human hand through a handle link that is attached by a yoke to the inner race of bearing set *II*. (See Figure 4.6.) The handle shaft is constructed of separate hollow aluminum segments that screw together and is topped off by a spherical 0.0635 m (2.5 in) diameter polycarbonate (Lexan^{TM}) handgrip. The handgrip sphere is joined to the top segment of the shaft through a force transducer that is discussed in detail in Section 4.5.4.

The length of the handle shaft, from the center of the spherical grip to the center of

[6]Note that bearing sets 1 and 2 in Figure 4.3 are actually embodied as the bearings between the shafts and housings of motors #1 and 2 respectively

handle link rotation at the intersection of the motor shaft axes, depends on the number of these handle segments incorporated. For the work reported in this document, the handle link length is 0.229 m (9 in). The trade-off for a larger workspace provided by the longer handle, though, is less force available at the human interface, since the given motor torque must be divided by the longer moment arm.

Range of Motion

The handle shaft and gimbal mechanism, as built, permit approximately ± 30 degrees of motion in each of α and β as measured with respect to the handle in the straight up position. Motion of the mechanism is limited by the gimbal impinging on itself, the outboard support posts, and the inboard motor supporting face plates. To prevent damage to any of the gimbal parts from impact at the limits of travel, spring loaded limit stops visible in Figure 4.6 further reduce the range of motion to ± 25 degrees in each axis. Referring back to Table 4.1, this angular range is within the near unity regime for the $|\mathbf{n}_3|$ normalizing factor. According to Table 4.2, the worst case within the range of motion leads to only 10 degrees of non-orthogonality between the motor axes.

The angular range of motion for the handle can be converted into translational measurements by using the Cartesian frame transformations of Equations (4.11), (4.12), and (4.13). With α held at zero, the total available horizontal displacement, x_m, measured at the height of the spherical grip center, is ± 0.097 m (± 3.8 in). As the handle moves over this range from the $\alpha = \beta = 0$ handle position to the limits of travel, the height of the spherical grip, z_m, decreases by 0.020 m (0.8 in). Because of the symmetry of the handle mechanism, y_m covers the same span when β is held to zero and α is free to change. When both axes are free to move to the corners of the workspace, the extreme value for either x_m or y_m is ± 0.088 m (± 3.4 in). The corresponding handgrip center's height decrease when the handle is displaced from the straight up position, *i.e.*, $\alpha = \beta = 0$, to the workspace corners is 0.040 m (1.6 in).

4.2.5 Manipulandum Mechanism Attributes

The spherical manipulandum mechanism described above offers a new configuration for a "semi-direct" coupling—using the "semi-direct drive" definition from Section 3.5—between a two degree of freedom linkage and two rotary actuators. This configuration enables both actuator housings to be tied to the same ground, obviating the need for one of the motors to carry the weight and inertia of the other as would be required in a *true* direct drive device. All motion in the mechanism takes place across ball bearing rotary joints to eliminate mechanical play and ensure low friction.

As with other semi-direct drive manipulator configurations (*e.g.*, Figure 3.4, the transfer of torques and motion between the actuators and the manipulandum endpoint is implemented without belts, gears, or flexible drive shafts.[7] The absence of such transmission elements reduces compliance and friction, and eliminates backlash between the motors and the external environment, making for a backdriveable mechanical system that is composed of structurally stiff rigid links.

The manipulandum mechanism, as built, restricts the handgrip workspace to a small portion of a complete spherical surface. Over this range, changes in x and y handgrip displacement components predominates over the z, giving rise to an approximation of planar motion. For the restricted range of motion in this device, the static torques produced by the two fixed base motors are nearly decoupled. (In fact, if only the horizontal force components are considered, the actuator's static torques are *completely* decoupled.) In addition, because of the restricted range of motion, the singularities of this spherical mechanism occur beyond the limits of the workspace, and thereby do not affect the manipulandum's operation.

Another appealing feature in the manipulandum design lies in the geometry, kinematics, and static force relations between the "natural" actuator shaft angle coordinates of

[7]Although the device as built includes flexible couplings for dealing with small misalignments, these couplings are not flexible drive shafts of the type used to transmit remote torques and motion. While the couplings reduce the torsional rigidity of the drive train somewhat, they do not introduce the friction or compliance of a long sheathed flexible shaft. With higher precision fabrication of the gimbal bearing housing components, the flexible couplings would become unnecessary.

the joystick mechanism and the global Cartesian frame. The forward and inverse transformations throughout Section 4.2.3 all show symmetries between x and y components in pairs of equations that yield relations for α and β quantities. Likewise, symmetries exist between α and β components in pairs of equations that describe x and y quantities. The presence of these symmetries in the transformation relations indicates the similarity of the mechanism with respect to the two manipulandum axes. This similarity facilitates both the development of software algorithms and hardware for manipulandum control, and the analysis of experimental data collected with the device.

4.2.6 Related Work in the Literature

The analysis and synthesis of many varieties of spherical mechanisms have been widely treated in the engineering literature. One reason may be that motions restricted to common surfaces, such as spheres or planes, can be described by simple geometry, without having to resort to the more global (and hence esoteric) mathematical methods that are required for general spatial mechanism kinematics.

The kinematics of 5R spherical closed chain mechanisms with arbitrary link length were analyzed by Tavkhelidze and Davitashvili [141]. Their results provide the general solution of the intermediate joints' angles and time derivatives as functions of the input to the two rotary joints at the opposite ends of the ground link. Subsequently, Davitashvili [47] developed a design method for specifying the link lengths of spherical 5R closed chains for the production of prescribed output angle trajectories as functions the input angles at the base joints. Both papers (references [141] and [47]) are relevant to the manipulandum mechanism derivations in Section 4.2.3, in that they arrive at a general description of the non-orthogonality angle ξ of Equation (4.7) for arbitrary, and not necessarily equal, spherical link lengths. Their work, however, did not formulate the Cartesian description of the manipulandum endpoint (handgrip) kinematics and statics.

The observation that the two degree of freedom joystick mechanism depicted in Figure 4.1 is equivalent to a 5R closed spherical chain with equal 90 degree link lengths (a

"right handed spherical pentagon") was also made by Carmichael [35]. Instead of the reduction of the spherical joint to three revolute pairs and the elimination of the swing arm yokes of the joystick mechanism as presented in Section 4.2.2, Carmichael's realization proceeded by eliminating the spherical pair and then reducing the slotted yokes to equivalent pin (revolute) joints. Again, derivation of the Cartesian statics and kinematics, including velocities and accelerations, of the joystick handgrip were not pursued. While Carmichael recommended that the performance of position sensing joysticks could be improved by replacing the conventional mechanism with an all rotary joint five link design, he did not report the construction of any such device.

At about the same time that the manipulandum mechanism design in this thesis was first published (1984) [121], Chaware and Amarnath [37] proposed a robot wrist that directly copied the slotted swing arm joystick mechanism of Figure 4.1. As in this design, the angle sensing elements in theirs would be replaced by rotary actuators. Chaware and Amarnath, however, did not consider eliminating the friction and backlash inherent in the conventional slotted yoke and ball-and-socket pairs by replacing them with ball bearing mounted revolute joints (as in this design) or by incorporating rolling contact between the slider and the swing arms in other forms such as recirculating balls or ball bearing mounted rollers. Fabrication of actual hardware based on their design has not been reported.

The need for dexterous robot wrists (the distal joints in manipulator linkage chains, *i.e.* the set closest to the end effector) has provided impetus for the design of a number of spherical mechanisms. Because of the way most industrial manipulators are built, the joints closest to the support base correspond to the kinematics of gross positioning of the manipulator end effector. The angular orientation of the end effector, with its position already determined, is typically controlled at the robot wrist. Since the wrist must be carried by the positioning actuators nearer to the robot base, minimizing wrist weight and inertia with respect to the base actuators is a major concern. Wrist inertia is primarily affected by the mass and location of actuators. Hence, solutions to the

wrist problem involve two basic approaches: 1) locating the wrist actuators closer to the robot base and driving the end effector remotely through a mechanical transmission; and 2) designing lighter and more compact motors and wrist mechansisms. As with the the arm loading manipulandum, design issues in the development of effective robot wrists include the distribution of actuator and linkage mass and the compliance, backlash and friction of transmission elements.

Among commercially available spherical robot wrist mechanisms, designs that are based on multiple bevel geared differentials have gained wide acceptance for industrial use. In such devices (see reference [131] for example), concentric hollow torque tubes driven by remote actuators transfer rotary motion from the base of the wrist to a double differential gear set in the wrist, forming closed chain mechanisms with multiple loops. In practice, these "three roll" wrists permit almost any three degree of freedom end effector orientation over the majority of the surface of a sphere. They are also structurally stiff. The friction and backlash in the gear trains of these mechanisms, though, precludes their use in situations that call for backdriveability, a prerequisite for a widely tuneable compliant manipulandum that is meant to interact with a human limb.

A number of other wrist designs have sought to replicate the range of motion of the three roll bevel gear devices without succumbing to the friction and backlash inherent in the geared differential mechanism, while still maintaining a compact package.

One approach to this robot wrist design problem has been to develop other mechanical transmissions between actuators and the end effector. Of special interest here are a number of configurations that embody joystick- or gimbal-like features. These mechanical wrist concepts, each described in the literature since the publication of the manipulandum design presented in this thesis [121], allow three degrees of freedom—pitch, yaw, and *roll*. The wrist mechanisms themselves are based on the equivalent of one [123], two [122, 123, 124], or four [101] Hooke (Cardan) joints that are encompassed by gimbal mounts. Unlike conventional U-joint (constant or nonconstant velocity) applications, where the operating angle between the input and output shaft axes is fixed with respect to

ground by supporting both of the shafts in rigid bearing mounts, these wrist mechanisms allow this angle to controlled, thereby setting wrist pitch and yaw. To change pitch and yaw angle, push-pull rods connect either hydraulic linear actuators or rotary motor driven lead screws to the base gimbal and tilt the proximal Hooke joint. In the multiple Hooke joint devices, the subsequent joints are coupled to the proximal joint by spur gear segments, drive chains, or connecting bars to increase the effective range of pitch and yaw motion. Once the pitch and yaw angles are set by the push-pull rods, these devices behave like standard U-joints, permitting continuous 360 degree end effector roll when a rotary input is provided at the base of the wrist.

These Hooke joint wrists enable as much or greater pitch and yaw motion than the manipulandum's equivalent α and β angles. The inclusion of the roll freedom by an external gimbal ring in the Rosheim devices, described in refernces [122, 123, 124], however, precludes replacement of the translational push-pull rods with fixed base direct or semi-direct drive rotary motors.[8] Similarly, the outer gimbal rings of Milenkovic's wrist design [101] cannot be actuated directly or semi-directly by fixed base rotary motors, making the use of push-pull rods unavoidable. Because these multiple Hooke joint wrists still include gears or chains, it is not clear that they are sufficiently free of backlash, friction and compliance for use in a controlled backdriveable limb loader.

Another approach to eliminating the backlash, friction, and compliance associated with mechanical transmission elements in remotely driven robot wrists has been the design of spherical electromechanical actuators that would be located directly at the wrist. While numerous spherical actuator designs have been proposed, none have yet advanced beyond the experimental stage to commercial availability[83]. One prototype under development is a spherical stepper motor intended for high-speed, accurate three degree of freedom robot end effector orientation (*i.e.*, high stiffness positioning tasks) [88, 89]. This stepper motor is comprised of a hemispherical stator with electromagnetic

[8]It is interesting to note that the pitch and yaw elements, internal to the outer gimbal ring that is needed to accomodate wrist roll in the Rosheim devices, are based either directly on the conventional joystick swing-arm yoke mechanism, or on a gimbal arrangement similar to the one described in Section 4.2.4.

coils at discrete locations, in which resides a spherical rotor with a pair of embedded permanent magnets. The rotor is supported inside the stator by a gimbal arrangement. Details of the gimbal have not been described. The development of a prototype spherical DC servo motor—a type of motor suitable for controlled compliance applications—has been reported as well[83]. In this actuator, the permanent magnet rotor is also suspended within a spherical stator by a gimbal, and as in single axis brushless DC motors, the electrical windings on the spherical stator are commutated electronically.

4.3 Electromechanical Actuator Selection

It has already been indicated above in the description of the spherical closed chain mechanism that a pair of single degree of freedom rotary electrical motors are employed for actuation of the arm loading manipulandum. Selection of the type and size of the motors from commercially available technology was aimed at best satisfying the performance goals set out in Section 3.2. These goals were based on surpassing a combination force, velocity, impedance, and bandwidth description of human arm capabilites. Constraints on available electrical power, size, safety, and details of electromechanical actuator characteristics led to some of these individual quantities being exceeded; others, however, were not fully met. The performance of the completed manipulandum system with respect to these quantities is described later in this chapter and in Chapter 5 as well.

The most straightforward statement of desired actuator performance is that the motors should enable the manipulandum to exceed the forces of even the most severe pathological tremors over a frequency band spanning up to 12 Hz, the maximum frequency of normal human tremor. To arrive at the force produced by a rotary actuator, its torque was simply divided by the moment arm of the manipulandum handle linkage. The tradeoff between the size of the workspace and available force at the manipulandum-human interface (*i.e*, handgrip) was then evaluated. Similarly, angular velocity at the motor shaft as a function of hand velocity at the other end of the handle lever of given length was also considered.

Another factor important to the identification of the particular type of rotary motor that would be suitable for the manipulandum was the range of physical characteristics (objects and fields) that the arm loading interface was intended to simulate. The goal was for the system hardware to permit emulation of physical objects with as wide a range of mechanical impedance as possible. This means that to "convince" the human kinesthetic sense that *all* impedances are possible, the manipulandum stiffness, damping, and inertia should ideally have to span from zero to infinity, at least over the range of human force and kinematic capabilities.[9] Since the manipulandum is intended to interact dynamically with the limb as far as tremor loading is concerned, the impedance of the device must at minimum be settable for operation in the range of human limb impedance. In terms of specifying the actuators for the manipulandum, the highest impedances indicate that available motor torques should be as large as possible. For the lowest impedances, the manipulandum should present minimal inertia and resistance to human hand motion, implying that motor's shaft friction and rotor inertia should be minimal.

The objective of minimizing the computation required to compensate for undesirable manipulandum characteristics, spelled out earlier, also played a substantial role in the specification of the type of motors to be used for simulating loads at the human operator's hand. To simplify control of the actuators, it is desirable for the motors to behave as closely as possible to linear torque sources—free of noticeable nonlinearities such as position dependent torque ripple and cogging. The presence of these position dependent fluctuations in motor torque would be sensed by the human operator/subject as the manipulandum handle is moved, compromising the fidelity of the physical object simulation.

Despite the need for large output torques, torque multiplying transmissions were excluded. Such transmissions would have also multiplied the friction and rotor inertia of the motor as well as add their own undesirable dynamics characteristics. Higher gear ratios would not only decrease the useable speed range of the system, but also increase

[9] At this stage, concerns of causality in the physical interaction between the human and these loads are ignored and the use of the term "impedance" is interchangeable with "admittance."

the friction seen at the transmission output, thereby compromising manipulandum backdriveability.

The characteristics of two direct-drive electromechanical actuator technologies, *brushless* and *printed armature brushed DC* servo motors, were examined. The differences between the two motor types stem from the location of their electrical windings. The windings in brushless motors are in the external stator. Consequently, the windings have better thermal contact with the external environment and can dissipate heat more effectively. Thus, they can sustain higher current without motor damage, resulting in greater continuous torque per-unit of motor weight. Because current is not transferred to the rotating armature, brushes and their inherent friction are avoided. However, since current in the stationary stator windings of brushless motors cannot be commutated mechanically as the motor rotates (as in brushed motors), current in the coil sets must be controlled electronically. An outcome of the electronic commutation is that commanded constant torques in commercially available brushless motor systems typically have from 5 to 10 percent superimposed torque ripple, unacceptable for the manipulandum application. Salisbury *et al.* [127] reported that brushless motor torque ripple can be reduced to approximately one-fifth of its original level with careful motor driver tuning and by programming more refined commutation tables. This level of improvement however was not felt to be sufficient for the arm loading interface in view of the increased computational burden entailed by a high resolution computer-based commutation look-up table.

Printed ("pancake") armature DC motors were selected for the manipulandum principally because of torque smoothness considerations. Unlike the armatures of conventional brushed DC motors which consist of sets of wire windings (*i.e.*, the rotor poles) passed through slots in a laminated soft iron core, the pancake motor armature is made of a thin ironless disk, in which the large number of curved copper commutator bars stamped in a radial pattern are the rotor poles. Instead of the stator permanent magnets being located circumferentially outside the rotor diameter as they are in an iron core brushed motor, the pancake motor's permanent magnets are arranged at a constant radius from

the rotor shaft on either side of the rotor disk. Since the printed armature contains no iron, motor cogging is eliminated, *i.e*, the armature does not exhibit "perferred" angular positions.[10] Torque ripple, occuring in powered motors when current-carrying brushes mechanically switch between adjacent rotor windings, is very small because the large number of conductors on the disk armature provide a smooth commutation path for the brushes.[11] In addition, since the rotor is ironless, it has very low inductance, which in turn nearly eliminates arcing during commutation, prolonging brush life. The absence of iron also reduces rotor inertia.

The particular printed circuit armature motor chosen for each manipulandum axis is Parvex model MC23S (manufactured by CEM-Parvex, Dijon, France; distributed at that time by PMI Motion Technologies, Commack NY and currently available from Alsthom International, Inc., Spring Valley NY). The ratings for the motors, while attached to a 0.53 m × 0.53 m × 0.013 m (21 in × 21 in × 0.5 in) aluminum plate heatsink without forced air cooling, are listed in Table 4.3.

Each motor with its position and velocity sensors, sold as a single pre-assembled unit by PMI, has a maximum diameter of 0.278 m (10.94 in) and an overall length of 0.273 m (10.75 in), excluding the motor output shaft. The weight of each motor/transducer package is approximately 25 kg (55 lb).

The MC23S motor was selected over other PMI/Parvex pancake armature models in the same rated stall torque grouping primarily because it offers the highest torque constant of all their motors—*i.e.* it produces the highest torque for a given input current. Also, the MC23S continuous stall current rating (11 A) is closely matched to, but still slightly exceeds, the continuous output current rating of the highest power PMI servo amplifier that can be run from the standard single phase 115 volt 20 A electrical line. The implication is that in this human-machine interaction application, for which the

[10]Cogging occurs in conventional brushed DC motors, even unpowered ones, because the stator magnets attract the exposed iron laminates of the rotor at "preferred" angular postions

[11]The representatives of Parvex, the manufacturers of the printed disk motors that were chosen for the manipulandum, implied in personal communication that ripple in their motors was below 0.5 percent of mean torque levels, the detection threshold of their factory's measurement equipment.

Continuous Torque	7.0 N-m (5.16 lb-ft)
Peak Torque	49.9 N-m (36.8 lb-ft)
Rated Speed	314.2 rad/s (3000 RPM)
Mechanical Power Out	2.2 kW (2.95 hp)
Rated Current	14.9 A
Peak Current (Demagnetizing)	100 A
Continuous Current @ 1 RPM	11 A
Rated Voltage	172 Vdc
Torque Constant	0.506 N-m/A (0.373 lb-ft/A)
Friction Torque	0.12 N-m (0.088 lb-ft)
Rotor Inertia	0.0023 kg-m^2 (0.0017 lb-ft-s^2)
Mechanical Time Constant	0.008 s
Armature Inductance	0.25 mH
Terminal Resistance	0.9 Ω
Number of Commutator Bars	153

Table 4.3: PMI MC23S motor ratings without forced cooling. (From manufacturer's specifications.)

continuous operating conditions will be at or near stall, the motor will neither incur damage from overheating nor is it oversized for the particular amplifier.

The amplifier system, alluded to in the previous paragraph, consists of a chassis (PMI; part no. CM-2) with two plug-in amplifier cards (PMI; part no. CX-75), one per motor, and a step-down transformer (PMI; part no. T-75-20) for AC line power input. The individual amplifier card closes a high gain current loop around its motor, enabling the combined servo amplifier and low ripple pancake armature motor to be treated as an ideal voltage controlled torque source. In addition, each amplifier card's current output is switched at 6 kHz by on-board pulse width modulation circuitry to increase amplifier power efficiency. Because the mechanical bandwidth of the actuators is much lower than the switching frequency, the pulse width modulation does not affect torque or acceleration smoothness of the motors. This 6 kHz oscillation, however, is audible, both in the motors and from inductive chokes that are included on the servo amplifier chassis to improve current feedback performance. Drawbacks associated with the 6 kHz tone

include the following: it grows in intensity as the motor torque increases, providing the human operator/subject with an audible cue of effort level; it is irritating and potentially damaging to the unprotected listener; and it can introduce disruptive 6 kHz voltage spikes and higher harmonic noise into sensitive electronic signals.

Each single-axis servo amplifier card is capable of delivering 10 A of continuous current at 75 volts with 30 A of peak current available for up to 0.5 seconds before folding back. In this application, however, both continous and peak current are set to 10 A so that nonlinear effects associated with foldback and operation near peak current [56] are not seen. The input command gains on the servo amplifier cards, exterior to the current feedback loop, were modified to operate at lower levels gains (0.3 to 13 A/volt).[12] Each servo amplifier card also includes hook-ups to remotely disable positive, negative or all current into the motors.

4.4 Mechanical/Electromechanical System Layout

The manipulandum handle mechanism, motors, and power amplifier equipment are all mounted on the two level cart depicted in Figure 4.9—the motors and handle mechanism supported on the upper level's solid aluminum base plate, and the servo amplifier chassis and AC power transformer that are carried in the lower level tray.

The components on the upper level are arranged so that the handle gimbal base described in Section 4.2.4 is bolted down to one quadrant of the 0.0254 m (1.000 in) thick machined jig plate. The motors occupy two adjacent quarters, separated from the handle gimbal by two 0.0191 m (0.750 in) thick aluminum plates to which the motor faces are bolted. The location of each motor with respect to its face plate is determined by counterbores that precisely fit the boss on the motor face. These face plates are attached at right angles to each other and then underneath to the jig plate base. Four triangular

[12]The original transconductance gain range set by the manufacturer is 130 times higher, probably due to the intent of having the motors run near their rated speed (3000 RPM) with low gain velocity signals fed back directly from the tachometer into the amplifiers. Peak velocities during normal operation in applications with the manipulandum will be much slower.

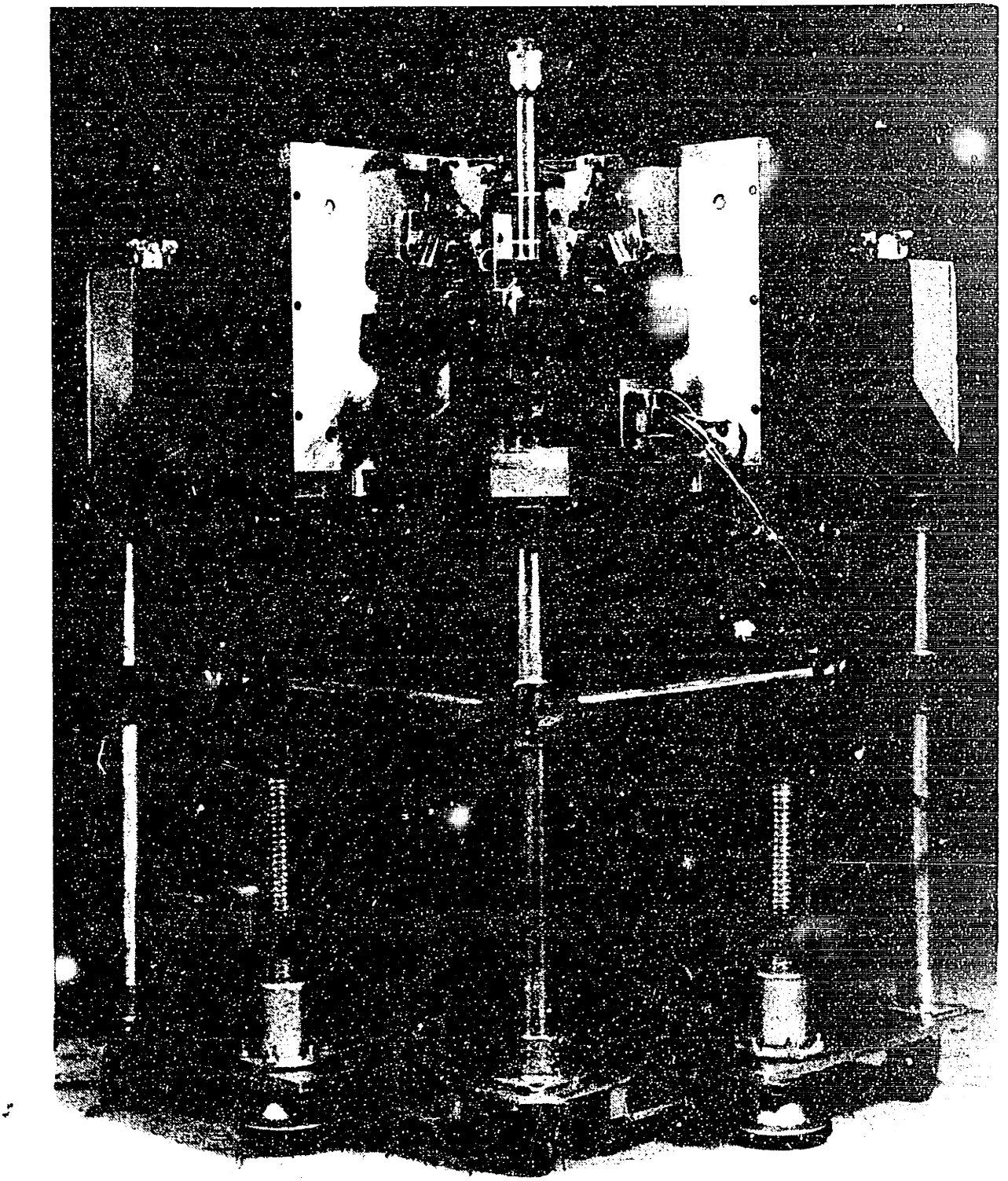

Figure 4.9: Manipulandum cart. (a) Front view showing the handle linkage quadrant on the top level, the pipe frame structure between the upper base plate and the lower level tray. The servo amplifier cards and chassis are under the enclosures in the depressed portion of the tray. The jack screew legs and the wheeled casters are attached to the raised perimeter of the lower level. The enclosures for the AC power latching relay circuitry are along the left and left rear of the lower tray perimeter; for the motor shorting relays, at the left and right rear of the upper level, behind the motor face plates.

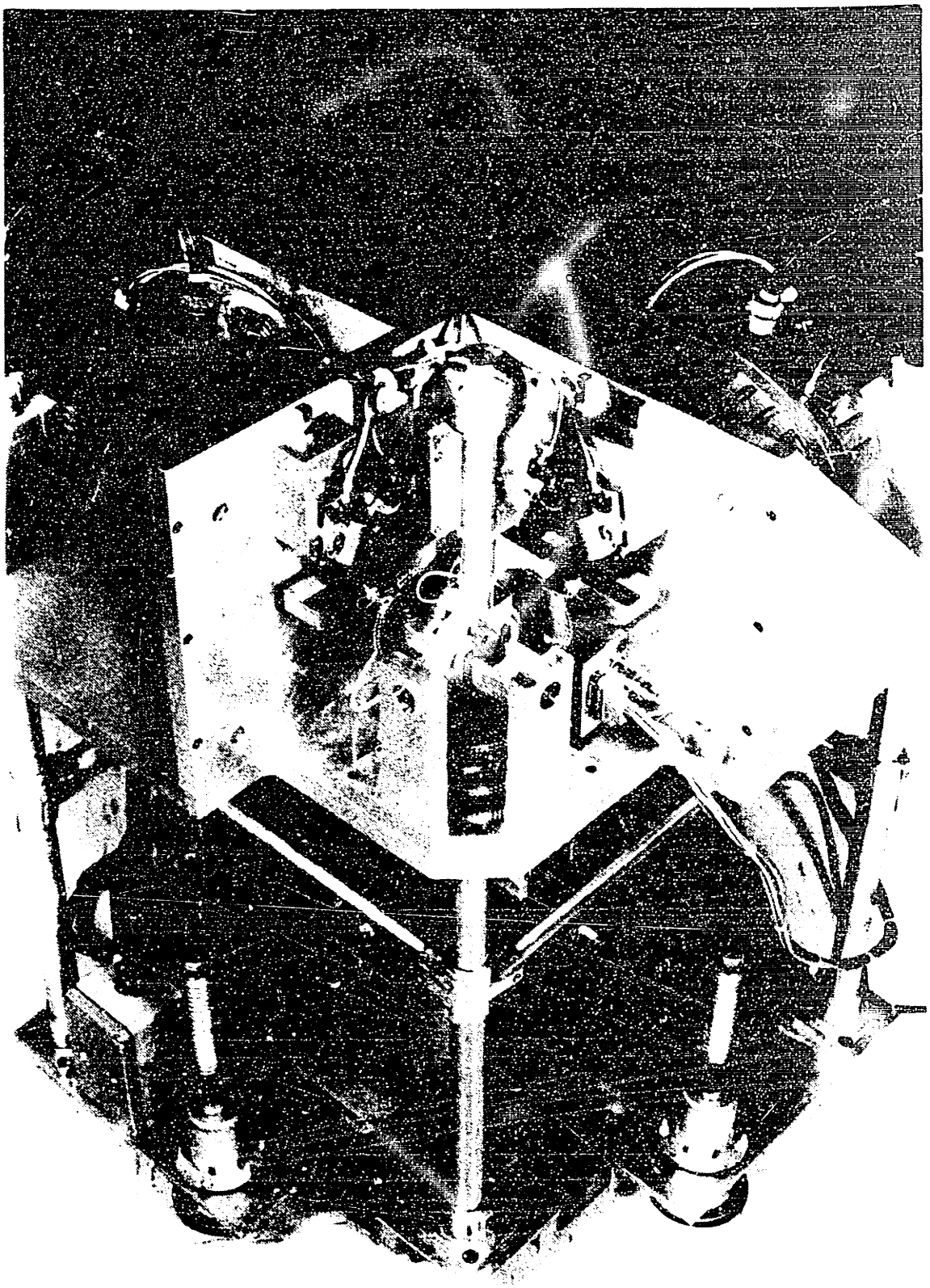

Figure 4.9 (continued): Manipulandum cart. (b) Overhead view showing the four quadrants of the top plate, including the handle linkage, the two motors, and the CIU.

aluminum gusset plates, two for each motor, join the vertical borders of the back (motor side) of each face plate to the top of the jig plate base for additional strength. The inside gussets of both motor mounts define the fourth quadrant on the cart's upper level—separated from the diagonally opposite handle gimbal support and adjacent motor areas. Two standoffs bolted to this quadrant of the jig plate permit the custom built electronic Control Interface Unit (CIU) to be secured to the cart if desired.

The upper level jig plate base has a surface area of 0.66 m × 0.66 m (26 in × 26 in) with a corner cut away in the handle quadrant to allow subjects closer access to joystick. The plate's thickness alone—not including stiffening from the face plates and gussets—theoretically limits its deflection to less than 50 μm (0.002 in) under the assumption that the weight of the motors can be treated as two point loads. The base and face plates also provide more than adequate thermal mass to sink the heat generated by the motors during continuous stall operation.

The underside of the upper level jig plate is bolted to a rigid frame made of 1 inch nominal schedule 40 aluminum pipe (0.033 m [1.380 in] OD, 0.027 m [1.049 in] ID), held together by structural fittings (Hollaender Manufacturing Co., Cincinnati OH; assorted part numbers). This frame is in turn bolted to the perimeter of the cart's lower level tray. The lower tray occupies the same plan area as the upper level jig plate, including the cutout in the handle quadrant. The tray consists of the raised perimeter onto which the pipe frame is bolted that in turn surrounds a slightly lowered middle area that carries the electrical power source components for the actuators—*i.e.*, the servo amplifier chassis and cards, and the step-down transformer. The electromechanical relays which power-up and shut down the system are housed inside sealed fiberglass cases that are mounted on the perimeter of the tray.[13]

Attached to the underside of the lower level tray perimeter are five sets of wheeled casters on which the manipulandum cart can be rolled, either when simply repositioning the equipment between tests or when transporting it to a new experiment location. Once

[13]The role of these relays in the maintenance of system safety is discussed in Section 5.5.

the manipulandum is in place, a set of three individually adjustable jack screw legs that pass through the perimeter of the tray can be lowered to level the manipulandum and prevent it from rolling on the floor. In addition, this tripod can be used to raise the entire manipulandum cart up to 0.125 m (5 in). This enables the handgrip at the end of the handle linkage to span heights from 1.02 m (40 in) to 1.04 m (45 in), a range that matches the shoulder height of most adults seated in either a fixed chair or wheelchair [48]. Note that there is sufficient clearance between the upper jig plate and the top of the jackscrew legs when the legs are fully retracted to permit a shorter pipe frame support to be substituted, making it possible to lower the handle by 0.25 m (10 in) for use with children or in situations that do not call for the adult hand to be at shoulder height.

On the upper level, a smooth Delrin^{TM} cover over the gimbal, shown in Figure 4.10, keeps the subject from being exposed to sharp edges or being pinched between components in the handle quadrant. A square cutout in the top of the cover, sealed by a very compliant leather automobile stickshift boot to the handle shaft directly below the spherical handgrip, permits the full range of joystick motion. In addition, this cover also protects the gimbal mechanism and bearings from external dirt.

For electrical safety reasons, custom made Lexan^{TM} enclosures cover the power aampifier circuitry and the step-down transformer connections. Provision is made for forced air flow and access to selected power amplifier adjustment trimpots. In addition, all exposed metal surfaces of the cart are grounded (to within 0.2 ohms) with respect to the AC main at the wall outlet. Because of the Lexan^{TM} handgrip, and the leather and Delrin^{TM} handle enclosure, the human operator/subject is not exposed to any electrically conductive surfaces during intended use.

The maximum plan area dimension of the manipulandum cart is such that it is small enough to pass through standard width doorways. The weight of the cart including motors, power amplifiers, transformers, and the custom Control Interface Unit (CIU) is on the order of 120 kg (265 lbs).

Figure 4.10: Manipulandum handle quadrant with Delrin cover. Also in place is the handgrip clamp which secures the spherical grip with respect to the cover and the motor face plates.

4.5 Transducers and Electronic Conditioning

As with the selection of the manipulandum mechanism configuration and the system actuators, the objective in choosing kinematics and force transducers is to reduce the computational burden associated with real-time control of the device. In terms of kinematics and force, this means directly sensing appropriate variables in coordinates advantageous for the control of handle impedances; this way computationally intensive geometric transformation of measurements may be avoided. By sensing velocity and acceleration, as well as displacement, computer based differentiation algorithms can also be circumvented.

This section treats the angular displacement, velocity, and acceleration sensors that are used to measure kinematics at the motor shafts, and the force transducer that detects force components at the human-machine interface (*i.e.*, at the handgrip) corresponding to torques about the motor shafts. Electronic conditioning essential to the production of *clean, full dynamic range* signals for both controller implementation and computer data acquisition is also discussed here.[14]

4.5.1 Displacement

Displacements are detected directly in the two manipulandum degrees of freedom,α and β, by incremental optical encoders (PMI; part no. BI25-2048-ABI-5-S) mounted by the vendor to the back of each of the motor/tachometer packages (see Figure 4.9). Each encoder has two 2048 line density tracks phase shifted relative to each other by 90 degrees and a third single pulse per revolution index channel. All three encoder output channels are TTL compatible and require an external 5 volt supply.

A single chip integrated circuit (Hewlett Packard, Palo Alto CA; part no. HCTL-2000) is employed to decode the readings from each encoder. Successive stages of this IC digitally filter the two incoming streams of pulses from an encoder to eliminate noise,

[14]The term clean is used to indicate the goal of low electronic noise, and correspondingly, high signal-to-noise ratio (SNR). Full dynamic range for the measurements, by boosting the transducer signal levels at every stage to the maximum linear range of the control circuitry and computer A/D conversion limits, further supports the goal of high SNR.

quadrature decode the two channels of pulse streams to increase the original angular resolution by a factor of four, and count the number of pulses from a start position, resulting in a 12 bit parallel word that describes relative shaft angle. The quadrature decoding of the encoder signals yields a resolution of 8192 counts per revolution, or 0.044 degrees. Since the manipulandum handle-gimbal mechanism limits shaft rotation to less than half of the 13 bit (8192 count) range of motion, the encoder index channel is not monitored and additional circuitry to enable counting beyond the 12 bit limit of the decoder IC is unnecessary.

So that the encoder-sensed position signals can be utilized by the manipulandum controller and stored by the computer through its A/D converter,[15] each HCTL-2000 decoder output stream converted into an analog signal by a 12 bit DAC. The decoder and D/A converter circuitry for both shaft angle encoders, as well as their 2 MHz clock source all reside on a card in the Control Interface Unit (CIU).[16] Because the encoder angle counter determines shaft angle relative to a start position, the analog output of the decoder circuitry is always zeroed when the CIU is powered up. The counters on either axis can also be re-zeroed independently by push button switches on the CIU's front panel.[17]

Correct operation of the encoder through the analog output stage of the decoder circuitry on both axes was verified by allowing the motors to run free with the manipulandum handle mechanism removed. The result of passing the quadrature multiplied 13 bit per revolution count through the HCTL-2000's 12 bit counter is a twice per revolution sawtooth analog waveform. After many consecutive motor revolutions, the occurrences of counter output sawtooth peaks still coincided with the alignment of visually discernable markers on the rotating motor shaft and the fixed face plate, indicating that the decoder circuitry had maintained its calibration.

[15]The A/D converter is used because of an insufficient number of available digital input ports.

[16]More detail on the contents and functions of the CIU is provided in the next chapter and in Appendix B.

[17]A special clamping fixture, employed to lock up the manipulandum handgrip when the apparatus is not in use, also serves as a jig to position the handle in the straight up (*i.e.* $\alpha = \beta = 0$) position when the encoder counters are re-zeroed.

4.5.2 Velocity

The angular shaft velocity of each actuator is measured by a tachometer (Parvex/PMI; part no. FC12T) that is integrally mounted at the back of each motor by the manufacturer. The maufacturer's specifications for tachometer output indicate a speed sensitivity of 0.0573 volt/rad/sec (6 volt/1000 RPM) ±5 percent. Ripple due to commutation with the 141 bars on the tachometer's disk armature, at speeds between 125 and 4000 RPM, is rated at 3 percent peak-to-peak with respect to the mean voltage level.

The raw output generated by each tachometer is transferred by shielded cable to the CIU and amplified by a factor of 10 using differential input, high common mode rejection ratio, intrumentation amplifiers. These two steps result in velocity signals that are free of contamination from the 6 kHz switching of the servo amplifiers.

The speed sensitivity of the tachometers was checked by counting the frequency of the twice per revolution cycling of the decoded analog outputs of the encoders during constant velocity operation. The actual velocity sensitivities of 0.0583 volt/rad/sec on tachometer #1 (α axis) and 0.0575 volt/rad/sec on tachometer #2 (β axis), determined from linear regressions of angular velocity measured from position reset cycle frequency versus tachometer voltage over the intended range of manipulandum operating speeds, were both within the manufacturer's tolerance. Voltage ripple measured during constant velocity tests at low speeds decreased from 6 percent at 5 RPM to 0.4 percent at 90 RPM—the ripple at the higher speed being significantly better than manufacturer's specification at 125 RPM.

4.5.3 Acceleration

Accelerations are sensed in manipulandum coordinates by single-axis translational accelerometers that are driven off the motor shafts at the output end, *i.e.*, in the handle mechanism quadrant. The individual accelerometers (Entran Devices, Inc., Fairfield NJ; part no. EGA-125SR-5D) are miniature piezoresistive devices that measure acceleration by monitoring the strain in a cantilever that supports a "proof mass." Unlike piezoelectric

sensors that require dynamic excitation above some minimum frequency (typically 2 Hz or higher) to produce an output signal, these accelerometers are capable of measuring accelerations with frequency content down to DC without signal attenuation, a necessity if human manual activity is to be measured and used by the manipulandum controller. The accelerometers have a 5 g range, of which only approximately 2 g is required for human applications in the drive configuration described below. These devices are internally damped to prevent damage to the sensor elements from shock load excitation of mass-beam resonance. The "useable" frequency band of the accelerometers is specified as being from DC up to 20 percent of the mass-beam resonant frequency, which for this particular model occurs at about 300 Hz.

To measure angular acceleration, a translational accelerometer must be aligned with its sensitive axis tangential to the rotary motion. However, since the shafts of the manipulandum motors lie in a horizontal plane, the output of an accelerometer that is mounted with its sensitive axis tangential to the motor shaft rotation will also be affected by the pull of gravity on its internal proof mass. Furthermore, the effects of gravity on the output signal will vary with motor shaft angle.

To remove this undesirable gravity component from the sensor signal, the cable and pulley drive arrangenment illustrated in Figure 4.11 was devised. In this drive system, a length of cable is routed from a pulley which is fixed to the motor shaft (1), down and around an idler (2), to a pulley (either 3a or 3b) that rotates in the horizontal plane about a vertical axis, back around a second idler (4), and then back up to the motor shaft pulley (1). The two ends of the cable length in each drive are fixed to the motor shaft pulley with set screws. By pulling on the cable segment prior to tightening the second set screw, the drive is pre-tensioned, preventing slippage between the cable and the driven accelerometer pulley. Motor #1 (the α axis) drives the upper pulley (3a) on the vertical shaft; motor #2 (the β axis) drives the lower pulley (3b). Thus, the accelerometers detect rotary motor acceleration, but in a horizontal plane, free from spurious gravity contributions.

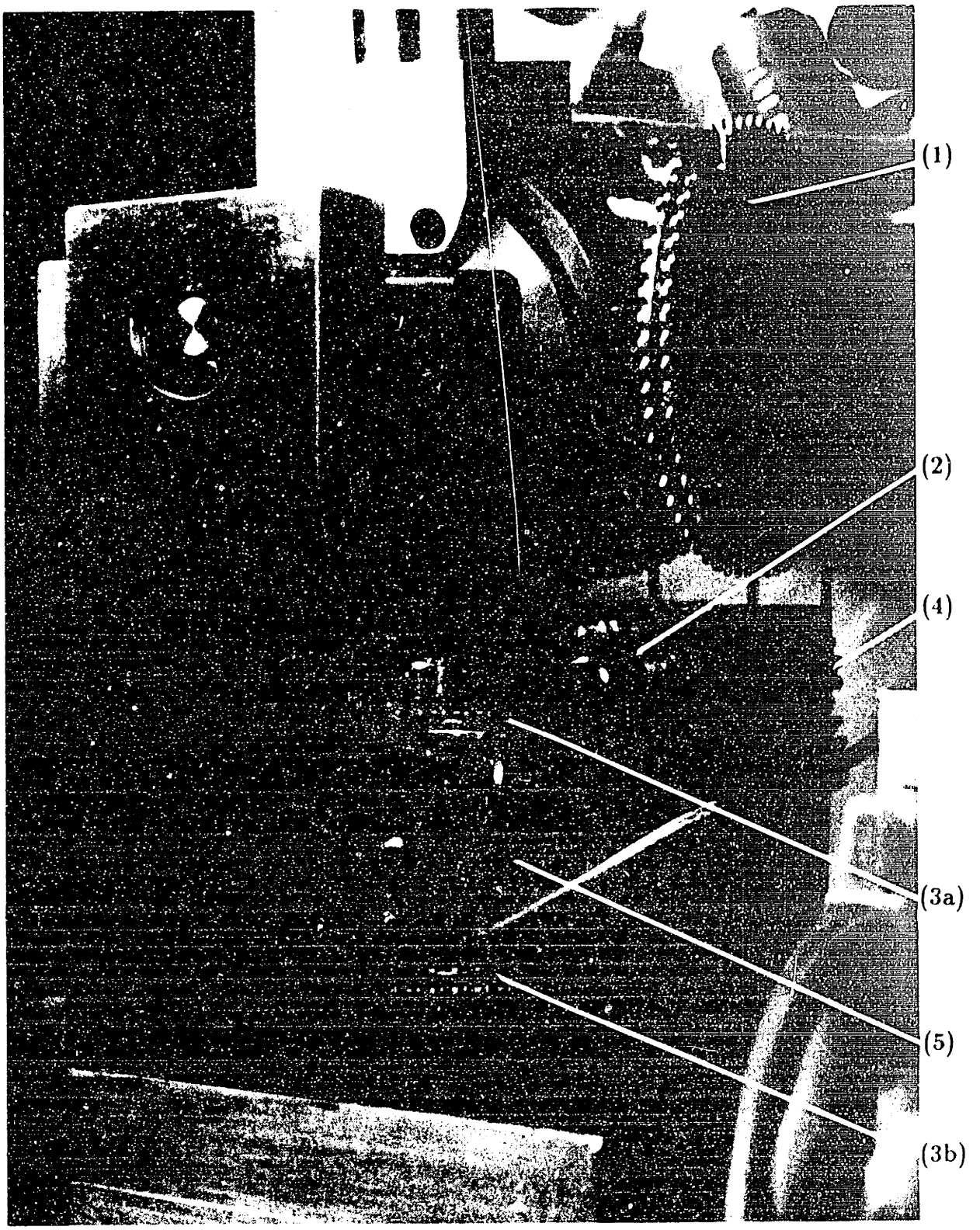

Figure 4.11: Accelerometer cable drive mechanism for axis #1. The flexible wire-rope cable is routed from (1) the motor shaft pulley, around (2) an idler, to (3a) the accelerometer pulley, back around (4) a second idler, to return back to (1) the motor pulley. Also visible are the accelerometer (5) for axis #2 and its pulley (3b).

The theoretical bandwidth of the cable drive transmision is derived from a simple model that includes the inertia of the driven accelerometer pulley and the stiffness of the wire rope cable that transmits motion. Since the combined motor armature and manipulandum inertia exceeds the driven accelerometer and its pulley's estimated inertia of 4.5×10^{-5} kg-m^2 (3.3×10^{-5} lb-ft-s^2) by nearly three orders of magnitude, the driver pulley on the motor shaft is treated as mechanical ground. With the wire rope (Sava Industries, Inc., Riverdale NJ; part no. 2047-SN) stiffness of 42.2×10^3 N/m per meter of cable (9500 lb/in per inch of cable), a second order model predicts a natural frequency, and hence bandwidth, of 475 to 800 Hz, depending on assumptions as to the position and effect of the drive train idlers. Because these frequencies are sufficiently above the useable accelerometer range, the effects of cable drive dynamics on acceleration measurements are neglected.

The DC sensitivity of each accelerometer at ±1 g acceleration of its proof mass was tested by rotating the device's sensitive axes in a vertical plane through a full 360 degrees. The observed α and β accelerometer sensitivities were 16.1 mv/g and 18.5 mv/g respectively. This method of finding the maximum output due to gravity was also employed to align the sensitive axis of the accelerometers tangent to the circumference of its supporting pulley disk.

Since the transducer output levels are so low (*i.e.*, millivolts), measures were taken to prevent signal degradation by noise, especially from the 6 kHz switching of the amplifier and motor currents. The accelerometers and their electrical leads are all shielded. The signals from the transducers' strain gauges are differentially amplified 100 times by instrumentation amplifiers in a pre-conditioning module in the handle quadrant on the upper level of the manipulandum cart. Locating the pre-amplifiers near the transducers minimizes the length of wire conducting low level signals, thereby further reducing noise exposure. Once the acceleration signals have been pre-amplified from millivolt to full volt levels, they are then carried over longer distance to the CIU without noise contamination.

Additional accelerometer signal conditioning was introduced because the transducers

failed to meet the manufacturer's specifications for initial offset and thermal bias drift after warm-up. Closer investigation revealed that the resistors in the manufacturer's thermal compensation unit did not match the values prescribed by their own calculations. Furthermore, neither accelerometer strain gauge bridge was well balanced; the four active elements in each bridge differed by as much as 5 percent in the α axis sensor and 15 percent in the β axis one. To correct these deficits, the thermal compensation circuitry for each device was rebuilt with precision resistors that matched the manufacturer's originally prescribed values and a trimmable potentiometer was added to balance each strain gauge bridge. These adjustments, installed in the pre-conditioning module, though somewhat effective, were still insufficient for dealing with sensor offset drift over long periods of time. The step that finally proved to be satisfactory for treating this problem was to high pass filter (first-order, 0.007 Hz break point) the pre-amplified acceleration signals at their input to the CIU. At tremor frequencies, where human manual output contains significant acceleration components, the phase shift and gain attenuation induced by the high pass filter are insignificant.

One other accelerometer characteristic, although within the manufacturer's specified tolerance, proved to be undesirable. While the transducers have a 0.7 damping factor at room temparature, the internal accelerometer fluid becomes less viscous during standard operation due to the heat generated by current flow through the resistive strain gauge elements. This reduced damping factor—0.4 of critical damping as specified by the manufacturer for the warmed-up device—does not affect the flatness of the frequency response in the "useable" operating range below 20 percent of the resonant frequency. It does, however, drastically increase the resonance that occurs in response to step or impulse loads.

4.5.4 Force/Torque

Force at the human-manipulandum interface is measured by a transducer embedded in the top end of the handle linkage shaft, underneath the spherical handgrip. The actual

transducer is a commercial miniature two-axis force joystick, modified to sense only the force components which lie in the plane that is tangent to the instantaneous location of the handgrip on the manipulandum's spherical surface workspace. As will be shown below, these force components can be related mathematically to the α and β torque components about the manipulandum motor shafts.

Miniature Force Joystick Selection

The choice of an "off the shelf" force transducer for the manipulandum was based on the desire to have a robust, self-contained, well characterized force sensor, without having to develop one "in-house." Instrumenting the manipulandum to sense force would require precise alignment of strain gauges for bonding, either at specific locations on the manipulandum itself, or in a custom designed transducer to be attached later. In addition to characterizing the performance of a custom made transducer (or of gauges bonded directly to the manipulandum), the design might have to include additional peripheral electronics for signal conditioning, and packaging to protect the sensor elements from damage.

At the time force/torque instrumentation was being considered for the manipulandum, commercially available robot wrist sensors with full six degree of freedom force *and* torque sensing were judged to be too bulky and massive for inclusion in or on the handle shaft. In addition, the transmission of full six degree of freedom force information from the strain gauge bridges in these devices to the exterior was bandwidth limited by hardwired digital serial communication.

The selection of the miniature two axis force joystick for the manipulandum sensor was made primarily because of its size, direct analog force signal output from each axis, sturdy package and lower cost (relative to multi axis force sensors).

The joystick unit itself (Measurement Systems Inc., Norwalk CT; part no. 469/20lb) is compact—0.045 m (1.75 in) maximum length by 0.024 m (0.936 in) maximum diameter with a mass of 0.025 kg (0.9 oz), not including external wiring. The force joystick's

operation is based on measurement of ben ding strains in a center beam which protrudes through an opening in its top cover. The beam is instrumented with four piezoresistive gauges bonded at ninety degree intervals around its circumference, with each pair of opposing elements joined in a half-bridge. The size the opening in the top cover imposes a mechanical limit on beam deflection. This maximum deflection corresponds to the bending caused by applying a 90 N (20 lb) perpendicular force to a specific calibration point on the beam, 6.3 mm (0.25 in) above the top surface of the transducer cover. For forces applied at this calibration point, the joystick sensitivity is rated at 15.7 mv/N (70 mv/lb) ±20 percent on either axis at the maximum allowable ±6 volt excitation across each half bridge.

The miniature joystick's cylindrical housing is seated inside a snuggly toleranced bore in the top end of the manipulandum handle shaft. It is prevented from being pulled up, out of its seat, by the snuggness of the bore walls, and from being rotated in the bore by nylon tip set screws around its circumference. The transducer is aligned with its own "marked" axis—determined by an engraved notch in its top cover—pointing away from motor #1 when the manipulandum handle is straight up, *i.e.*, when $\alpha = \beta = 0$.

Force Transducer Coordinate Transformations

An *orthogonal* transducer coordinate frame (t_1, t_2, t_3), with its origin at the calibration point on the miniature force joystick beam and orientation fixed with respect to the transducer body, is constructed as shown in Figure 4.12. Axis t_2 always points in the direction of the notch in the transducer cap, axis t_1 lies in the plane tangent to the work space surface and denotes the other sensitive axis of the transducer, and t_3 always points straight up from the transducer cover along the length of the undeformed beam element. Having now defined the right-handed orthogonal system of the three principle force transducer axes, the mapping from the (t_1, t_2, t_3) frame into the Cartesian (x, y, z) frame, first described in Figure 4.5, can now be derived.

As depicted in Figure 4.8, the handle shaft yoke is bolted directly to the inner race of

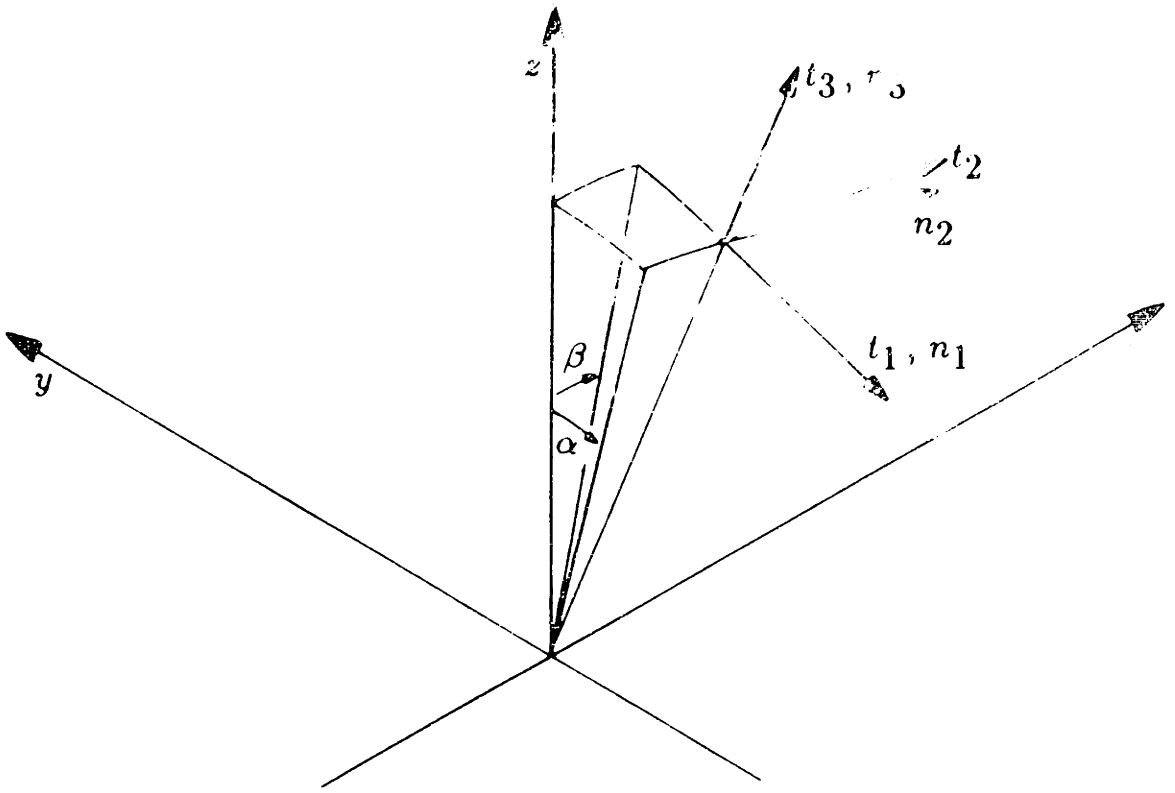

Figure 4.12: Force transducer coordinate system. See text for further details.

gimbal bearing set *II*. In turn, the outer race of bearing set *II*, in turn, is driven directly by the shaft of motor #1. Also, from Section 4.2.3, it is noted that plane P_1 rotates with motor shaft #1. Thus, transducer axes t_2 and t_3 must lie in plane P_1.

According to Figure 4.12, t_1 must always be perpendicular to this plane and, therefore, is parallel to $\mathbf{n}_1$, the normal to surface P_1. From Equation (4.1) then, since $\mathbf{n}_1$ has magnitude one, the unit vector in the t_1 direction is

$$\mathbf{e}_{t_1} = -\cos\alpha\,\mathbf{j} - \sin\alpha\,\mathbf{k} \tag{4.53}$$

Since axis t_3 points along the undeformed transducer beam element, it is always colinear with the $\mathbf{e}_3$ unit vector that indicates the manipulandum handle shaft orientation. Referring to Equation (4.5) then

$$\mathbf{e}_{t_3} = \frac{\cos\alpha\sin\beta}{\sqrt{1-\sin^2\alpha\sin^2\beta}}\,\mathbf{i} - \frac{\sin\alpha\cos\beta}{\sqrt{1-\sin^2\alpha\sin^2\beta}}\,\mathbf{j} + \frac{\cos\alpha\cos\beta}{\sqrt{1-\sin^2\alpha\sin^2\beta}}\,\mathbf{k} \tag{4.54}$$

Since the remaining transducer axis, t_2, is always perpendicular to the other two axes, its unit vector can be found from

$$\mathbf{e}_{t_2} = \mathbf{e}_{t_3} \times \mathbf{e}_{t_1} \tag{4.55}$$

Working out the cross product,

$$\mathbf{e}_{t_2} = \frac{\cos\beta}{\sqrt{1-\sin^2\alpha\sin^2\beta}}\,\mathbf{i} + \frac{\sin\alpha\cos\alpha\sin\beta}{\sqrt{1-\sin^2\alpha\sin^2\beta}}\,\mathbf{j} - \frac{\cos^2\alpha\sin\beta}{\sqrt{1-\sin^2\alpha\sin^2\beta}}\,\mathbf{k} \tag{4.56}$$

The orthonormal rotation matrix $\mathbf{R}$, relating the orientation of forces in transducer coordinates to coordinates in the fixed Cartesian base, can now be constructed from

$$\mathbf{R} = \begin{bmatrix} \mathbf{e}_{t_1} \\ \mathbf{e}_{t_2} \\ \mathbf{e}_{t_3} \end{bmatrix} \tag{4.57}$$

Substituting from Equations (4.53), (4.56), and (4.54),

$$\mathbf{R} = \begin{bmatrix} 0 & -\cos\alpha & -\sin\alpha \\ \frac{\cos\beta}{\sqrt{1-\sin^2\alpha\sin^2\beta}} & \frac{\sin\alpha\cos\alpha\sin\beta}{\sqrt{1-\sin^2\alpha\sin^2\beta}} & -\frac{\cos^2\alpha\sin\beta}{\sqrt{1-\sin^2\alpha\sin^2\beta}} \\ \frac{\cos\alpha\sin\beta}{\sqrt{1-\sin^2\alpha\sin^2\beta}} & -\frac{\sin\alpha\cos\beta}{\sqrt{1-\sin^2\alpha\sin^2\beta}} & \frac{\cos\alpha\cos\beta}{\sqrt{1-\sin^2\alpha\sin^2\beta}} \end{bmatrix} \tag{4.58}$$

Using the rotation matrix, forces in the transducer coordinate frame, $\mathbf{F}_t$, can be resolved into the inertial Cartesian frame according to

$$\mathbf{F}_t = \mathbf{R}\,\mathbf{F} \tag{4.59}$$

in which

$$\mathbf{F}_t = \begin{bmatrix} F_{t_1} \\ F_{t_2} \\ F_{t_3} \end{bmatrix}$$

and $\mathbf{F}$ is as defined in Equation (4.37).

Explicitly, the components of Equation (4.59)

$$F_{t_1} = -F_y\cos\alpha - F_x\sin\alpha \tag{4.60}$$

$$F_{t_2} = F_x\frac{\cos\beta}{\sqrt{1-\sin^2\alpha\sin^2\beta}} + F_y\frac{\sin\alpha\cos\alpha\sin\beta}{\sqrt{1-\sin^2\alpha\sin^2\beta}} - F_z\frac{\cos^2\alpha\sin\beta}{\sqrt{1-\sin^2\alpha\sin^2\beta}} \tag{4.61}$$

$$F_{t_3} = F_x\frac{\cos\alpha\sin\beta}{\sqrt{1-\sin^2\alpha\sin^2\beta}} - F_y\frac{\sin\alpha\cos\beta}{\sqrt{1-\sin^2\alpha\sin^2\beta}} + F_z\frac{\cos\alpha\cos\beta}{\sqrt{1-\sin^2\alpha\sin^2\beta}} \tag{4.52}$$

It is important to remember that the force transducer is not instrumented to sense F_{t_3} component force—*i.e.*, along the orientation of the manipulandum handle shaft. This results in having two measurements that must be resolved into three components, and the conclusion that the pair of Equations (4.60) and (4.61) alone cannot lead to a unique

solution of the interface force components F_x, F_y, and F_z. However, in the case where the subject is restricted from applying forces in the F_z direction, resolution of the components is possible.

The correspondence between force components measured at the transducer, F_{t_1} and F_{t_2}, and actuator shaft torques, τ_α and τ_β, can also be stated. When $\tau_\beta = 0$, Equations (4.46), (4.47), and (4.48) yield relations for F_x, F_y, and F_z, which upon substitution into Equations (4.60) and (4.61) become

$$F_{t_1} = \left[\frac{\sqrt{1 - \sin^2\alpha \sin^2\beta}}{R_o \cos\beta}\right] \tau_\alpha \tag{4.63}$$

$$F_{t_2} = 0 \tag{4.64}$$

The term in brackets multiplying τ_α is recognized as the reciprocal of the equivalent moment arm R_α associated with torques about the α axis from Equation (4.50). Thus,

$$F_{t_1} = \left[\frac{1}{R_\alpha}\right] \tau_\alpha \tag{4.65}$$

$$F_{t_2} = 0 \tag{4.66}$$

These two equations confirms that τ_α only gives rise to a transducer signal in the t_1 component—which is expected, since, as noted above, this transducer axis is always perpendicular to plane P_1 that rotates with α axis actuator, motor #1.

When τ_α is set to zero, the substitution for F_x, F_y, and F_z from Equations (4.46), (4.47), and (4.48) into Equations (4.60) and (4.61) yields the following relations between transducer readings and the torque about motor shaft #2:

$$F_{t_1} = \left[\frac{\sin\alpha \sin\beta \sqrt{1 - \sin^2\alpha \sin^2\beta}}{R_o \cos\alpha}\right] \tau_\beta \tag{4.67}$$

$$F_{t_2} = \left[\frac{1 - \sin^2\alpha \sin^2\beta}{R_o \cos\alpha}\right] \tau_\beta \tag{4.68}$$

Accounting for the reciprocal of the equivalent moment arm term, R_β, from Equation (4.52), Equations (4.67) and (4.68) reduce to

$$F_{t_1} = \left[\frac{\sin\alpha \sin\beta}{R_\beta}\right] \tau_\beta \tag{4.69}$$

$$F_{t_2} = \left[\frac{\sqrt{1 - \sin^2\alpha \sin^2\beta}}{R_\beta}\right] \tau_\beta \tag{4.70}$$

Equations (4.69) and (4.70) indicate that torque τ_β, will result in output signals from both transducer channels. Unlike the shaft of motor #1 which directly drives the handle shaft and the affixed force transducer coordinate frame through angle α, motor #2's transmission to the handleshaft is only "semi-direct." [18] The consequence is the rolling of transducer axes t_1 and t_2 about the t_3 axis with respect to P_2 in Figure 4.5, i.e. the imaginary plane that is fixed to the shaft of motor #2. This rolling detracts from the symmetry between Equations (4.65) and (4.66) and Equations (4.69) and (4.70) with regard to the respective shaft torques and equivalent moment arms, causing F_{t_2} to be dimished by the square root term and F_{t_1} to be nonzero in response to torque τ_β. Recalling the non-orthogonality condition described by Equation (4.7), the factors altering Equations (4.69) and (4.70) respectively are recognized to be the cosine and sine of ξ, the deviation of the angle between planes P_1 and P_2 from 90 degrees. However, over most of the manipulandum workspace, this non-orthogonality is small, permitting the relation between actuator shaft torques and force transducer readings to be approximated as being similar for both axes.

[18] Referring to Figure 4.8, the handle shaft yoke is coupled to motor #2 through bearing sets *I* and *III*.

Moment Cancellation Mechanism

If the center of the spherical handgrip were joined directly to the calibration point on the beam element of the miniature force joystick, complications would arise due to the susceptibility of the transducer beam to bending strains from factors other than forces in the t_1 and t_2 directions. Not only will the instrumented beam bend from perpendicularly applied pure forces, it will also as a result of pure moment loading. The problem is that the transducer gauges are incapable of distinguishing between forces and moments.

To counteract the force joystick's moment sensitivity, the moment cancellation mechanism, or "decoupler," illustrated in Figure 4.13 was developed to attach the spherical handgrip to the manipulandum shaft. The mechanism is based on a combined spherical and thrust bearing arrangement. The ball of the spherical bearing is pressed over an adapter sleeve which is fitted onto the force transducer's beam element such that the center of the ball coincides with the beam element's calibration point. The spherical bearing race is then joined through a collar to a flat thrust washer which is held between the ball complements of two retainers, that are held in turn between two flat thrust washers. The handgrip slips over the top end of the spherical bearing race collar and is kept in place by circumferential set screws. Vertical preload on the stacked thrust bearings is maintained by the top cover of the decoupler housing.

The moment cancellation mechanism works because the spherical bearing prevents bending moments about the t_1 and t_2 axes and twist of the handgrip about the t_3 axis from being transmitted to the transducer beam. Moments about the t_1 and t_2 axes, though, are opposed by reaction forces in the thrust bearing stack, thus allowing them to be absobed by the mechanism housing.

The effectiveness of the moment cancellation mechanism was demonstrated in tests during which moments were applied to the transducer by means of weights that were suspended from a horizontal arm secured perpendicularly to the t_3 axis. Prior to the installation of the "decoupler," a *moment* developed by applying a particular force (*i.e.*, by hanging a weight) at a 0.0254 m (1.0 in) radius, produced transducer voltages that

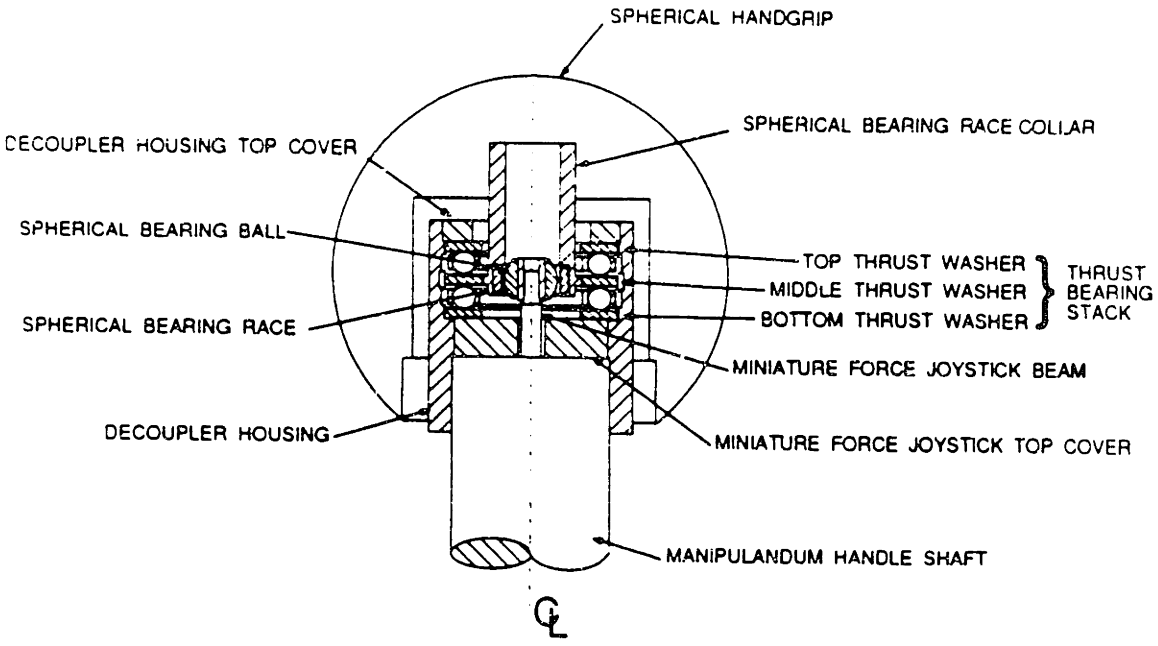

Figure 4.13: Force transducer moment cancellation mechanism. See text for additional details.

were 40 percent greater than when the same force was applied perpendicularly to the transducer beam as a "pure" force. With the thrust bearing arrangement in place, sensitivity to moments was reduced over 1000 fold, without noticeable change to the "pure" force response.

There are drawbacks, however, in the decoupler design. The use of the spherical bearing to join the middle thrust washer to the transducer introduces both friction and backlash. This results in hysteresis in the force transducer outputs of approximately 0.04 N (0.009 lb) in both axes and ~25 μm (~0.001 in) of play in the handgrip that is palpable to the human user. Increasing the bearing preload reduces play, but at the expense of heightened friction. Even though the transducer is modified so that it responds only to the two force components that lie tangent to the spherical work surface, couples applied to the spherical handgrip—which are not detectable at the beam element—still cause the manipulandum handle to rotate about the motor shaft axes. One solution to this problem may be to restrict the subject's ability to apply moments to the manipulandum by altering the manner in which the handle is grasped. A more viable solution may involve expanding the system measurement capability to embrace both of the moment and both of the force components that cause handle link motion.

Force Transducer Output

Because the voltage outputs directly from the force transducer are also at the millivolt level, noise reduction procedures similar to the ones used for the accelerometers are followed. The transducer itseld is shielded by its own aluminum case and the hollowed-out top segment handle shaft in which it is seated. It is connected via shielded cable to instrumentation amplifiers that reside in the same preconditioning module as the accelerometer compensation and pre-amplification components. The instrumentation amplifiers serve to increase the force signal gain by a factor of ten and also to null transducer offsets prior to transmission to the CIU.

The two axis force transducer was calibrated with the manipulandum handle shaft

locked in the upright position. The handle orientation for these tests was set by a clamp that fixed the handle shaft beneath the base of the decoupler housing to the motor face plates. Calibration forces were generated by suspending known weights from a length of smooth, lightweight, stainless steel wire rope over a very low friction pulley. These forces were transmitted to the transducer by attaching the other end of the wire rope horizontally to the spherical bearing collar of the "decoupler." The cable pull direction was aligned parallel to the notch in the transducer cover for the t_2 axis calibration and perpendicular to it for the t_1 tests. Records of pre-conditioning module output voltage versus applied forces up to 49 N (11 lb) were obtained for both axes.

The plotted force transducer calibration curves were very linear in appearance, except for the slight hysteresis of 0.04 N (0.009 lb) attributed to friction and backlash in the "decoupler" mechanism. Linear regressions performed on these data showed force transducer sensitivities corresponding to 0.0150 V/N (0.0668 V/lb) for the t_1 axis and 0.0146 V/N (0.0651 V/lb) for the t_2 axis prior to preamplification—both within the manufacturer's specifications for the miniature joystick without the custom moment cancellation mechanism in place. The correlation coefficients (R^2) for the regressions, 0.9994 and 0.9992 for the t_1 and t_2 axes respectively, attest to the linearity of the calibration data.

The alignment of the transducer with respect to the fixed motor shaft axes was also examined. In these tests, the handle shaft was locked in the straight up position ($\alpha = \beta = 0$) by clamping the handle at the spherical handgrip with respect to the motor face plates. In this position, if the alignment of the transducer was perfect and the motor shafts were truly coplanar and orthogonal to each other, motor #1 would only produce a reading in transducer axis t_1, according to Equations (4.65) and (4.66), and motor #2 would only produce a reading in t_2 according to Equations (4.69) and (4.70). In the tests, however, torque from powering only motor #1, in addition to the major t_1 axis transducer voltage, also produced a small signal (approximately 2.5 percent of the t_1 output) in the t_2 axis. Similarly, torque from powering only motor #2 led to a minor component (approximately 4 percent of the t_2 signal) in the t_1 axis. These small signal

components indicate a slight rotation of the transducer about the t_3 axis with respect to the actions of the motors; -1.5 degrees between axis t_1 and motor #1 and -2.3 degrees between axis t_2 and motor #2. This 0.8 degree difference between the two axes implies that not only is the transducer rotated with respect to the motor shaft axes, but that a slight deviation from orthogonality may exist either in the strain gauge mounting inside the miniature joystick, the alignment of the motors with respect to each other, or both. Because the effects of these misalignments were considered small, further adjustments were not attempted.

4.5.5 Additional Electronic Preconditioning

In addition to the electronic preconditioning described for the sensors throughout Section 4.5, all undergo low pass filtering in the CIU prior to their introduction into the manipulandum controller. The second order filters on all eight transducer channels (*i.e.*, four signals per manipulandum axis) were identically tuned with a cutoff at 250 Hz, and as such contribute negligible delay and attenuation to signals in the frequency band of human motion. The purpose of these filters was mostly cosmetic: to reduce artifacts from the 6 kHz motor and servo amplifier switching and the 2 MHz encoder decoder clock so that transducer signals appeared "cleaner" (*i.e.*, less noisy) during system debugging and calibration.

4.6 Open Loop Manipulandum Characteristics

Up until this point, the kinematics and statics of a hypothetical manipulandum mechanism, made of rigid massless links with frictionless joints, have been derived. Factors such as friction, inertia, and compliance in the "as-built" manipulandum will lead to departures from ideal system performance. These factors, and how they limit system bandwidth and force capabilities, are examined in this section.

4.6.1 Friction

The friction in the overall mechanical system, between the force transducer at the top of the manipulandum handle shaft and the motor housing mounts, was examined from the torque and velocity records of tests during which the handle was moved back and forth manually, with the motors' electrical terminals unconnected. The α and β axes were studied one at a time by clamping the axis not being tested in the upright (zero angle) position with a block that was wedged into the limit stop arrangement depicted in Figure 4.6. Because pure moments cannot be measured by the the force transducer, but could still result in handle motion, care was taken during these tests to apply forces directly at the "decoupler's"spherical bearing collar with the handgrip removed (see Figure 4.13). This way, the moment arm through which force couples could be developed were minimized, thereby reducing the ability to apply moments at the transducer. The tests were restricted to slow reciprocating movements that spanned the full travel available to the handle. Motion in each direction lasted approximately one second, with a full stop of similar duration before returning. These slow movements were intended to minimize dynamic force effects caused by the acceleration of the manipulandum inertia.

Torque versus angular velocity for tests of each axis with the protective leather boot removed, are plotted in Figure 4.14. Torques about the motor shafts were calculated by multiplying the force measured at the transducer by the 0.229 m (9 in) handle length since, according to Equations (4.50) and (4.52), $R_\alpha = R_\beta = R_o$ when the axis not being tested is locked in the straight-up position. Each plot is overlaid from approximately ten movement cycles and only contains data from the portion of the motion during which the handle link slows to a stop. The starting portion of each cycle was not plotted so that effects related to the acceleration of stiction break-out would not be shown. The deviations of the torque-velocity curves in Figure 4.14 from the characteristic signum function expected for friction are assumed to be caused by acceleration effects that arose due to imprecise manual regulation of handle velocity (a fault of the test method), and by the mechanical traits of the manipulandum mechanism itself. One such trait is the

elastic wind-up that was plainly visible during the actual tests and is evident in these plots as the velocity reversal occuring immediately prior to the handle's coming to a stop. The wind-up is due primarily to pre-stressing of the flexible couplings joining each motor to the handle mechanism by the accelerometer cable drive.

The torque required in either axis to keep the manipulandum handle moving against friction is 0.25 N-m (0.18 lb-ft), or less, according to the plateaus exhibited in Figure 4.14—about double the friction specified in Table 4.3 for the MC23S motor alone. This value is approximately the same whether or not the protective leather boot is in place.

The friction contributions of individual manipulandum components to this overall level were evaluated by suspending weights from the limit stop blocks that are keyed to the motor shafts, as the disassembled manipulandum was reassembled. The motors, due to brushes and bearings, each had 0.11 N-m (0.08 lb-ft) of friction—both within manufacturer's specifications. The gimbal mechanism itself, when unattached to the two motors, had negligible friction—the internal friction in the gimbal was insufficient to prevent the handle from toppling over sideways under its own weight. Attaching the gimbal to the two motors and bolting down the gimbal base to the top plate of the manipulandum cart, however, because of minor misalignments, added 0.03 N-m (0.02 lb-ft) of friction to each axis (at this stage of reassembly, there was enough friction to hold the handle up against gravity). Pre-tensioning the accelerometer drive cables to their operating stress level brought the friction up to 0.22 N-m (0.16 lb-ft) in each axis, sufficiently close to the values measured during the earlier tests in which the handle was manually pushed back and forth. It is not clear what portion of this final jump in friction is due to the effects of the cable drive tension on the gimbal bearings, and what portion is due to friction in the accelerometer cable drive assembly itself.

The motor and gimbal friction losses observed during the slow movement tests with the unpowered system reported above correspond to approximately 5 percent of the 5.06 N-m (3.73 lb-ft) theoretical motor torque capacity at maximum continuous amplifier

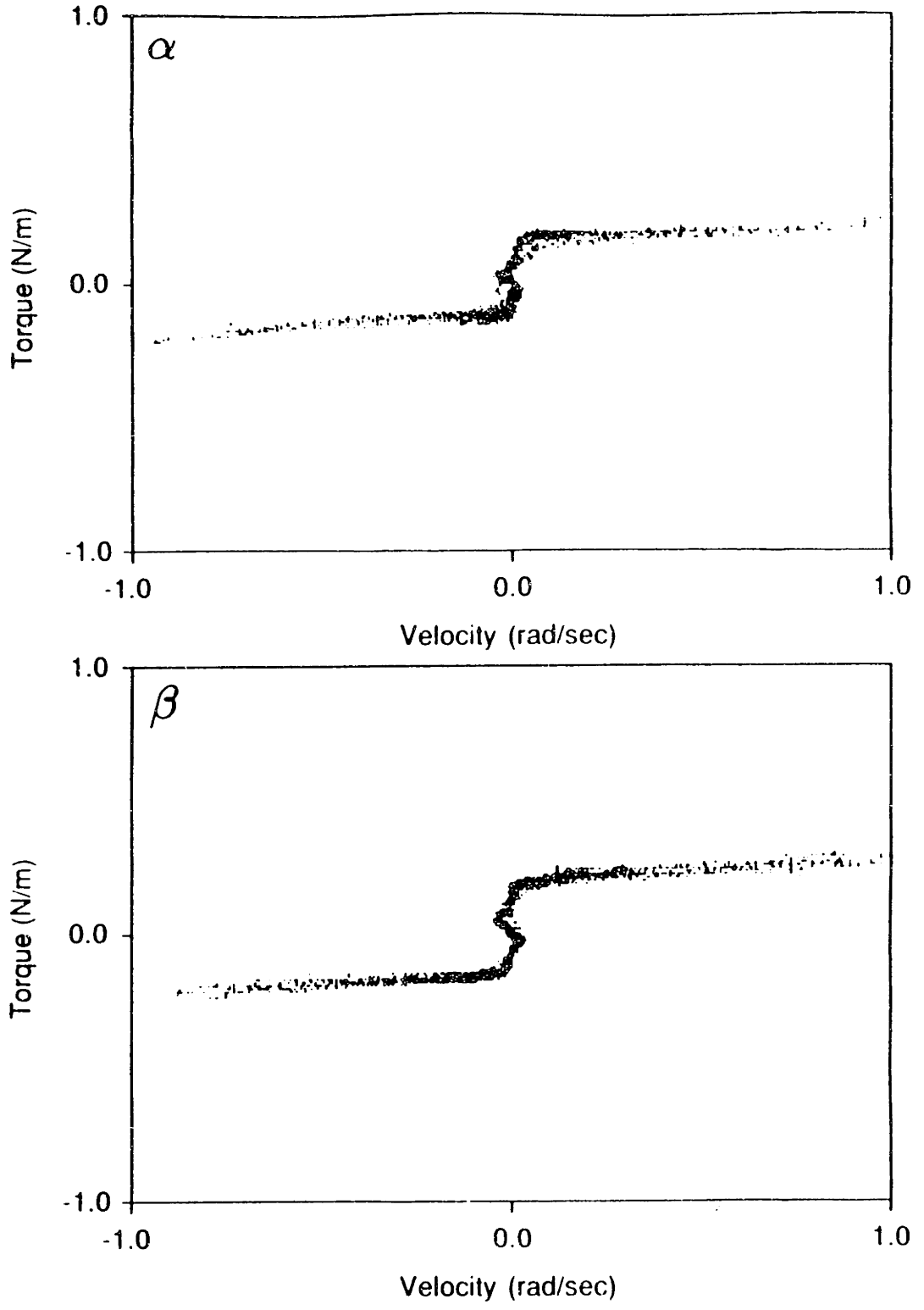

Figure 4.14: Passive manipulandum friction in the α and β axes. Both the negative and positive velocity regions of each plot contain only the portion of the motion cycle during which the handle was slowed to a stop. The inflection points near zero torque correspond to velocity reversals due to elastic wind-up. Each plot represents the accumulation of data from several movement cycles.

current output. *Measurements* of available torque, as detected by the force transducer when the motors were driven at maximum rated continuous amplifier current, showed that losses were of this or slightly greater magnitude. These measurements made at the force transducer with the handgrip clamped in the upright position, showed maximum continuous torque outputs of ±4.75 N-m (±3.50 lb-ft) for motor #1 and ±4.60 N-m (3.40 lb-ft) for motor #2. The higher losses for axis #2 are consistent with greater friction losses through the less direct transmission path from motor to hand grip—two bearing sets (*I* and *III*), rather than the one (bearing set *II*) of axis #1. At stall conditions, the percentages of motor torque lost to friction described here amount to a power dissipation of from 4.5 to 10 watts per axis in the form of heat, shared between the motors and the handle linkage.

4.6.2 Inertia and Compliance

Inertia

The inertial properties of the manipulandum linkage were evaluated analytically for rotations about the α and β axes by considering the inertial contributions of the motors and the individual components that make up the gimbal and handle. Because of the mass distributions resulting from the symmetries of the individual components, determination of the linkage inertias was simplified, enabling satisfactory estimates to be made without resorting to complex solid modelling techniques.

For rotations α and β, respectively about the fixed x and y axes of Figure 4.5), the four element inertia tensor, $\mathbf{I}_m$, can be expressed as

$$\mathbf{I}_m = \begin{bmatrix} I_{\alpha\alpha_m} & I_{\alpha\beta_m} \\ I_{\beta\alpha_m} & I_{\beta\beta_m} \end{bmatrix} \tag{4.71}$$

The presence of non-zero off-diagonal product of inertia terms in the tensor would indicate that angular velocity about one axis leads to angular momentum about the other axis, and as such only applies to the individual manipulandum linkage components that can actually undergo *both* α and β rotations. However, because the mass distribution of these

parts, as designed, ensures that the α and β axes of rotation always lie in planes of mass symmetry, the product of inertia terms vanish, leaving only the diagonal entries. Thus,

$$\mathbf{I}_m = \begin{bmatrix} I_{\alpha\alpha_m} & 0 \\ 0 & I_{\beta\beta_m} \end{bmatrix} \tag{4.72}$$

Numerical values for the diagonal terms, $I_{\alpha\alpha_m}$ and $I_{\beta\beta_m}$, were derived by summing the inertia contributions of all the individual elements in the manipulandum linkage. The inertias of the individual elements with respect to the fixed α and β rotational axes were obtained either from manufacturers' specifications or from estimates based on a particular component's shape and mass density. The inertia values for major groupings of all the individual components are listed in Table 4.4 for the straight-up handle position. The table also denotes whether the inertia of a specific component grouping with respect to one of the axes is affected by the angular displacements about the other axis. In particular, the inertia of one assembly, the gimbal, is broken down into two parts—one portion that changes as a function of off-axis (*i.e.*, the other axis') angle, and the other which does not. The overall inertias with respect to the two axes, summed from the entries in Table 4.4, are 0.01842 kg-m^2 for $I_{\alpha\alpha_m}$ and 0.01841 kg-m^2 for $I_{\beta\beta_m}$. These totals are so similar because they are dominated by contributions from symmetric components—*i.e.*, identical entries in both the α and β axis columns. Since the dominant elements affected by off-axis angle are also symmetric, overall inertias with respect to both axes are altered to nearly the same extent by similar off-axis displacements.

Compliance

Upon clamping the manipulandum motor shafts with the limit stop block arrangement described in Section 4.6.1 for the friction tests, the compliance in the linkage between the force transducer and the locked motor shafts becomes apparent as the handgrip is pushed upon with moderate force. Much of the compliance is centered at the flexible couplings that were installed to ease alignment requirements during fabrication as described in Section 4.2.4.

Manipulandum Component	Off-Axis Effect	α Axis Inertia ($kg-m^2$)	β Axis Inertia ($kg-m^2$)
Motor, Tach, Encoder & Limit Stop Block	N	2.8×10^{-3}	2.8×10^{-3}
Accelerometer Drive	N	1.0×10^{-4}	1.0×10^{-4}
Gimbal (a)	N	1.7×10^{-4}	3.0×10^{-5}
Gimbal (b)	Y	1.5×10^{-4}	2.8×10^{-4}
Handle Shaft & Force Transducer	Y	8.5×10^{-3}	8.5×10^{-3}
Spherical Grip	Y	6.7×10^{-3}	6.7×10^{-3}

Table 4.4: Manipulandum component inertias.

The stiffness between the top of the handle shaft and each of the clamped motor shafts was determined by applying forces measured at the transducer while monitoring the resulting deflection of the handle shaft with a dial indicator. The rotational stiffnesses calculated from these data were 325 N-m/rad (4.18 lb-ft/deg) about axis #1 and 200 N-m/rad (2.57 lb-ft/deg) about axis #2. The lower stiffness between the handle link and motor shaft #2—as with the higher friction losses mentioned in Section 4.6.1—is attributed to the less direct drive train for this axis.

Another source of compliance that was examined is the strain element of the force transducer. An estimate of its stiffness was derived from the 560 μm (0.022 in) maximum deflection limit of the "decoupler" collar measured with respect to the top of the decoupler housing at the force transducer's 90 N (20 lb) output saturation threshold imposed by the miniature force joystick's mechanical limit stops. The assumption of a linear displacement versus force relation over the operating range of the transducer up to these limits, yields a stiffness value of 1.6×10^5 N-m (909 lb/in).

Lumped Parameter Models

Based on the compliance and inertia properties characterized above, the simple linear lumped parameter model schematized in Figure 4.15 was formulated to describe either

axis. The model elements for either axis consists of three inertial lumps: the *motor-tach-encoder-limit stop* inertia, I_r; the *accelerometer drive-gimbal-handle shaft* inertia, I_g; and the 0.129 kg (4.5 oz) mass of the spherical handgrip, m_s. In turn, the inertias are separated by two compliances: the rotary compliance, $1/K_f$, from the "decoupler" housing to the clamped motor shaft, localized in the model between I_r and I_g at the flexible coupling; and the translational compliance of the force transducer beam element, $1/K_x$, at a radius of L, between I_g and m_s. The numerical values of the model parameters for each axis are included in Figure 4.15, along with the bond graph reticulation that led to the mathematical description of handle link dynamics.

The aim in developing this model was to estimate the frequency limits imposed by the mechanical handle and motor components on the operation of the overall manipulandum system. As such, the model does not include any damping at this stage. Because the real manipulandum handle does not fall over under its own weight, gravity effects are also excluded. The model treats the two manipulandum axes independently because the kinematic description of the mechanism derived in Section 4.2.3 shows the two axes to be decoupled when either motor shaft angle is zero.

The eigenvalues from the state-space description of the lumped parameter model, representing the frequencies at which the mechanical system has a tendency to oscillate, were obtained for a number of different conditions that could be experimentally replicated. These conditions, illustrated in Figure 4.16, include: 1) both ends of the three lump model free; 2) the motor shaft at the limit stop blocks clamped with the handle end free; and 3) the spherical handgrip clamped and the motor end free. The model predictions for these three cases, for both axes, are listed in Table 4.5.

The frequencies for these clamping conditions were determined experimentally by examining the dynamic response of the passive mechanism (*i.e*, with motors unpowered) to sharp taps administered by a hard steel hammer to the different lumped inertias in the system. The mechanical response to these impulsive disturbances was observed by monitoring the force transducer and tachometer outputs on a storage oscilloscope.

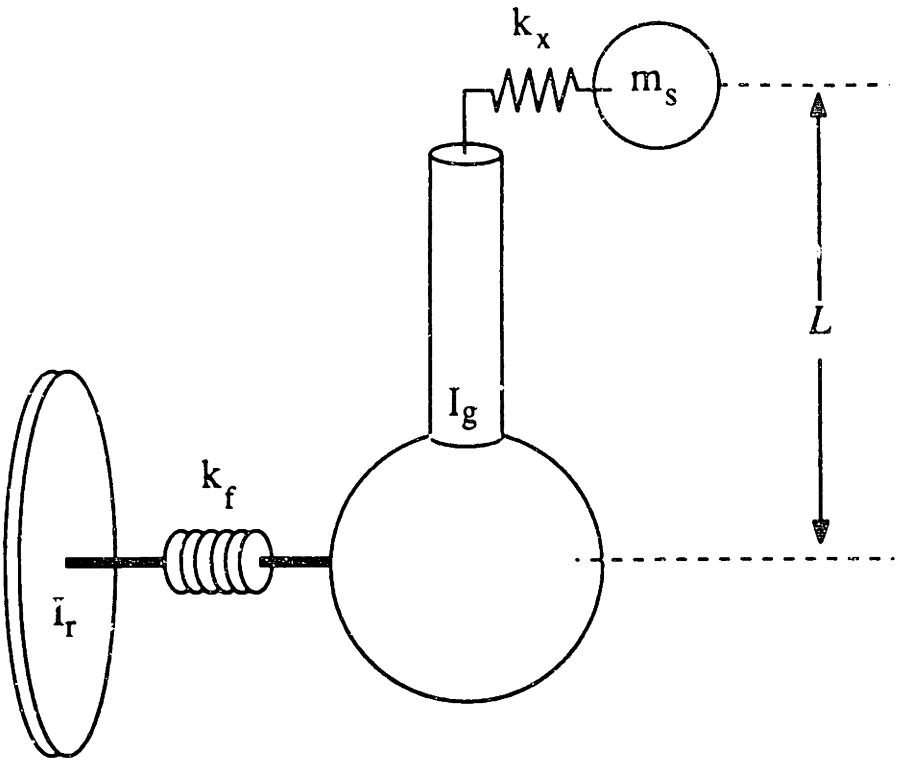

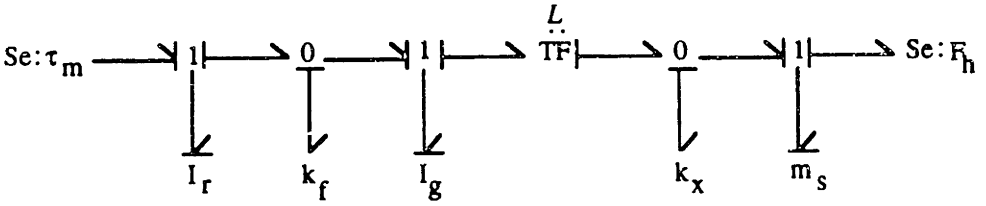

	I_r* (kg-m2)	I_g* (kg-m2)	m_s** (kg)	k_f** (N-m/rad)	k_x** (N/m)	L** (m)
AXIS 1	0.0028	0.0089	0.125	325.	160000	0.229
AXIS 2	0.0028	0.0089	0.125	250.	160000	0.229

* Estimated
** Measured

Figure 4.15: Lumped parameter model for single manipulandum axis. Model parameters values are as indicated for each axis.

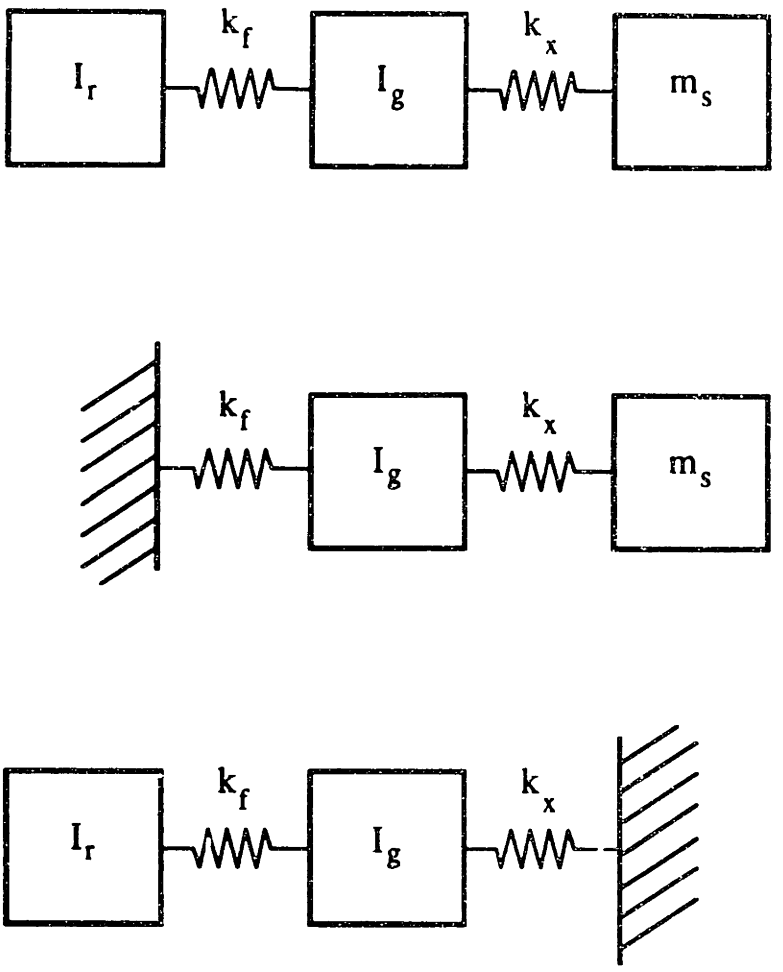

Figure 4.16: Manipulandum model clamping conditions.

Model Condition	Axis 1 (Hz)	Axis 2 (Hz)
1	0	0
	58.6	46.1
	235.9	235.6
2	22.8	17.9
	235.9	235.6
3	53.1	42.0
	157.4	156.4

Table 4.5: Manipulandum oscillatory frequencies predicted from lumped parameter model. The 0 Hz entries for model condition #1 denotes the free-body mode of either axis, corresponding to the tendancy of the whole untethered linkage to accelerate in the direction of the applied force disturbance.

Simultaneous high and low frequency oscillations were detected under all three clamping conditions. The frequencies of the oscillations, counted directly from the oscilloscope display, are reported in Table 4.6. Both the low and high frequency oscillations detected during each test were very lightly damped, having $\zeta < 0.10$ according to log decrement estimates of the response amplitude decay.

Model Condition	Axis 1 (Hz)	Axis 2 (Hz)
1	58.4	48.2
	240	220
2	22.2	20.1
	240	220
3	54.0	43.6
	167	167

Table 4.6: Experimentally measured manipulandum oscillatory frequencies.

Because the damping ratios were so small, the natural frequencies of the mechanism are nearly identical to the experimentally observed damped frequencies listed in Table 4.6. The low damping also justifies its exclusion in the model formulation, at least as far as

the determination of system bandwidth is concerned. The validity of the model inertial and stiffness estimates is substantiated by the close concurrence between the model frequencies in Table 4.5 and the experimentally measured frequencies in Table 4.6.

It is interesting to note from the model and the experimental data that the frequency of the first oscillatory mode for the unclamped mechanism (model condition #1) does not change significantly when the spherical grip is rigidly clamped (model condition #3). This implies that a human hand, with significantly more compliance than the rigid clamp, especially at the palm (see reference [115] for example), will have even less effect on the first oscillatory mode's frequency upon coupling to the spherical handgrip. In addition, when the inertia entries in Table 4.4 that are susceptible to off-axis angle changes were re-evaluted at angles other than zero[19] and then substituted back into the three lump model (model condition #1), both the slow and fast oscillatory mode frequencies calculated for each axis were raised by less than 1.0 Hz over the range of manipulandum motion.

Compensator Design

The frequency of the first oscillatory mode of either axis in the unclamped free-body condition implies that the manipulandum linkage itself imposes a bandwidth limitation on the overall system. The absence of sufficient inherent damping in the mechanism also indicates a propensity for resonance at these frequencies, and, hence, a potential source of controller implementation difficulties. The steadiness of the frequencies predicted for these oscillations by the model in response to rigid clamping of the handle linkage endpoint and to inertia alterations due to off-axis angle changes, however, suggests that a fixed parameter compensator may be useful in dealing with these resonances.

The compensators that were implemented to deal with these resonances are essentially notch filters that were tuned to the oscillatory frequencies predicted by the lumped parameter models. They were designed according to a root locus procedure devised

[19]For the elements of $I_{\alpha\alpha_m}$, the angle change requires multiplying that term by $R_\alpha{}^2$ from Equation (4.50) and then dividing through by $R_o{}^2$, in effect reducing the inertia by the square of the relative decrease in moment arm. For the $I_{\beta\beta_m}$ terms, the same procedure is followed using $R_\beta{}^2$ from Equation (4.52) instead.

by Abul-Haj [5], in which both the frequency and depth of the notch are specified by locating a pair of zeros that cancel the offending resonant pole pair. The original poles are then replaced by a critically damped double pole at the same frequency. The actual compenstator circuitry is located in the CIU, in line with the inputs to each axis' servo amplifier.

The effectiveness of the compensators is demonstrated in Figure 4.17. These plots show the velocity of the handle (as measured by the tachometer at the motor shaft) for each axis, in response to a 5 Hz square wave voltage input to the transconductance servo amplifiers. The upper plot in each pair depicts the superposition of first oscillatory mode on the fundamental 5 Hz response of the handle in the absence of compensation; the lower plot shows the near complete attenuation of this mode due to the compensators.

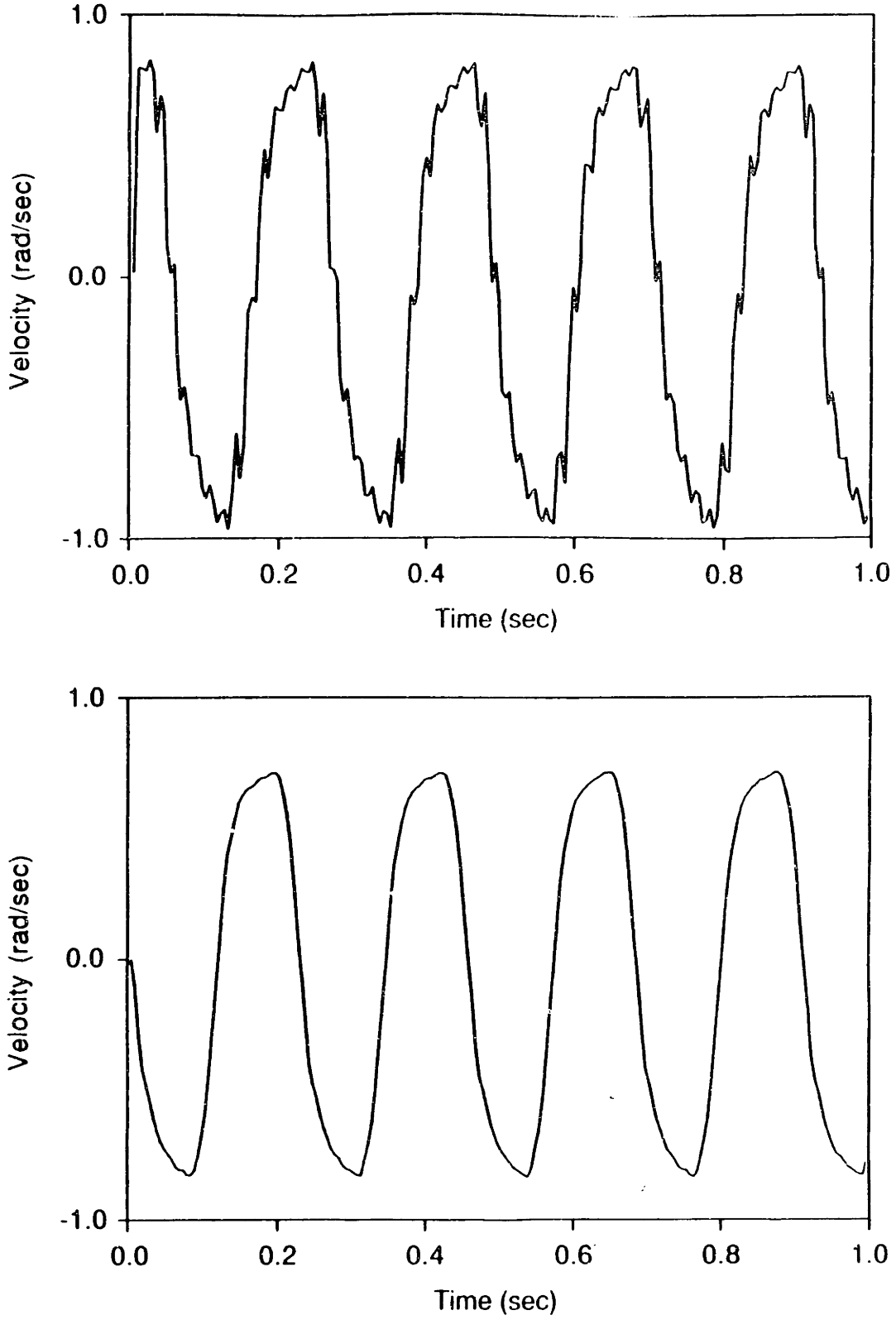

Figure 4.17: Notch filter compensator performance. (a) Axis #1. *Top*) Prior to inclusion of compensator showing first mode resonance superimposed on 5 Hz square wave response; *bottom*, after inclusion of notch filter compensator.

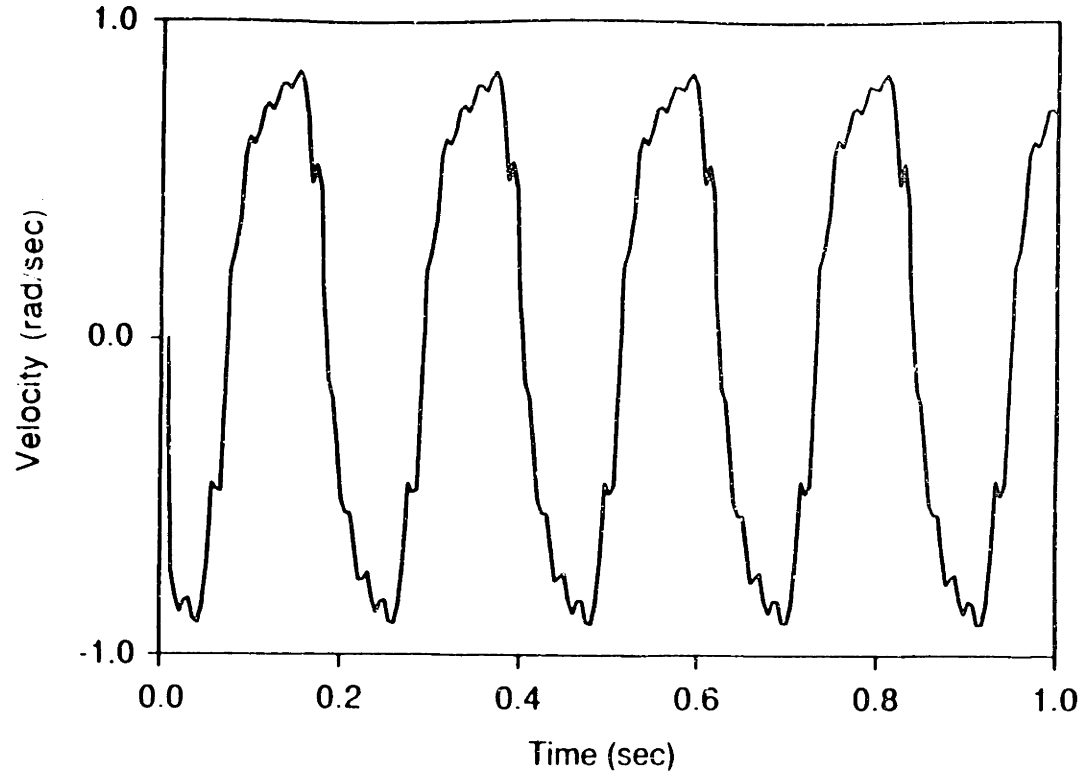

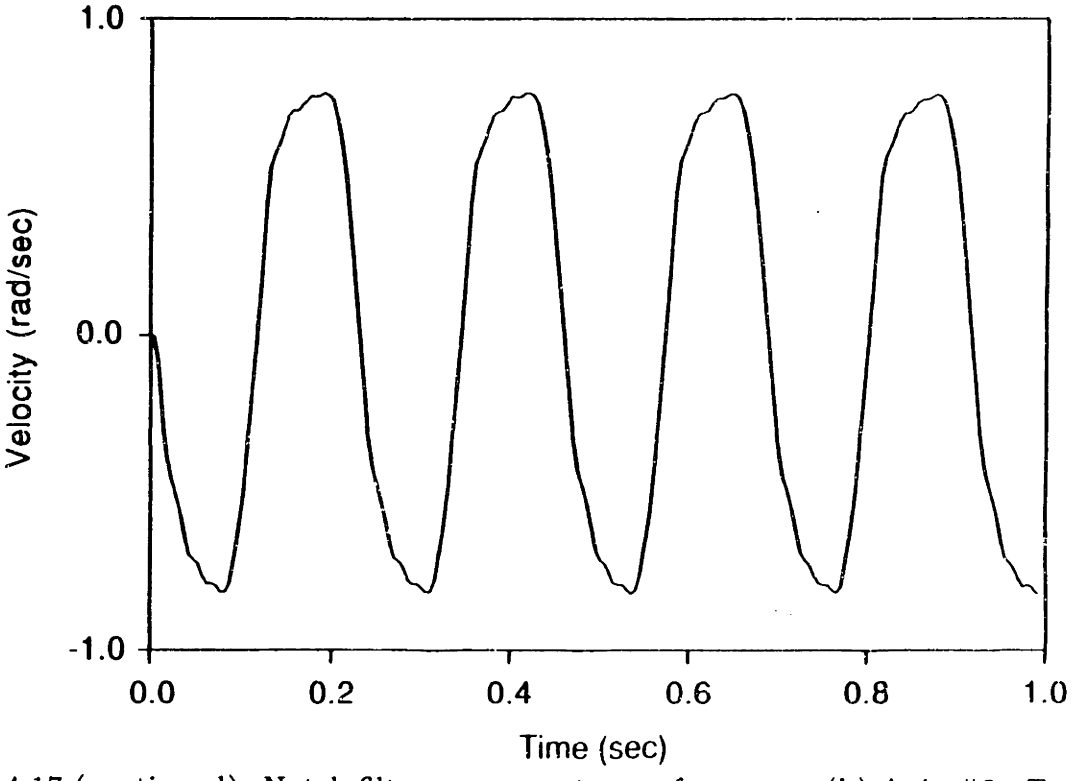

Figure 4.17 (continued): Notch filter compensator performance. (b) Axis #2. *Top*, prior to inclusion of compensator showing first mode resonance superimposed on 5 Hz square wave response; *bottom*, after inclusion of notch filter compensator.

Chapter 5

System Supervision and Control

5.1 Overview

This chapter describes the supervision and control of the various functions that contribute to an effective kinesthetic and visual virtual environment system for research in manual control. The functions to be controlled include: 1) emulation of mechanical objects at the manipulandum interface to the human operator (*i.e.*, the experimental subject) during the performance of manual tasks; 2) maintenance of safety during human interaction with the manipulandum; 3) visual presentation to the subject of the task being performed in the virtual environment; and 4) data storage for subsequent evaluation of the subject's performance during interaction with the system. "Supervision" is required to ensure that these four functions can be executed simultaneously without degrading the overall system performance.

As will be shown in this chapter, the mechanism, actuator, and sensor configuration selected for the manipulandum alleviate much of the need for numerically intensive computation in the real-time control of the system. In addition, the underlying emphasis in the organization of the supervision and control architecture has been the distribution of the computational burden so that bottlenecks limiting the effective bandwidth of the system are avoided.

The restrictions imposed by the computing equipment available for this project provided the impetus for distributing computation and eliminating many of the numerically

intensive aspects of real-time controller implementation. The computer itself is based on an LSI-11/23 processor (Digital Equipment Corp., Maynard MA) running under the RT-11SJ operating system. The major constraint encountered in using this computer is a 64 kByte limit on the size of executable program code at any one time in directly addressable memory—although up to three times more virtual memory may be addressed for data storage only.

The other factor to be considered is this computer's speed. Faye [56] described a digital controller running on an LSI-11/73 processor (nominally four times faster than an LSI-11/23) for a two degree of freedom planar five-bar arm-loading manipulandum as being able to achieve sampling frequencies of 285.6 Hz—the equivalent of an analog bandwidth of from 7.2 to 14.3 Hz. Wlassich [151], in discussing similar control algorithms on an LSI-11/23 for a manipulator with the same planar five-bar configuration, listed sampling frequencies on the order of 120 Hz, corresponding to an anlog bandwidth of no more than 6 Hz. The bandwidth values in both of these cases takes into account the real-time control of manipulator endpoint loads, safety maintenance, and data logging. Neither system, however, involved presentation of a video display. Thus, it is improbable that these two systems, in view of their allotted computed power, would be capable of satisfying one fundamental requirement for the virtual environment system in this work: that its mechanical bandwidth exceed the range of human tremor frequency.

In this system, the LSI-11/23 is assigned the role of host computer. It supervises overall system operation and collects data during the course of experiments. The custom built Control Interface Unit (CIU) is responsible for feedback control in the simulation of mechanical loads at the manual interface and for monitoring system safety, as well as the conditioning of transducer signal described in the previous chapter. The details of the real-time video display are executed by a separate personal computer that runs independently of the remainder of the system. The host computer, in acting as system supervisor, sets and constantly updates the mechanical load control parameters in the CIU and transfers data on the subject's manual activity to the video display computer.

The hardware, software, and performance associated with each of these components are covered in the remainder of this chapter.

5.2 Load Controller

5.2.1 Background

It can be understood from freshman physics that, in principle, a motor with the characteristics of a pure torque source can be made to emulate the properties of basic linear mechanical spring, damper, and inertia elements; and that, from collections of these elements, more complex lumped parameter loads can be assembled. Controlling a rotary motor to produce a resistive torque that is a linear proportional function of angular displacement from a reference point endows the motor shaft with the characteristics of a rotary spring, centered at the reference point. Similarly, a resistive motor torque that is a linear proportional function of the shaft angular velocity or acceleration exhibits the characteristics of a rotary viscous damper or rotary inertia respectively. Colburn and Evarts [39] suggested this linear feedback scheme as the means to control the mechanical load parameters of a single axis manipulandum for human neurophysiological studies.

Rotary spring and damper emulation about a motor shaft in a sense is equivalent to P-D (proportional-derivative) feedback action in a position servo system, where the objective is accurate position regulation by rejecting external disturbances while maintaining rapid non-oscillatory response dynamics. In traditional linear servo design however, the external environment is treated as the source of disturbances to be rejected, rather than an entity with which harmonious interaction should occur. As such, traditional servo systems are restricted to large position feedback gains and, consequently, high stiffnesses. More general human interaction with a load simulating motor requires a wider span of stiffness and damping levels—including positive, negative and zero values. Furthermore, feedback gains for human interactive applications need not be linear or time invariant.

Robotics researchers have investigated strategies for the active modulation of manipulator endpoint compliance so that interaction with the external environment (as in

contact with hard objects) would be more forgiving than what occurs with unyielding motion or force control schemes.[1] Hogan [74, 75, 76] addressed the problem of interaction between manipulators and more general environments and, observing that causality prohibits satisfying endpoint force and kinematic commands simultaneously, recognized that it is the mechanical impedance of the manipulator as seen by the environment which must be explicitly controlled. In the framework cast by Hogan, where the manipulator's impedance is controlled, the dynamic forces that arise at the manipulator-environment interface are determined by the difference between a commanded virtual (or reference) trajectory and the actual motion as constrained by the environment. The impedances set by such a controller are not restricted to being linear (*i.e.*, springs, dampers, and masses) nor do they have to be time invariant. A number of design methodologies for implementing impedance controllers have been proposed [13, 41, 65, 66, 84].

Impedance control has been applied in a number of experimental investigations. These applications include: the control of a wearable elbow prosthesis emulator in which the impedance and virtual elbow position trajectory were determined from the myoelectric activity in the remnant musculature [5]; the development of a two degree of freedom loading manipulandum for human arm dynamics research [56]; and studies of the effectiveness of impedance control algorithms for free motion and contact tasks, both with and without endpoint force sensing [44, 151]. While the elbow prosthesis impedance was controlled directly at its single rotary joint, the impedances of the planar two degree of freedom armlike devices in references [44, 56, 151] were controlled with respect to a fixed Cartesian frame, thereby requiring significant computation to transform endpoint impedance objectives into a pair of rotary actuator command signals. The digital control update rates for two of these manipulator implementations were cited above in Section 5.1.

[1] See reference [149] for concise review of force control in robotics.

5.2.2 Joint Axis Control and Endpoint Impedance

The ultimate objective for the load controller of a truly versatile manipulandum is to have the ability to produce any arbitrary mechanical impedance field as seen from the environment, where the environment in this case is the human operator's hand. In principle, if unlimited computational power were available, these mechanical load fields could range from constant linear impedances (*i.e.*, simple springs, dampers, and inertias) in a fixed external Cartesian reference frame, to complicated nonlinear time varying impedances in different coordinate systems, provided that the desired behavior could be achieved within the constraints imposed by the manipulandum linkage workspace. As noted later in this chapter and in Appendix B, the CIU does provide the connections for both analog-to-digital and digital-to-analog conversion, so that purely digital control may be implemented. It has already been pointed out in Section 5.1, however, that the development of more elaborate controllers would be hindered by the restricted capabilities of the available computer.

To alleviate the demands of computing the coordinate transformations required to specify the endpoint impedance of the manipulandum in fixed Cartesian coordinates, a linear joint axis control architecture is proposed, in which the linear controller modulates linear impedances with respect to the α and β actuator axes. The resultant load fields would then have principal axes that coincide with these fixed rotational axes and, in the special case where the kinematics about a particular actuator shaft are the only feedback to that actuator, the loads emulated by each motor would be equivalent to the rotary inertia, viscosity, and stiffness described at the begining of Section 5.2.1.

The inspiration for selecting this *joint* space impedance controller implementation was the observation made at the end of Section 4.2.3: that the static actions of the two manipulandum motors are always decoupled in the horizontal xy plane. Also, when the controlled impedances are set identically about both rotary axes, the load field perceived at the manipulandum endpoint will be isotropic—i.e., the load field's orientation will be indiscernible to the human operator—because of the symmetry of the manipulandum

handle mechanism.

General Linear Joint Space Controller

The joint space control law can be stated in vector form as

$$\mathbf{P}_{m_a} = \mathbf{P}_{m_s} + \mathbf{P}_{m_d} + \mathbf{P}_{m_i} \tag{5.1}$$

where $\mathbf{P}_{m_a}$ is the vector of actuator torques being controlled. $\mathbf{P}_{m_a}$ has the same directional components as $\mathbf{P}_m$, described by Equation (4.38), and is the sum of simulated rotary stiffness, viscous, and inertial load terms.

The simulated spring, damper, and inertia terms on the right hand side of Equation (5.1) are defined as follows:

$$\mathbf{P}_{m_s} = \mathbf{K}(\mathbf{q}_m - \mathbf{q}_{m_O}) \tag{5.2}$$

$$\mathbf{P}_{m_d} = \mathbf{B}(\dot{\mathbf{q}}_m - \dot{\mathbf{q}}_{m_O}) \tag{5.3}$$

$$\mathbf{P}_{m_i} = \mathbf{I}(\ddot{\mathbf{q}}_m - \ddot{\mathbf{q}}_{m_O}) \tag{5.4}$$

where $\mathbf{q}_m$ is the vector of actual displacement measurements in the generalized manipulandum coordinates defined by Equation (4.18), and $\dot{\mathbf{q}}_m$ and $\ddot{\mathbf{q}}_m$ are the corresponding velocity and acceleration measurements. $\mathbf{q}_{m_O}$, $\dot{\mathbf{q}}_{m_O}$, and $\ddot{\mathbf{q}}_{m_O}$ denote instantaneous displacement, velocity, and acceleration reference commands and together form the virtual trajectory. $\mathbf{K}$, $\mathbf{B}$, and $\mathbf{I}$, respectively, are 3×3 gain matrices of stiffness, damping and inertia simulation coefficients.

Because the manipulandum as built neither has actuators nor permits motion in the r component, the third row and third column entries of these gain matrices are all zero valued. Hence, upon expansion, they become

$$\mathbf{K} = \begin{bmatrix} K_{11} & K_{12} & 0 \\ K_{21} & K_{22} & 0 \\ 0 & 0 & 0 \end{bmatrix} \tag{5.5}$$

$$\mathbf{B} = \begin{bmatrix} B_{11} & B_{12} & 0 \\ B_{21} & B_{22} & 0 \\ 0 & 0 & 0 \end{bmatrix} \tag{5.6}$$

$$\mathbf{I} = \begin{bmatrix} I_{11} & I_{12} & 0 \\ I_{21} & I_{22} & 0 \\ 0 & 0 & 0 \end{bmatrix} \tag{5.7}$$

The diagonal elements of each gain matrix set feedback gains from kinematics about a particular actuator axis back to that actuator's controller; off-diagonal entries represent cross-coupled feedback gains from one actuator's kinematics to the other's controller.

The Cartesian representation of actively controlled linear joint space impedances can be derived from the manipulandum mechanism kinematic and static transformations stated in Section 4.2.3. Starting with the forward geometric transformations of Equations (4.14), (4.15), and (4.16), summarized compactly by the functional form

$$\mathbf{q}_m = \mathbf{L}_m(\mathbf{x}) \tag{5.8}$$

and recalling the force relation of Equation (4.42),

$$\mathbf{F} = \mathbf{J}_m^T \mathbf{P}_m$$

displacement of the simulated rotary springs of Equation (5.2) relative to their instantaneous reference position results in force components, $\mathbf{F}_s$, given by

$$\mathbf{F}_s = \mathbf{J}_m{}^T \mathbf{K} \left[\mathbf{L}_m(\mathbf{x}) - \mathbf{L}_m(\mathbf{x}_o) \right] \tag{5.9}$$

$\mathbf{x}$ is the vector defined by Equation (4.19), describing the translational displacement of the manipulandum handle in the Cartesian frame. $\mathbf{x}_o$ is the instantaneous centering position of the stiffness field with respect to that frame. $\mathbf{J}_m$ is the manipulandum linkage Jacobian as expressed by Equation (4.22).

Employing the force relation of Equation (4.42) and the velocity transformation of

Equation (4.17), the rotary viscous damper represented by Equation (5.3) becomes

$$\mathbf{F}_d = \left[\mathbf{J}_m{}^T \mathbf{B}\, \mathbf{J}_m\right] (\dot{\mathbf{x}} - \dot{\mathbf{x}}_o) \tag{5.10}$$

with respect to the fixed Cartesian frame.

Applying the force relation of Equation (4.42) and the time derivative of Equation (4.17) to Equation (5.4) yields

$$\mathbf{F}_i = \left[\mathbf{J}_m{}^T \mathbf{I}\, \mathbf{J}_m\right] (\ddot{\mathbf{x}} - \ddot{\mathbf{x}}_o) + \left[\mathbf{J}_m{}^T \mathbf{I}\, \dot{\mathbf{J}}_m\right] (\dot{\mathbf{x}} - \dot{\mathbf{x}}_o) \tag{5.11}$$

the Cartesian force components that result from simulation of rotary inertias in joint axis coordinates. The second term on the right hand side of Equation (5.11) contributes velocity product terms arising from the time derivative of the Jacobian, $\dot{\mathbf{J}}_m$, indicating that simulation of rotary inertias in joint axis coordinates generates Coriolis and centripetal forces in the fixed Cartesian frame. However, in situations where these velocity dependent forces are significant, and their elimination is deemed necessary, augmented digital control routines may be required to computate appropriate cancellation torques.

Linear Joint Space Controller—Special Case

In the special case where the reference displacement, velocity, and acceleration vectors are set to zero, *i.e.*,

$$\mathbf{q}_{m_o} = \dot{\mathbf{q}}_{m_o} = \ddot{\mathbf{q}}_{m_o} = \mathbf{0}$$

and the off-diagonal cross-coupled feedback terms are eliminated from the gain matrices in Equations (5.5), (5.6), and (5.7), the actuator torques, τ_{α_a} and τ_{β_a}, under joint space impedance control reduce to

$$\tau_{\alpha_a} = I_{11}\ddot{\alpha} + B_{11}\dot{\alpha} + K_{11}\alpha \tag{5.12}$$

$$\tau_{\beta_a} = I_{22}\ddot{\beta} + B_{22}\dot{\beta} + K_{22}\beta \tag{5.13}$$

In the following, the Cartesian representation of the rotary impedances described by Equations (5.12) and (5.13) is developed under the assumption that, with the manipulandum handle in close to an upright position over its entire workspace, motion and forces are predominantly parallel to the xy plane. As such, terms that give rise to z component forces or arise from z motion are negelected. Also, since there is no motion in the r component, $r = R_o$.

Expanding Equation (5.9), the x and y components resulting from the stiffness terms of the joint axis controller defined by Equations (5.12) and (5.13) are

$$F_{x_s} = K_{22} \cos\beta \frac{\sqrt{1 - \sin^2\alpha \sin^2\beta}}{R_o \cos\alpha} \tan^{-1}\left(\frac{x}{z}\right) \tag{5.14}$$

$$F_{y_s} = K_{11} \cos\alpha \frac{\sqrt{1 - \sin^2\alpha \sin^2\beta}}{R_o \cos\beta} \tan^{-1}\left(\frac{y}{z}\right) \tag{5.15}$$

Recognizing the equivalent moment arm terms from Equations (4.50) and (4.52), Equations (5.14) and (5.15) can be rewritten as

$$F_{x_s} = K_{22} \frac{\cos\beta}{R_\beta} \tan^{-1}\left(\frac{x}{z}\right) \tag{5.16}$$

$$F_{y_s} = K_{11} \frac{\cos\alpha}{R_\alpha} \tan^{-1}\left(\frac{y}{z}\right) \tag{5.17}$$

Expanding the inverse tangent terms,

$$F_{x_s} = K_{22} \frac{\cos\beta}{R_\beta} \left(\frac{x}{z}\right) \left[1 - \frac{1}{3}\left(\frac{x}{z}\right)^2 + \frac{1}{5}\left(\frac{x}{z}\right)^4 - \cdots\right] \tag{5.18}$$

$$F_{y_s} = K_{11} \frac{\cos\alpha}{R_\alpha} \left(\frac{y}{z}\right) \left[1 - \frac{1}{3}\left(\frac{y}{z}\right)^2 + \frac{1}{5}\left(\frac{y}{z}\right)^4 - \cdots\right] \tag{5.19}$$

Substituting for the power series terms in square brackets with the inverses of the geometric relations of Equations (4.14) and (4.15), and replacing the remaining z outside the square brackets with the right hand side of Equation (4.10) yields

$$F_{x_s} = \frac{K_{22}}{R_\beta^2}\left[1 - \frac{\tan^2\beta}{3} + \frac{\tan^4\beta}{5} - \cdots\right]x \tag{5.20}$$

$$F_{y_s} = \frac{K_{11}}{R_\alpha^2}\left[1 - \frac{\tan^2\alpha}{3} + \frac{\tan^4\alpha}{5} - \cdots\right]y \tag{5.21}$$

The x and y damping components due to the joint axis controller expressed in Equations (5.12) and (5.13) are, by expanding Equation (5.10),

$$F_{x_d} = B_{22}\cos^2\beta\left[\frac{1 - \sin^2\alpha\sin^2\beta}{R_o^2\cos^2\alpha}\right]\dot{x} \tag{5.22}$$

$$F_{y_d} = B_{11}\cos^2\alpha\left[\frac{1 - \sin^2\alpha\sin^2\beta}{R_o^2\cos^2\beta}\right]\dot{y} \tag{5.23}$$

Substituting for the equivalent moment arm terms from Equations (4.50) and (4.52)

$$F_{x_d} = \frac{B_{22}}{R_\beta^2}\left(\cos^2\beta\right)\dot{x} \tag{5.24}$$

$$F_{y_d} = \frac{B_{11}}{R_\alpha^2}\left(\cos^2\alpha\right)\dot{y} \tag{5.25}$$

Similarly, the x and y inertia terms resulting from the joint axis impedance controller, after expanding Equation (5.11), are

$$\begin{aligned} F_{x_i} &= \frac{I_{22}}{R_\beta^2}\left(\cos^2\beta\right)\ddot{x} \\ &\quad + \frac{I_{22}}{R_0^2\cos\alpha}\left[\sin\alpha(1-\sin^2\beta\cos 2\alpha)\dot{\alpha}\right]\dot{x} \\ &\quad - \frac{I_{22}}{R_0^2\cos\alpha\cos\beta}\left[(\cos^3\alpha\sin\beta)\dot{\beta}\right]\dot{x} \end{aligned} \tag{5.26}$$

$$\begin{aligned} F_{y_i} &= \frac{I_{11}}{R_\alpha^2}\left(\cos^2\alpha\right)\ddot{y} \\ &\quad + \frac{I_{11}}{R_0^2\cos\beta}\left[\sin\beta(1-\sin^2\alpha\cos 2\beta)\dot{\beta}\right]\dot{y} \\ &\quad - \frac{I_{11}}{R_0^2\cos\alpha\cos\beta}\left[(\sin\alpha\cos^3\beta)\dot{\alpha}\right]\dot{y} \end{aligned} \tag{5.27}$$

Substituting for $\dot{\alpha}$ and $\dot{\beta}$ from Equations (4.23) and (4.24), and restricting motion to x and y components gives

$$\begin{aligned} F_{x_i} &= \frac{I_{22}}{R_\beta^2}\left(\cos^2\beta\right)\ddot{x} \\ &\quad - \frac{I_{22}}{R_0^3}\left[\frac{\sin\alpha}{\cos\beta}\sqrt{1-\sin^2\alpha\sin^2\beta}(1-\cos 2\alpha\sin^2\beta)\right]\dot{x}\dot{y} \\ &\quad - \frac{I_{22}}{R_0^3}\left[(\cos\alpha\sin\beta)\sqrt{1-\sin^2\alpha\sin^2\beta}\right]\dot{x}^2 \end{aligned} \tag{5.28}$$

$$\begin{aligned} F_{y_i} &= \frac{I_{11}}{R_\alpha^2}\left(\cos^2\alpha\right)\ddot{y} \\ &\quad + \frac{I_{11}}{R_0^3}\left[\frac{\sin\beta}{\cos\alpha}\sqrt{1-\sin^2\alpha\sin^2\beta}(1-\sin^2\alpha\cos 2\beta)\right]\dot{x}\dot{y} \\ &\quad + \frac{I_{11}}{R_0^3}\left[(\sin\alpha\cos\beta)\sqrt{1-\sin^2\alpha\sin^2\beta}\right]\dot{y}^2 \end{aligned} \tag{5.29}$$

Respectively, the second and third terms of Equations (5.28) and (5.29) are Coriolis and

centripetal forces caused by the rotational nature of handle link velocities with respect to the motor shafts. In situations where translational accelerations $\ddot{x}$ and $\ddot{y}$ are significant, the first term of Equations (5.28) and (5.29) can be considered to dominate the inertial force components, due to $\sin\alpha$ and $\sin\beta$ being small for motion lying primarily in the xy plane.

The contributions of the joint space controlled stiffness, damping, and inertia to the planar Cartesian approximation can be summarized from Equations (5.20), (5.21), (5.24), (5.25), (5.28), and (5.29) in vector form as:

$$\tilde{\mathbf{F}} \simeq \mathbf{I}'\ddot{\tilde{\mathbf{x}}} + \mathbf{B}'\dot{\tilde{\mathbf{x}}} + \mathbf{K}'\tilde{\mathbf{x}} \tag{5.30}$$

in which

$$\tilde{\mathbf{F}} = \begin{bmatrix} F_x \\ F_y \end{bmatrix} \tag{5.31}$$

and

$$\tilde{\mathbf{x}} = \begin{bmatrix} x_m \\ y_m \end{bmatrix} \tag{5.32}$$

The Cartesian matrices that result from the joint axis load simulation are

$$\mathbf{K}' = \begin{bmatrix} \frac{K_{22}}{R_\alpha^2}\left(1 - \frac{\tan^2\beta}{3} + \cdots\right) & 0 \\ 0 & \frac{K_{11}}{R_\beta^2}\left(1 - \frac{\tan^2\alpha}{3} + \cdots\right) \end{bmatrix} \tag{5.33}$$

$$\mathbf{B}' = \begin{bmatrix} \frac{B_{22}}{R_\beta^2}\cos^2\beta & 0 \\ 0 & \frac{B_{11}}{R_\alpha^2}\cos^2\alpha \end{bmatrix} \tag{5.34}$$

and

$$\mathbf{I}' = \begin{bmatrix} \frac{I_{22}}{R_\beta^2}\cos^2\beta & 0 \\ 0 & \frac{I_{11}}{R_\alpha^2}\cos^2\alpha \end{bmatrix} \tag{5.35}$$

Upon examining the resultant Cartesian gain matrices for the planar approximation, $\mathbf{K}'$, $\mathbf{B}'$, and $\mathbf{I}'$, the following should be noticed:

1. The x and y components of the simulated stiffness, damping and inertia matrices are decoupled—*i.e.*, all off-diagonal entries are zero-valued.

2. Axis #1 feedbacks (K_{11}, B_{11}, and I_{11}) only contribute to y forces, while axis #2 feedbacks (K_{22}, B_{22}, and I_{22}) contribute only to x forces.

Even though explicit cross-coupling is not present in the transformed Cartesian frame impedances, instantaneous geometric dependences still affect the elements of the impedance matrices, both from the squared equivalent moment arm lengths, $1/R_\alpha^2$ and $1/R_\beta^2$, as well as from the $\cos^2\alpha$, $\cos^2\beta$, and tangent series terms. Over the maximum extent of handle link motion, these geometric dependences lead to a ± 20 percent deviation in the individual matrix entries from their values when the handle is in the straight-up position—*i.e.*, when $\alpha = \beta = 0$, and the combined trigonometric and equivalent moment arm terms reduce to $1/R_o^2$.

5.2.3 Joint Axis Controller Implementation

One approach to the implementation of the joint axis based load simulator described by Equations (5.12) and (5.13) is to develop a *digital* controller that would feed back the kinematic measurements and apply the appropriate gain adjustments. With a computer in the feedback loop, the joint space gains and reference inputs could then actually be updated based on instantaneous measurements of angular displacements and velocities so that, for instance, the geometric factors in $\mathbf{K}'$, $\mathbf{B}'$, and $\mathbf{I}'$, or the Coriolis and centripetal

terms of Equations (5.28) and (5.29) could be eliminated from the resulting loads in fixed Cartesian coordinates.

The presence of the sampled data path in a digital controller (even without dynamically updated feedback gains), however, imposes limits on system bandwidth. These limits arise primarily because of the fixed overhead associated with the finite time interval required for multi-channel analog-to-digital data acquisition, and, depending on controller complexity, the time to execute computer code. In addition, digital controllers which approximate anlog designs only provide stable behavior up to frequencies that are much slower than the sampling rate. Values commonly cited in control engineering textbooks suggest that sampled data system bandwidths only range up to from one-fourtieth to one-tenth of the digital sampling frequency, depending on the system and the controller.[2]

To avoid the bandwidth limitations inherent in computer-based digital control, a hard-wired electronic version of the joint axis impedance controllers described by Equations (5.12) and (5.13) was implemented in the CIU. The controller for one axis is illustrated in block diagram form in Figure 5.1. Since the two axes of the manipulandum mechanism are kinematically similar, the controller for the second axis has an identical architecture. Also, because the two axes of the impedance controller (both in joint axis pace and in the planar approximation) are decoupled, each axis is treated independently, without any electronic cross-communication being provided between the two in the controller circuitry.

The controller utilizes direct measurements of joint axis kinematics from the shaft angle encoders, tachometers, and accelerometers, represented respectively in Figure 5.1 as $G_p(s)$, $G_v(s)$, and $G_a(s)$. In addition to the kinematic feedback, the joint axis controller makes use of sensor-based torque signals. The torque for each joint axis is derived from Equations (4.63) and (4.68), ignoring both geometry dependent terms and the minor off-axis force contribution identified in Equation (4.67. Under these assumptions, equiv-

[2]For example, see Åström and Wittenmark [16], pp. 178-179, or Franklin *et al.* [61], pp. 555-556.

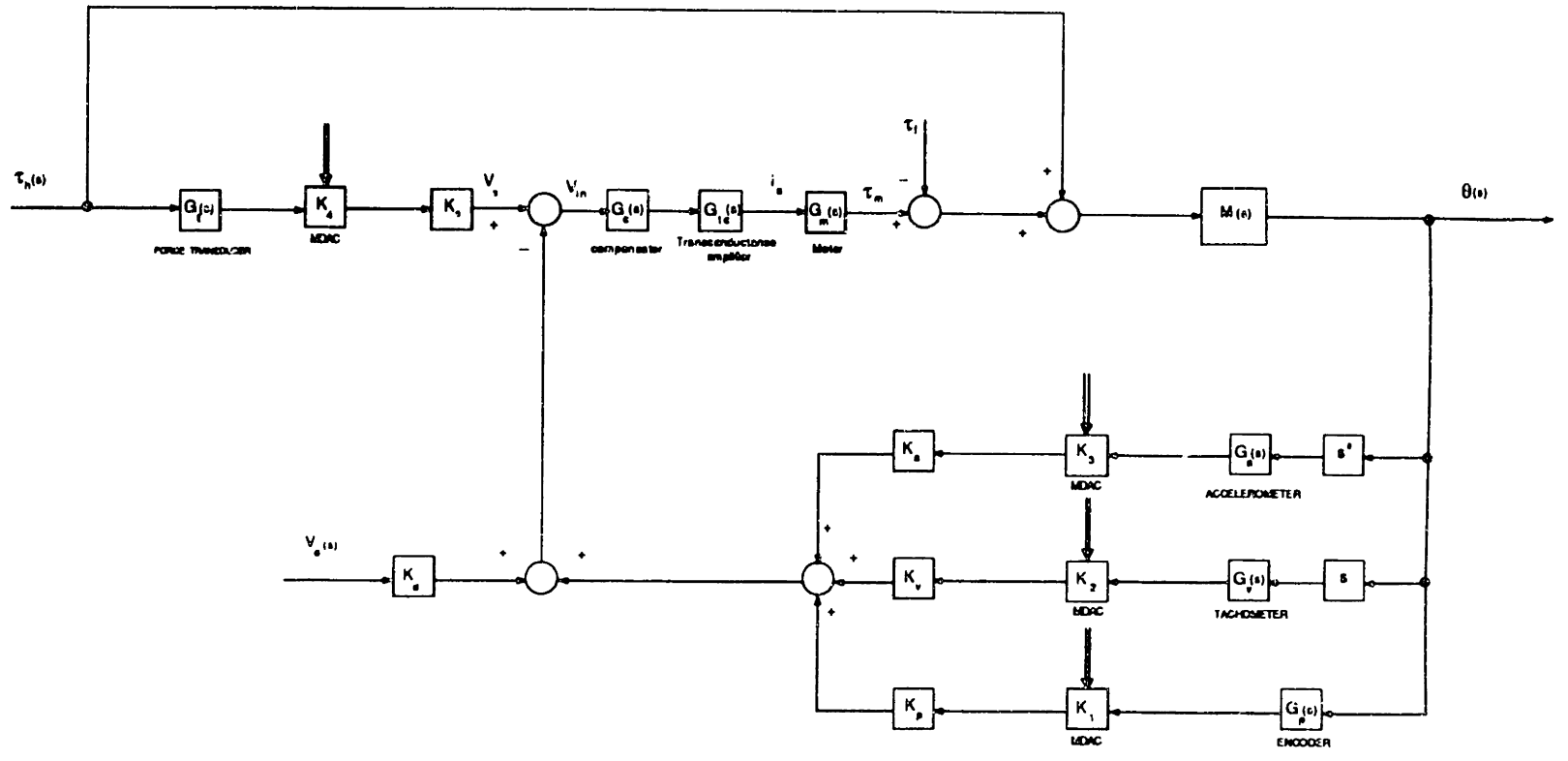

Figure 5.1: Joint axis impedance controller block diagram. See text for details.

alent torque transducer outputs are approximated by multiplying the F_{t_1} and F_{t_2} force transducer outputs by the handle shaft length R_o. These equivalent torque transducers are denoted as $G_t(s)$ in Figure 5.1.

The major mechanical hardware and related components, described in Chapter 4, are present in the forward path of the block diagram illustrated by Figure 5.1. These include the notch filter compensator, $G_c(s)$, transconductance power amplifier, $G_{tc}(s)$, motor, $G_m(s)$, and the manipulandum linkage $M(s)$. For the sake of modelling the controller implementation, the manipulandum linkage is treated as a single lumped inertia, I_m. Linkage compliance is not incorporated into the model at this point because mechanism resonances occur at frequencies well above the content of torque (*i.e.*, force) input from the operator/subject's hand, τ_h. In addition, all friction in the linkage is included as motor friction, τ_f. It is also assumed here that all of the manipulandum inertia and friction resides proximal to (*i.e.*, below) the torque (force) transducer site.[3]

The paths from the kinematics and torque transducers back to the power amplifiers all transmit analog signals. K_p, K_v, K_a, and K_t, respectively, are constant pre-adjusted gains in the displacement, velocity, acceleration, and torque (force) signal lines. All the dynamic effects associated with transducer conditioning are included in $G_p(s)$, $G_v(s)$, $G_a(s)$, and $G_t(s)$ themselves. Different controller feedback gains are programmable through the variable attenuation blocks: K_1, K_2, K_3, and K_4.

These individual attenuation blocks are implemented with multiplying digital-to-analog converters (MDACs), in a configuration described by Abul-Haj [5]. The individual MDAC (Analog Devices, Inc., Norwood MA; part no. AD7545LN) has an attenuation range of zero to unity, with a 12 bit resolution. A thirteenth bit is used to toggle circuitry that either inverts or maintains the sign of the attenuated signal. The MDACs are programmed via the digital output port of the host computer and include internal latching so that the most recent attenuation command is saved until the next update. While the programmed gains are discrete valued, *i.e.*, incremental due to fixed integer digital set-

[3]Strictly speaking this is not true. The inertia of the spherical handgrip is located distal to (*i.e.*, above) the force transducer.

tings, the MDAC output, like its input, is a continuous analog signal, and as such is not prone to the lag problems caused by the sample-and-hold phenomena of purely digital control.[4] In many applications where controller gains do not require precise updating at frequent intervals, the MDACs can be left at their previously latched settings while the host computer calculates subsequent attenuation values. In particular, when simple constant gains are required, the MDACs may only need to be programmed once, at the outset of an experiment, thereby completely freeing the host computer for other tasks.

Having described the individual components of the controller, the single axis block diagram of Figure 5.1 can be simplified by grouping the various blocks. The elements associated with the transducers become

$$H_p(s) = K_1 K_p G_p(s) \tag{5.36}$$

$$H_v(s) = K_2 K_v G_v(s) \tag{5.37}$$

$$H_a(s) = K_3 K_a G_a(s) \tag{5.38}$$

$$H_t(s) = K_4 K_t G_t(s) \tag{5.39}$$

The electromechanical portion of the single axis system, from the notch filter compensator through the motors, is characterized by

$$H_m(s) = G_c(s) G_{tc}(s) G_m(s) \tag{5.40}$$

The system, reduced by employing Equations (5.36) through (5.40), is depicted by the simpler block diagram in Figure 5.2. The elements of the block diagram, evaluated at unity gain (*i.e.*, zero attenuation) MDAC settings are listed in Table 5.1. Higher frequency dynamic effects due to transducer signal conditioning filters and actuator and

[4] Abul-Haj [5] equates the MDAC operation with a continually updatable linearization process, which offers a first-order linear approximation to general functions, as opposed to the zeroth order approximation of the zero-order sample-and-hold common to most digital feedback systems.

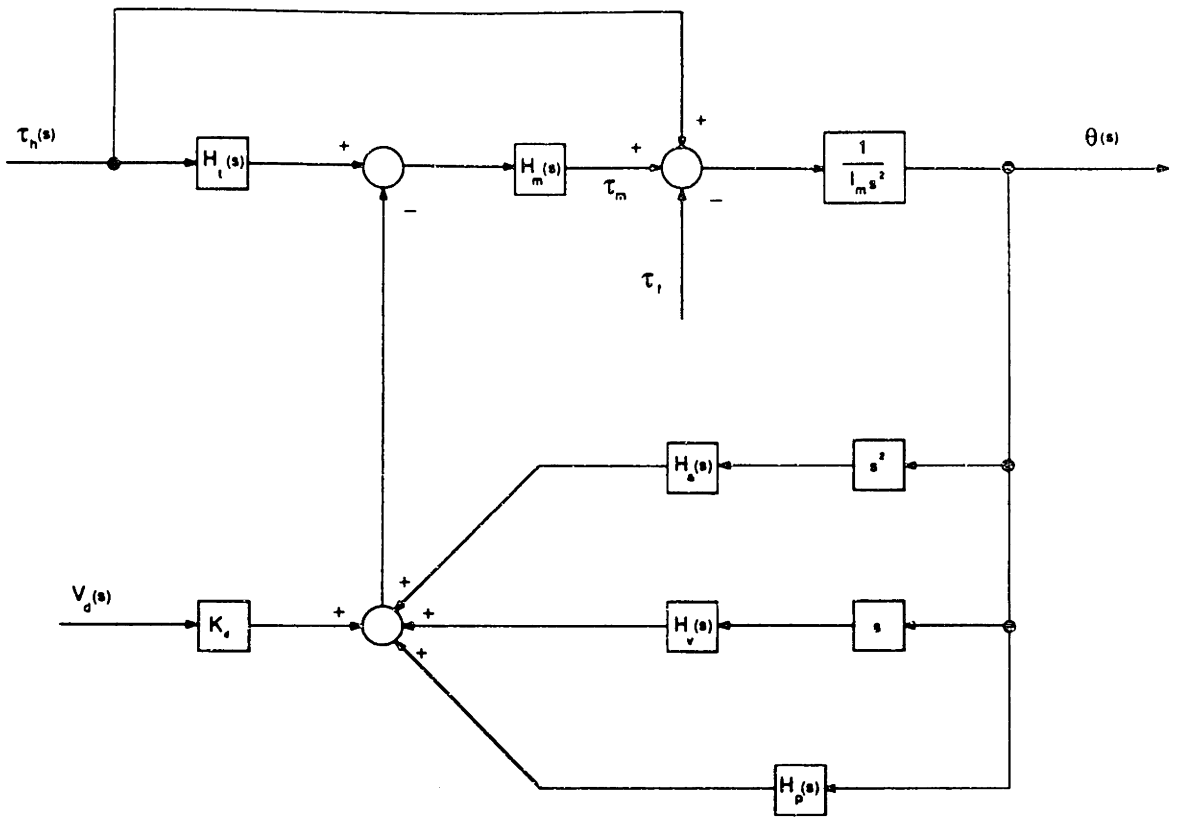

Figure 5.2: Joint axis impedance controller: reduced block diagram. See text for details.

sensor bandwidths are ignored. In addition, K_p, K_v, K_a, and K_t were trimmed precisely in the controller circuitry to ensure equal gains in both axes for each of H_p, H_v, H_a, and H_t.

From the block diagram in Figure 5.2, the position of the handle, $\theta(s)$, is given by:

$$(1 + H_t H_m)\tau_h(s) - K_d H_m V_d(s) - \tau_f = \left[(I_m + H_a H_m)s^2 + H_v H_m s + H_p H_m\right]\theta(s) \qquad (5.41)$$

where V_d is a voltage input to the CIU received from the host computer D/A port, representing a reference (or virtual) trajectory. V_d can also be thought of as a source of

Parameter	Units	Axis 1	Axis 2
H_p	V/rad	25.5	25.5
H_v	V/(rad-s^{-1})	1.47	1.47
H_a	V/(rad-s^{-2})	0.00794	0.00794
H_t	V/(N-m)	0.737	0.737
H_m	(N-m)/V	9.2	8.6
I_m	kg-m^2	0.018	0.018

Table 5.1: Reduced block diagram parameter values. Refer to Figure 5.2

perturbations or other disturbances to the hand.

Simplifying further by defining spring, damper, and inertia simulation terms,

$$K = H_p H_m \tag{5.42}$$

$$B = H_v H_m \tag{5.43}$$

$$I = H_a H_m \tag{5.44}$$

a dimensionless torque feedback gain,

$$G = H_t H_m \tag{5.45}$$

and a perturbation torque that results from the reference trajectory voltage input,

$$\tau_p(s) = K_d H_m V_d(s) \tag{5.46}$$

Equation (5.41) can be restated as

$$\tau_h(s) = \left[\frac{(I_m + I)s^2 + Bs + K}{(1+G)}\right]\theta(s) + \frac{\tau_p(s)}{(1+G)} + \frac{\tau_f}{(1+G)} \tag{5.47}$$

In principle, from Equation (5.47), K can contribute positive (resistive) or negative spring forces; B can result in positive (dissipative) or negative (destabilizing) viscous damping; and I can either augment or decrease the passive device inertia I_m. The $(1+G)$ term, denoting the effects of torque feedback, modifies not only the other controlled settings K, B, I, and τ_p, but can also alter perceived linkage friction and inertia. The role of the controller variables K, B, I, and G in modulating the mechanical "feel" of the manipulandum handle was verified experimentally and is reported in the next section.

5.3 Simulated Mechanical Loads

5.3.1 Stiffness

The capability of the powered manipulandum to simulate the "feel" of spring loads was tested one axis at a time. During each test, the joint space controller parameter K [Equation (5.47)] of the axis being examined was set to a constant, while the K of the other axis, and the remaining controller parameters, B, I, and G, of both axes were kept at zero. Stiffness was quantified from the instantaneous torque—measured by the force transducer—and motor shaft angle monitored as the handle was manually displaced. To minimize unmeasurable couples during these tests, the spherical handgrip was removed and the handle was grasped directly at the force transducer "decoupler" collar shown in Figure 4.13.[5] All handle motions were slow and regular to reduce acceleration and minimize inertial effects.

Typical data collected from the stiffness tests are presented in Figure 5.3 as plots of motor shaft angle versus the torque calculated from force measured at the top end of the handle linkage. At lower spring constant settings, the effects of friction are apparent in the separate torque-displacement trajectories for forward and backward handle motion. At higher stiffness settings, clipping due to actuator saturation is evident.[6]

[5]Refer to the discussion on minimizing applied moments at the begining of of Section 4.6.1.

[6]Recalling the comments on pancake armature motor torque ripple in Section 4.3, it is interesting to note that no ripple was palpably evident at the manipulandum handle while conducting the stiffness tests. The absence of discernible torque fluctuations consistent with the spatial distribution of the 153 commutator bars on the motor armature in the plots of Figure 5.3 further attests to the smoothness of

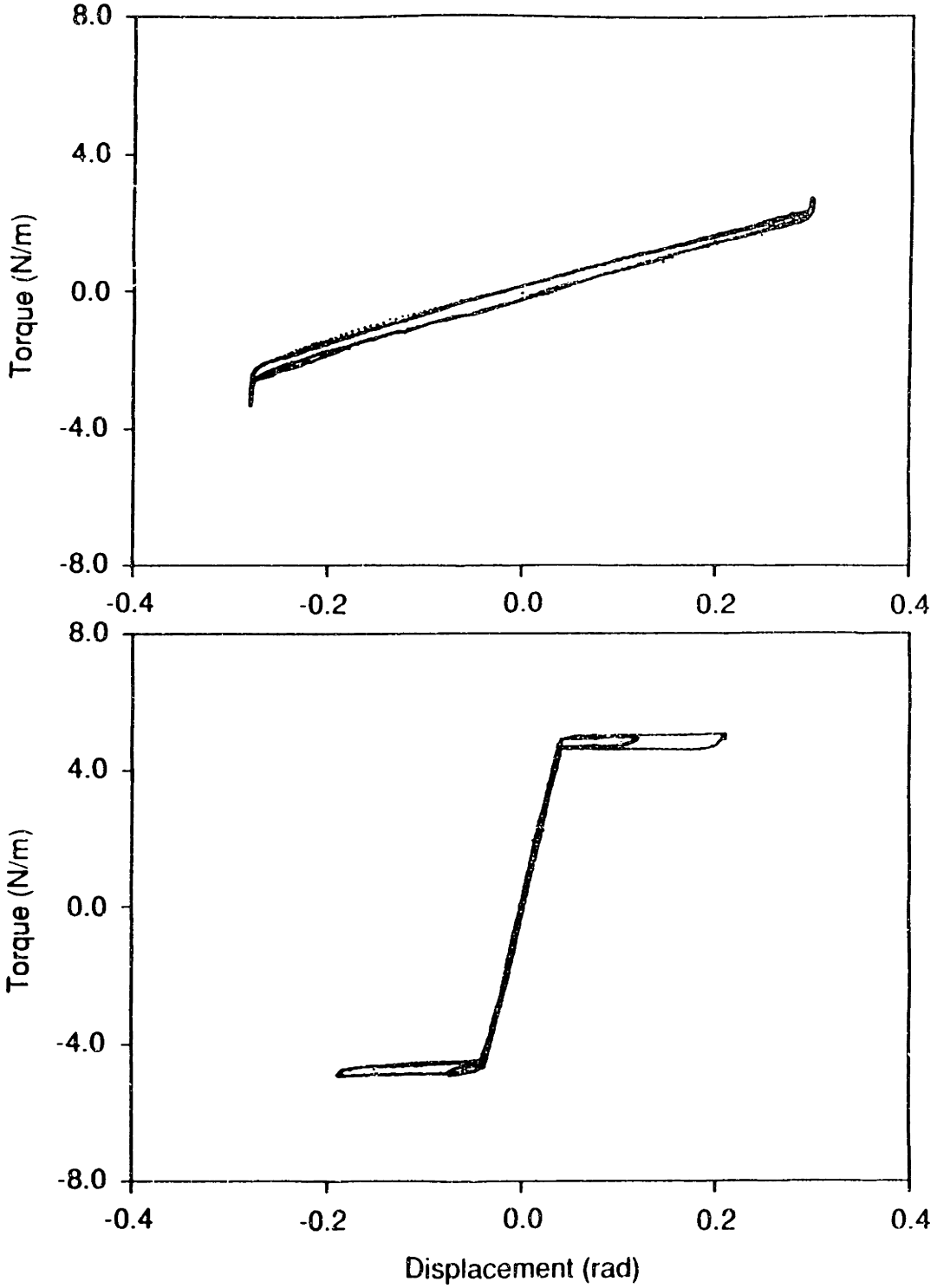

Figure 5.3: Torque versus angular displacement for low, K = 7.5 (N-m)/rad, (*top* plot), and high, K = 117.6 (N-m)/rad, (*bottom* plot) stiffness spring simulations about axis 1. The inflections at the extreme displacements in the low stiffness test are caused by the increased resistance encountered as the handle shaft abuts against the edges of the cutout in the gimbal cover (see Figure 4.10. The gap in the center of the low stiffness plot indicates the difference between resistive force for motion in one direction (*i.e.*, increasing angle) versus motion in the opposite direction (*i.e.*, decreasing angle) due to Coulomb friction. The torque plateaus in the high stiffness case are caused by actuator saturation.

Prior to analysis, saturated torque and displacement readings were eliminated from each data set, and all individual torque values were corrected for friction effects by either adding or subtracting a 0.25 N-m friction constant (see Section 4.6.1), depending on the instantaneous velocity direction. The simulated spring stiffnesses from these tests during which the handle was repeatedly moved back and forth were quantified from the slopes of linear regression analyses of torque against displacement—*i.e.*, torque as the dependent variable. The results of the regressions for both axes, averaged from three individual tests at each joint controller setting (*i.e.*, K_1 MDAC gain), are reported in Table 5.2 along with the corresponding theoretical stiffness prediction from Equations (5.36), (5.40), and (5.42). The correlation coefficient associated with each individual regression calculation was always greater than $R^2 = 0.990$, and typically above $R^2 = 0.995$, indicative of the linearity of corrected torque-displacement relation.

K_1	Axis 1		Axis 2	
Setting	Theory	Measurement	Theory	Measurement
0.031	7.3	7.5 ± 0.4	6.8	7.4 ± 0.2
0.063	14.6	15.2 ± 0.2	13.7	14.3 ± 0.4
0.125	29.2	28.2 ± 0.3	27.4	28.0 ± 0.8
0.250	58.3	58.4 ± 1.2	54.8	55.9 ± 2.0
0.375	87.5	90.5 ± 1.5	82.2	83.2 ± 0.6
0.500	116.6	117.6 ± 4.0	109.6	113.1 ± 3.8
0.625	145.7	145.1 ± 4.1	136.9	136.6 ± 2.5
0.750	174.9	169.1 ± 6.9	164.3	164.9 ± 4.1
0.875	204.1	199.6 ± 3.3	191.7	193.2 ± 2.2
1.000	233.2	227.8 ± 4.8	219.1	220.0 ± 3.9

Table 5.2: Theoretically predicted and experimentally measured rotary stiffness about each axis in (N-m)/rad units as a function of MDAC setting K_1. Each "measurement" value is reported as the mean ± s.d. of regression slopes of torque versus angular displacement data from three experiments at the same MDAC setting.

Recalling lumped parameter model condition #1 from Figure 4.16, it should be noted that the electromechanically simulated springs described here, in effect, are situated

the pancake motors' output.

between the rotor inertia, I_r, and ground. Thus, the compliance felt at the handle during these tests results from the series combination of the simulated springs with k_f and k_x of the lumped parameter model. The combined stiffness for the maximum simulated spring constants[7] in Table 5.2 in series with the passive handle mechanism compliances, corresponds to 136 and 105 (N-m/rad) about axes #1 and #2 respectively, down from 228 and 220 (N-m/rad). Converting to the translational spring equivalent for the 0.229 m handle shaft length, these constants are respectively 3100 and 2000 N/m (17.7 and 11.4 lb/in) in the y and x directions.

The stiffness of the simulated springs resulting from proportional position feedback also determines the positioning bandwidth of the system for that controller setting. Resonant frequencies *measured* with the stiffest simulated spring constants, indicative of the maximum positioning bandwidth under linear analog control, were 15.6 and 15.0 Hz respectively for axes #1 and #2. These values are in close agreement with predictions made for the lumped parameter model of Figure 4.15 when the maximum stiffness simulated springs were included between inertia I_r and ground.

Negative spring simulations which cause the manipulandum handle to behave unstably, toppling over upon power-up if not held in place, were also explored. Under this type of control, grasping the handle gives a sensation akin to balancing an inverted pendulum. Formal verification of negative stiffness settings, however, was not carried out because of the difficulty of safely following the same test protocol used to examine the positive (resistive) springs.

5.3.2 Damping

The capabilty of the manipulandum to simulate viscous damping loads was verified in a manner similar to the spring tests. The damping parameter B [Equation (5.47)] of the axis under examination was set to a constant value, while the B of the other axis, and the K, I, and G variables of both joint controllers were zeroed. Again, the handle

[7]Note that these are the highest stiffness values obtainable with the analog controller as configured. Stiffer simulated springs are still possible with digital feedback.

linkage was moved back and forth manually by grasping the force transducer decoupler collar. In these tests, though, handle motion was quickened to achieve a wider range of velocities.

Typical data representing the damping tests are shown in Figure 5.4 as plots of equivalent motor shaft torque, calculated from force transducer measurements, versus shaft angular velocity. Friction is visible in the low damping torque-velocity trajectory as the crook near zero velocity. At higher damping levels, actuator saturation effects are evident as a clipping effect.

The damping constants for each of the repetitive motion tests was determined from linear regressions of torque against velocity after all data were corrected for direction dependent friction effects and torque saturation. The results of the regression analyses, averaged from three individual tests at each joint controller damping setting (MDAC attenuation K_2), are presented in Table 5.3 along with the corresponding damping levels predicted theoretically from Equations (5.37), (5.40), and (5.43). Correlation coefficients, R^2, associated with these regressions were slightly lower than those in the stiffness tests, but still typically between 0.95 and 0.99. These lower R^2 values were attributed to heightened inertial effects associated with the faster back-and-forth motion during these tests.

K_2	Axis 1		Axis 2	
Setting	Theory	Measurement	Theory	Measurement
0.031	0.42	0.40 ± 0.03	0.39	0.38 ± 0.02
0.063	0.84	0.84 ± 0.04	0.79	0.78 ± 0.02
0.125	1.68	1.65 ± 0.04	1.58	1.50 ± 0.05
0.250	3.36	3.25 ± 0.14	3.16	3.07 ± 0.14
0.375	5.04	5.04 ± 0.08	4.73	4.61 ± 0.12
0.500	6.72	6.75 ± 0.10	6.31	6.16 ± 0.29

Table 5.3: Theoretically predicted and experimentally measured rotary damping about each axis in units of (N-m)/(rad-s^{-1}) as a function of MDAC setting K_2. Each "measurement" value is reported as the mean ± s.d. of regression slopes of torque versus angular velocity data from three experiments at the same MDAC setting.

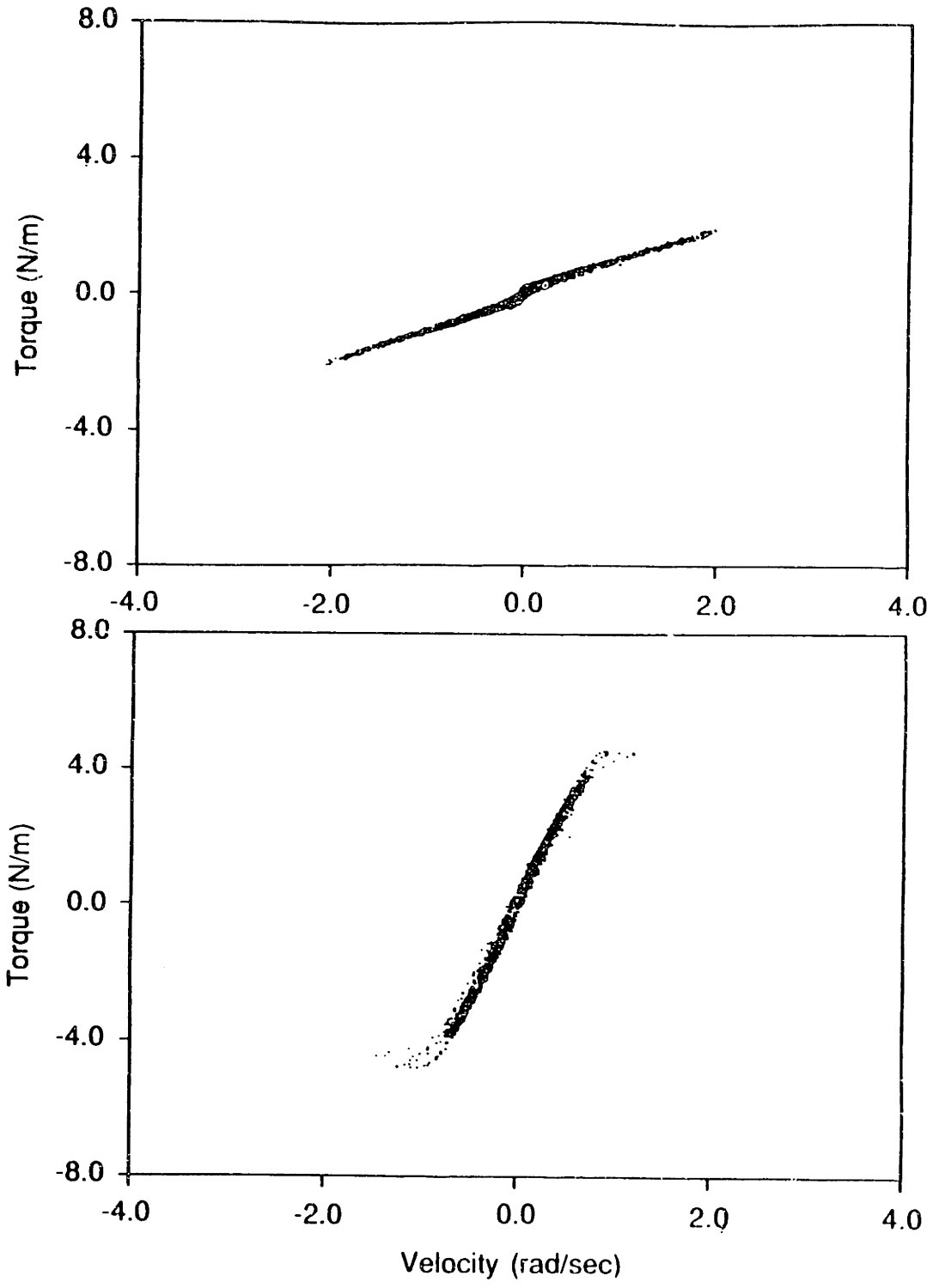

Figure 5.4: Torque versus angular velocity for low, $B = 0.84$ (N-m)/(rad-s^{-1}), (*top* plot), and high, $B = 5.05$ (N-m)/(rad-s^{-1}), (*bottom* plot) viscous damping simulations about axis 1. The crook near the origin in the low damping plot is due to linkage friction. The torque clipping in the high damping case are due to actuator saturation.

The highest simulated damping value at which the manipulandum could be operated corresponded to MDAC settings of $K_2 \simeq 0.5$, as indicated by Table 5.3. Higher gain settings triggered a vibratory instability at approximately the frequency of the handle linkage's first resonant mode (50 to 60 Hz). The source of this instability appeared to be tachometer ripple—similar oscillations were detected when the handle and gimbal mechanism was detached from the motors, leaving only the structurally stiff rotor in the velocity feedback loop. Nonetheless, given the passive handle inertia I_m and the stiffest simulated springs, even with this stability limit, viscous damping levels in excess of the critical value ($\zeta = 1.0$) were still achievable.

Several destabilizing negative damping settings, which caused the manipulandum handle and coupled human arm to oscillate wildly, also were examined briefly. An extensive tabulation of manipulandum performance in this operating regime was precluded by safety considerations.

5.3.3 Inertia

Rather than manually pushing the handle linkage back and forth at the force transducer as in the stiffness and damping tests described above, a non-contacting method was employed to verify the inertia simulation capabilities of the manipulandum system.[8]

In these tests, a moderate non-saturating spring, corresponding to $K_1 = 0.0625$, centered in the upright position, was simulated for the axis under examination. An initial transient was applied manually to this axis by drawing the handle shaft (with the spherical grip in place) away from the spring center location and then releasing it. The frequency of the die-away oscillatory response for each test was then counted from the shaft velocity record and compared with a prediction based on the measured stiffness and an estimate of the combined inertia ($I_m + I$) of Equation (5.47), where I was derived from Equations (5.38), (5.40), and (5.44). Each axis was tested separately—K and I

[8]The manually forced motion method used in the stiffness and damping tests was abandoned because of the noisier appearance of plotted acceleration data when compared with the position, and velocity records from the previous tests. The linear regression results for the simulated inertia trials utilizing this method, however, did closely match the theoretical inertia predictions.

were always set to zero for the joint axis not being studied. Also, damping B and force feedback gain G were zeroed in both axes throughout the inertia tests.

The damping ratios observed for all transient response decay envelopes were very low; hence, measured damped oscillatory frequencies were assumed to equal the natural frequencies in each case. Also, since the simulated springs were significantly more compliant than the passive mechanism components (specifically the flexible couplings), the inertia of the handle mechanism, I_m, was treated as a single lumped value. Measured oscillatory frequencies averaged from four tests are compared with theoretical predictions for axes #1 and #2 in Tables 5.4 and 5.5, at the stated stiffness values, over a range of K_3 inertia settings. The maximum $K_3 = 0.375$ setting reported in the tables corresponds to the stability limit encountered for the augmented inertia simulations. One possible cause of the instability, as mentioned at the end of Section 4.5.3, is the very underdamped response characteristic of the accelerometers, the source of the signals used for inertia simulation. A detailed analysis to confirm this conjecture or to identify other potential causes of instability, however, was not performed.

The human operator's perception when manually accelerating the handle for the tabulated range of stable inertia settings, with or without the simulated spring in place, is clearly one of augmented inertia.[9] The range of stable inertias listed in Tables 5.4 and 5.5 are equivalent to point masses of 0.34 to 0.86 kg (0.76 to 1.9 lb) at the end of a massless rod with the length of the manipulandum handle shaft.

Setting $I < 0$ with positive acceleration feedback reduced perceived inertia without diminishing other intrinsic passive manipulandum properties, such as friction. Stable behavior in this feedback regime, with the human operator's hand coupled to the handle, was observed for $-0.125 < K_3 < 0$—the maximum magnitude corresponding to a fifty percent reduction of I_m. The comparison of measured versus predicted natural frequency, was not followed through for negative K_3 values.

[9] As an aside, it was noted from the informal comments of naïve operators that many were confounded by their expectation that inertia ought to be perceived as weight, which, of course, it is not.

K_3	Inertia ($kg - m^2$)	Natural Frequency (Hz)	
Setting	Theory	Theory	Measurement
0.0	0.018	4.6	4.7 ± 0.07
0.031	0.020	4.4	4.4 ± 0.04
0.063	0.023	4.1	4.1 ± 0.01
0.125	0.027	3.8	3.8 ± 0.03
0.250	0.036	3.3	3.3 ± 0.02
0.375	0.045	2.9	2.9 ± 0.03

Table 5.4: Theoretically predicted and experimentally measured natural oscillatory frequencies at different simulated inertia settings K_3 combined with a simulated spring stiffness of $K = 15.2 \frac{N-m}{rad}$ for axis #1.

K_3	Inertia ($kg - m^2$)	Natural Frequency (Hz)	
Setting	Theory	Theory ‡	Measurement
0.0	0.018	4.5	4.6 ± 0.06
0.031	0.020	4.3	4.3 ± 0.03
0.063	0.023	4.0	4.1 ± 0.02
0.125	0.026	3.7	3.8 ± 0.06
0.250	0.035	3.2	3.2 ± 0.03
0.375	0.044	2.9	2.9 ± 0.00

Table 5.5: Theoretically predicted and experimentally measured natural oscillatory frequencies at different simulated inertia settings K_3 combined with a simulated spring stiffness of $K = 14.3 \frac{N-m}{rad}$ for axis #2.

5.3.4 Force Feedback

As discussed at the end of Section 5.2.3, force feedback—more appropriately *torque* feedback in this case, since the load simulating controller is implemented in joint axis coordinates—has the ability to modify the perceived mechanical characteristics of the handle linkage. When H_t is set positive in Equation (5.45), the denominator dividing the right hand side of Equation (5.47), $(1 + G)$, is greater than unity. Thus, it has the effect of attenuating properties that are physically enclosed within the loop between the force transducer and the motor.[10] These properties include the passive mechanism inertia and friction, as well as the simulated load settings, K, B, and I.

The effects of this attenuating feedback were explored for certain intrinsic passive mechanism properties and controlled simulated loads. As in the spring, damping, and inertia tests treated above, force feedback was examined one axis at a time. However, since the force signals to be fed back into the load simulation controller are produced by the force sensor, only situations that give rise to interface forces at the transducer can be studied. Thus, all of these tests were performed by manually driving the handle back and forth at the force transducer decoupler collar. As such, only three elements of Equation (5.47)—passive friction, controlled resistive stiffness, and dissipative viscous damping—were examined.

Tests similar to those discussed in Section 4.6.1 and illustrated in Figure 4.14, during which the friction of the unpowered manipulandum handle mechanism was quantified, were repeated at force feedback levels of $K_4 = 0.250$ and 0.375. The attenuated friction values measured at these force feedback settings were approximately 0.09 and 0.07 N-m in either axis, in agreement with predictions based on the dimensionless gains of $G = 1.686$ and 2.529 for axis #1, and $G = 1.585$ and 2.376 for axis #2, derived

[10]The role of G, as represented in Figure 5.2 by elements H_t and H_m, is that of feedforward. In effect, when $G > 0$, "positive" feedforward acts as an actively powered "assist," akin to automobile power steering or power brakes, thereby masking intrinsic mechanism dynamics and external disturbances. This attenuation of disturbances and undesirable dynamic characteristics is what would be expected if the force being applied by the actuator to its attached linkage were being servoed based on the measured interaction forces between the linkage and the external environment. Hence, the terminology "negative force feedback," utilized in robotics force control research to describe this condition, is employed here.

from Equations (5.39), (5.40), and (5.45). It was noted at these settings, although not measured, that the handle inertia "felt" significantly smaller with force feedback than without. The effect of force feedback in attenuating the feel of inertia is readily discernible in instances when the feedback is suddenly disabled while in the midst of a handle movement.

The ability to mask friction and other intrinsic mechanical properties enhances the fidelity of load simulations, as is evident upon comparing stiffness and damping with force feedback in the sample plots of Figure 5.5 against approximately equal stiffness and damping levels without force feedback in Figures 5.3 and 5.4. The reduction of friction closes up the loop in the torque-displacement (stiffness) plot and flattens the crook in the torque-velocity (damping) plot. This improvement in linearity was also reflected in higher R^2 correlation coefficients for the entire test sets of damping and stiffness with force feedback. Stiffness and damping constants, determined from linear regressions of the test data, matched predictions based on the $K/(1+G)$ and $B/(1+G)$ coefficients[11] of Equation (5.47) even more closely than the experimentally quantified and predicted values without force feedback reported in Sections 5.3.1 and 5.3.2.

The price to be paid for the more linear impedance behavior, in addition to weaker spring and damping constants because of the force feedback attenuation, is decreased stability. At the highest force feedback gain settings tested, $G = 2.529$ for axis #1, and $G = 2.376$ for axis #2, the handle vibrated even when it was free-standing and untouched by the human hand. Finger tip contact with the handgrip further increased the magnitude of the oscillations. At $G = 1.686$ for axis #1 and $G = 1.585$ for axis #2, this vibrational instabilty at the first resonant mode frequency of the handle mechanism (approximately 60 Hz in axis #1 and 50 Hz in axis #2) could be triggered by very firm two-handed grasp of the spherical grip. At the lowest settings examined, $G = 0.843$ and 0.792 for axes #1 and #2 respectively, the instability could only be induced by the rigid mechanical clamp that was used to lock the spherical grip for tests of actuator torque

[11]Force feedback gains in these tests were set to $G = 0.843$ and 1.686 for axis #1, and $G = 0.792$ and 1.585 for axis #2.

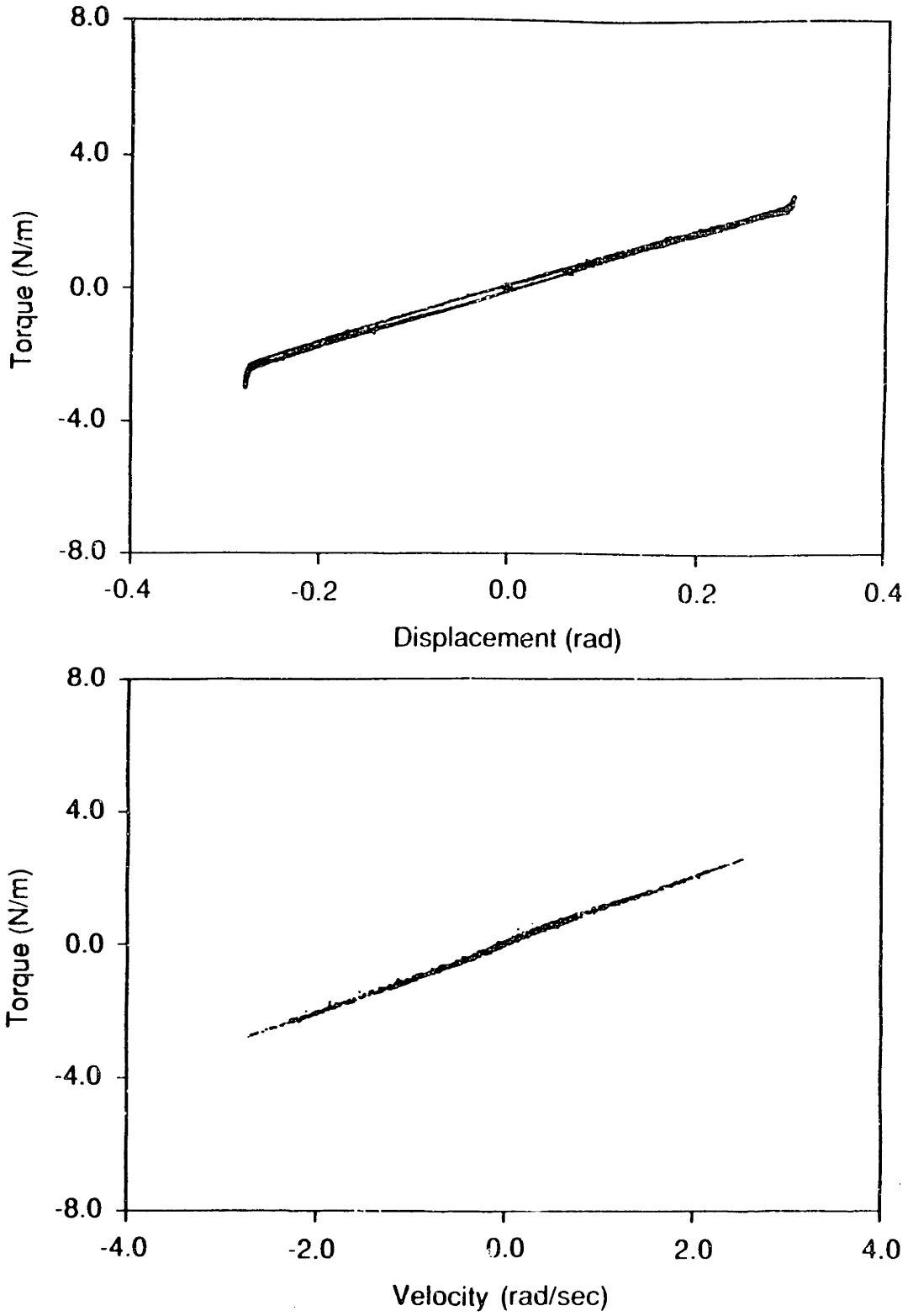

Figure 5.5: Effect of negative force feedback on simulated stiffness (*top* plot) and damping (*bottom* plot). Measured stiffness was 7.9 (N-m)/rad for settings of $G = 0.843$ and $K = 14.6$ (N-m)/rad. Measured damping was 0.91 (N-m)/(rad-s^{-1}) for settings of $G = 0.843$ and $B = 1.68$ (N-m)/(rad-s^{-1}).

capacity described in Section 4.6.1.

The instability observed here, which reduces permissible manipulandum force feedback gains as stiffer and stiffer external environments are contacted, is consonant with the tradeoff between force feedback gain and the stiffness of the environment and sensors proposed by Whitney [148] for automated assembly tasks. Analyses by Colgate [41] and Eppinger [54, 53] attribute this instabilty to the noncollocation[12] of a distal force sensor at the linkage endpoint with respect to proximal actuators at the base of the manipulandum linkage. Based on this understanding, an alternate approach to masking the manipulandum inertia, not examined as part of this work, might include feedback from both the acceleration and force transducers, especially in view of these sensors being mounted at different locations on the handle linkage.

If the sign of the K_4 MDAC attenuation is reversed to yield "positive force feedback," the denominator term in Equation (5.47), $(1 + G)$ becomes less than unity. As G is decreased to -1, both the passive linkage characteristics, I_m, τ_f, and other unmodelled dynamics, as well as the actively controlled manipulandum properties, I, B, and K, are magnified. The resistive actuator torques produced under *positive* force feedback in response to force at the handle were perceived to be substantially amplified versions of the friction and elastic wind-up depicted in Figure 4.14. Since the force transducer only senses *normal* forces and not pure torques as discussed in Section 4.5.4, couples applied to the spherical handgrip, while still causing handle motion, are not detected, and hence, are unopposed by the controller. As a result, any attempts by the subject/operator to apply an unmeasurable couple and simultaneously balance the rotary handle shaft with a transduced normal force, causes the handle to actively push the operator's hand around the work space.

When set for "positive feedback," with $G < -1$, the handle would buck violently whenever the operator contacted the spherical grip. Because of safety considerations, a detailed study of manipulandum behavior in this control regime was not undertaken.

[12]Collocation implies that the sensor and actuator are in the same location, without any intervening dynamics due to either modelled or unmodelled structural compliances in the linkage.

5.4 Virtual Object Simulation

5.4.1 Criteria for Effective "Feel"

The notion of what makes for effective "feel" in manual control interfaces (joysticks, trackballs, rotary cranks and knobs, *etc.*) has been a topic of investigation for over the last five decades. The term "feel" usually connotes the mechanical characteristics of the interface device because of their effect on the tactual and proprioceptive sensation of the human operator. Because mechanical characteristics not only trigger specific sensory feedback, but affect the mechanics of the coupled limb and external load as well, the qualities of "feel," and how realistic they seem, are essential in governing manual response so that the human operator/subject may successfully evaluate, learn, and execute motor tasks.

Poulton [110], in reviewing research into human interaction with moveable manual controllers (as opposed to rigid isometric interfaces), listed a number of mechanical traits to be avoided for such interfaces, along with others that should be included. He noted the deleterious effects of large inertia and stiction on response quickness, and of friction and backlash on manual control accuracy. In addressing accidental actuation from either "jolting" environments or "unattended" situations because of the human operator having let go of the interface, Poulton recommended spring returns and viscous damping to maintain the position of the controller.

A research plan outlined by Book and Field [28] listed telemanipulator characteristics that included innate (or simulated) mechanical linkage, actuator, and controller properties which they sought to relate to unilateral (*i.e.*, non-force-reflecting) master-slave system performance. Mechanical characteristics cited were: stiffness, inertia, friction and backlash.

In describing the manual interface to the "molecular docking" system mentioned in Section 2.3, Ming *et al.* [102] listed similar traits that degraded force display performance. The manual interface in their application, a refitted Argonne-E3 manipulator,

suffered from excessive inertia of its links and friction, backlash, and compliance in its transmission. Ming *et al.* remarked that these factors, combined with computation delays that resulted in a 3 to 5 Hz digital update rate, prevented the effective simulation of hard contact within their virtual environment.

Jex [81] described four simple tests that have been applied to evaluate the quality of simulation in "artificial control feel" devices. Successful performance of these tests, which together encompass mechanism, actuator and controller issues, is taken to indicate that the device is probably capable of simulating any load field or virtual object. Jex's tests for a "good force feel simulator" are the following:

- Under inertia and friction cancelling control, the device should feel like "a stick of balsa wood," with negligible inertia, friction, or jitter.
- When set for coulomb friction, the device should stay in place upon release by the human operator, without creep or jitter.
- When pushed up against a simulated hard stop, the device should come to an abrupt stop, and not demonstrate perceptible compliance.
- A simulated mechanical centering detent should not be excessively compliant; force reversals while traversing the detent should be crisp.

All four of these criteria must be met without external mechanical adjustment of the loading interface.

The first two criteria are related most closely to the passive *mechanical* properties of a load simulating interface, and how well these properties can be masked. In the case of the spherical-mechanism manipulandum described in this thesis, the friction of the passive uncontrolled device is sufficient to maintain position when the operator lets go of the handle, as mentioned in Section 4.6.1. The ability to negate both the friction and the linkage inertia under negative force feedback was discussed in Section 5.3.4. Reduction of inertia alone, accomplished under acceleration feedback, was treated in Section 5.3.3.

The last two criteria are somewhat more elaborate and can only be implemented by programming the load simulator to fabricate the virtual wall and detent. A factor in successfully creating both of these virtual objects is quickness of activation; as noted, the loads must be "crisp," changing the force at the human-machine interface very abruptly in both cases. This requirement clearly is a function of system bandwidth. Since these simulated objects are quite simple, computer code execution time does not pose an overwhelming burden, and the result of these tests reflects primarily the actuator and mechanical transmission fidelity in delivering the load structure commanded by the system controller. An additional consideration for the simulated wall is how hard or immovable it is, which to a large extent depends on system force capabilities.

5.4.2 Walls

The implementation of a virtual wall and a detent in the manipulandum workspace was taken on as a challenge to meet the third and fourth of Jex's criteria. The wall simulation is treated in this section; the detent in the next.

The wall is modelled simply, as a massless plate backed by a very stiff spring, K_w, with rest length α_o, in parallel with a very viscous damper, B_w, as depicted in Figure 5.6. In addition, the massless plate and the spring and damper are constrained from extending past position α_o. Thus, when the manipulandum handle is away from the wall, (*i.e.*, $\alpha > \alpha_o$), no resistance is encountered. Moving the handle to the left when $\alpha \leq \alpha_o$, increases resistive force.

The actual implementation of the wall was carried out in joint space, about axis #1, with $\alpha_o = 0$, corresponding to the handle in the upright position. The angular displacement of the handle shaft, α, was monitored continuously by the host LSI-11/23 computer, via its A/D converter, sampling at 1 kHz. For $\alpha > \alpha_o$, MDACs K_1 and K_2 on axis #1 were kept at zero. As the handle shaft crossed over to $\alpha \leq \alpha_o$, these two MDACs were switched on to make $K = K_w$ and $B = B_w$ in Equation (5.47). When the computer detected that the handle had returned to $\alpha > \alpha_o$, K and B were re-zeroed.

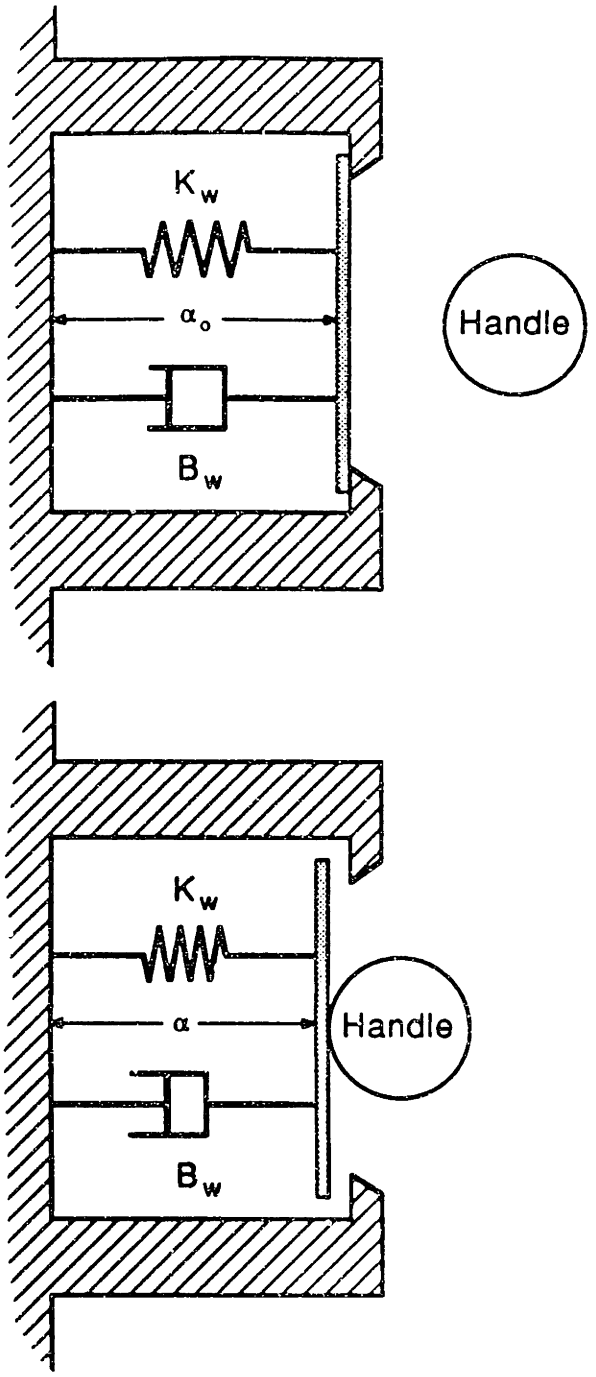

Figure 5.6: Simulated wall model. The upper figure shows the handle at position $\alpha > \alpha_o$, where α_o is the location of the wall with respect to mechanical ground. In the lower figure the handle is at $\alpha \leq \alpha_o$, in contact with the wall.

A record of displacement points for repeated impacts with the virtual wall, including one interval during which the handle was slid along the wall, is depicted in Figure 5.7 as a plot of α versus β. The corresponding plot of the torque and displacement about axis #1, along with the direction of handle travel, is shown in Figure 5.8. The peak in torque for increasing α corresponds to a sticky sensation felt as the handle was withdrawn from the wall. This "stickiness" is attributed to delay in the A/D sampled displacement signal used for the supervision of the MDAC controlled wall stiffness gains. Because of this delay, K and B were not turned off immediately upon crossing $\alpha_o = 0$, causing the restorative spring torque to keep pulling the handle back toward α_o until the MDACs were reset by the supervisor. The source of the delay was the fifth-order low pass anti-aliasing filter at the input to the A/D converter,[13] contributing a 180 degree phase lag at 22 Hz, equal to 90 msec at this frequency.

A second wall implementation, in which the input A/D displacement signal was not prefiltered, is shown in Figure 5.9. In this second implementation, where the supervisor is only delayed by the 1 msec sampling interval, the "sticky feel" is eliminated, leaving only the passive device friction upon pulling away from the wall.

Hybrid analog-digital walls, in which analog velocity feedback was combined with digital position feedback were also examined. By implementing digital position feedback, the virtual wall location α_o could be easily altered. Also stiffer walls are possible because higher K_w gains are then available. Using this hybrid feedback, a four sided virtual enclosure made of non-sticky walls was devised as a system safety measure to keep the handle linkage away from the limit switches at the edges of travel shown in Figure 4.6.

Another method of simulating walls, in which the position signal and the direction of the force at the handle were employed to switch on positive force feedback, *i.e.*, $(1 + G)$ in Equation (5.47), with $G \simeq -1$, was attempted. In principle, when the transition from $G = 0$ to $G = -1$ occurs (*i.e.*, as the simulated wall is contacted), the perceived inertia and friction of the handle would be greatly magnified, conveying the impression that the

[13]Refer to Appendix B for more details of the anti-aliasing filters.

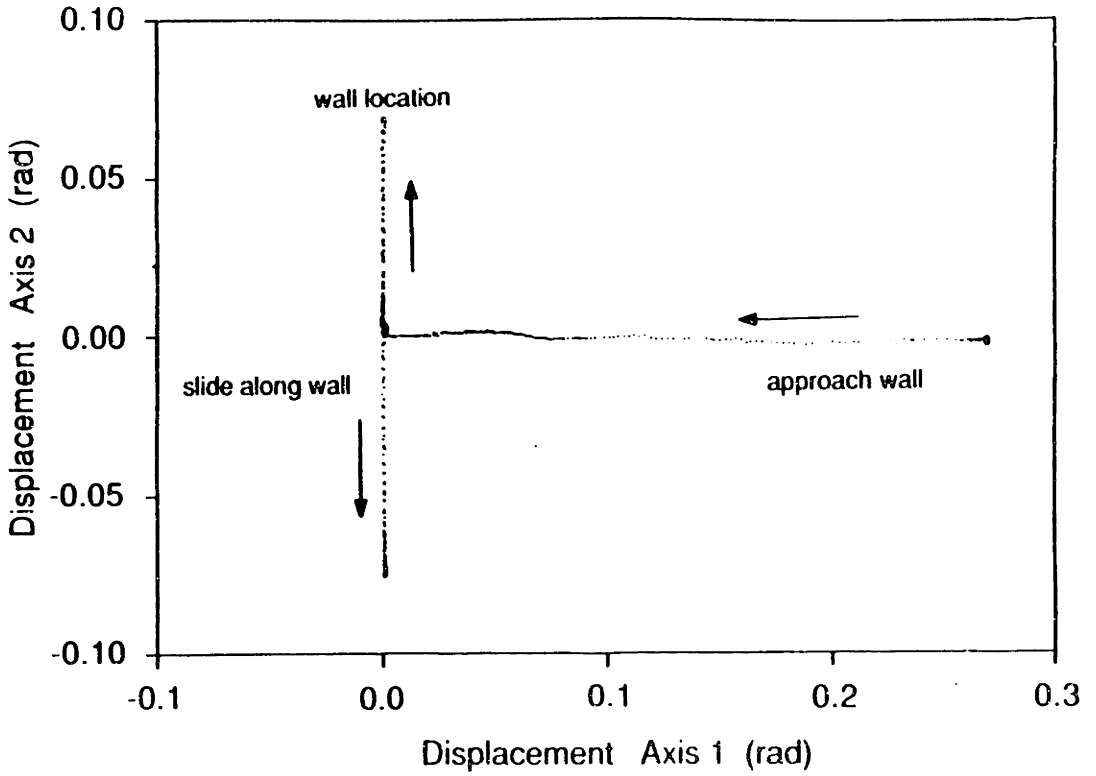

Figure 5.7: Simulated wall performance—α versus β displacement. The crossplot shows the two dimensional handle position as it moves toward and then slides along the wall.

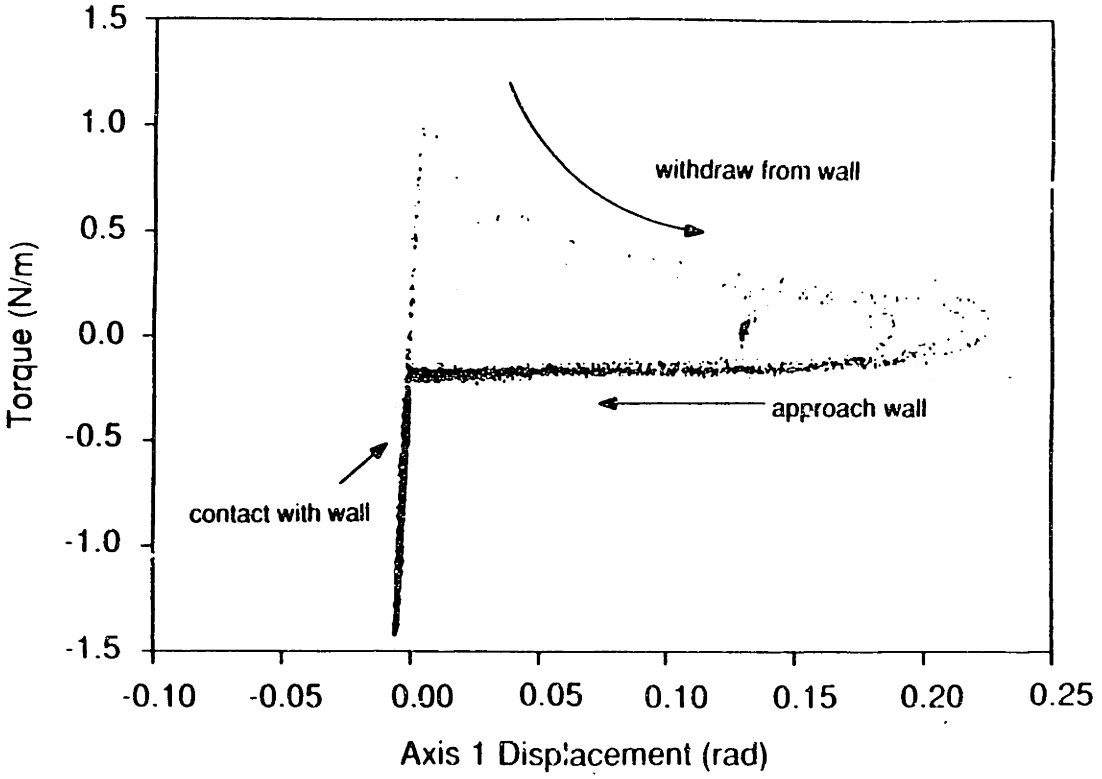

Figure 5.8: Simulated wall performance—torque versus displacement with supervisor lag. The plot shows the torque measured by the force transducer as the handle approached, contacted, and rapidly withdrew from the wall over repeated cycles. The torque level above zero indicate a "sticky" elastic torque that attracts the handle back to the wall. The difference in torque for approach and withdrawal motion far away from the wall is due to directionally dependent coulomb friction.

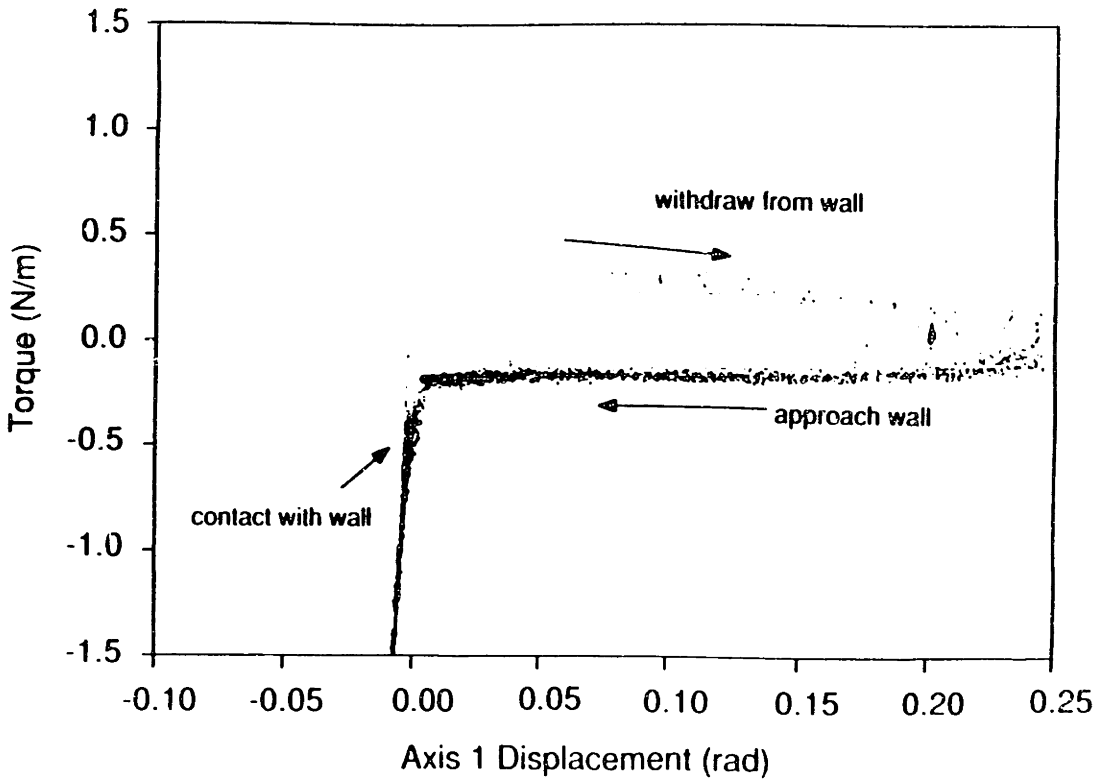

Figure 5.9: Simulated wall performance—torque versus displacement without supervisor lag. The plot shows the torque measured by the force transducer over repeated cycles as the handle approached, contacted, and rapidly withdrew from the wall, this time *without* the lag introduced by the anti-aliasing filters. Note that the absence of the torque peak associated with wall "stickiness" leaves only the difference in torques due to directionally dependent friction.

hand had encountered a massive object that could not slide because of high frictional resistance. Satisfactory performance was not achieved with this method, however, because of the force transducer's inabilty to sense the pure moments that still could still cause handle motion. In effect this transducer shortcoming made it possible to pass through α_o without triggering the wall, as well as to continue moving *inside* the wall by continuing to apply unmeasured pure moments. A solution to this problem would be a more general transducer capable of sensing *all* relevant forces *and* moments.

5.4.3 Detents

The virtual mechanical detent is modelled in two degrees of freedom as a spring loaded ball plunger that moves with the bottom of the handle shaft and a flat-bottomed indentation with sloping sides fixed in the the manipulandum reference frame at $\alpha = \beta = 0$, as illustrated in Figure 5.10. When the center of the plunger ball passes over the edge of the indentation, the spring force causes the ball to be pushed into the indentation, locking the handle shaft at the $\alpha = \beta = 0$ position. The resistance that opposes te handle when breaking out of the detent depends on the steepness of the sides and the depth of the indentation. Backlash about the center of the detent is adjustable by changing the size of the flat bottom of the indentation.

How the virtual detent is implemented is depicted schematically in Figure 5.11 for one of the axes (α). Away from the detent zone, no action is taken by the load control supervisor. When either $-\alpha_2$ or $+\alpha_2$ are crossed from the outside, the supervisor switches on a digital spring simulation with stiffness K_d and a reference position at either $-\alpha_1$ or α_1, depending on whether α is negative or positive, thereby drawing the handle toward the center zone. Analog damping, B_d, is also switched on to partially smooth out the abrupt transitions. Upon crossing $-\alpha_1$ from $-\alpha_2$, or α_1 from α_2, the spring and damper are shut off, leaving the handle in the center zone about α_o. In moving away from the center to the outside region, the opposite route must be taken, requiring that the spring region be broken through. In this implementation, the size of the center dead zone, $2\alpha_1$,

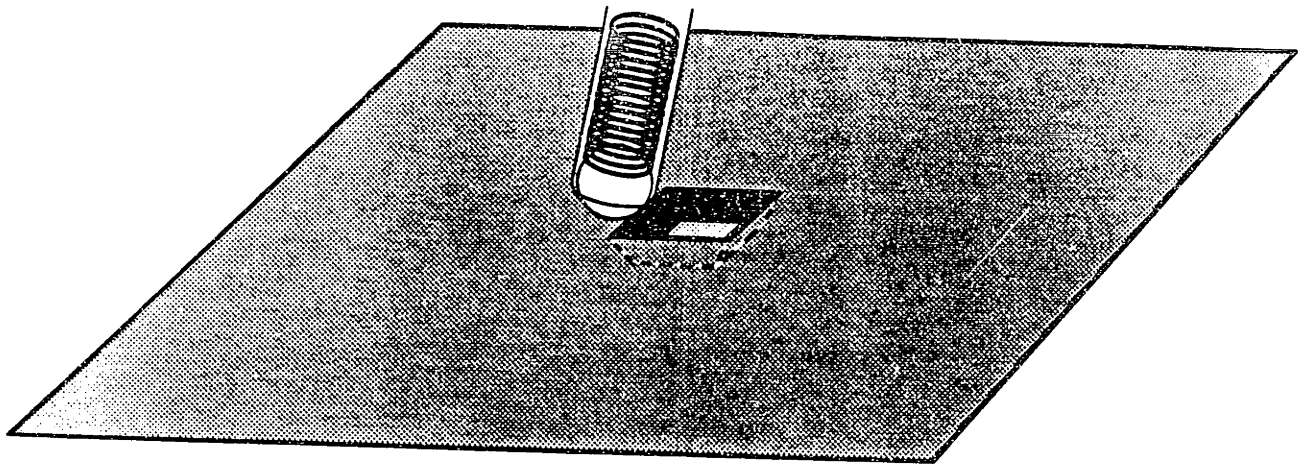

Figure 5.10: Spring loaded detent model. See text for details.

the width of the spring region, $|\alpha_2 - \alpha_1|$, the detent spring stiffness, K_d, and the damping viscosity B_d can all be adjusted. The implemetation of the detent for the other axis (*i.e.*, β) is treated identically.

The detent simulation was tested successfully at supervisor update rate in excess of 1 kHz. The simulated detent acted to grab the handle once the detent zone was entered and then pulled the handle to center and held it in place. Freeing the handle from the simulated detent required applying effort at the handgrip to overcome the simulated centering spring until the handle broke out of the zone. All transitions upon being captured by the detent and, after, when breaking free, were distinctly palpable and felt crisp as demanded by Jex's "good force feel simulator" criteria.

Figure 5.12 depicts a sample record of torque versus angular displacement for one of the axes (α) as the detent is approached and the handle and operator's hand is drawn in to the detent center zone, followed by a break-out from the zone on the opposite side.

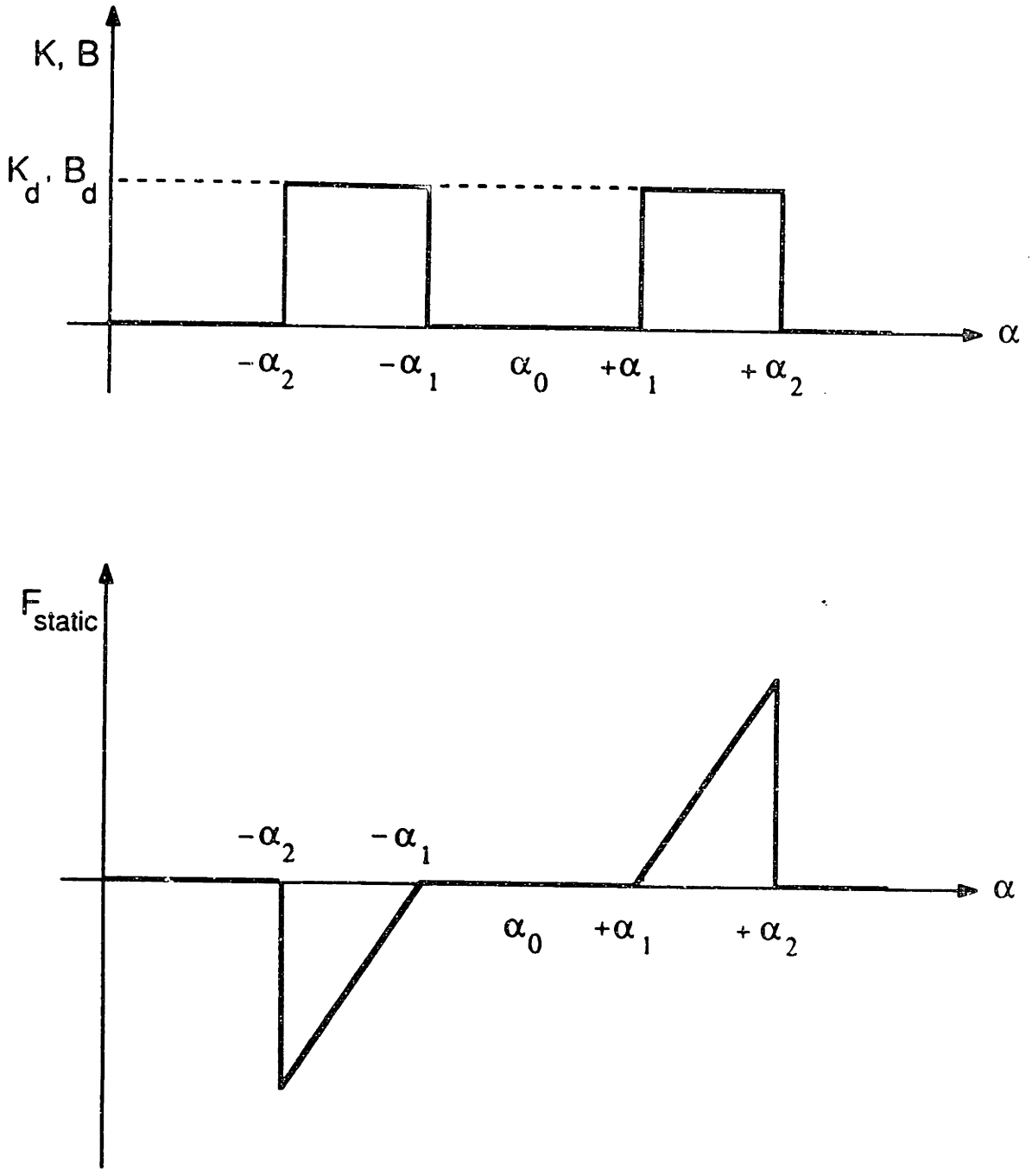

Figure 5.11: Detent implementation for the α axis. The β axis is treated identically. *Upper figure*) The load control supervisor changes stiffness K and damping B from zero to K_d and B_d respectively upon entering the detent zone. The stiffness and damping are inactive for $|\alpha| \leq \alpha_1$ in the center region about α_o, and when $|\alpha| \geq \alpha_2$. Note that this K,B profile is in effect only when the β axis is within its detent region, *i.e.*, $|\beta| \leq \alpha_2$ for a square detent. *Lower figure*) The static force on the handle (*i.e.*, forces due to the spring action only) versus position, for the K versus position profile in the upper figure, shows the action of detent walls in returning the handle to the center region.

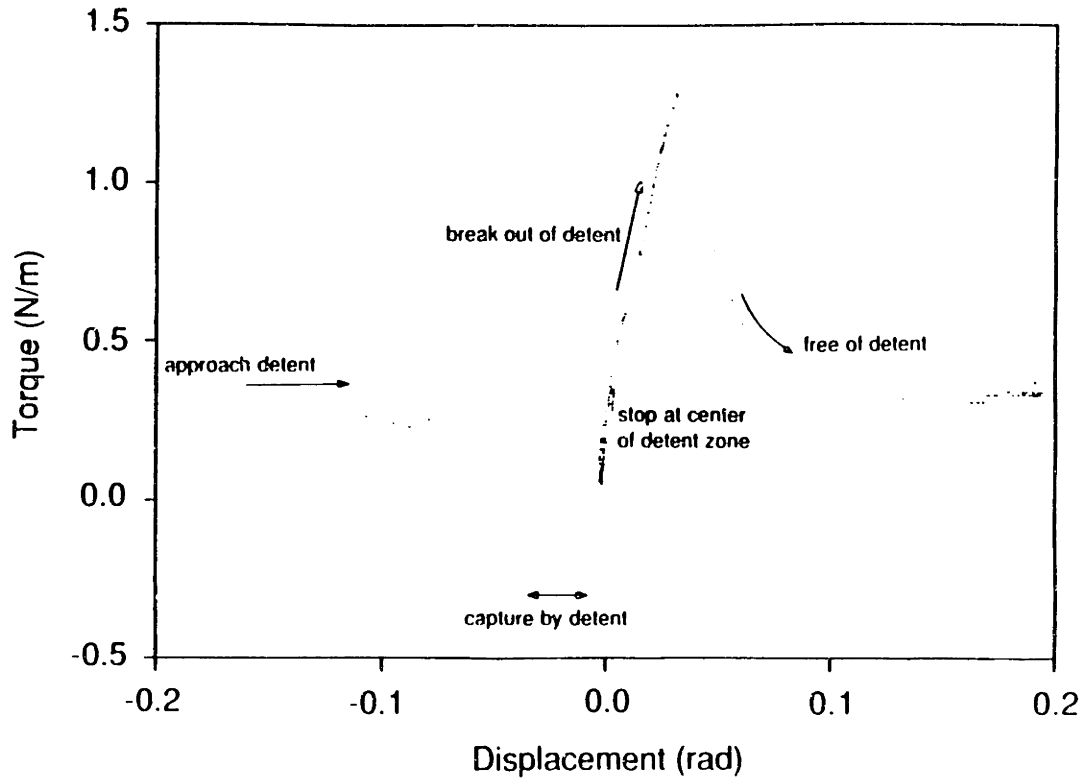

Figure 5.12: Detent performance: handle torque versus displacement in the α axis when the β axis is in its detent region, *i.e.*, $|\beta| \leq \alpha_2$. The handle, being moved in the direction of increasing displacement, first is captured by the detent and drawn to the center, where it comes to a stop. The handle is then pushed through increasing resistive spring force until it breaks free of the detent on the other side.

5.5 Safety

The safety of human-machine interaction was as much a concern in the development of the manipulandum as its ability to provide general controlled loading and simulate virtual objects. When the mechanical power ratings of the actuators in this system are considered, it becomes evident that the human subject who volunteers to participate in experimental investigations with the manipulandum, is being asked to "shake hands" with a device that has force, velocity, and acceleration capabilities similar to those of an industrial robot. In an industrial setting, this type of intimate interaction between human and machine is rarely tolerated. A robot's workspace is often surrounded by physical barriers which prevent the human from entering into harm's way, or by infrared curtains or contact sensing floormats that detect the intruder's presence and trigger an immediate shutdown of all equipment. This section describes the measures that were taken to eliminate potential hazards in the limb loading manipulandum and ensure its safety for human use.

Potential mechanical hazards from interaction with the manipulandum were broken down into two categories. The first category occurs in situations where the human is attached to the machine either through a restraint or his/her own grasp; the second is when the machine, at first unattached to the human, suddenly comes into contact with a hand or other body part. Under the first set of circumstances, the hand may, because of manipulandum position, be caught in awkward or uncomfortable postures. When in these situations the hand and associated limb segments may be driven at excessive velocities, accelerations, or forces, leading to injury. In the second set of circumstances, the hand, or some other body part, suffers the impact of the moving manipulandum linkage, and may be suddenly pinned in an awkward posture between the handle link and another hard or sharp surface in the handle link quadrant. In addition to impact injuries, the moving manipulandum linkage may again induce excessive velocities, accelerations, and forces in the limb itself.

If the stall torque rating of the individual actuators is considered, it is without doubt

that, in static situations, an able-bodied adult subject grasping the handgrip can match the forces produced at the end of the manipulandum handle, and thus easily prevent handle motion. On the other hand, the force bandwidth of the system (determined from the first resonant mode of the mechanical system, as discussed in Section 4.6.2), permits comparable force magnitudes to be produced at up to approximately 60 Hz, far in excess of the range of human capabilities. Such forces at these frequencies could cause excessive oscillatory accelerations and velocities of the subject's entire hand and arm, or could impart a high intensity vibration at the palm of the hand. Injury could occur from sudden large amplitude disturbances or might result from chronic low level irritation.

In situations where the human is not in contact with the handle linkage, the torque developed at the motor accelerates only the handle inertia. Based on the 5 N-m rated motor torque and 0.018 kg-m^2 handle inertia, a maximum handle link angular acceleration of 280 rad/s^2, corresponding to a 6.5 g tangential acceleration at the spherical grip, was estimated.[14] With a step acceleration of this magnitude, it was also predicted that the handle link would swing across its 50 degree workspace in approximately 80 msec, begining from a standing start.

A combination of mechanical, electromechanical, hard-wired electronic, and computer software measures were invoked to deal with these safety issues. Passive mechanical features that enhance safety include the Delrin^{TM} cover and leather boot to eliminate the danger of fingers becoming caught in the gimbal mechanism—as described in Section 4.4—for either mechanical hazard situation. As noted in the same section, the cover and the Lexan^{TM} handgrip also insulate the subject from electrical contact with the device.[15]

The active strategy for maintaining safety is simple—make it difficult to turn the system on, and extremely easy to turn off. To prevent inadvertant powering of the

[14]The added inertia of the human arm would reduce this acceleration significantly. This suggests that one measure for limiting dangerous accelerations and the resultant velocities in the handle linkage, in addition to preventing impact between the human and the handle, is to keep the human securely attached to the handle through a splinting arrangement.

[15]Additionally, in terms of electrical safety, it was mentioned in Section 4.4 that exposed metal surfaces on the manipulandum cart are all properly grounded.

manipulandum in uncontrolled situations, activation of the machine has to be deliberate, following this specific sequence of steps:

1. Power up the Control Interface Unit (CIU) to enable the AC power latching relay circuit.

2. Activate the latching relay circuit for AC power to the servo amplifier.

3. Execute the computer code that clears all MDACs and permits the manual enable/disable push button (maintained type action, but useable as a momentary switch) connected to the CIU to enable servo amplifier output.

4. Press this maintained/momentary push button to enable the servo amplifiers to power motors.

Only once *all* of these steps have been carried out, can the motors be activated to permit load simulation by the manipulandum.

The steps outlined above for the safe power-up of the system depend on the host computer as well as the CIU. Hard-wired electronic circuitry on the CIU safety card, when powered under non-fault conditions, closes a relay located in the AC power latching circuit on the perimeter lower level of the manipulandum cart next to the servo amplifier chassis, mentioned earlier in Section 4.4 and visible in Figure 4.9. The latching circuit, schematized in Figure 5.13, once enabled by the CIU controlled relay, can be started by a momentary push-button "on" switch at the latching relay enclosures on the manipulandum cart.[16] Once started, the latching circuit powers the coils of the other relays, thereby connecting the AC line to the servo amplifier input and the servo amplifier output to the two motors, as well as disconnecting the short circuit applied (for dynamic braking) across the terminals of the two motors when not powered. At this stage, all relays of the circuit shown in Figure 5.13 are set to permit current to flow

[16]This green "on" button on the outside of the latching circuitry enclosure, along with a red "off" button and a green indicator lamp, are distinct from the hand-held momentary/maintained enable/disable push-button switch mentioned above in the four step start-up procedure.

through the motors, but still require the momentary/maintained enable/disable push button to deactivate "disable circuitry" on the individual servo amplifier cards. To render this momentary/maintained push button operational, however, the CIU safety card must first receive the appropriate a D/A input from the host computer.[17]

As alluded to in the previous paragraph, several system fault conditions can cause the safety card in the CIU to prevent or halt system operation. These conditions include: excessive acceleration; position limit switch contact; and either AC or DC power failure in the CIU.

The detection of excessive acceleration simply involves comparison of the acceleration signals with a preselected threshold. The four position limit switches, located at the bounds of handle linkage travel, detect the second fault condition. The limit switches, visible in Figure 4.6, are each constructed from a subminiature momentary switch and a sturdy "machine shop" quality spring stop, with the plunger of the spring stop impinging directly on the switch actuator lever. The limit switches are are mounted by the pair on adjustable blocks bolted onto each of the motor face plates. When the range of permissible handle travel in a particular direction is exceeded, the "winged" collar keyed to that motor shaft pushes on the particular spring stop button and closes the switch contact. The signals from the limit switches and the acceleration threshold detection circuitry are *hard-wired* with electronic .OR. logic, so that either of these conditions—or a power interruption to the electronics in the CIU—triggers a full system shutdown, without depending on the execution of *any* software.

The full system shutdown involves four actions: electronically disabling the servo amplifier power output, unlatching AC power into the servo amplifiers, opening the connection between the servo amplifiers and the motors, and short circuiting the motor terminals for dynamic braking. All but the first action in this sequence depend on the activation of electromechanical relays with response times as listed in Figure 5.13. The

[17]In the event of a computer crash, the computer D/A output is cleared, disabling servo amplifier output to both motors. Note that the zeroing of all computer D/A channels is a hardware condition, occurring independently of any software execution.

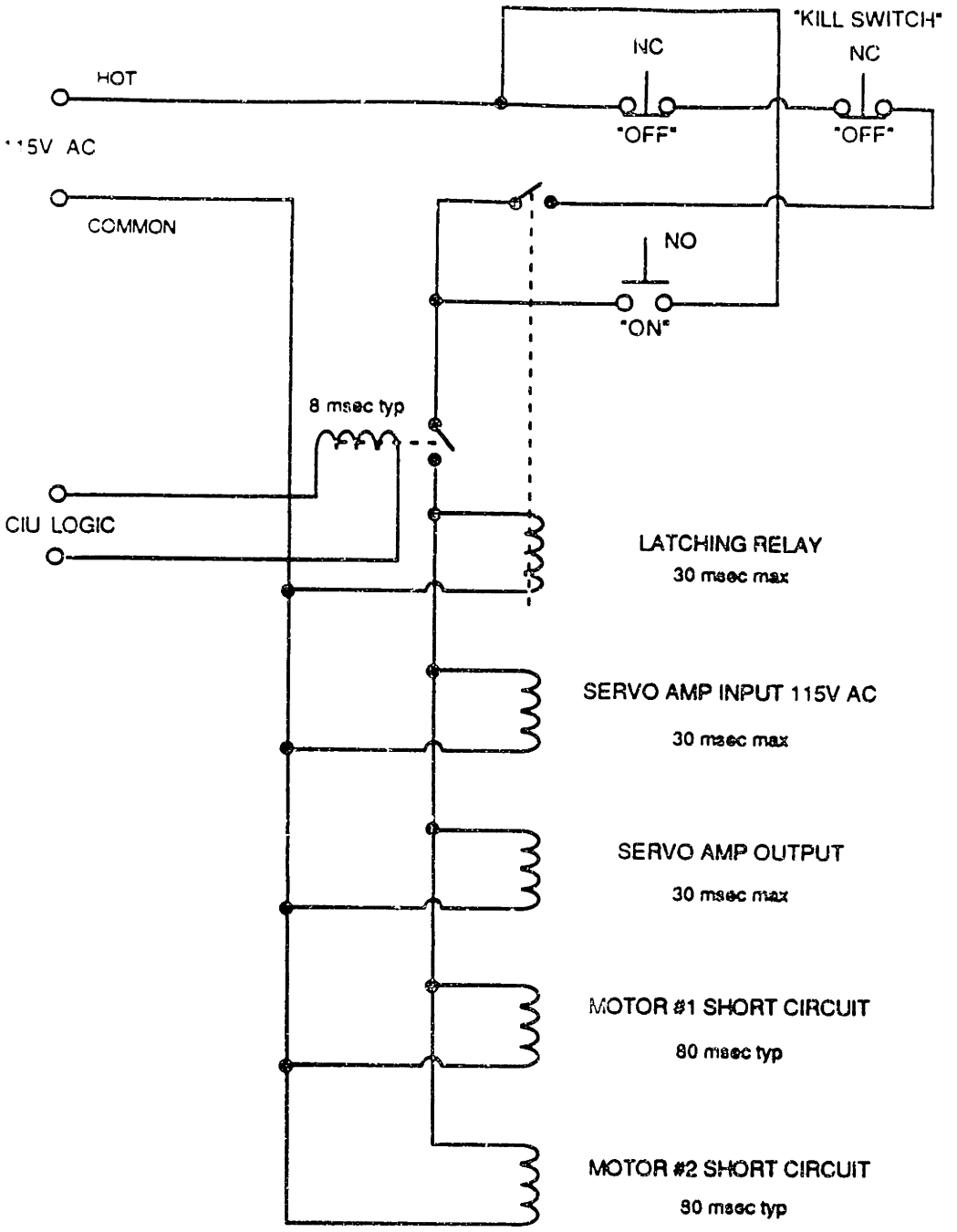

Figure 5.13: AC power relay circuitry. Included are the activation push-button switches, the coils of all relays, and the contacts of the actual latching relay and of the relay controlled by the CIU safety card. Included are the maximum activation/de-activation times of the individual relays. Refer to the text for additional details.

disabling of the servo amplifier output relies on integrated circuit logic (built onto the servo amplifier cards by the manufacturer), and, as a result, has a significantly quicker response time.

As noted above, two types of aberrant acceleration conditions are possible in the manipulandum system—ballistic accelerations during which the handle linkage takes off across the workspace, and vibratory accelerations due to instabilties. The effectiveness of the acceleration triggered shutdown procedure in these two situations was demonstrated for the vibratory instabilities described in Section 5.3.2 and 5.3.4, and for torque steps at the maximum continuous amplifier current rating. In the latter case, without the acceleration safety circuitry, the handle was able to traverse 40 degrees from a standing start in approximately 70 msec (in agreement with the prediction mentioned earlier in this section), before shutdown was triggered by limit switches. With acceleration detection in place, power output from the servo amplifiers was disabled in less than 5 msec, resulting in only seven degrees of handle motion.[18]

As a third line of defense, the system is equipped with manual override capabilities for shutdown. These capabilities include a "panic button" in series with the "off" momentary switch in the latching circuit (see Figure 5.13), the hand-held momentary/maintained push button that communicates via the CIU with the enable/disable electronics on the servo amplifier cards. The panic button shuts down the system by resetting the AC relays, thereby unlatching AC power into the servo amplifiers, opening the connection between the servo amplifiers and the motors, and short-circuiting the motor terminals. The significance of the latching circuit is that, after any fault event which causes the relays to release, including a failure in the AC power main, the system will not be restored with the motors in an energized state. To bring the system back up to operation from shutdown after any failure event entails following steps (2) through (4) of the start-up

[18]It is important to note that the severest human accelerations, including tremor of different frequencies and displacement amplitudes, were unable to trip the acceleration detection circuitry when the threshold was set to a level effective for preventing vibratory instabilities and ballistic motions of the manipulandum handle. The shock of vigorous collisions with the *simulated* walls described in Section 5.4.2, however, could produce acceleration magnitudes s that were sufficient to trigger shutdown, suggesting that the safety threshold should be relaxed for hard contact studies.

sequence itemized above. During safe operation, the momentary/maintained switch held by the experimenter serves as the normal, "graceful," method for cutting power to the motors without triggering a system shutdown.

5.6 Video Display

The visual presentation of a virtual manual task to the human operator/subject is often essential for convincing immersion in a simulated environment. In many activities, visual information often plays a key role, if not the only role, in on-line evaluation of how well a new manual skill is being learned. In certain situations where kinesthetic information is of poor quality or completely unavailable, such as in the control of powered prosthetic limbs or in teleoperation without force reflection, visual communication may be the only feedback channel that can serve the human.

An effective visual presentation of a virtual space should be sufficiently convincing so that the human operator/subject does not have to expend unnecessary cognitive effort in trying to decipher what the visual image is meant to represent. For some simulations, effective presentation may require elaborately detailed, realistic images. In other situations, needlessly complex images may appear cluttered and prove to be distracting, hindering the subject's manual performance. Similarly, delays or other dynamic effects between manual actions and their visual transmission to the human operator may be perceived either as a hindrance or as an essential facet of the environment under simulation.

The objective for the present system is to provide the subject with a visual image that captures only the salient features of the task that his/her hand is carrying out in the virtual environment. The purpose of linking the manipulandum to a video display in this work is to demonstrate that the instantaneous characteristics of human performance, as measured by the manipulandum transducers, can be transferred to the display in real time, without seriously taxing the operating bandwidth of the overall system. As such, a simple video presentation is sufficient. More detailed displays, which may potentially enhance the quality of the representation, are left for future work.

The organizing principle in setting up the real-time video display for this system, as described at the begining of this chapter, and followed for the development of the control and supervision of the limb loading manipulandum, has been the distribution of computation to lighten the burden on the host LSI-11/23 processor. The video processor's role in the system is to accept information from the host computer on the current state of the human-manipulandum interface and construct the displayed image. This information could include any functionaL combination of transducer signals (*i.e.*, displacement, velocity, acceleration, and force) that are monitored by the LSI-11/23 for load supervision or stored for off-line analysis. The detail and complexity of how this information is presented to the subject is solely the responsibilty of the video processor.

An Amiga 1000 personal computer (Commodore Business Machines, Inc., West Chester, PA), selected primarily because of its very competitive price, is the video processor employed for the simulated environment system. The Amiga, touted as being capable of real-time animation, is based on the Motorola 68000 microprocessor, and includes custom graphics coprocessors to enhance its ability to quickly draw relatively complex images. The computer comes with its own 0.033 m (13 in) diagonal RGB monitor and is equipped with an RS-232C compatible serial port, a parallel port, and stereophonic audio output.[19] To take advantage of its hardware capabilities, however, the Amiga requires its own unique operating system: AmigaDOS. Because AmigaDOS is so dissimilar to other, more popular, operating systems, the Amiga programmer unfortunately cannot benefit from the abundance of programming manuals, system guides, and software that is available commercially for other personal computers.

A pursuit tracking task, in which the human operator is asked to follow a moving target on the video monitor, was chosen to demonstrate the real-time visual presentation capabilities of the system. The operator's tracking response is the instantaneous two degree of freedom displacement of the manipulandum handle in α and β coordinates. Other measured variables, such as velocity, acceleration, or force, could have been presented as

[19]Details of the Amiga computer memory configuration and attached peripherals can be found in Appendix A.

easily. As noted earlier, the manipulandum handle coordinates very closely approximate the x and y planar projection of hand position, and thus were displayed directly on the monitor. Transformations into the exact (x,y) variables or some other coordinate system could have been accomplished with additional programming of the Amiga. The aim in preparing the tracking display on the Amiga, though, was to keep the computation cycle time faster than the 30 Hz raster screen refresh rate for double-buffered, high resolution mode. By adhering to this goal, the display can continue to operate at this hardware limited update rate.

The display driver code, as written, requests instantaneous target and response cursor locations over the serial line from the LSI-11/23 at a frequency of 30 Hz, as dictated by the screen refresh rate. The instantaneous two dimensional target location (stored as a complete target trajectory record in the host computer memory in advance of the experimental run) and the current manipulandum position, are transfered back to the Amiga over the serial line at 9600 baud in response to this request. Each frame sent back to the Amiga consists of four bytes of video data—the x and y target and the x and y response (handle) location—followed by several marker bytes, the exact number of which depends on the update rate of the host computer supervisor algorithm.[20] Once the data frame has been acquired by the Amiga, the x and y target and response coordinates are sorted from the markers, and are then shifted and rescaled. The rescaling constants were chosen to expand the 256 unit (one byte) dynamic range of each coordinate, enforced by the serial line transmission, to use as large a square region of the 640 by 400 pixel screen as possible without the cursors encountering the edges of the display.

The video screen display is stark, with a target cursor (a red diamond) and a response cursor (a white cross) on an empty black background, as shown in Figure 5.14. These cursors are drawn on the screen as connected line segments without resorting to the Amiga's more advanced coprocessor "bob" or "sprite" graphics. The line segment drawing technique was deemed sufficient because it was already faster than the 30 Hz

[20]Details of the LSI-11/23 code execution and communication between the two computers is discussed in the next section.

screen hardware refresh rate. "Sprites" and "bobs" which allow equally fast display of more intricate images may be valuable tools for future applications.

The video display and serial communication software was written entirely in C (Aztec C68K for the Amiga, Manx Software Systems, Shrewsbury NJ) and makes heavy use of libraries provided with the AmigaDOS operating system.[21] Pseudo code which summarizes the general scheme for the display and host computer interface protocol on the Amiga is given in Figure 5.15.

5.7 Host Computer and System Supervision

Throughout the description of the various facets of the virtual environment system's design—the manipulandum mechanism configuration, the actuator and sensor selection, the load controller, and video display implementation—the goal of distributing computation to maximize the host processor speed and the overall system bandwidth has been emphasized again and again. The result, as summarized by Figure 5.16, is that the local control of mechanical load emulation by the manipulandum and the maintenance of system safety are delegated to hard-wired electronic circuitry in the CIU, while the details of the visual presentation to the human operator/subject are handled by a separate graphics computer. The host LSI-11/23, which is freed by these components from the details of their function, still is solely responsible for the supervision of the entire system. These host supervisory tasks include: initializing load simulating parameters in the CIU; monitoring of manipulandum kinematics and force transducers, and updating load parameters in the CIU based on the current measurements; and communicating the state of the manipulandum-human interface via the CIU to the video display processor. The only non-supervisory function carried out by the LSI-11/23 is the storage of sampled transducer measurements for subsequent off-line analysis of the human subject's performance.

[21] A concise outline of the Amiga and how to compile and link programs with Aztec C can be found in [95].

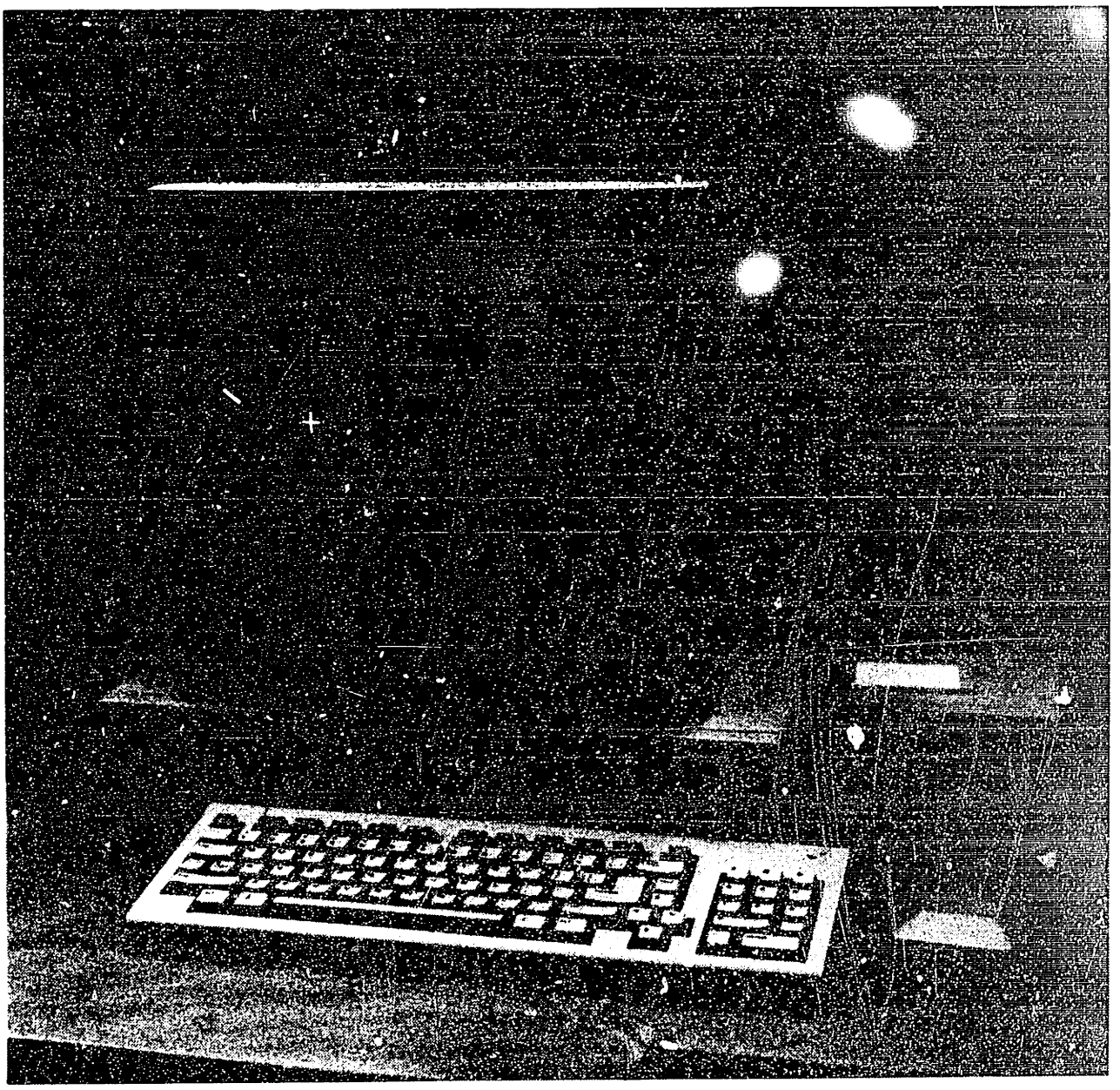

Figure 5.14: Pursuit tracking video display.

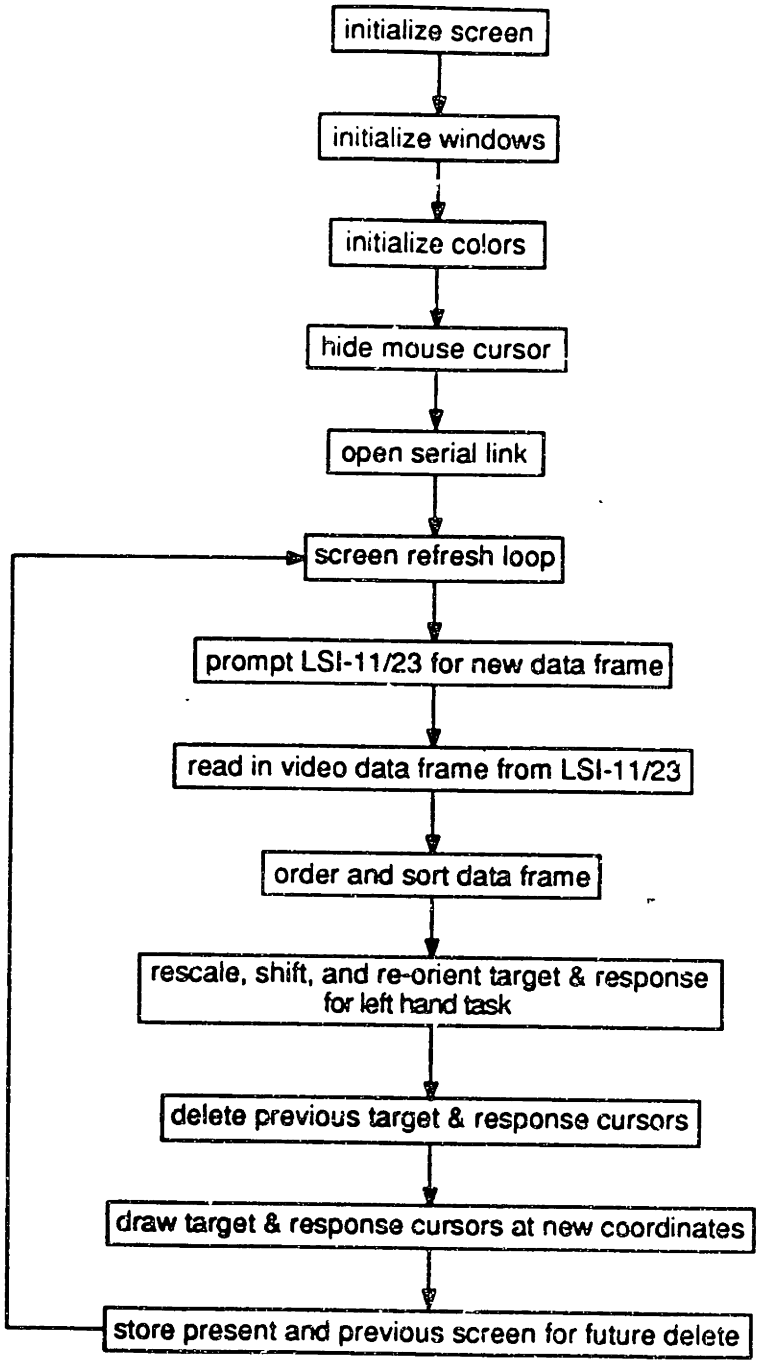

Figure 5.15: Video display pseudo code.

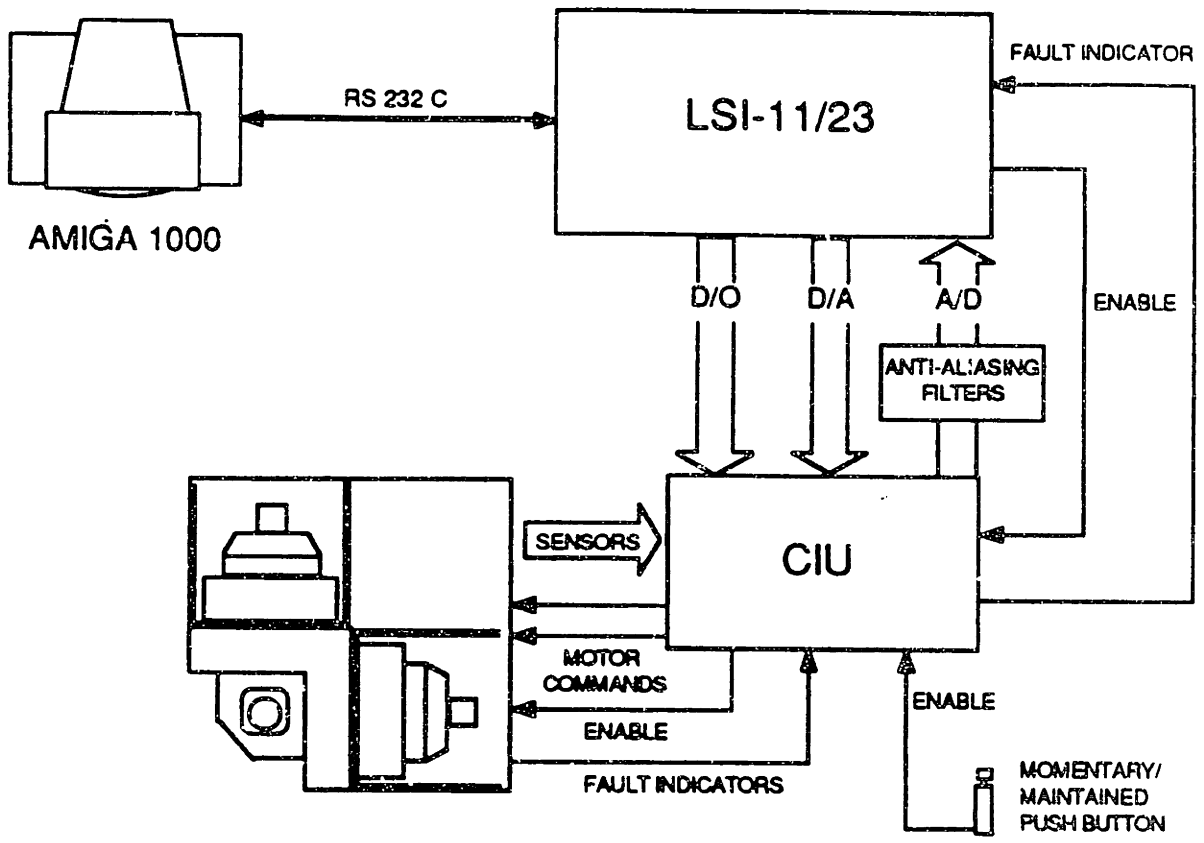

Figure 4.16: Control distribution and system communication between the manipulandum, CIU, host LSI-11/23 computer, and Amiga 1000 video display.

The efficacy of the control distribution stategy was demonstrated by the operating speeds achieved for the host computer's supervisory functions during the execution of a protocol described here that would be typical of many experimental situations with human subjects. The computer code to execute this standard experimental protocol is broken into two parts. The main program, written in RT-11 FORTRAN IV, requests initial MDAC gains to simulate loads and the names of files containing pre-calculated target trajectory records to be presented on the tracking display.

The routine that performs the real-time supervision tasks and data storage is coded in MACRO-11 assembly language to maximize speed. The routine first sets the MDAC gains, defining the manipulandum handle load field, and then waits for the experimenter to start the protocol. After a "carriage return" response is entered at the computer keyboard, the host computer begins monitoring handle displacement to implement a virtual four-walled enclosure that surrounds the workspace, thereby preventing the subject from moving the handle into the limit switches and inadvertently triggering a system shutdown. Also upon the "carriage return," the host begins responding to the Amiga data requests, and target and response cursors appear on the tracking display monitor.

Each experimental run is divided into two contiguous portions. Both portions are identical in terms of the feel of the manipulandum handle and the appearance of the tracking display to the human subject. The first part is a practice period during which sampled data is not stored, but used only to supervise the virtual enclosure and to drive the video display. The practice period is followed immediately by the test interval during which the sampled data is saved. The practice period may be programmed for any length time interval. The data storage interval however is limited by the available memory size for the LSI-11/23 system architecture.[22] For the system as currently configured, this limit is 4096 stored integer points for each data channel—*i.e.*, transducer signal, target history, and virtual trajectory commands to the manipulandum.

The constant monitoring of the manipulandum displacements for the safety enclosure

[22]Details on the configuration of this LSI-11/23 system and the amount of memory available are given in Appendix A.

implementation, the transfer of target and response locations for the tracking display, and data storage, as described above, all occur concurrently in the host computer. Each of these events is timed at a different base rate, as illustrated in Figure 5.17. The monitoring, as well as the wall enclosure implementation, occurs at the same 1000 Hz rate as the A/D sampling of all eight transducer signals. Every tenth sample burst, data, including virtual trajectory commands to the manipulandum actuators, in addition to the transducer signals, is held in a software buffer. If the data storage portion of run is then currently being executed, the contents of this buffer are copied into virtual arrays for writing onto disk at the end of test, yeilding an effective storage rate of 100 Hz.

During the entire run, the Amiga continually prompts the host computer via the serial line to transferred back new target and response values. Provided each of these calls for new tracking data are met, the Amiga keeps sending requests at the 30 Hz rate determined by an internal clock synchronized to its hardware screen refresh. When one of these requests is received by the host, a nine byte video frame buffer, consisting of four data bytes and five markers (see Section 5.6), is packed at the begining of the next 100 Hz cycle. The video frame is then sent over the next nine ticks of the 1000 Hz monitoring "clock," one byte at a time via the 9600 baud serial line, back to the Amiga. As a result, this video frame buffer is empty by the start of the next 100 Hz cycle, and is ready to be refilled at the next 30 Hz request from the Amiga. In the event that the Amiga is not requesting data, the CIU-based manipulandum controller, and the host-based wall-monitoring and data storage continue to run unaltered.

Some of the operating speeds and bandwidths observed during the examination of system performance for the sample protocol, which includes simulation of general load fields surrounded by virtual walls, stand out. First, general force production as seen at the handgrip is limited by the analog bandwidth of the system—*i.e.*, the 50 to 60 Hz cutoff determined by the resonance of the handle mechanism. Second, the hard-walled enclosure implementation, which is simulated concurrently with the general load field, is updated at a rate of 1.0 kHz—at the same time that data is being stored and transferred

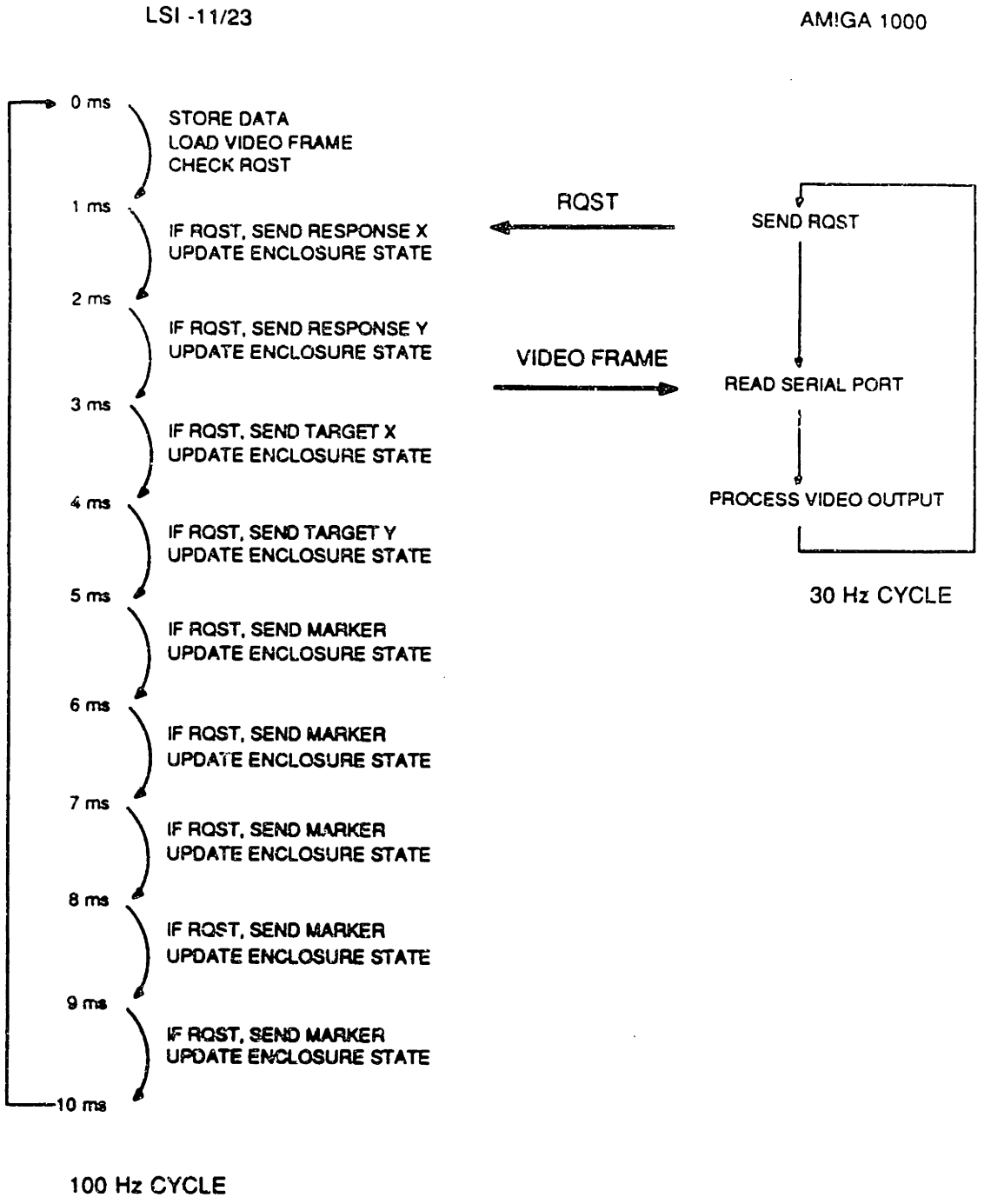

Figure 5.17: System supervision and control event timing diagram. See text for details.

to the Amiga. As a benchmark for comparison, the host computer, while executing only the A/D acquisition routine with data storage of the eight transducer signals in virtual memory arrays, cannot run any faster than 1.4 kHz.

Chapter 6

Tremor Experiments

The potential of the virtual environment system as a tool for tremor research is discussed in this chapter. Included is an informal "proof of concept" demonstration of the system from tests on a subject with pathological tremor. Following is a proposed protocol for a series of whole-arm tremor experiments to investigate possible coupling between oscillations in different limb segments and identify tremogenic mechanisms associated with the individual oscillations. Finally, the feasibility of aligning and constraining a subject's arm for this protocol is examined through tests in which a passive armlike manipulator linkage was connected to the manipulandum.

6.1 Preliminary Experiments with a Human Subject

A visit to the Newman Laboratory by a tremor-disabled individual (for participation in another research project) provided the opportunity for an informal test of the virtual environment system's capabilities. The participant in these preliminary experiments was a 28 year old woman with large amplitude intention tremor[1] due to multiple sclerosis, manifested primarily as an oscillatory humeral adduction-abduction motion in the left arm. Although the subject was right handed, all tests were therefore performed with her left arm.

[1]The term "intention tremor" is used to describe tremor that is exacerbated by dynamic tasks requiring precise motion [137].

During the tests, the subject was seated in a comfortable chair, facing the front of motor #1, with her shoulders roughly at the height of the manipulandum handgrip. The chair was positioned so that when grasping the spherical handgrip over the top, the subject's elbow was flexed to approximately 90 degrees, with the long axis of her forearm horizontal and parallel to the shaft of motor #1. The subject's arm was not otherwise supported during the experiments.

The subject was instructed to move the manipulandum handle continuously in slow (approximately 5 to 10 seconds per cycle) smooth circles, without contacting the virtual-walled "safety enclosure," mentioned at the end of Sections 5.4.2 and 5.7, that surrounds the handle workspace. She was reminded frequently to maintain her arm in the horizontal plane and not rest it on the handle quadrant cover. Visual feedback was provided by permitting the subject to watch her hand. The tracking display was not used in these preliminary tests.

Four tests were performed. A different mechanical loading condition was applied to the subject's arm in each test by programming the gains of the manipulandum load controller in the CIU. The four conditions were the following: 1) "no-load," with the motors unpowered (*i.e.*, only passive inertia and friction present); 2) added damping, corresponding to 1.6 N-m/(rad-sec^{-1}) for each axis; 3) added inertia, corresponding to a doubling of the passive inertia to 0.036 kg-m^2 for each axis; and 4) added stiffness, corresponding to 15 N-m/rad for each axis with the spring field centered at straight-up handle position. All load settings were stable (*i.e.*, the linkage did not move when not grasped by the subject) and did not saturate the actuators over the range of displacement, velocity, and acceleration produced by the subject. Each test lasted 41 seconds (4096 samples at 100 Hz). The subject was allowed approximately five minutes of rest following each test.

The complete motion records from the four 41 second tests—no-load, added damping, added inertia, and added stiffness—are depicted in Figure 6.1, in the order in which the tests were performed. The stiffness plot readily stands out from the other three by virtue

of the smaller and more jagged track.

Power spectra of the acceleration measured in each axis for this series of tests are shown in Figure 6.2. The peaks in these spectra, indicative of tremor activity, are in the 5 to 6 Hz band, with the exception of the inertia test, where the main activity is shifted down to ~2.25 Hz. The power spectra confirm the highly oscillatory appearance of the stiffness test diplacement crossplot, in which acceleration power densities at the peak frequency are 20 (α axis) to 100 (β axis) times greater than in the no-load condition.

Two factors affected the quality of the data in these preliminary tests. Both are related to inadequate regulation of experimental conditions. First, the subject's arm was not constrained to the horizontal plane, and thus was free to oscillate involuntarily out of the horizontal plane.[2] Second, in the absence of a pursuit tracking task to pace the subject's voluntary hand motion, the displacement trajectories were neither very repeatable (either between tests or within an individual trial), nor were they very circular. These observations re-emphasize the need to both impose appropriate arm restraints as well as to include a visually mediated tracking task in formal experimentation.

The results of these informal tests demonstrate that tremor characteristics can be affected by loads simulated at the manual interface of the virtual environment system. While these data are intriguing, four tests are too few upon which to base any conjectures regarding the subject's tremor.

6.2 Proposed Whole-Arm Tremor Experiments

A protocol for future experimental studies of whole arm tremor is proposed here. These studies would investigate two issues raised in Section 1.4: 1) the coupling between tremor oscillations at adjacent joints in the arm; and 2) the tremogenic mechanisms responsible for the individual oscillations at these joints.

These experiments examine tremors in the two degree of freedom situation where the

[2]The relative smoothness of the *hand* motion crossplots for the no-load, damping, and inertia conditions belies the vigorous tremor motion observed (visually) at the *shoulder*.

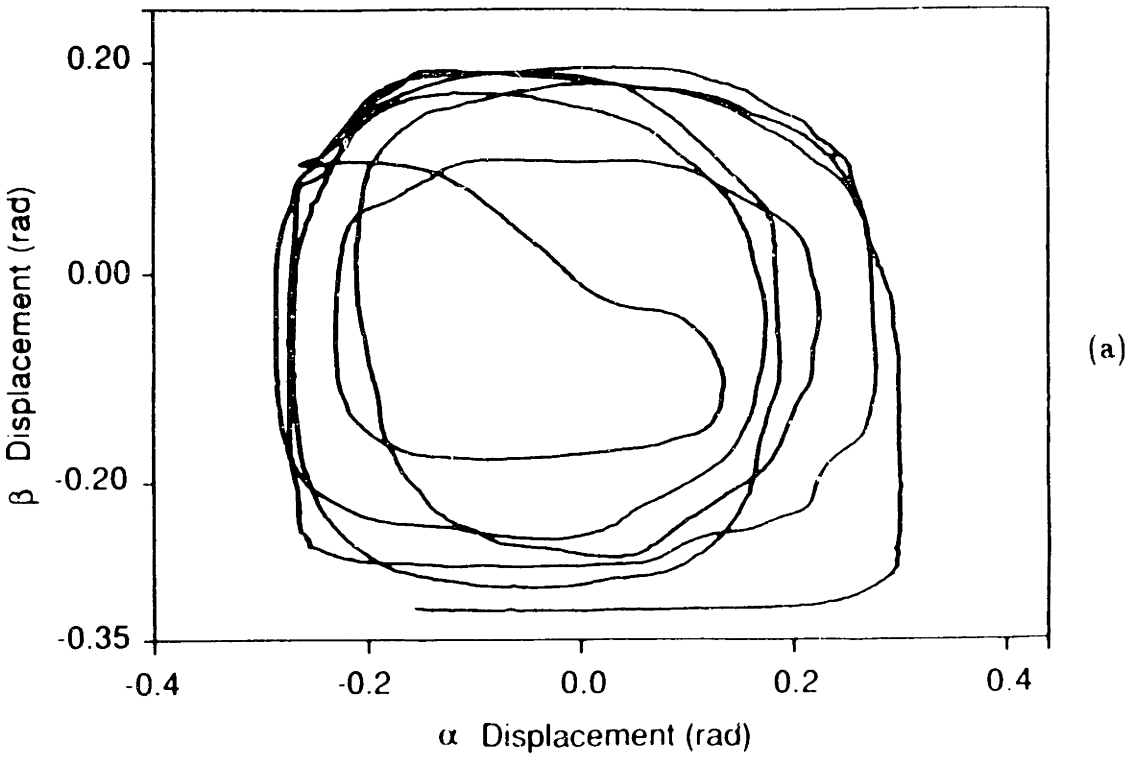

(a)

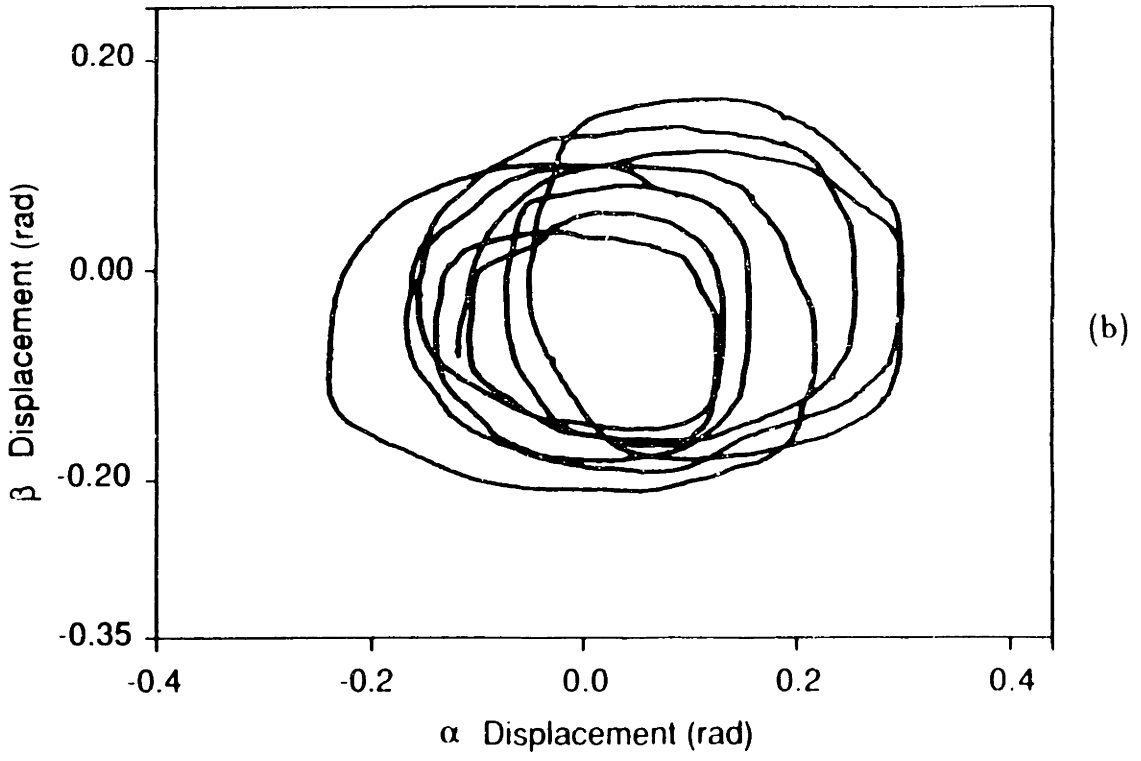

(b)

Figure 6.1: Two dimensional displacement trajectories from tremor subject with: (a) passive, *i.e*, unpowered manipulandum, and (b) simulated damping, B = 1.6 N-m/(rad-sec^{-1}), settings for both axes.

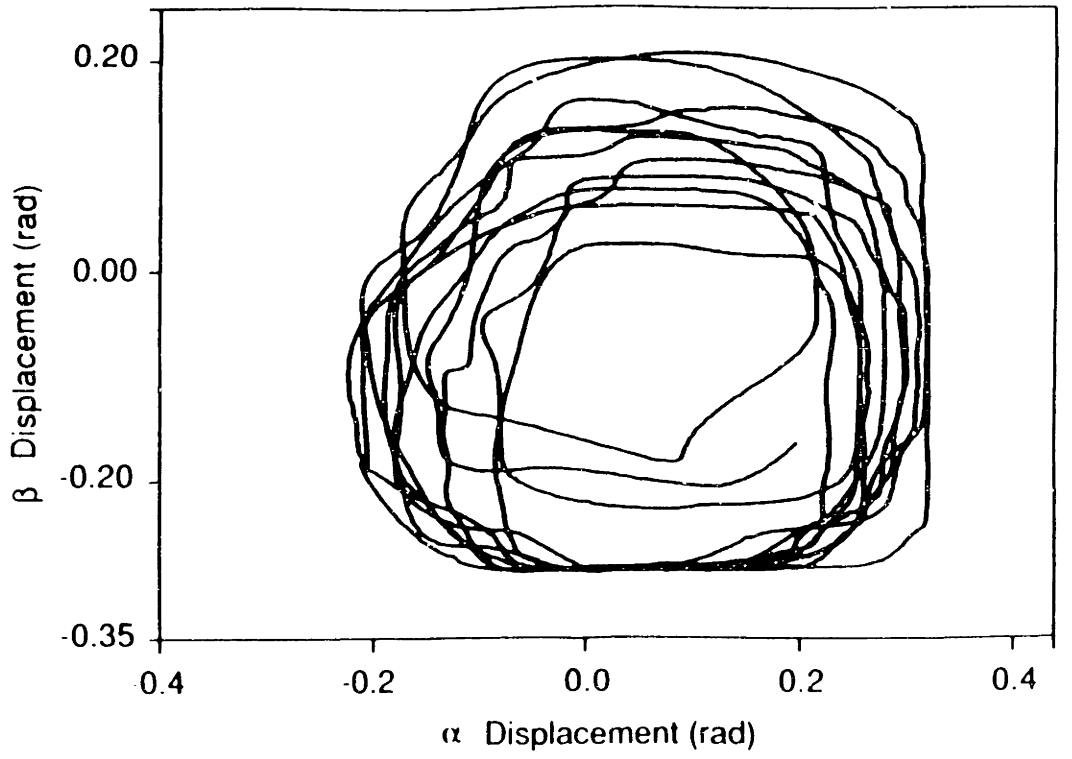

(c)

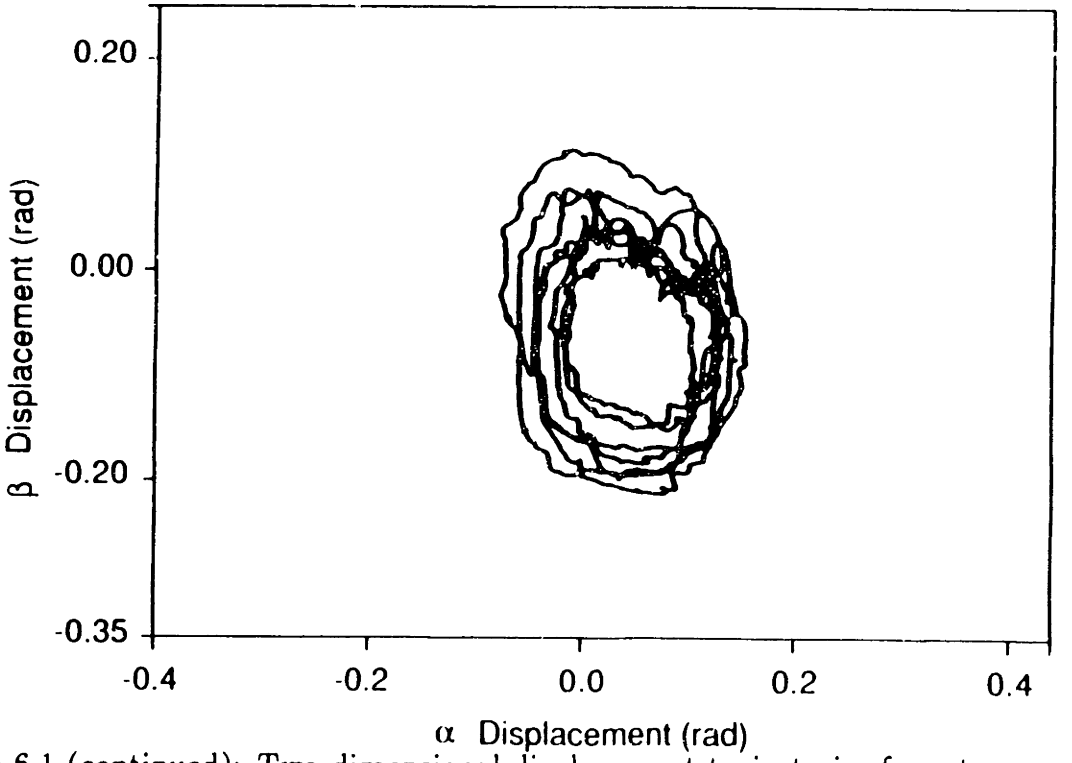

(d)

Figure 6.1 (continued): Two dimensional displacement trajectories from tremor subject with: (c) with simulated augmented inertia, $I + I_m = 0.036$ kg-m^2, settings for both axes, and (d) added simulated stiffness, $K = 15$ N-m/rad, settings for both axes.

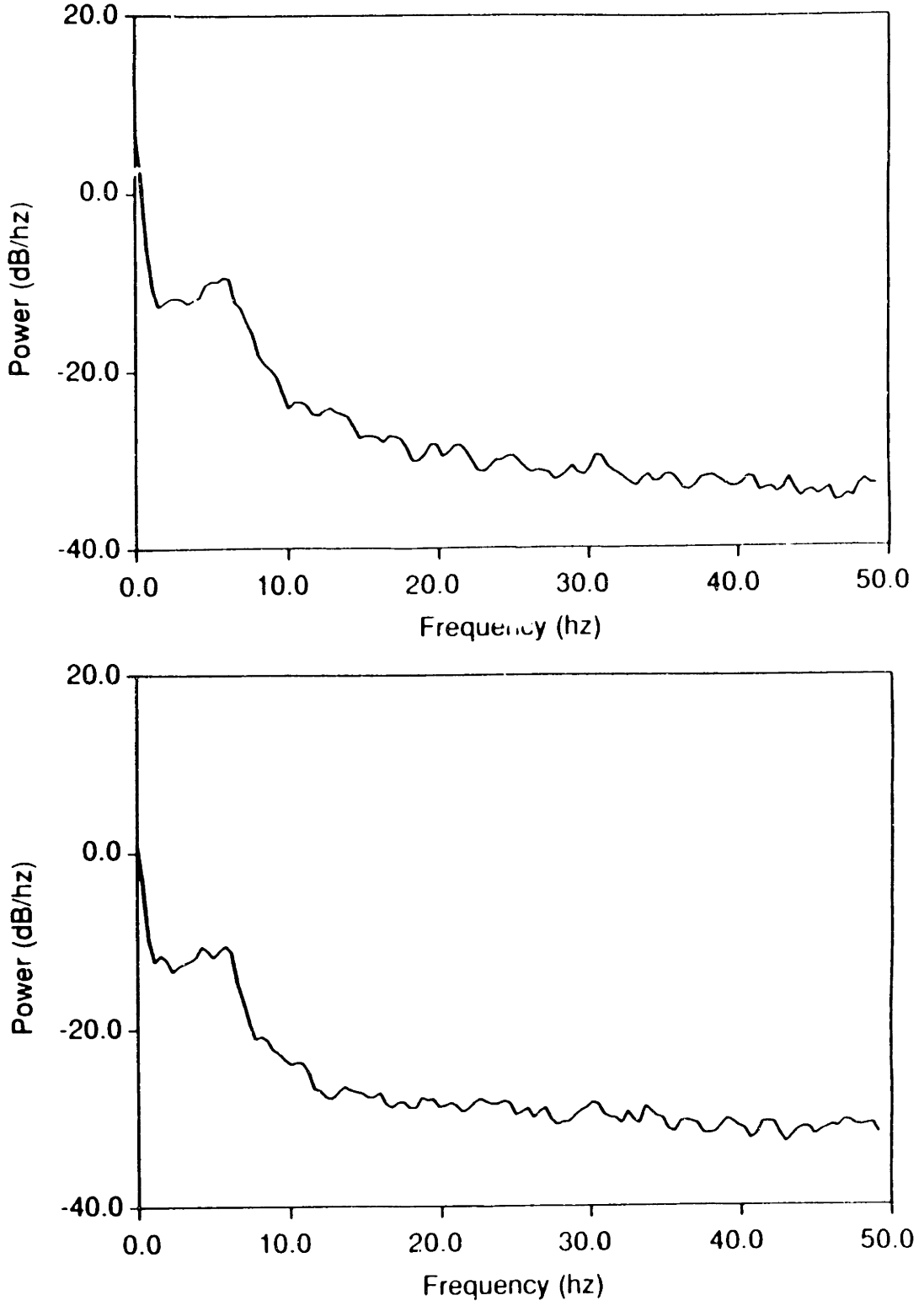

Figure 6.2: (a) Acceleration spectra from tremor subject with passive, *i.e*, unpowered manipulandum. *Top*) α axis acceleration density versus frequency; *bottom*) β axis acceleration density versus frequency.

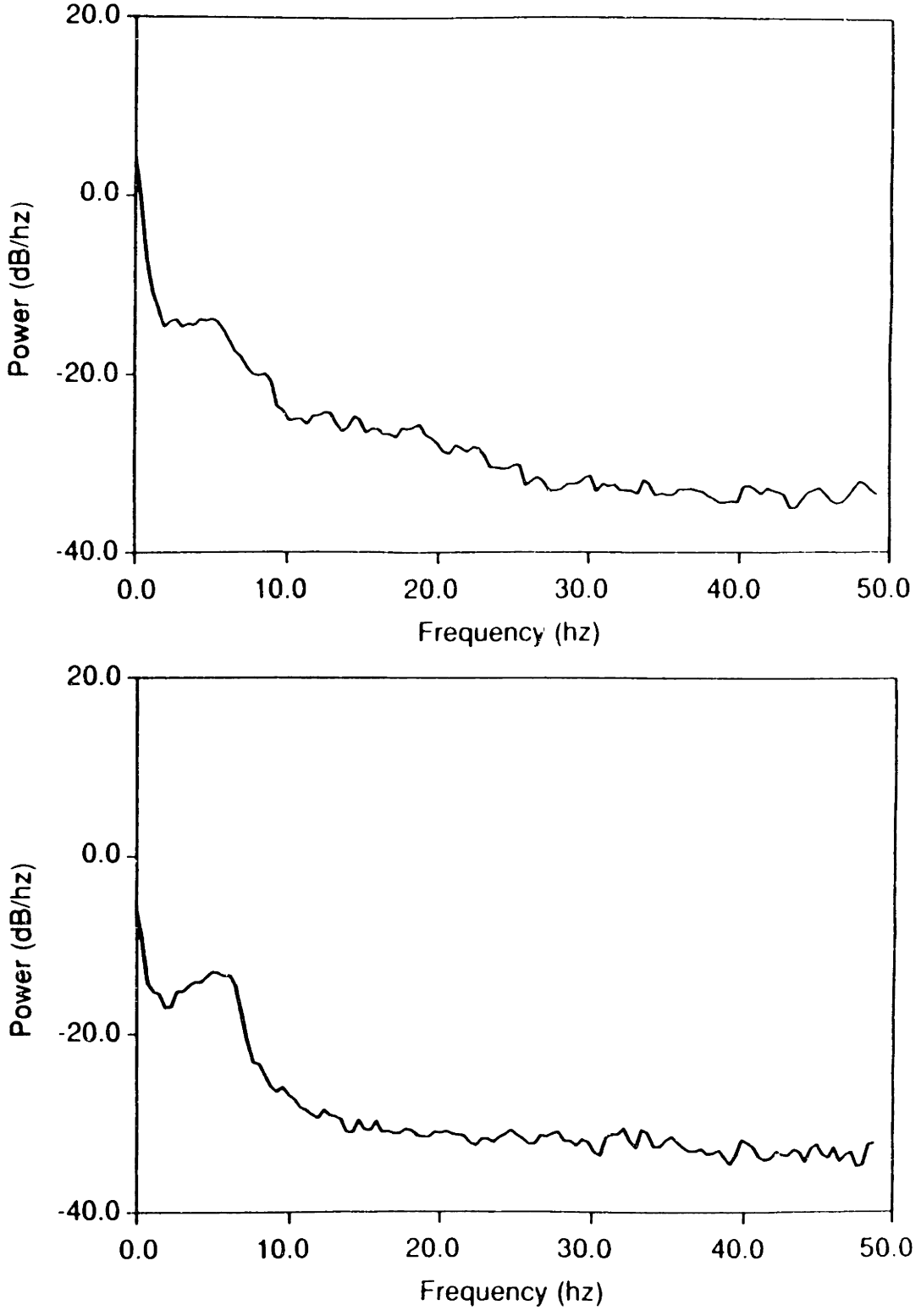

Figure 6.2 (continued): (b) Acceleration spectra from tremor subject with simulated damping, B = 1.6 N-m/(rad-sec^{-1}), for both axes. *Top*) α axis acceleration density versus frequency; *bottom*) β axis acceleration density versus frequency.

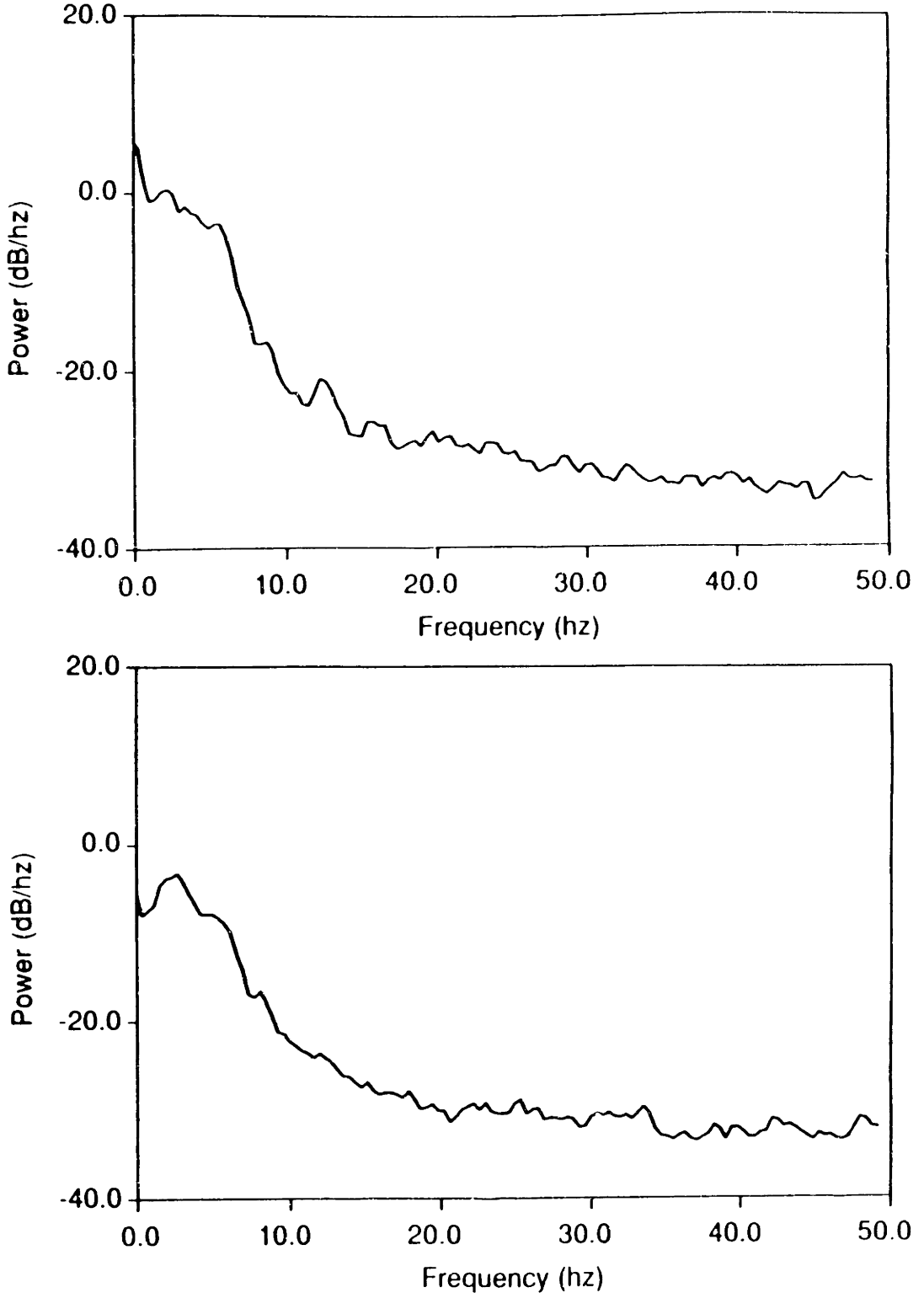

Figure 6.2 (continued): (c) Acceleration spectra from tremor subject with augmented inertia, $I + I_m = 0.036$ kg-m^2, for both axes. *Top*) α axis acceleration density versus frequency; *bottom*) β axis acceleration density versus frequency.

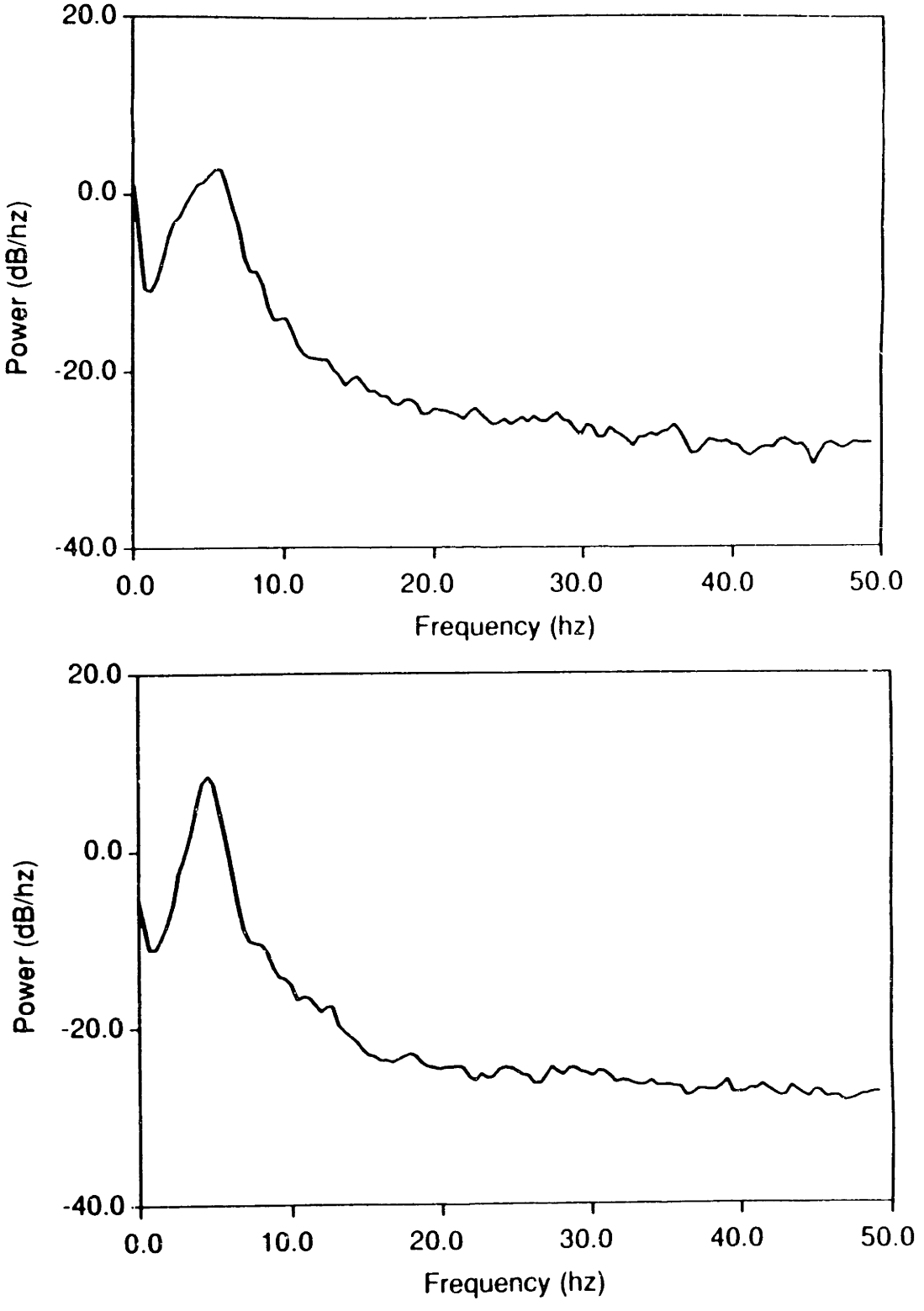

Figure 6.2 (continued): (d) Acceleration spectra from tremor subject with simulated stiffness, $K = 15$ N-m/rad, for both axes. *Top*) α axis acceleration density versus frequency; *bottom*) β axis acceleration density versus frequency.

arm is constrained to a horizontal plane and only motions at the elbow and shoulder are permitted. The protocol relies upon:

- Pursuit tracking tasks to elicit different voluntary patterns of joint motion.
- Selective splinting to eliminate either elbow or shoulder motion.
- Imposition of a variety of mechanical loading conditions at the subject's hand.

Presented here are a general description of the proposed experimental setup, including fixturing needs for confining the arm to a horizontal plane and arm trajectories to be used in the tracking tasks; an itemization of the parameters to be varied from test to test; a brief description of data analysis methods; and an interpretation of potential observations from these tests.

6.2.1 Subject Selection

Subjects recruited for this protocol should have tremor present in the whole arm during voluntary movement—*i.e.*, there should be clear evidence of both shoulder and elbow involvement. The tremor should be large enough to ensure that its mechanical characteristics are clearly visible at the hand-manipulandum interface, but not so severe as to obliterate purposeful movement and make manual tracking tasks overly frustrating to the subject. In addition, the subject should have sufficient cognitive ability and visual acuity to perform pursuit tracking tasks, and the temperament to withstand the potential boredom of lengthy test series.

6.2.2 Experimental Setup

A schematic representation of a subject interacting with the virtual environment system—*i.e.*, the limb loading manipulandum and the video display—is shown in Figure 6.3. The particular setup illustrated is configured for arm motion about this nominal posture in the horizontal plane. With the shoulder locked in the depicted position, elbow motion gives rise to hand path E; with the elbow locked and the shoulder free to move, the hand

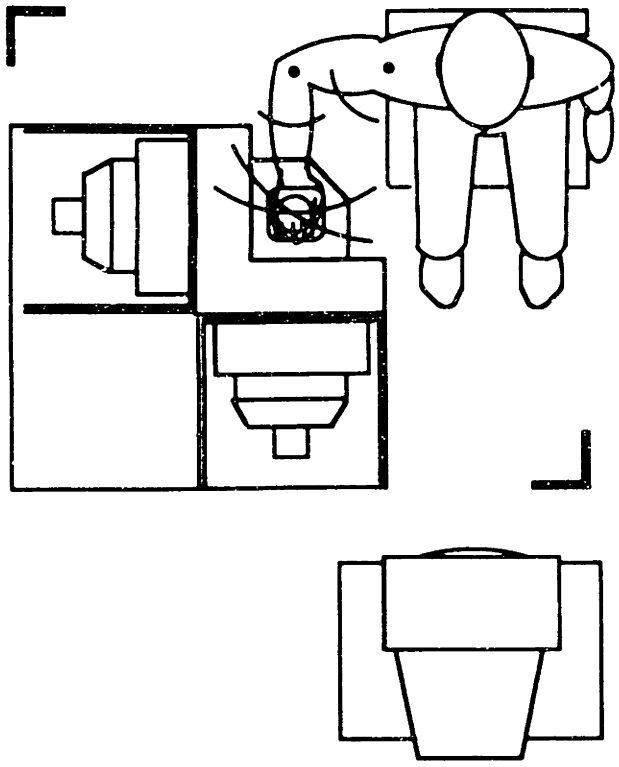

Figure 6.3: Proposed test set up for tremor experimentation. Seated subject is shown grasping the manipulandum handrip at shoulder height while facing the video display.

follows path S. If a different spatial relation between shoulder and elbow trajectories E and S is desired, then the location of the subject's chair relative to the manipulandum can be adjusted. Also, since the manipulandum is mechanically symmetric to the user (that is identically programmed load simulations about either the α or β axis are approximately equivalent), and because the display on the video monitor can be easily reoriented through software, the setup depicted in Figure 6.3, can easily be transposed for left-handed experiments by rotating the manipulandum cart counter-clockwise by 90 degrees and moving it to the other side of the subject.

Arm Support and Constraints

The manipulandum was designed to accommodate general whole arm motion with only the arm's attachment to the handle linkage constrained to two degrees of freedom. However, since the joints of the arm permit motion and force in seven degrees of freedom and the manipulandum can only measure and apply loads in two, additional constraints are needed to restrtict the arm. A passive linkage such as a "mobile arm support,"[3] which has a configuration similar to the planar mechansim in Figure 3.1, could serve to maintain the upper arm and forearm in a horizontal plane, and by coupling it to the subject's arm through a wrist splint, prevent motion at the wrist.

To preclude prehension, the wrist splint should be fastened to the manipulandum handle.[4] This, however, presents a problem. Assuming that the subject is securely seated in the testing chair, as shown in Figure 6.3, and that the wrist splint and mobile arm support are in place, ideally, the subject's arm motion becomes truly planar. The difficulty is that the quasi-planar manipulandum workspace in actuality is a small portion of a spherical surface. If the splint and support for the arm, and the arm itself, were perfectly rigid, the wrist splint fastener would have to accommodate the additional degrees of freedom needed to maintain kinematic compatibility between the subject's arm and the manipulandum handle. (An implementation of such a fastener is presented below in Section 6.3.)

Pursuit Display

All tests in the protocol would involve the presentation of pursuit tracking tasks on the video monitor. The response cursor location would be controlled by the subject through the position of the manipulandum handle. The display screen would show a direct mapping (*i.e.*, no transformations other than linear scaling) of the sensed angles

[3] A commercially available assistive device to support the arm of the motor impaired that is also known as a "ball bearing feeder" or a "balanced forearm orthosis"[80].

[4] Eliminating prehension is important since some of the muscles involved in grasp also span the elbow. Furthermore, by attaching the subject's arm to the manipulandum handle, potential hazards due to impact described in Section 5.5 are reduced.

α and β, which, as discussed in Section5.6, are a reasonable approximation of planar Cartesian coordinates.

6.2.3 Experimental Protocol

The experiments to examine hypothetical coupling between oscillations in adjacent joints require additional restraint in the plane of movement at the shoulder and elbow during the performance of the various tracking tasks. The restraints are removeable splints to immobilize either the elbow or shoulder joints in the "neutral" posture depicted in Figure 6.3. Thus, applying the elbow splint reduces motion at the hand to the single degree of freedom arc S. Similarly, splinting the shoulder leaves only motion E.[5]

Four target trajectories are proposed to elicit desired joint motion corresponding to the E and S paths of Figure 6.3 (one joint motion), as well as their "sum" and "difference," Δ_1 and Δ_2 (two joint motion), as shown in Figure 6.4. The choice of spatial trajectory would depend on the individual conditions for a particular test.[6]

Using three joint splinting conditions (elbow, shoulder, or neither joint) and the four spatial target trajectories in Figure 6.4, a total of six feasible combinations may be implemented. These combinations are listed in Table 6.1.

Tremogenic mechanisms associated with oscillations present for each of the splinting and trajectory conditions in Table 6.1 can be probed using the same mechanical loading rationale described in Section 1.3.5. Loading conditions should include augmented inertia and augmented stiffness to test the role of biomechanics in the oscillations. Randomly timed perturbations should be included to determine if tremor oscillatory phase can be entrained by peripheral disturbances, indicating reflex loop participation.

How data from experiments under the splinting and external loading conditions out-

[5]Again, recall from Section 6.2.2 that the relative spatial relation between paths E and S can be changed by changing the seating position of the subject.

[6]*Spatial* preview could be provided by displaying the entire target trajectory throughout the task. The target cursor itself would be presented as a marker that moves *along* the selected spatial trajectory. Instantaneous target position on the trajectory would be governed by low bandwidth pseudo random signals. The combination of unpredictable target pacing with known spatial characteristics should lead to tasks that are unpredictable yet easy for the subject to perform.

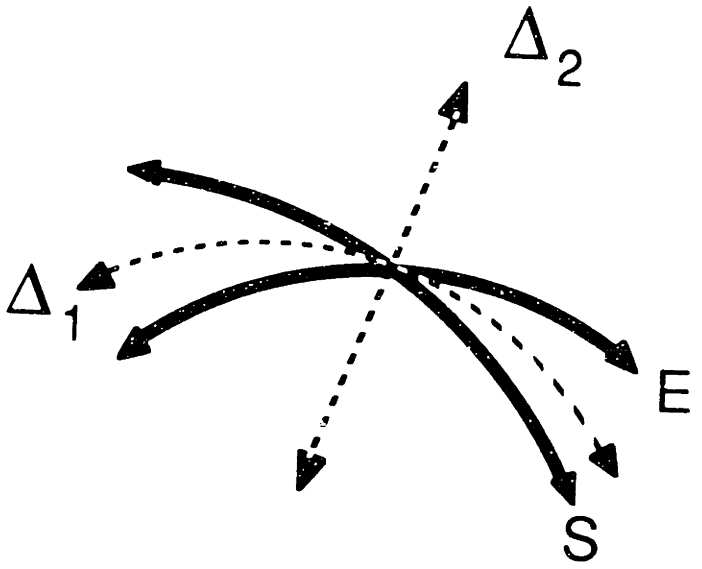

Figure 6.4: Pursuit target trajectories. E elbow motion, S shoulder motion, Δ_1 and Δ_2 are the "sum" and "difference" combinations of E and S.

lined in this section may be interpreted is discussed in Section 6.2.5, following a description of suggested data analysis procedures.

6.2.4 Data Analysis

The manipulandum is equipped to directly measure two degree of freedom kinematics and force at the interface between the subject's hand and the machine. This amounts to eight transducer signals, in addition to the two pursuit target coordinates and perturbation commands to the motors, at each sampling burst. Sampling at 100 Hz over a 40 second interval leads to approximately 48,000 data points per test, all referred to the α and β coordinates of the manipulandum handle mechanism.

It is of interest to study the kinematics and dynamics of tremor and voluntary motion from these tests with respect to the following coordinate systems: the manipulandum coordinates in which the tracking tasks are displayed; fixed Cartesian coordinates which can be used to describe the absolute hand motion; and arm joint angle coordinates which

Shoulder Condition	Elbow Condition	Target Trajectory
Free	Free	E
Free	Free	S
Free	Free	Δ_1
Free	Free	Δ_1
Splinted	Free	E
Free	Splinted	S

Table 6.1: Arm splint and target trajectory combinations

form the basis of the splinting restraints. Kinematic and static force transformations from the (α, β) manipulandum coordinates to the fixed base Cartesian frame were presented in Section 4.2.3. Further transformations from this Cartesian description to arm coordinates based on shoulder and elbow angle are derived in Appendix C for the general case in which a fastener between the wrist splint and the handle provides the extra degrees of freedom required for the planar arm to conform to the manipulandum handle workspace. To examine the dynamics of the arm, it is necessary to have reliable displacements, velocities, and accelerations as a result of the kinematic transformations as well as reasonable estimates of the inertia distribution of the limb. A variety of methods are available for estimating limb segment inertias *in vivo*, ranging from anthropometric scaling techniques to CT and magnetic resonance imaging.[7]

Once the kinematics at the various transformation stages and the arm joint dynamic torques have been computed, both time and frequency domain data analysis can proceed. Time domain evaluation is needed to determine whether random perturbations are able to entrain a particular tremor oscillation. Frequency domain techniques are important for identifying the frequency bands associated with tremorous activity, and are helpful for determining the magnitude of the oscillations in these bands.

The incorporation of pursuit tracking in the experimental protocol not only indicates to the subject the motion desired, but also permits the fidelity of voluntary response to be

[7]See reference [33] for a review of body segment parameter estimation techniques.

evaluated. In cases where the standard autospectrum methods such as those used to obtain the spectra in Figure 6.2 prove to be insufficient for isolating statistically significant tremor, the presence of a pursuit target signal may still allow tremor to be extracted. Using slightly more sophisticated techniques [10], the coherent activity between the target and response can be removed, leaving a remnant spectrum containing response components that cannot be predicted linearly from the target signal. Based on the assumption that perfect target pursuit results from *linear* tracking, the remnant spectrum thus is comprised of nonlinear and noise components only, from which the tremor can then be more readily identified.

6.2.5 Potential Observations and Interpretation

Tremor Coupling

The results of frequency domain analysis will help determine what, if any, relation exists between tremors at the elbow and tremors at the shoulder. Tremors in different joints at unrelated frequencies would be independent of each other. If tremor is present in both joints at the same frequency, and the tremor *torque* magnitude driving one of the joints does not change when the other is splinted, the tremor at the splinted joint would be the result of mechanical coupling (*i.e.*, Coriolis and centripetal terms). If tremor torques at one joint are reduced by the imposition of splinting on the other, neural factors would be implicated for the oscillations at both joints—either due to independent sources or through sensory coupling. However, if separate tremor oscillations, judged not to be coupled mechanically according to the splinting argument above, maintain a constant phase relation when one of the oscillations is reset by a perturbation, then neural coupling would be indicated.

Tremogenic Mechanisms

If the frequency domain data were to show a particular tremor's frequency to be decreased by augmented inertia or elevated by augmented stiffness at the hand, limb and load

biomechanics would be a factor in generating the tremor. Time domain histories can be evaluated to detect whether random limb perturbations were able to re-entrain any particular oscillation. Clearly, short-term entrainment would be detected in the die-away mechanical response of the limb to the perturbation. However, if a tremor's frequency is not affected by changes in inertia or stiffness, and it remains in the new phase set by the perturbation then a reflex feedback role in sustaining the tremor is likely. The absence of changes in frequency with added inertia or stiffness, combined with the failure to be re-entrained by mechanical perturbations, would indicate that the tremor has a central source and is not altered by peripheral inputs to the limb.

6.3 Protocol Feasibility Study

The feasibilty of aligning a subject's arm with respect to the manipulandum and of calculating its joint kinematics based on manipulandum sensor measurements was examined in tests conducted with a planar armlike linkage similar in configuration to the one illustrated in Figure 3.4. This linkage is the skeleton of the "Controlled Energy Dissipation Orthosis" developed by Baiges [19] for the suppression of tremor by viscous damping. The linkage itself was structurally stiff and had low friction. The linkage's base was anchored to a sturdy, general purpose "subject testing" chair developed by Maxwell [98].

To conduct these tests, a mechanical coupling was built to provide the kinematic compatibility required for the planar orthosis to be joined to the manipulandum linkage. This "compatibility" coupling, shown in Figure 6.5 attached to the spherical handgrip, adds three more degrees of freedom to the end of the handle linkage, which when combined with the three degrees of freedom already present in the manipulandum handle (α axis, β axis, plus rotation about the handle shaft due to the force transducer moment cancellation bearings), permits general six degree of freedom position and orientation.

Prior to the tests, the manipulandum and orthosis linkage were leveled using a bull's eye level. They were then joined together through the "compatibility" coupling, and positioned such that the manipulandum handle was upright and the orthosis linkage

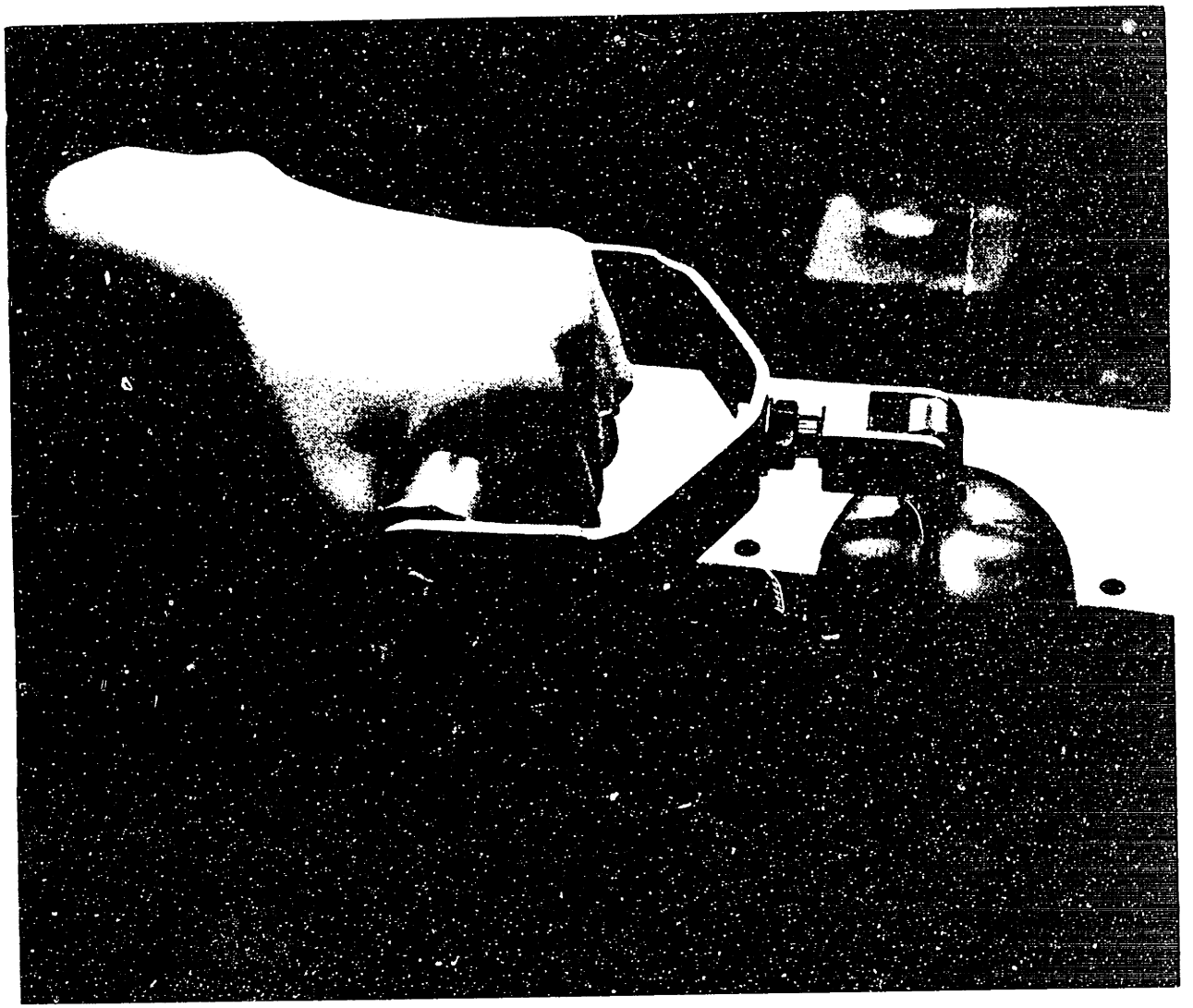

Figure 6.5: Handle linkage to planar arm "compatibility" coupling. The three aditional degrees of freedom provided by the coupling are all ball bearing mounted. They include, begining from the hand, a pitch axis through the center of the grip bar, a roll axis, and a second pitch axis at the top of the manipulandum's spherical handgrip. Refering to Appendix C, the distance between the two pitch axes is equivalent to L_H, the length of the third link that is attached distal to the planar arm linkage.

was in the nominal subject arm position illustrated in Figure 6.3. The position of the manipulandum cart and the test chair base were secured by lowering their respective jack screw footpads to the floor.

Two tests were conducted. In the first test, the linkage "elbow" joint was locked at approximately 90 degrees (the elbow angle in Figure 6.3), and the "shoulder" was slowly moved back and forth while the manipulandum sensor outputs were sampled by the host LSI-11/23 computer. In the second test, the sensors were sampled while the linkage "shoulder" was locked at approximately zero degrees (the shoulder angle in Figure 6.3), and the "elbow" was moved back and forth. All motions were slow and smooth to minimize inertial forces that could cause deflection of the orthosis links or the manipulandum handle, or motion of the test chair. The manipulandum motors were not powered during these tests.

The transformations of the kinematic measurement data from these tests were carried out in two stages: the first from (α, β) manipulandum coordinates to a fixed Cartesian frame as described in Section 4.2.3; the second from the fixed Cartesian frame to arm linkage joint kinematics as described in Appendix C. The length parameters necessary for the second set of transformations were measured from the projection cast by the orthosis linkage onto the floor, as determined by suspending a plumb bob from each joint axis.

The arm linkage joint displacements computed from the manipulandum-based measurements for each test are shown in Figure 6.6. In either test, the displacement as *computed* for the joint which was actually locked seemed to indicate that motion, although small (approximately one-twentieth the magnitude of displacements in the free joint), was still present. The apparent ± 0.2 degree angle variation for the locked joints correspond to less than ± 1.8 mm (± 0.07in) at the manipulandum handle. The *computed* joint velocities demonstrated similar results. However, since the back and forth motions were so slow, computed accelerations in both the free and locked joints were negligible.

Examination of the clamping blocks that were used to immobilize the orthosis link-

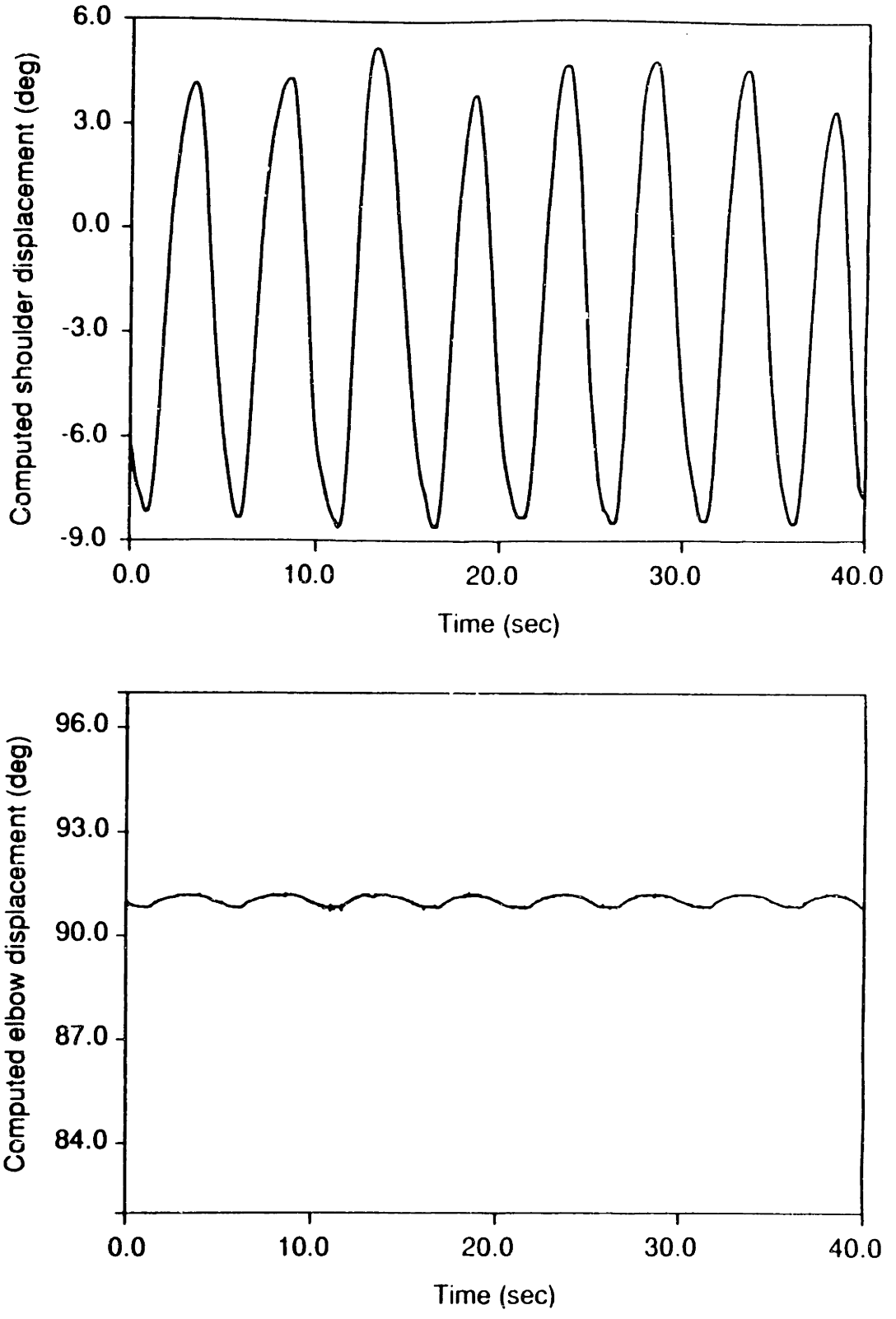

Figure 6.6: Locked joint test trajectoriess. (a) Elbow joint fixed. *Top*) Computed shoulder joint angle, *bottom*) computed elbow joint angle.

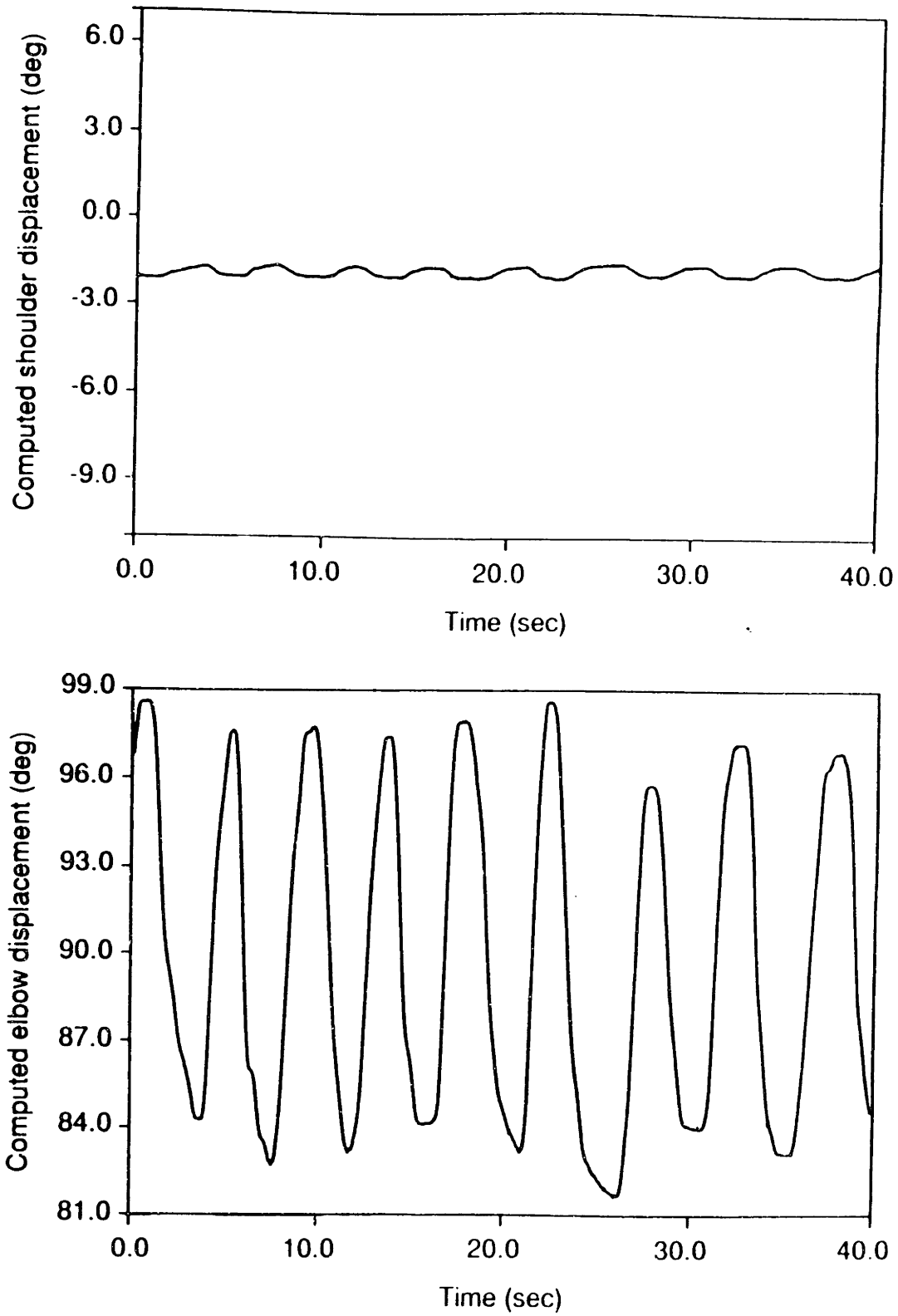

Figure 6.6 (continued): Locked joint tests trajectories. (b) Shoulder joint fixed. *Top*) Computed shoulder joint angle, *bottom*) computed elbow joint angle.

age's joints confirm that they should have been very effective when in place, especiallv at the "elbow." Since the joint angles are determined from displacements measured by the manipulandum shaft encoders, the fact that they are not completely consistent with the locked joint experiment condition (*i.e.*, not constant) indicates that the sensed α and β coordinate trajectories did not match those expected for rigid link mechanism assumption upon which Appendix C is based. One potential source for the "computed" motion at the locked joints may be that structural compliance in the setup—the orthosis links, its test chair base, the compatibility coupling, and the manipulandum handle mechanism—affected the location of the arm linkage endpoint, *i.e.*, at its interface with the manipulandum. This is not particularly likely since friction (that might possibly restrict joint motion and cause link bending) and accelerations (which might contribute to link bending by inertial forces) were very small. The second, and more plausible, possibility is that, due to the imprecision of the bull's eye level alignment method, the orthosis plane was not exactly parallel to the manipulandum frame's base plane, as was assumed for the development of the transformations described in Appendix C. Thus, the "shoulder" and "elbow" axes were not perfectly perpendicular to the manipulandum frame's base plane and the formulation, which now incorrectly assumes that all arm rotation can be projected onto the manipulandum xy base, has no choice but to assign out-of-plane rotational motion which is causing small deviations in α and β measurements to the locked joint of the planar arm linkage.

The results of these tests have important implications for the splinting of human arm joints in the protocol described in Section 6.2. The difficulties of aligning the orthosis linkage parallel to the manipulandum base and preventing structural deflection will be compounded with a human subject. Clearly, human flesh is much more compliant that the rigid orthosis links. Furthermore, a human subject will inevitably shift position somewhat in a chair; the orthosis was bolted to the test chair. The potential for both of these effects to distort the measurement of small amplitude tremor motions must be dealt with.

Rather than attempting to develop more rigorous arm restraints, it is suggested that instrumention such as the TRACK system for 3-D kinematic data acquisition, currently in the Newman Laboratory [94], could augment the quantification of actual arm link orientation and position by supplying additional measurements. By incorporating the augmented capability to measure whole arm kinematics, there would not be a need to be solely dependent upon the two degree of freedom manipulandum instrumentation to reconstruct arm motion, thus alleviating requirements for external splinting and restraints for some human experimentation applications. However, the role of splints and fixtures similar to the compatibility coupling would have to be preserved if the force capabilities of the arm are to be limited to the two degrees of freedom in which the manipulandum can apply loads.

Chapter 7

Accomplishments and Further Work

7.1 Summary

This thesis has described the development of a virtual environment system for the study of human arm tremor. The system consists of a manual interface for the application of actively controlled mechanical loads to the arm in two degrees of freedom and a visual interface to present pursuit tracking tasks. While a number of other kinesthetic interfaces have been developed to couple human operators to virtual environments (some of much greater complexity than the system described here), none have been built with the specific goal of enabling the study of tremor.

The accomplishments of this thesis are summarized here.

- An outcome of choosing design specifications to meet the needs of tremor research is higher manual interface bandwidth than in comparable systems. Because the computing facility available for the real-time control of this system was no more advanced than the computers used in comparable systems, the approach followed to obtain this performance was to design the hardware so as to eliminate many of the numerically intensive facets of controller implementation.

  The primary measure taken to prevent computational bottlenecks in the control and supervision of the system was the selection of a mechanical configuration for

the manual interface that would reduce the need for geometric transformations. A number of other factors drove the design detail, including the need for backdriveability and low inertia.

- The resulting design for the manual interface is a novel spherical five-link closed chain mechanism that joins the shafts of two fixed base electric motors to a handle which is grasped by the human subject. This "semi-direct-drive" gimbal mechanism does not employ belts, cables, gears, or flexible driveshafts. All motion within the gimbal occurs across rotary ball bearing joints. As a consequence, the gimbal *itself* has little friction or backlash and is completely backdriveable. Most importantly, with this mechanism, the two motors are approximately decoupled over the handle workspace.

- Because the motors are nearly decoupled, and since the handle workspace is approximately planar, orthogonal mechanical loads at the handle endpoint can be implemented by controlling the actuators in joint axis coordinates without the computation of geometric transformations. The computational burden for real-time control of the system is further reduced by two additional features: direct measurement of displacement, velocity, and acceleration to avoid numerical differentiation of kinematic variables; and a hardwired digitally supervised analog controller that eliminates data sampling (and its inherent bandwidth limitations) for the simulation of many simple loads.

- The dynamic characteristics of the unpowered manual interface were determined from measurements and modelling of system properties. Because of the inclusion of flexible couplings between the motors and the gimbal mechanism to relax alignment constraints during fabrication, the mechanical bandwidth of the interface is limited by its first mode resonance to approximately 50 Hz. Although this value is lower than what it would be without the flexible couplings, it is well above the needs for the proposed tremor research.

- The ability of the active system to simulate a variety of mechanical loads under computer control was demonstrated, including simple springs, dampers, and inertias. Also observed was the ability of negative force feedback to mask some of the intrinsic friction and inertia of the manual interface as perceived by the human subject.

  The challenge of simulating more complicated physical objects—walls and detents—was successfully met. The simulation of these two objects, in addition to the ability to mask friction and inertia of the interface, are commonly used subjective determinants of how effective a "force feel" device will be in simulating any general load. In the course of examining wall simulations, the importance of controller lag on the quality of the simulation "feel" was shown.

- The update rate of the system was evaluated for operation during a standard tremor loading experiment. This case entails the simulation of a simple load field (*i.e.*, spring, damper, and inertia) surrounded by a four wall safety enclosure concurrent with the generation of a pursuit tracking task on the visual display and the storage of data from all transducers. In this instance, the physical simulation controller was updated by the host computer at 1000 Hz. As a benchmark for comparison, the maximum host computer rate for data sampling and storage alone is 1400 Hz.

- The utility of the system as a tremor research tool was demonstrated in a set of informal experiments with a tremor disabled subject. The data from preliminary tests showed that tremor frequency and magnitude, in two degrees of freedom, could be altered with the application of mechanical loads simulated at the manual interface. In addition, a protocol for more detailed, two degree of freedom experiments to investigate tremogenic mechanisms was explored.

7.2 Recommendations for Further Work

7.2.1 Continued System Development

By actually building the virtual environment system and evaluating its performance, insight was developed on how the system could be improved in the future, either through redesign or the selection of different components. Recommendations are as follows:

Gimbal mechanism. The precise alignment requirements for the fabrication and assembly of the gimbal and for its attachment to the fixed base motors necessitated the use of flexible couplings. Because of these couplings, support posts were introduced to increase the vertical stiffness of the handle mechanism.

Ensuring that all three gimbal axes (α, β, and ξ) intersect at a single point turns out to be the only critical issue in assembling the gimbal. Provision for adjusting the axes' intersection, combined with precision machining, would eliminate the need for flexible couplings and the support posts as well. The result would be a much stiffer structure with the same low friction as the current gimbal. A consequence of the improved stiffness would be a higher mechanical bandwidth.

Motors. The brush and bearing friction in the present motors account for most of the friction in the manual interface. In addition, higher torque levels (approaching the static capabilities of the human arm), with the same time response characteristics as the present motors are desirable. These two factors make it advisable to re-examine brushless motors, especially if torque ripple becomes less of a factor as more advanced motor commutation algorithms are made possible by more powerful microcontrollers or DSP ICs.

Power amplifiers. The present servo amplifiers switch at only 6 kHz. This sound is an irritant to the subject and can provide audible cues on the state of actuator operation. Selecting amplifiers with a higher inaudible switching frequency would eliminate this problem. Changing to a linear amplifier would help to alleviate

electronic noise in the vicinity of the virtual environment system as well.

Sensors. The present force transducer measures only two components tangent to the spherical surface workspace. Unfortunately, the handle linkage can be moved by externally applied moments as well. Purchasing or building a four axis (or greater) force transducer would allow measurement of all moments and forces that can cause handle motion. Use of a six axis transducer would permit any general human manual output to be studied. If a commercial transducer is considered, the standard serial interface should be avoided due to greatly reduced data transmission rates.

Using better damped accelerometers would improve the quality of acceleration measurements, and might allow the range of simulated augmented inertia to be extended further. Micromachining technologies are beginning to make inexpensive monolithic accelerometers commercially available.

Computing. More powerful, relatively inexpensive single board computers, industrial microcontrollers, and DSP boards in multi-processor environments are now widely available (they were not at the outset of this project). This technology could be incorporated into the system to enhance controller capabilities in the simulation of complex environments as well as to further increase bandwidth. They may also serve to supplant the hardwired analog controller in the CIU if data throughputs are sufficient.

7.2.2 Experimental Studies

With the system now in place, research in a number of areas is envisioned. These fields include:

Tremor. The study of whole arm tremor should proceed, following the protocol proposed in Chapter 6. Of special interest would be the inclusion of the TRACK kinematic data acquisition system to monitor whole limb motion, both when the arm is splinted and when it is free, in order to determine the effectiveness of planar

constraints. The incorporation of the six axis force transducer suggested above into the apparatus, combined with kinematic data from the TRACK system, would permit more general evaluation of six degree of freedom arm motion and forces during interaction with the two dimensional virtual environment.

Virtual environments and telepresence. Other potential research appications for the virtual environment system could develop in any area which involves the study of dynamic interaction between the human arm and precisely controlled external environments. Among these areas are teleoperation-telepresence and virtual environment research where the dynamics of interaction play a key role in the perception and accurate manipulation of remote or virtual objects by the human operator.

Simulation psychophysics. A promising area of research with this system, because of its high quality kinesthetic presentation, would be an exploration of the essential features (*i.e.*, the minimum technology) required to represent objects or environments. One immediate line of research could further explore the importance of bandwidth (or update rate) of the manual interface for effective simulation. The effect of visual and audio (a capabilty of the current video display computer) feedback in altering these essential features could also be examined.

Manipulator control. Finally, the system could be employed in studying control of motion and interaction at the remote end of teleoperated systems and in autonomous robotic manipulators. The reduction of computation enabled by the geometry of this system in implementing two degree of freedom impedance control may be applicable to the investigation of manipulator control strategies.

Bibliography

[1] *General-Aviation Control Loader.* NASA Technical Support Package LAR-13707, Langley Research Center, Hampton, VA.

[2] *Stedman's Medical Dictionary*, 23rd Edition. Williams and Wilkins Co., Baltimore, 1976.

[3] *Bulletin of the Division of Electrical Engineering.* National Research Council of Canada, 2(3):3, 1983.

[4] *Selspot Today.* Selspot AB, Molndal, Sweden, March 1987.

[5] C. J. Abul-Haj. *Elbow-Prosthesis Emulation: A Technique for the Quantitative Assessment of an Assistive Device.* PhD thesis, Department of Mechanical Engineering, M.I.T., Cambridge, MA, June 1987.

[6] J. J. Ackmann, A. Sances Jr., S. J. Larson, and J. B. Baker. Quantitative evaluation of long-term Parkinson tremor. *IEEE Transactions on Biomedical Engineering*, BME-24(1):49–56, 1977.

[7] B. D. Adelstein. *Peripheral Mechanical Loading and the Mechanism of Abnormal Intention Tremor.* Master's thesis, Department of Mechanical Engineering, M.I.T., Cambridge, MA, July 1981.

[8] B. D. Adelstein, M. L. Aisen, and M. J. Rosen. Essential tremor characteristics under isometric and unconstrained conditions. *Neurology*, 37, Supplement 1:263, 1987.

[9] B. D. Adelstein and M. J. Rosen. The effect of mechanical impedance on abnormal intention tremor. In *Proceedings of the 9th Northeast Bioengineering Conference*, pages 205–209, New Brunswick, NJ, March 1981. Permagon Press.

[10] B. D. Adelstein and M. J. Rosen. Tremor mechanism identification by peripheral limb loading. In *Proceedings of the 8th Annual Conference of the IEEE Engineering in Medicine and Biology Society*, volume 3, pages 1872–1875, Fort Worth, TX, November 1986.

[11] M. L. Aisen and N. G. La Rocca. Quantitative assessment of tremor in multiple sclerosis patients: A new technique. *Assistive Technology*, 1(1):3–6, 1989.

[12] J. W. Albers, A. R. Potvin, W. W. Tourtellotte, R. W. Pew, and R. F. Stribley. Quantification of hand tremor in the clinical neurological examination. *IEEE Transactions on Biomedical Engineering*, BME–20(1):27–37, 1973.

[13] R. J. Anderson and M. W. Spong. Hybrid impedance control of robotic manipulators. *IEEE Journal of Robotics and Automation*, 4(5):549–556, 1988.

[14] H. Asada and K. Youcef-Toumi. Analysis and design of a direct-drive arm with a five-bar-link parallel drive mechanism. *ASME Journal of Dynamic Systems, Measurement and Control*, 106:225–230, 1984.

[15] H. Asada and K. Youcef-Toumi. *Direct-Drive Robots: Theory and Practice.* MIT Press, Cambridge, MA, 1987.

[16] K. J. Åström and B. Wittenmark. *Computer Controlled Systems: Theory and Design.* Prentice Hall, Englewood Cliffs, N. J., 1984.

[17] A. Atkin, V. B. Brooks, and S. Pischinger. A torque device for studies of primate limb movements. *Physiology and Behavior*, 12:127–129, 1974.

[18] W. D. Atkinson, K. E. Bond, G. L. Tribble, and K. R. Wilson. Computing with feeling. *Computers and Graphics*, 2:97–103, 1977.

[19] I. J. Baiges and M. J. Rosen. Development of a whole-arm orthosis for tremor suppression. In *Proceedings of the 12th Annual RESNA Conference*, pages 290–291, New Orleans, LA, 1989.

[20] Baltimore Therapeutic Equipment Co., Hannover, MD. BTE Work Simulator. Product literature.

[21] J. J. Batter and F. P. Brooks Jr. GROPE-1: A computer display to the sense of feel. In *Information Processing 1971, Proceedings of the IFIP Congress 71*, pages 759–763, Ljubljana, Yugoslavia, August 1971. North-Holland Publishing Company.

[22] A. K. Bejczy and K. Corker. Manual control communication in space teleoperation. In *Theory and Practice of Robots and Manipulators, RoManSy '84, Proceedings of the 5th International CISM-IFToMM Symposium*, pages 224–232, 1984.

[23] A. K. Bejczy and M. Handlykken. Generalization of bilateral force-reflecting control of manipulators. In *Theory and Practice of Robots and Manipulators, RoManSy '81, Proceedings of the 4th International CISM-IFToMM Symposium*, pages 242–255, Zaborow, Poland, September 1981.

[24] A. K. Bejczy and J. K. Salisbury. Kinesthetic coupling between operator and remote manipulator. In *Proceedings of the ASME International Computer Technology Conference*, pages 197–211, San Francisco, CA, 1980.

[25] C. Billian and G. I. Zahalak. A programmable limb testing system (and some measurements of intrinsic muscular and reflex-mediated stiffnesses). *Journal of Biomechanical Engineering*, 105:6–11, 1983.

[26] Biodex Corp., Shirley, NY. Product literature.

[27] W. Birg, M. Klar, W. U. Weitbrecht, and F. Mundinger. Die Objektivierung von Tremor und kinetischen Storungen mit Hilfe eines Prozeßrechners. *Fortschr. Neurol. Psychiat.*, 47:326–330, 1979.

[28] W. Book and L. Field. Experiments relating task and manipulator characteristics to performance. In *Proceedings of the International Conference on Cybernetics and Society*, pages 225–226, Washington, DC, September 1977.

[29] W. J. Book and D. A. Ruis. Control of robotic exercise machine. In *Proceedings of 1981 Joint Automatic Control Conference*, Charlottesville, VA, June 1981. Paper number WA-2A.

[30] B. Boshes. Measurement of tremor. *Journal of Neurosurgery*, 24:324–330, 1966.

[31] V. B. Brooks. *The Neural Basis of Motor Control.* Oxford University Press, New York, 1986.

[32] F. P. Brooks Jr. The computer "scientist" as toolsmith—studies in interactive computer graphics. In B. Gilchrist, editor, *Information Processing 1977, Proceedings of the IFIP Congress 77*, pages 625–634, Toronto, August 1977. North-Holland Publishing Company.

[33] G. A. Brown. *Determination of Body Segment Parameters Using Computerized Tomography and Magnetic Resonance Imaging.* Master's thesis, Department of Mechanical Engineering, M.I.T., Cambridge, MA, August 1987.

[34] D. B. Calne and M. H. Lader. Electromyographic studies of tremor using an averaging computer. *Electroencephalography and Clinical Neurophysiology*, 26:86–92, 1969.

[35] M. W. J. Carmichael. Elementary joystick mechanisms. In *Proceedings of the Fifth World Congress on Theory of Machines and Mechanisms*, volume 2, pages 1464–1467, Montreal, July 1979. The American Society of Mechanical Engineers.

[36] R. A. Chase, J. K. Cullen Jr., S. C. Sullivan, and A. K. Ommaya. Modification of intention tremor in man. *Nature*, 206(4983):485–487, 1965.

[37] P. R. Chaware and C. Amarnath. A novel wrist joint design for manipulators. In *International Symposium on Design and Synthesis*, pages 479–482, Tokyo, July 1984.

[38] W. L. Chen. Simulation for training and decision-making in large-scale control systems, Part 2: Civil aircraft pilot trainers. *Simulation*, 35(2):42–44, 1980.

[39] T. R. Colburn and E. V. Evarts. Use of brushless DC torque motors in studies of neuromuscular function. In J. E. Desmedt, editor, *Cerebral Motor Control in Man: Long Loop Mechanisms, Progress in Clinical Neurophysiology, Volume 4*, pages 153–166. S. Karger, Basel, 1978.

[40] J. E. Colgate. *The Design of a Dynamics Measuring Device.* Master's thesis, Department of Mechanical Engineering, M.I.T., Cambridge, MA, January 1986.

[41] J. E. Colgate. *The Control of Dynamically Interacting Systems.* PhD thesis, Department of Mechanical Engineering, M.I.T., Cambridge, MA, August 1988.

[42] R. Contini. Body segment parameters, part II. *Artificial Limbs*, 16(1):1–19, 1972.

[43] K. M. Corker. *Investigation of Neuromotor Control and Sensory Sampling in Bilateral Teleoperation.* PhD thesis, University of California, Los Angeles, CA, 1984.

[44] S. L. Cotter. *Nonlinear Feedback Control of Manipulator Endpoint Impedance.* Master's thesis, Department of Mechanical Engineering, M.I.T., Cambridge, MA, July 1982.

[45] P. D. Cussons, P. B. C. Matthews, and R. B. Muir. Enhancement by agonist or antagonist muscle vibration of tremor at the elastically loaded human elbow. *Journal of Physiology (London)*, 302:443–461, 1980.

[46] I. Darian-Smith. The sense of touch: Performance and peripheral neural processes. In I. Darian-Smith, editor, *Handbook of Physiology: Section I The Nervous System III*, pages 739–787. Oxford University Press, 1984.

[47] N. S. Davitashvili. Designing five-link hinged mechanisms taking into account the angle drive. *Mechanism and Machine Theory*, 18(6):481–489, 1983.

[48] N. Diffrient, A. R. Tilley, and D. Harman. *Humanscale.* MIT Press, Cambridge, MA, 1981.

[49] W. K. Durfee. *Task Control with an Electrically Stimulated Antagonist Muscle Pair.* PhD thesis, Department of Mechanical Engineering, M.I.T., Cambridge, MA, June 1985.

[50] R. J. Elble. Physiologic and essential tremor. *Neurology*, 36:225–231, 1986.

[51] R. J. Elble, C. Higgins, and C. J. Moody. Stretch reflex oscillations and essential tremor. *Journal of Neurology, Neurosurgery, and Psychiatry*, 50:691–698, 1987.

[52] R. J. Elble and J. E. Randall. Motor-unit activity responsible for 8- to 12-Hz component of human physiological finger tremor. *Journal of Neurophysiology*, 39(2):370–383, 1976.

[53] S. D. Eppinger and W. P. Seering. Understanding bandwidth limitations in robot force control. In *Proceedings of the 1987 IEEE International Conference on Robotics and Automation*, pages 904–909, Raleigh, NC, April 1987.

[54] S. D. Eppinger and W. P. Seering. Modeling robot flexibility for endpoint force control. In *Proceedings of the 1988 IEEE International Conference on Robotics and Automation*, pages 165–170, Philadelphia, PA, April 1988.

[55] S. Fahn. Cerebellar tremor: Clinical aspects. In L. J. Findley and R. Capildeo, editors, *Movement Disorders: Tremor*, pages 355–363. Oxford Univeristy Press, New York, 1984.

[56] I. C. Faye. *An Impedance Controlled Manipulandum for Human Movement Studies.* Master's thesis, Department of Mechanical Engineering, M.I.T., Cambridge, MA, June 1986.

[57] K. Flowers. Ballistic and corrective movements on an aiming task. *Neurology*, 25:413–421, 1975.

[58] J. D. Foley and A. Van Dam. *Fundamentals of Interactive Computer Graphics.* Addison-Wesley, Reading, MA, 1984.

[59] C. P. Fong and K. Corker. Force/torque feedback task simulation for advanced remote manipulators. In *Proceedings of the 1984 Summer Computer Simulation Conference*, pages 1229–1234, Boston, July 1984.

[60] J. R. Fox and J. E. Randall. Relationship between forearm tremor and the biceps electromyogram. *Journal of Applied Physiology*, 29:103–108, 1970.

[61] G. F. Franklin, J. D. Powell, and A. Emami-Naeini. *Feedback Control of Dynamic Systems.* Addison-Wesley, Reading, MA, 1986.

[62] H.-J. Freund, H. Hefter, V. Homberg, and K. Reiners. Determinants of tremor rate. In L. J. Findley and R. Capildeo, editors, *Movement Disorders: Tremor*, pages 195–204. Oxford Univeristy Press, New York, 1984.

[63] H.-J. Freund, H. Hefter, V. Homberg, and K. Reiners. Differential diagnosis of motor disorders by tremor analysis. In L. J. Findley and R. Capildeo, editors, *Movement Disorders: Tremor*, pages 27–35. Oxford Univeristy Press, New York, 1984.

[64] J. D. Frost. Triaxial vector accelerometry: A method for quantifying tremor and ataxia. *IEEE Transactions on Biomedical Engineering*, BME-25(1):17-27, 1978.

[65] A. A. Goldenberg. Force and impedance control of robot manipulators. In *Modeling and Control of Robotic Manipulators and Manufacturing Process, ASME Winter Annual Meeting, Volume DSC-6*, pages 161-168, Boston, December 1987.

[66] A. A. Goldenberg. Implementation of force and impedance control in robot manipulators. In *Proceedings of the 1988 IEEE International Conference on Robotics and Automation*, pages 1626-1632, Philadelphia, PA, April 1988.

[67] J. C Boileau Grant. *An Atlas of Anatomy.* The Williams and Wilkins Co., Baltimore, 1962.

[68] M. A. Gresty and L. J. Findley. Definition, analysis and genesis of tremor. In L. J. Findley and R. Capildeo, editors, *Movement Disorders: Tremor*, pages 15-26. Oxford Univeristy Press, New York, 1984.

[69] S. S. Hacisalihzade, M. Mansour, and C. Albani. Optimization of symptomatic therapy in Parkinson's disease. *IEEE Transactions on Biomedical Engineering*, BME-36(3):363-372, 1989.

[70] D. G. Hagner and J. G. Webster. Telepresence for touch and proprioception on teleoperator systems. *IEEE Transactions on Systems, Man, and Cybernetics*, 18(6):1020-1023, 1988.

[71] M. Handlykken and T. Turner. Control system analysis and synthesis for a six degree-of-freedom universal force-reflecting hand controller. In *Proceedings of the 19th IEEE Conference on Decision and Control*, pages 1197-1205, Albuquerque, NM, 1980.

[72] D. A. Harris and E. Henneman. Feedback signals from muscle and their efferent control. In V. B. Mountcastle, editor, *Medical Physiology*, pages 703-717. The C. B. Mosby Company, St. Louis, 1980.

[73] R. L. Hewer, R. Cooper, and M. H. Morgan. An investigation into the value of treating intention tremor by weighting the affected limb. *Brain*, 95:579-590, 1972.

[74] N. Hogan. Impedance control: An approach to manipulation: Part I—Theory. *ASME Journal of Dynamic Systems, Measurement and Control*, 107:1-7, March 1985.

[75] N. Hogan. Impedance control: An approach to manipulation: Part II—Implementation. *ASME Journal of Dynamic Systems, Measurement and Control*, 107:8-16, March 1985.

[76] N. Hogan. Impedance control: An approach to manipulation: Part III—Applications. *ASME Journal of Dynamic Systems, Measurement and Control*, 107:17–24, March 1985.

[77] J. M. Hollerbach. A recursive Lagrangian formulation of manipulator dynamics and a comparative study of dynamics formulation complexity. *IEEE Transactions on Systems, Man and Cybernetics*, SMC–10(11):730–736, 1980.

[78] V. Homberg, H. Hefter, K. Reiners, and H.-J. Freund. Differential effects of changes in mechanical limb properties on physiological and pathological tremor. *Journal of Neurology, Neurosurgery, and Psychiatry*, 50:568–579, 1987.

[79] I. W. Hunter, S. Lafontaine, P. M. F. Nielsen, P. J. Hunter, and J. M. Hollerbach. A tele-microrobot for manipulation and dynamic mechanical testing of single living cells. In *Proceedings of the IEEE Micro Electro Mechanical Systems Conference*, pages 102–106, Salt Lake City, UT, February 1989.

[80] Jaeco, Orthopedic Specialties, Hot Springs, AR. Jaeco Arm Positioner. Product literature.

[81] H. R. Jex. Four critical tests for control-feel simulators. In *Proceedings of the 23rd Annual Conference on Manual Control*, Cambridge, MA, 1988.

[82] G. C. Joyce and P. M. H. Rack. The effects of load and force on tremor at the normal human elbow joint. *Journal of Physiology (London)*, 240:375–396, 1974.

[83] K. Kaneko, I. Yamada, and K. Itao. A spherical DC servo motor with three degrees of freedom. In *Symposium on Robotics, ASME Winter Annual Meeting, Volume DSC-11*, pages 433–443, Chicago, November 1988.

[84] H. Kazerooni, P. K. Houpt, and T. B. Sheridan. Robust compliant motion for manipulators, Part II: Design method. *IEEE Journal of Robotics and Automation*, RA-2(2):93–105, 1988.

[85] P. J. Kilpatrick. *The Use of a Kinesthetic Supplement in an Interactive Graphics System.* PhD thesis, Department of Computer Science, University of North Carolina at Chapel Hill, Chapel Hill, NC, 1987.

[86] G. V. Kondraske. A capacitive displacement transducer for tremor measurement. In *Proceedings of the Sixth Annual Conference of the IEEE Engineering in Medicine and Biology Society*, pages 432–435, Los Angeles, CA, September 1984.

[87] Y. Lamarre and M. Weiss. Harmaline-induced rhythmic activity of alpha and gamma motoneurons in the cat. *Brain Research*, 63:430–434, 1973.

[88] K.-M. Lee and S. Arjunan. Force/torque sensing and micro-motion manipulation of a spherical stepping wrist motor. In *Proceedings of 1988 American Control Conference*, pages 950–955, Atlanta, GA, June 1988.

[89] K.-M. Lee, G. Vachtsevanos, and C. Kwan. Development of a spherical stepper wrist motor. In *Proceedings of the 1988 IEEE International Conference on Robotics and Automation*, pages 267–272, Philadelphia, PA, April 1988.

[90] R. G. Lee and R. B. Stein. Resetting tremor by mechanical perturbations: A comparison of essential tremor and parkinsonian tremor. *Ann. Neurol.*, 10:523–531, 1981.

[91] O. C. J. Lippold. Oscillation in the stretch reflex arc and the origin of the rhythmical, 8–12 c/s component of physiological tremor. *Journal of Physiology (London)*, 206:359–382, 1970.

[92] S. M. Livingstone and D. I. Crecraft. Design of an artificial elbow: An electromechanical solution. In *Basic Problems of Prehension, Movement, and Control of Artificial Limbs*, pages 32–36, London, November 1968. The Institution of Mechanical Engineers.

[93] J. M. Mansfield. *The Design of a Lightweight Elbow Prosthesis Simulator.* Master's thesis, Department of Mechanical Engineering, M.I.T., Cambridge, MA, May 1988.

[94] P. K. Mansfield. *A Large Volume Kinematic Data Acquisition and Reduction System.* PhD thesis, Department of Mechanical Engineering, M.I.T., Cambridge, MA, February 1990. To be submitted.

[95] T. R. Mariano. *Simulation of the Man-Machine Interface for Upper Limb Neural Prostheses.* Master's thesis, Department of Mechanical Engineering, M.I.T., Cambridge, MA, August 1987.

[96] C. D. Marsden, J. C. Meadows, G. W. Lange, and R. S. Watson. Variations in human physiological finger tremor, with particular reference to changes with age. *Electroencephalography and Clinical Neurophysiology*, 27:169–178, 1969.

[97] P. B. C. Matthews and R. B. Muir. Comparison of electromyogram spectra with force spectra during human elbow tremor. *Journal of Physiology (London)*, 302:427–441, 1980.

[98] S. M. Maxwell. PhD thesis in progress, Department of Mechanical Engineering, M.I.T., Cambridge, MA.

[99] McFadden Systems Inc., Santa Fe Springs, CA. Product literature.

[100] T. A. McMahon. *Muscles, Reflexes, and Locomotion.* Princeton University Press, Princeton, New Jersey, 1984.

[101] V. Milenkovic. New nonsingular robot wrist design. In *Robots 11 Conference Proceedings*, Chicago, IL, April 1987.

[102] O. Ming, M. Pique, J. Hughes, N. Srinivasan, and F. P. Brooks Jr. Using a manipulator for force display in molecular docking. In *Proceedings of the 1988 IEEE International Conference on Robotics and Automation*, pages 1824–1829, Philadelphia, PA, April 1988.

[103] P. Molina-Negro and J. Hardy. Semiology of tremors. *Canadian Journal of Neurological Sciences*, 2:23–29, 1975.

[104] M. H. Morgan, R. L. Hewer, and R. Cooper. Intention tremor—a method of measurement. *Journal of Neurology, Neurosurgery, and Psychiatry*, 38:253–258, 1975.

[105] R. S. Mosher. From Handyman to Hardiman. *Society of Automotive Engineers Transactions*, 76:588–597, 1967. Report Number 670088.

[106] W. R. Murray. *Essential Factors in Modeling the Modulation of Impedance about the Human Elbow.* PhD thesis, Department of Mechanical Engineering, M.I.T., Cambridge, MA, May 1988.

[107] F. A. Mussa-Ivaldi, N. Hogan, and E. Bizzi. Neural, mechanical, and geometric factors subserving arm posture in humans. *Journal of Neuroscience*, 5(10):2732–2743, October 1985.

[108] A. M. Noll. *Man-Machine Tactile Communication.* PhD thesis, Department of Electrical Engineering, Polytechnic Institute of Brooklyn, Brooklyn, NY, June 1971.

[109] J. D. B. Paines. *Optimization of Manual Control Dynamics for Space Telemanipulation: Impedance Control of a Force Reflecting Hand Controller.* Master's thesis, Department of Mechanical Engineering, M.I.T., Cambridge, MA, August 1987.

[110] E. C. Poulton. *Tracking Skill and Manual Control.* Academic Press, New York, 1974.

[111] A. Prochazka and P. St. J. Trend. Instability in human forearm movements studied with feed-back-controlled muscle vibration. *Journal of Physiology (London)*, 402:421–442, 1988.

[112] D. W. Repperger. Biodynamic resistant control stick. United States Patent Number 4,477,043, October 1987.

[113] D. W. Repperger and C. Goodyear. Active controllers and the time duration to learn a task. In *Proceedings of the 21st Annual Conference on Manual Control*, pages 18.1–18.12, Moffets Field, CA, June 1985.

[114] D. W. Repperger and D. McCollor. Active sticks—A new dimension in controller design. In *Proceedings of the 20th Annual Conference on Manual Control*, pages 719–734, 1984.

[115] D. D. Reynolds and R. J. Falkenberg. Three- and four-degrees-of-freedom models of the vibration response of the human hand. In A. J. Brammer and W. Taylor, editors, *Vibration Effects on the Hand and Arm in Industry*, pages 117–132. John Wiley and Sons, New York, 1982.

[116] R. R. Rietz and R. N. Stiles. A viscoelastic-mass mechanism as a basis for normal postural tremor. *Journal of Applied Physiology*, 37(6):852–860, 1974.

[117] P. O. Riley and M. J. Rosen. Evaluating manual control devices for those with tremor disability. *Journal of Rehabilitation Research and Development*, 24(2):99–110, 1987.

[118] J. G. Robson. The effect of loading upon the frequency of muscle tremor. *Journal of Physiology (London)*, 149:29–30, 1959.

[119] P. E. Roland. Sensory feedback to the cerebral cortex during voluntary movement in man. *The Behavioral and Brain Sciences*, 1:129–171, 1978.

[120] M. J. Rosen. Tremor suppressing hand controls. United States Patent Number 4,689,449, August 1987.

[121] M. J. Rosen and B. D. Adelstein. Design of a two-degree-of-freedom manipulandum for tremor research. In *Proceedings of the Sixth Annual Conference of the IEEE Engineering in Medicine and Biology Society*, pages 47–51, Los Angeles, CA, September 1984.

[122] M. E. Rosheim. A new pitch-yaw-roll mechanical robot wrist actuator. In *Robots 9 Conference Proceedings*, Detroit, MI, June 1985.

[123] M. E. Rosheim. Four new robot wrist actuators. In *Robots 10 Conference Proceedings*, Chicago, IL, April 1986.

[124] M. E. Rosheim. Singularity-free hollow spray painting wrist. In *Robots 11 Conference Proceedings*, Chicago, IL, April 1987.

[125] J. C. R[illegible]beek and R. J. Janssen. Computer-controlled manipulator/display system for human-movement studies. *Medical and Biological Engineering and Computing*, pages 304–308, 1984.

[126] M. A. Russo. Master's thesis in progress, Department of Mechanical Engineering, M.I.T., Cambridge, MA.

[127] K. Salisbury, W. Townsend, B. Eberman, and D. DiPietro. Preliminary design of a whole-arm manipulation system (WAMS). In *Proceedings of the 1988 IEEE International Conference on Robotics and Automation*, pages 254–260, Philadelphia, PA, April 1988.

[128] M. Salzer. Three-dimensional tremor measuremnts of the hand. *Journal of Biomechanics*, 5:217–221, 1972.

[129] E. M. Schmidt. Electronically controlled load for monkey manipulandum. *Electroencephalography and Clinical Neurophysiology*, 35:95–97, 1973.

[130] T. B. Sheridan. Human supervisory control of robot systems. In *Proceedings of the IEEE International Robotics Conference*, San Francisco, April 1986.

[131] T. Stackhouse. A new concept in robot wrist flexibility. In *Proceedings of the 9th International Symposium on Industrial Robots*, pages 589–599, Washington DC, 1979.

[132] R. B. Stein and M. N. Oguztoreli. Tremor and other oscillations in neuromuscular systems. *Biological Cybernetics*, 22:147–157, 1976.

[133] R. B. Stein and M. N. Oguztoreli. Reflex involvement in the generation and control of tremor and clonus. In J. E. Desmedt, editor, *Physiological Tremor, Pathological Tremors and Clonus, Progress in Clinical Neurophysiology, Volume 4*, pages 28–50. S. Karger, Basel, 1978.

[134] R. N. Stiles. Mechanical and neural feedback factors in postural hand tremor of normal subjects. *Journal of Neurophysiology*, 44(1):40–59, 1980.

[135] R. N. Stiles. Lightly damped hand oscillations: Acceleration-related feedback and system damping. *Journal of Neurophysiology*, 50(2):327–343, 1983.

[136] R. N. Stiles and J. E. Randall. Mechanical factors in human tremor frequency. *Journal of Applied Physiology*, 23:324–330, 1967.

[137] A. Struppler, F. Erbel, and F. Velho. An overview on the pathophysiology of Parkinsonian and other pathological tremors. In J. E. Desmedt, editor, *Physiological Tremor, Pathological Tremors and Clonus, Progress in Clinical Neurophysiology, Volume 4*, pages 114–128. S. Karger, Basel, 1978.

[138] I. E. Sutherland. The ultimate display. In *Information Processing 1965, Proceedings of the IFIP Congress 65*, pages 506–508, New York, May 1965. North-Holland Publishing Company.

[139] G. G. Sutton and K. Sykes. The effect of withdrawal of visual presentation of errors upon the frequency spectrum of tremor in a manual task. *Journal of Physiology (London)*, 190:281–292, 1967.

[140] A. Tadros. Master's thesis in progress, Department of Mechanical Engineering, M.I.T., Cambridge, MA.

[141] D. S. Tavkhelidze and N. S. Davitashvili. Kinematic analysis of five-link spherical mechanisms. *Mechanism and Machine Theory*, 9:181–190, 1974.

[142] H. Teravainen, E. Evarts, and D. Calne. Effects of kinesthetic inputs on Parkinsonian tremor. In L. J. Poirier, T. L. Sourkes, and P. J. Bedard, editors, *Advances in Neurology*, pages 161–173. Raven Press, New York, 1979.

[143] H. P. Van Cott and R. G. Kinkade. *Human Engineering Guide to Equipment Design.* U. S. Government Printing Office, Washington DC, 1972.

[144] J. Vertut and P. Coiffet. *Teleoperation and Robotics: Evolution and Development.* Prentice-Hall, Englewood Cliffs, NJ, 1984.

[145] T. Villis and J. Hore. Effects of changes in mechanical state of limb on cerebellar intention tremor. *Journal of Neurophysiology*, 40(5):1214–1224, 1977.

[146] T. Villis and J. Hore. Central neural mechanisms contributing to cerebellar tremor produced by limb perturbations. *Journal of Neurophysiology*, 43(2):279–291, 1980.

[147] G. Werner. Higher functions of the nervous system. In V. B. Mountcastle, editor, *Medical Physiology*, pages 629–646. The C. B. Mosby Company, St. Louis, 1980.

[148] D. E. Whitney. Force feedback control of manipulator fine motions. *ASME Journal of Dynamic Systems, Measurement and Control*, 99:91–97, 1977.

[149] D. E. Whitney. Historical perspective and state of the art in robot force control. In *Proceedings of the 1985 IEEE International Conference on Robotics and Automation*, pages 262–268, St. Louis, MO, March 1985.

[150] C. M. Winey III. *Computer Simulated Visual and Tactile Feedback as an Aid to Manipulator and Vehicle Control.* Master's thesis, Department of Mechanical Engineering, M.I.T., Cambridge, MA, June 1981.

[151] J. J. Wlassich. Nonlinear force feedback impedance control. Master's thesis, Department of Mechanical Engineering, M.I.T., Cambridge, MA, February 1986.

[152] R. R. Young and K.-E. Hagbarth. Physiological tremor enhanced by manoeuvres affecting the segmental stretch reflex. *Journal of Neurology, Neurosurgery, and Psychiatry*, 43:248–256, 1980.

[153] G. I. Zahalak and S. C. Cannon. Predictions of the existence, frequency, and amplitude of physiological tremor in normal man based on measured frequency-response characteristics. *Journal of Biomechanical Engineering*, 105:249–257, 1983.

[154] D. H. Zilm, E. M. Sellers, R. C. Frecker, and H. Kunov. The nature and etiology of normal and alcohol withdrawal tremor. *IEEE Transactions on Biomedical Engineering*, BME-26(1):3-10, 1979.

Appendix A

Computer Hardware

This appendix lists the components of the two computer systems employed in the virtual environment system.

A.1 LSI-11/23 System Components

The hardware components of the host computer system that are used in the implementation of the virtual environment system are listed in this appendix. The portable microcomputer system was configured principally by Durfee [49] begining in 1982.

- Q-Bus backplane in an ADAC System 1000 Chassis (ADAC Corp., Woburn MA).
- LSI-11/23 CPU (Digital Equipment Corp., Maynard MA; part no. KDF11-AA).
- Floating point processor (Digital Equipment Corp.; part no. KEF11-AA).
- 196 kByte RAM distributed over two 64 kByte memory boards (Digital Equipment Corp.; part no. MSV11-DD) and two multifunction boards (Digital Equipment Corp.; part no. MXV11-AC) each with 32 kBytes.
- RS232C serial communication ports—two channels on one of the above multifunction boards and a four channel serial card (Digital Equipment Corp.; part no. DLV11-J) for a total of six serial lines.

- One 1 MByte floppy disk drive (emulating RX02) and one 7.8 MByte Winchester drive (emulating a reduced RL02) with disk controller (Data Systems Design, Inc., present name Qualogy, Inc., San Jose CA.; part no. DSD-880-L11-A).
- Real time clock (ADAC Corp.; part no. 1601 GPT).
- A/D converter with 16 channel multiplexed, pseudo differential input with 100 kHz per channel, 12 bit bipolar conversion (ADAC Corp.; part no. 1032AD 16PD-4-1PGA-0).
- Digital I/O with 16 bit input and 16 bit output parallel TTL compatible digital communication (ADAC Corp.; part no. 1632TTL-16I-16O).
- D/A with four channel output, each with 12 bit resolution and $\pm$ 10 volt range (ADAC Corp.; part no. DA-4-A-V-0-0).
- VT125 graphics terminal consisting of a VT100-AA terminal with VT1XX-CB graphics upgrade (Digital Equipment Corp.)

Additional peripherals employed in this work that were connected to the host computer serial ports include:

- Dot matrix line printer (Epson America, Inc., Torrance CA; part no. FX-100) augmented by a serial interface and 8 kByte data buffer (Practical Peripherals, Inc., Westlake Village CA; part no. MBS-8K).
- Six color graphics pen plotter (Hewlett Packard Co., San Diego CA; part no. HP 7545A).

A.2 Amiga Personal Computer

The graphics computer used for visual display in the virtual environment system is an Amiga 1000 (Commodore Business Machines, Inc., West Chester PA). Its components include:

- The base 256 kByte memory with a 256 kByte add-on memory cartridge (part no. Amiga 1050) plus an add-on internal memory board (Spirit Techonology Corp., Salt Lake City UT; part no. IN1000) partially populated with 512 kByte DRAM, for a total of 1 Mbyte.
- 13 inch diagonal, raster scan, RGB monitor (part no. Amiga 1080). Capable of 640 by 400 resolution at 30 Hz refresh rate in high resolution double buffered interlace mode.
- Two 880 kByte 3.5 inch floppy disk drives, one internal to the main unit, the other drive (part no. Amiga 1010) is external.

Appendix B

Control Interface Unit Components

This appendix summarizes the functions performed by the six circuit cards internal to the Control Interface Unit (*i.e.*, the CIU or "blue box"), and three related boards. Together, these custom designed components are responsible for sensor signal conditioning, system safety, and load control at the manual interface.

Card 1 Displacement sensor signal conditioning comprised of optical encoder quadrature decoding, on-board D/A conversion, and offset and bias adjustment.

Card 2 Tachometer signal pre-amplification.

Regulated ± 6 volt supplies for force transducer.

Second order low pass filtering (240 Hz cutoff) on all sensor signals—displacement, velocity, acceleration, and force—to attenuate servo-amplifier PWM switching noise and encoder decoder clock noise before introduction to CIU back plane.

First order high pass filtering (0.007 Hz breakpoint) of accelerometer signals to remove sensors' offset drift.

Card 2a (in a separate preamplifier module in handle mechanism quadrant) Force transducer and accelerometer signal pre-amplification.

Power supply connections for both accelerometers and the two-axis force transducer.

Card 3 Feedback gain adjust for analog impedance controller. Includes parallel interface for LSI-11/23 16-bit digital output port, feedback channel select, feedback sign select, and feedback gain set (*i.e.*, MDAC attenuation level).

Card 4 Impedance controller feedback summing structure for each axis. Includes further gain adjustment and precise offset trim for each feedback signal, reference input (virtual trajectory) from computer D/A into each axis, and summing amplifier to combine gain adjusted sensor feedback signals.

Notch filter compensation for mechanical resonances in each axis.

Card 5 Safety monitoring circuitry for servo amplifier disable and system shutdown. Includes acceleration threshold detection, limit switch activation detection, and additional inputs from computer DAC and servo amplifier enable pushbutton.

Hardwired shutdown logic also contained on this card. Shutdown logic connects to: relay in overall system's AC power latching circuitry; and to the motor disable built into each servo amplifier card.

Card 5a (in a small box in handle quadrant) Position limit switch debouncer.

Card 6 Further gain adjustment of all eight sensor signals (independent of feedback lines) to maximize dynamic range prior to anti-alias filtering and A/D conversion by LSI-11.

Card 6a (separate module lies in path between Card 6 and LSI-11/23 A/D converter) Fifth-order lowpass anti-aliasing filters based on switched capacitor ICs for all eight sensor signals. All filters set to 25 Hz cutoff to reduce noise corruption of low level signals.

An alternate "break-out" box to join card 6 and the host computer A/D converter, without passing through antialiasing filters, was also constructed.

Appendix C

Serial Three Link Arm Kinematics

The transformation of kinematics from manipulandum coordinates (*i.e.*, as measured by the system transducers) into three link arm coordinates, for either a natural human arm or a mechanical linkage constrained to the degrees of freedom as shown in Figure C.1, involves two series of computational steps. The first steps transfer values from the fixed manipulandum reference frame (x, y, z) into an inertial frame (x_e, y_e, z_e) that has its origin fixed at the "shoulder" joint. The second series of steps entail the calculation of angular quantities at the "shoulder," "elbow," and "wrist" joints based on arm endpoint (*i.e.*, manipulandum endpoint) location and motion in the shoulder reference frame.

C.1 Manipulandum to "Shoulder" Frame Transformations

The transformations from the Cartesian manipulandum endpoint coordinates, (x, y, z), used throughout the thesis text, into the "shoulder" based reference frame, (x_e, y_e, z_e), are given by

$$x_e = x + L_x \tag{C.1}$$

$$y_e = y + L_y \tag{C.2}$$

$$z_e = z - R_o \tag{C.3}$$

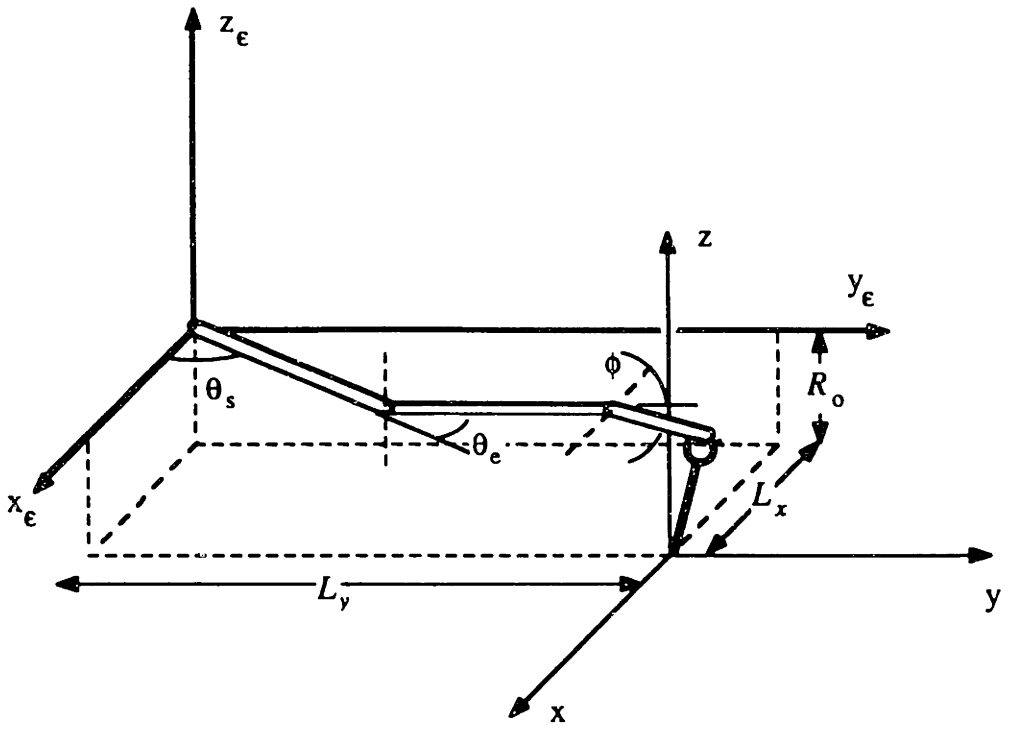

Figure C.1: Three link serial arm, including links, joints, and the shoulder and manipulandum fixed coordinate frames. (x, y, z) and $(x_\epsilon, y_\epsilon, z_\epsilon)$ are fixed inertial frames; the former with its origin at the center of the manipulandum linkage rotation and the latter with its origin at the shoulder joint. The proximal most link, rotating about z_ϵ with angle θ_s as measured from the x_ϵ axis, has length L_u. The next link, of length L_f, rotates with respect to link L_u through angle θ_e, where the axis of θ_e is parallel to the axis of θ_s. The distal arm link, shown attached to the top of the manipulandum link, has length L_H and lies in line with link L_f. Link L_H rotates out of the (x_ϵ, y_ϵ) plane through angle ϕ.

Referring to Figure C.1, the constants L_x and L_y are the (x, y) coordinates of the manipulandum frame's origin in the shoulder reference frame; R_o, the manipulandum handle shaft length, is the z coordinate.

Differentiating once, the velocity relations are:

$$\dot{x}_e = \dot{x} \tag{C.4}$$

$$\dot{y}_e = \dot{y} \tag{C.5}$$

$$\dot{z}_e = \dot{z} \tag{C.6}$$

Differentiating a second time, the acceleration relations are:

$$\ddot{x}_e = \ddot{x} \tag{C.7}$$

$$\ddot{y}_e = \ddot{y} \tag{C.8}$$

$$\ddot{z}_e = \ddot{z} \tag{C.9}$$

C.2 Arm Joint Quantities from "Shoulder" Frame Kinematics

The arm linkage depicted in Figure C.1 consists of three serial links plus ground. Starting from the torso or mechanical ground, the links include an "upper arm" of length L_u, a forearm of length L_f, and a "hand' of length L_H.[1] The "shoulder" and "elbow" in the linkage are modelled as simple pin joints that restrict the upper arm and forearm to motion in the horizontal plane. θ_s, the shoulder angle, denotes the rotation of the upper arm link as measured with respect to the (x_e, y_e, z_e) reference frame. The elbow angle,

[1]The hand link here serves the same role as the "compatibility" coupling described in Section 6.3. It is included between the manipulandum hand grip and the forearm link of the planar manipulator to provide an extra degree of freedom corresponding to wrist flexion-extension with the anatomical forearm pronated.

θ_e, gives the rotation of the forearm link with respect to the upper arm link. The "wrist" of the chain is treated as a pin joint with a horizontal axis that lies perpendicular to the forearm, such that changes in wrist angle ϕ cause the hand to be elevated or lowered out of the plane that constrains the two proximal arm segments.

The forward geometry for the three link arm is expressed by

$$x_e = L_u \cos\theta_s + (L_f + L_H \cos\phi)\cos(\theta_s + \theta_e) \tag{C.10}$$

$$y_e = L_u \sin\theta_s + (L_f + L_H \cos\phi)\sin(\theta_s + \theta_e), \tag{C.11}$$

$$z_e = L_H \sin\phi \tag{C.12}$$

where x_e, y_e, and z_e are now the Cartesian coordinates describing the location of the hand link "endpoint" (*i.e.*, its interface with the manipulandum endpoint).

The Jacobian

$$\mathbf{J}_e = \frac{\partial \mathbf{x}_e}{\partial \mathbf{q}_e} \tag{C.13}$$

where

$$\mathbf{x}_e = \begin{bmatrix} x_e \\ y_e \\ z_e \end{bmatrix} \tag{C.14}$$

and

$$\mathbf{q}_e = \begin{bmatrix} \theta_s \\ \theta_e \\ \phi \end{bmatrix} \tag{C.15}$$

is derived from the forward kinematic relations described by Equations (C.10), (C.11),

and (C.12). Explicitly, the terms of the Jacobian are

$$\mathbf{J}_e = \begin{bmatrix} -\left[L_u \sin\theta_s + L_f^* \sin(\theta_s + \theta_e)\right] & -L_f^* \sin(\theta_s + \theta_e) & -L_H \sin\phi \cos(\theta_s + \theta_e) \\ \left[L_u \cos\theta_s + L_f^* \cos(\theta_s + \theta_e)\right] & L_f^* \cos(\theta_s + \theta_e) & -L_H \sin\phi \sin(\theta_s + \theta_e) \\ 0 & 0 & L_H \cos\phi \end{bmatrix} \tag{C.16}$$

in which

$$L_f^* = L_f + L_H \cos\phi \tag{C.17}$$

The Jacobian can then be used to express the forward velocity transformation

$$\dot{\mathbf{x}}_e = \mathbf{J}_e \dot{\mathbf{q}}_e \tag{C.18}$$

and, by differentiating again, the forward acceleration transformation

$$\ddot{\mathbf{x}}_e = \mathbf{J}_e \ddot{\mathbf{q}}_e + \dot{\mathbf{J}}_e \dot{\mathbf{q}}_e \tag{C.19}$$

To compute the joint angles, the inverese geometric relations are set up and solved in the following order:

$$\phi = \sin^{-1}\left(\frac{z_e}{L_H}\right) \tag{C.20}$$

$$\theta_e = \cos^{-1}\left(\frac{x_e^2 + y_e^2 - L_u^2 - (L_f + L_H \cos\phi)^2}{2L_u (L_f + L_H \cos\phi)}\right) \tag{C.21}$$

$$\theta_s = \tan^{-1}\left(\frac{y_e}{x_e}\right) - \tan^{-1}\left(\frac{(L_f + L_H \cos\phi)\sin\theta_e}{L_u + (L_f + L_H \cos\phi)\cos\theta_e}\right) \tag{C.22}$$

The inverse velocity transformation is given by

$$\dot{\mathbf{q}}_e = \mathbf{J}_e^{-1}\dot{\mathbf{x}}_e \tag{C.23}$$

Thus, inverting the Jacobian in Equation (C.16),

$$\mathbf{J}_e^{-1} = \begin{bmatrix} \left(\frac{\cos(\theta_s+\theta_e)}{L_u \sin\theta_e}\right) & \left(\frac{\sin(\theta_s+\theta_e)}{L_u \sin\theta_e}\right) & \left(\frac{\tan\phi}{L_u \sin\theta_e}\right) \\ -\left(\frac{L_u\cos\theta_s + L_f^*\cos(\theta_s+\theta_e)}{L_u L_f^* \sin\theta_e}\right) & -\left(\frac{L_u\sin\theta_s + L_f^*\sin(\theta_s+\theta_e)}{L_u L_f^* \sin\theta_e}\right) & -\left(\frac{\tan\phi(L_f^*+L_u\cos\theta_e)}{L_u L_f^* \sin\theta_e}\right) \\ 0 & 0 & \left(\frac{1}{L_H\cos\phi}\right) \end{bmatrix} \tag{C.24}$$

and then substituting into Equation (C.23) yields the inverse velocity relations:

$$\dot{\theta}_s = \left(\frac{\cos(\theta_s+\theta_e)}{L_u\sin\theta_e}\right)\dot{x}_e + \left(\frac{\sin(\theta_s+\theta_e)}{L_u\sin\theta_e}\right)\dot{y}_e + \left(\frac{\tan\phi}{L_u\sin\theta_e}\right)\dot{z}_e \tag{C.25}$$

$$\begin{aligned} \dot{\theta}_e = & -\left(\frac{L_u\cos\theta_s + (L_f + L_H\cos\phi)\cos(\theta_s+\theta_e)}{L_u(L_f+L_H\cos\phi)\sin\theta_e}\right)\dot{x}_e \\ & -\left(\frac{L_u\sin\theta_s + (L_f + L_H\cos\phi)\sin(\theta_s+\theta_e)}{L_u(L_f+L_H\cos\phi)\sin\theta_e}\right)\dot{y}_e \\ & -\left(\frac{\tan\phi(L_f + L_H\cos\phi + L_u\cos\theta_e)}{L_u(L_f+L_H\cos\phi)\sin\theta_e}\right)\dot{z}_e \end{aligned} \tag{C.26}$$

$$\dot{\phi} = \left(\frac{1}{L_H\cos\phi}\right)\dot{z}_e \tag{C.27}$$

The inverse acceleration transformation is derived by rearranging Equation (C.19) such that

$$\ddot{\mathbf{q}}_e = \mathbf{J}_e^{-1}\ddot{\mathbf{x}}_e - \mathbf{J}_e^{-1}\dot{\mathbf{J}}_e\dot{\mathbf{q}}_e \tag{C.28}$$

which is equivalent to the derivative with respect to time of Equation (C.23). Thus, the complete acceleration transformations upon expanding Equation (C.28) are

$$\begin{aligned}
\ddot{\theta}_s &= \left(\frac{\cos(\theta_s+\theta_e)}{L_u \sin\theta_e}\right)\ddot{x}_e + \left(\frac{\sin(\theta_s+\theta_e)}{L_u \sin\theta_e}\right)\ddot{y}_e + \left(\frac{\tan\phi}{L_u \sin\theta_e}\right)\ddot{z}_e \\
&+ (\cot\theta_e)\,\dot{\theta}_s^2 + \left(\frac{L_f + L_H\cos\phi}{L_u\sin\theta_e}\right)\left(\dot{\theta}_s+\dot{\theta}_e\right)^2 \\
&+ \left(\frac{L_H}{L_u\sin\theta_e\cos\phi}\right)\dot{\phi}^2
\end{aligned} \tag{C.29}$$

$$
\begin{aligned}
\ddot{\theta}_e \;=\; & -\left(\frac{L_u\cos\theta_s + (L_f + L_H\cos\phi)\cos(\theta_s+\theta_e)}{L_u\,(L_f + L_H\cos\phi)\sin\theta_e}\right)\ddot{x}_e \\
& -\left(\frac{L_u\sin\theta_s + (L_f + L_H\cos\phi)\sin(\theta_s+\theta_e)}{L_u\,(L_f + L_H\cos\phi)\sin\theta_e}\right)\ddot{y}_e \\
& -\left(\frac{\tan\phi\,(L_f + L_H\cos\phi + L_u\cos\theta_e)}{L_u\,(L_f + L_H\cos\phi)\sin\theta_e}\right)\ddot{z}_e \\
& -\left(\frac{L_u + (L_f + L_H\cos\phi)\cos\theta_e}{(L_f + L_H\cos\phi)\sin\theta_e}\right)\dot{\theta}_s^2 \\
& -\left(\frac{L_f + L_H\cos\phi + L_u\cos\theta_e}{L_u\sin\theta_e}\right)\left(\dot{\theta}_s + \dot{\theta}_e\right)^2 \\
& -\left(\frac{L_H\,(L_f + L_H\cos\phi + L_u\cos\theta_e)}{L_u\,(L_f + L_H\cos\phi)\sin\theta_e\cos\phi}\right)\dot{\phi}^2 \\
& +\left(\frac{2L_H\sin\phi}{L_f + L_H\cos\phi}\right)\left(\dot{\theta}_s + \dot{\theta}_e\right)\dot{\phi}
\end{aligned}
\tag{C.30}
$$

$$
\ddot{\phi} \;=\; \left(\frac{1}{L_H\cos\phi}\right)\ddot{z}_e + (\tan\phi)\,\dot{\phi}^2 \tag{C.31}
$$

Appendix D

Informed Consent Document

The Committee on the Use of Humans as Experimental Subjects (COUHES) in accordance with the Department of Health and Human Services and M.I.T. regulations requires documentation of informed consent. The approved Informed Consent Statement, which must be signed by each subject, is included in the following pages.

INFORMED CONSENT STATEMENT

Project Title: Whole Arm Tremor Response to Non-Invasive Mechanical Loading

We are interested in studying how tremors and other unintentional movements respond to externally applied mechanical loads. We hope to learn from these tests what causes different types of unintentional movements and use this information to help us develop 1) devices such as wearable braces and wheelchair controls that selectively reduce abnormal movements in the tremor disabled and 2) methods to help diagnose different types of tremor and involuntary movement.

You will be asked to view a screen on which two markers will appear. One will move the way the arm we are testing moves, while the other will be under our control and may move unpredictably. The limb that we will test will be fitted comfortably to an apparatus that measures its position, force and other mechanical quantities. You will be asked to try to move the limb being tested in such a way as to make your marker on the screen keep up with the target, somewhat like a video game. In some experiments the apparatus will apply forces that may make it easier for you to perform this tasks; in others it will not.

The target catching task will be performed repeatedly for a few minutes at a time. Between trials, you may rest as long and as frequently as necessary for your comfort. An experimental session will last at least an hour — counting breaks — but beyond that point their length and scheduling will be suited to your capacity and convenience.

Data from our equipment related to your movements and other information, including your and our comments, obtained during each session will be kept in a confidential file. If this information is used for education or published reports, your name will be withheld. Still photographs and short sequences of video tape may be taken for our records if you consent, but this material will not be used for education or publication if you request that it be kept confidential.

The measurement and loading device which you will operated will be fitted to you and produce no discomfort. Although much of the equipment we will use is electronic in nature, no shock hazard is present. Sometimes, small electrodes will be placed on your skin to measure muscle action. No pain or shocks or discomfort of any kind are involved from these electrodes.

You may withdraw from participation in this study at any time. You are encouraged to ask questions and make comments or suggestions at any time. The success of these experiments depends to some extent on your willingness to do so.

The goal of these studies is limited. We will not, as part of this study, be able to build a practical tremor-suppressing device for you to use in normal activities. If these experiments are successful, the design of such devices will have been helped by your participation. There are, at present, more conventional methods of treatment which may be more appropriate for your movement disorder. It has not been conclusively demonstrated that the techniques to be tried in these experiments are useful alternatives to present methods of treatment.

I have fully explained to _____ the nature
Subject/Parent/Guardian
and purpose of the above procedure and will answer all questions to the best of my ability.

_____ _____
Date Investigator's Signature

I have been satisfactorily informed of the above-described procedure and I agree to participate in these experiments.

In the unlikely event of physical injury resulting from participation in this research, I understand that medical treatment will be available from the M.I.T. Medical Department, including first aid, emergency treatment and follow-up care as needed, and that my insurance carrier may be billed for the cost of such treatment. However, no compensation can be provided for medical care apart from the foregoing. I further understand that making such medical treatment available, or providing it, does not imply that such injury is the Investigator's fault. I also understand that by my participation in this study I am not waiving any of my legal rights. (Further information may obtained by calling the Institute's Insurance and Legal Affairs Office at 253-2822.).

I understand that I may also contact the Chairman of the Committee on the Use of Humans as Experimental subjects, Dr. George Wolf (MIT 56-213, 253-6781), if I feel that I have been treated unfairly as a subject.

_____
Subject/Parent/Guardian

_____ _____
Date Witness to Signature